

**ORIGAMI AND TENSEGRITY:
STRUCTURES AND METAMATERIALS**

A Dissertation
Presented to
The Academic Faculty

By

Ke Liu

In Partial Fulfillment
of the Requirements for the Degree
Doctor of Philosophy in the
School of Civil and Environmental Engineering

Georgia Institute of Technology

May 2019

Copyright © Ke Liu 2019

**ORIGAMI AND TENSEGRITY:
STRUCTURES AND METAMATERIALS**

Approved by:

Dr. Glaucio H. Paulino
School of Civil and Environmental
Engineering
Georgia Institute of Technology

Dr. Paolo Gardoni
Department of Civil and Environ-
mental Engineering
*University of Illinois at Urbana-
Champaign*

Dr. Robert J. Lang
Lang Origami

Dr. Arash Yavari
School of Civil and Environmental
Engineering
Georgia Institute of Technology

Dr. Phanish Suryanarayana
School of Civil and Environmental
Engineering
Georgia Institute of Technology

Dr. Tomohiro Tachi
Graduate School of Arts and Sci-
ences
University of Tokyo

Dr. David Zeb Rocklin
School of Physics
Georgia Institute of Technology

Date Approved: December 05, 2018

Dedicated to
my parents, Mr. Tianxiong Liu and Mrs. Wenhong Zhang,
for their endless support

ACKNOWLEDGEMENTS

I wish to thank my advisor Prof. Glaucio Paulino. None of this work would have been possible without him. Working with Prof. Paulino has been a wonderful experience. I learned so much from him about not just how to do good research, but also how to be a good person in general. Prof. Paulino has set an example of excellence as a researcher, mentor, instructor, and role model. His passion, insight, and long term vision have greatly influenced my research. From a personal perspective, his caring, support, and integrity have always been inspirational. I would like to extend my acknowledgement to Mrs. Berta Paulino, wife of my advisor, for bringing inspiration to my research from an artistic perspective, and for her caring and support.

I would like to thank Prof. Paolo Garodni, Dr. Robert Lang, Prof. Arash Yavari, Prof. Phanish Suryanarayana, Prof. Tomohiro Tachi, and Prof. Zeb Rocklin for participating in my Ph.D. defense committee. Prof. Paolo Garodni and Prof. Tomohiro Tachi have been invaluable collaborators who enriched my experience and knowledge. I am also very thankful to the invaluable suggestions, comments and feedback from Prof. Arash Yavari, Prof. Phanish Suryanarayana, Prof. Zeb Rocklin, and Dr. Robert Lang.

I am grateful to Prof. Jerry Qi, Dr. Jiangtao Wu, Dr. Pradeep Pratapa, Dr. Tomas Zegard, and Larissa Novelino for their contributions to the research. It is a great pleasure to collaborate with all of them. I wish to thank Prof. Evgeni Filipov, Prof. Yan Chen, and Dr. Yves Klett for helpful discussions, ideas, and feedback about my research, which have been very helpful.

I am also very grateful to my friends and colleagues who have provided insight, and spurred discussions throughout my graduate study. I wish to acknowledge Xiaojia (Shelly) Zhang, Heng Chi, Tuo Zhao, Emily Sanders, Oliver Giraldo-Londoño, Yang Jiang, Devyani Choudhary, Wei Peng, Fernando Senhora, Erol Unal, Weichen Li, Cameron Talischi, Daniel Spring, Sofie Leon, Arun Gain, Junho Chun, and Javier Vila Morán. I also wish to

thank other friends who have made my experience at graduate school so enjoyable: Liqun Lu, Tao Zhu, Yang Zhang, Sensen Li, Jilai Ding, Xiaotang Du, Xinjun Dong, Dan Li, Yidong Qin, Taiyu Song, Xi (Sisi) Liu, Yijian Zhang, Yanjie Tong, Qi Liu, Zonglin Li.

I thank Prof. Tomohiro Tachi and Prof. Yasushi Yamaguchi for hosting my five-month visit to the University of Tokyo, which has been an amazing and unforgettable experience. I owe a debt of gratitude to Qiqi Gao and Duosheng Yu for their kind help while I was in Tokyo, Japan.

I wish to thank the machine shop of the School of CEE, especially Andy Udell and Blake Baklini, who have helped me to assemble custom devices that are important to my research. Moreover, I wish to thank other staff members who helped me at the School: Robert Simon, Carol Maddox, Daniela Estrada, Melisa Hubbs, Christy Lanoue, Belal El-naggar, and Jamia Luckett.

I wish to thank Dr. David Lawrence and Dr. Kate Williams for teaching me how to be a great teacher – I learned a lot and had much fun working on the “Tech-to-Teaching” program.

I gratefully acknowledge the support from the US National Science Foundation (NSF) through grant no.1538830 (Geometric Mechanics of Cellular Origami Assemblages), China Scholarship Council (CSC), the Raymond Allen Jones Chair endowment, and Georgia Tech. Without their funding, I would not have the opportunities to pursue my research goals and attend workshops and conferences.

Finally and most importantly, I want to thank my parents, Tianxiong and Wenhong, for their endless support and unconditional love. I cannot thank them enough for all the things that they have done for me. I feel so fortunate to be their son.

TABLE OF CONTENTS

Acknowledgments	iv
List of Tables	xiii
List of Figures	xiv
Chapter 1: Introduction	1
1.1 Origami	2
1.2 Tensegrity	4
1.3 Organization of The Thesis	7
I Origami	9
Chapter 2: Nonlinear Structural Analysis of Non-rigid origami	10
2.1 Introduction	10
2.2 Nonlinear formulation for bar-and-hinge models	14
2.2.1 Principle of stationary potential energy	14
2.2.2 Implementation of bar elements	16
2.2.3 Rotational spring elements: basic description	19
2.2.4 Geometry of rotational spring element: enhanced description	21
2.2.5 Verification using finite differences	28

2.2.6	Constitutive relationships for bars	28
2.2.7	Constitutive relationships for rotational springs	30
2.3	Discretization schemes	33
2.3.1	The N4B5 scheme and its generalization to polygonal panels	34
2.3.2	The N5B8 scheme and its generalization to polygonal panels	35
2.4	Solution algorithms for nonlinear analysis	37
2.4.1	Force loading	37
2.4.2	Displacement loading	39
2.5	Origami simulations	41
2.5.1	A simple fold	41
2.5.2	Folding and bending of Miura-ori	43
2.5.3	Pop-through defect of Miura-ori: bistability	48
2.5.4	Multi-stability of the Kresling pattern	50
2.5.5	Displacement load on a generalized Miura-ori	54
2.6	Concluding Remarks	54
Chapter 3: Geometry and Mechanics of Hyperbolic Paraboloid Origami		57
3.1	Introduction	57
3.2	Analytical limit of the folded geometry	60
3.2.1	Isometric geometry of corrugations	60
3.2.2	The differential geometry of global shape	68
3.2.3	The unexpected solution	71
3.2.4	Discussion on the analytical solution	72

3.3	Physical shape of folded hypar origami	73
3.3.1	Sample fabrication and testing	76
3.4	Numerical investigation	77
3.4.1	Bar-and-hinge implementation for numerical simulations	77
3.4.2	Simulated folding process	79
3.4.3	On special bistability of the hypar origami	79
3.5	Hypar tessellation with many stable states	81
3.6	Concluding Remarks	84
Chapter 4:	Big influence of small imperfections in origami assemblages	85
4.1	Introduction	85
4.2	Theoretical consideration on the impact of geometric imperfections	86
4.2.1	First-order rigid foldability	89
4.3	Results and Discussion	91
4.3.1	Experimental Quantification	91
4.3.2	Numerical Quantification	94
4.4	Correlation with Geometric Design Constraints	97
4.4.1	Hypothesis for the correlation between Kawasaki excess and mechanical properties	99
4.5	Materials and Methods	103
4.5.1	Sample fabrication	103
4.5.2	Miura-ori Compression test	104
4.5.3	Stretching stiffness	104
4.5.4	Folding and bending stiffness	106

4.6 Concluding Remarks	109
Chapter 5: Geometric Mechanics of the Morph Pattern	
5.1 Introduction	111
5.2 Geometry and configuration space of the Morph pattern	112
5.2.1 Poisson's ratio	117
5.2.2 In-plane linear stiffness	118
5.3 Out-of-plane bending of the Morph pattern	121
5.3.1 Coordinate system, vertices and normals	122
5.3.2 Constraints on bending rotations	124
5.3.3 Bending curvatures	125
5.3.4 Poisson's ratio in bending	129
5.3.5 Out-of-plane bending stiffness	130
5.4 Recovery of standard Eggbox relationships from the Morph pattern	132
5.5 Recovery of standard Miura-ori relationships from the Morph pattern	133
5.6 Hybrid patterns	135
5.6.1 Configuration space of hybrid patterns	136
5.6.2 In-plane Poisson's ratio of hybrid patterns	138
5.6.3 Mode locking during in-plane deformation	140
5.7 Concluding Remarks	141
Chapter 6: Periodic origami pattern with programmable multi-stability: Breaking connectedness of configuration space	
6.1 Introduction	143

6.2	Geometry of the standard “Shrimp” unit cell	144
6.3	Creating topological bistability by breaking connectedness of configuration space	147
6.3.1	Estimating peak energy during the non-rigid folding range	149
6.3.2	Estimating stored energy after snapping	152
6.3.3	Determining emergence of bistability	153
6.4	Verifying bistable behavior by numerical simulations	153
6.5	Assembling “Shrimp” tessellations with programmable multi-stability . . .	156
6.6	Fabricating the “Shrimp” pattern	156
6.7	Concluding Remarks	160
II	Tensegrity	162
Chapter 7:	Tensegrity topology optimization by force maximization on arbitrary ground structures	163
7.1	Introduction	163
7.2	Overview of form-finding methods	165
7.3	Topology optimization formulation	169
7.3.1	Formulation	169
7.3.2	Mixed integer linear programming (MILP) reformulation	175
7.3.3	Matrix notation for the topological constraints	176
7.3.4	An illustrative example of the topological constraints	179
7.3.5	Structural Analysis of Tensegrity Structures	180
7.3.6	Ground structure method	185
7.4	Numerical examples: verification and extension	186

7.4.1	On Reproducing Known Tensegrities: A Verification Study	187
7.4.2	Tower tensegrity	188
7.4.3	Spherical tensegrity	193
7.5	Free-form design	197
7.5.1	Double-layer tensegrity dome	197
7.5.2	Taubin's heart	199
7.6	Discussion on numerical aspects: implementation and efficiency	200
7.7	Fabrication of the tensegrity models aided by additive manufacturing	201
7.8	Concluding Remarks	203
Chapter 8: Programmable Deployment of Tensegrity Structures by Stimulus-Responsive Polymers		205
8.1	Introduction	205
8.2	Deployment of a simple 3-strut tensegrity	208
8.3	Deployment of a 6-strut tensegrity with reduced degree-of-freedom	209
8.4	Deployment of tower tensegrities with programmed sequence	211
8.5	Design philosophy	213
8.5.1	Stiffness of tensegrity designs	213
8.5.2	Design of struts	215
8.5.3	Design of cables	218
8.5.4	Finite element analysis	219
8.5.5	Theoretical, finite element, and experimental results	223
8.6	Methods and materials	225
8.6.1	Sample fabrication	225

8.6.2	Deployment control	225
8.6.3	Compression tests of the deployed tensegrity	226
8.7	Concluding Remarks	226
Chapter 9: Automated Generation of Tensegrity Tessellations for Metamaterials with Tunable Stiffness and Bandgaps		230
9.1	Introduction	230
9.2	Topology design formulation	233
9.3	Geometry of tessellation units	237
9.4	Variations of tessellation strategy	239
9.5	Tunable elastostatic properties	240
9.5.1	Computation of identification matrix \mathbf{M}	244
9.5.2	Computation of homogenized elasticity tensor	246
9.6	Tunable elastodynamic bandgaps	248
9.7	Concluding Remarks	250
III Closure		257
Chapter 10:Conclusions & Future Work		258
10.1	Summary of Contributions	259
10.2	Future Work	261
References		282

LIST OF TABLES

4.1	Paper Material Properties	108
7.1	Computational results for designs shown in Fig. 7.7	188
7.2	Computational results for designs shown in Fig. 7.8	188
7.3	Computational results for designs shown in Fig. 7.11	193
7.4	Computational results for designs shown in Fig. 7.13	194
7.5	Computational results for designs in Section 7.4.3	195
9.1	Tensegrity tessellations	254

LIST OF FIGURES

1.1 Origami Pegasus. Designed by Satoshi Kamiya [27]. Folded by Ke Liu (thesis author).	3
1.2 Origami art pieces. The later two designs are aided by computational design algorithms. (a) A traditional origami of crane bird, folded by Ke Liu. (b) An origami deer designed by Robert Lang [48]. (c) An origami bunny designed by Tomohiro Tachi [16].	3
1.3 A polyhedral tensegrity sculpture. Designed by Ke Liu using a computational optimization algorithm. Struts are in red, made of wood; cables are in blue, which are made of 3D printed rubber-like material.	5
1.4 Applications of tensegrity structures. (a) The outdoor sculpture “Needle Tower” created by Kenneth Snelson (1968) [8]. (Image courtesy of Kenneth Snelson.) (b) Tensegrity robot design investigated by NASA [1] for outer space missions. (Adapted from [1].) (c) A baby playing with a tensegrity toy. (Image reproduced from [57]. ©2016 Manhattan Toy).	6
2.1 (a) The Miura-ori unit cell. (b) A bar-and-hinge model for a unit cell of Miura-ori. The black bars represent creases and boundaries of the origami and the blue bars are added to model in-plane and out-of-plane deformations of the panels (online version in color).	12
2.2 Components of a bar element, which is part of an origami assemblage.	17
2.3 Components of a rotational spring element, which is part of an origami assemblage.	19
2.4 (a) Geometry of a rotational spring element. The two triangles lies on two intersecting planes, painted with two different colors. The three space vectors (i.e., \mathbf{r}_{ij} , \mathbf{r}_{kj} , $\mathbf{r}_{\ell k}$), drawn with solid lines are sufficient to define the dihedral angle between the two planes. (b)-(d) An illustration of the consistent assignment for rotation angle θ of a rotational spring element turning from 0 to 2π (360°).	21

2.5	The difference between the analytical expressions and finite difference approximations versus the rotation angle θ (in degree) for a single rotational spring element - see Section 2.5.1 and Fig. 2.10.	29
2.6	Different hyperelastic material models in uniaxial strain based on the Ogden model. The plot shows normalized (2nd P-K) stress vs. principal stretch (λ_1).	30
2.7	Proposed nonlinear elastic constitutive model of rotational springs, with consideration of local contact. (a) dihedral angle vs. moment per unit length M , and (b) dihedral angle vs. tangent rotational stiffness k . The parameters k_0 , θ_1 and θ_2 are tunable. The neutral angle θ_0 yields the relaxed state with $M = 0$	32
2.8	(a) Illustration of a N4B5 model. (b) A hexagonal origami panel triangulated by the generalized N4B5 scheme. (c) The tributary area of a bar element, used to approximate the areas of bars.	34
2.9	(a) Illustration of a N5B8 model. (b) Discretization of a single quadrilateral panel. (c) Illustration for d_{ij} and h_{ij} . (d) Triangulation by the generalized N4B5 scheme.	35
2.10	The simple fold example. (a) Geometry and boundary conditions. (b) Force diagram at node D.	42
2.11	(a) Equilibrium path, F_{ext} versus θ . (b) F_{BD} versus θ	43
2.12	(a) Paper-made Miura-ori model. (b) An isometric view of the initial configuration of the numerical model and boundary conditions for the bending simulation. The angle ξ between two edges is used to specify the initial configuration of a Miura-ori, which equals 118.27° for the compression simulation and 90° for the bending simulation. In the bending simulation, support $S1$ restricts displacements in x , y , z directions; $S2$ fixes x , z directions; $S3$ confines only x translations. Unit forces are applied toward the $-z$ direction on nodes marked with blue circles. Displacement u is measured at one of the loading nodes as the z -displacement, marked with a yellow circle (same node as $S3$). The blue dots show the nodes that are used to approximate the global principal curvatures near the center of the origami sheet. (c) A flattened unit cell of the Miura-ori. We take $a = 0.02$, $b = 0.02$, and $\alpha = 60^\circ$ for the simulations. (d) Illustration of the boundary conditions in the compression simulation from a side view. (e) Side view of the boundary conditions for the bending simulation.	45

2.13 Compressed folding of Miura-ori. The in-plane compression starts from an almost flat state (i.e. at L_{initial}). (a) Equilibrium path, displacement versus load factor (λ). The insets demonstrate the folded shapes along the compression process. The black profiles in the three insets outline the unfolded planar pattern. (b) In-plane tangential Poisson's ratio ν_{LW} versus folding ratio (L/L_{unfold}). The analytical solutions are obtained based on the formulae presented in reference [35].	46
2.14 Bending of Miura-ori. (a) Equilibrium path, displacement u versus load factor λ . Displacement u is measured at one of the loading nodes as the z -displacement, as shown in Fig. 2.12. (b) Two views of the final state (at point "C") of the bended Miura-ori, with pictures of both the paper model and the numerical model.	48
2.15 The Miura-ori "pop-through defect". (a) The paper-made Miura-ori model in a regular partially folded configuration. (b) The Miura-ori model in the "pop-through" state, which is a stable configuration. (c) The numerical model and boundary conditions for simulation. The angle ξ is 112.61° . Support $S1$ fixes displacements in x , y , z directions, $S2-S6$ fix displacements in x , z directions, and $S7$ fixes y , z displacements. From $S8$ to $S12$, restrictions only apply in z direction. Load is applied as a unit force toward the $-z$ direction on the node marked with blue circle. Displacement u is the z -displacement measured at the loading node – also marked with yellow circle. (d) A flattened unit cell of the Miura-ori. We take $a = 0.02$, $b = 0.02$, and $\alpha = 60^\circ$	49
2.16 Quantitative measurements. (a) Equilibrium path, u versus λ , during the deformation process of a "pop-through defect" on Miura-ori. The insets show zoom-in views of the deformed Miura-ori near the central region. Reference of these insets to the global configuration is illustrated in (b). (b) Several key frames of deformed configurations along the simulation, corresponding to the 4 points ("A" to "D") on the equilibrium path. At stage C, the corresponding configuration is in a stable state, and the digital rendering shows a similar configuration to the physical model shown in Fig. 2.15(b). The yellow dashed circles mark the zoom-in regions for insets in (a). (c) Change of stored energy breakdown in the system throughout the deformation history. Critical states are marked by red dots and corresponds to (b).	51

3.2 Schematic of the global and local configurations of a hypar origami. (a) A surgery on the hypar origami takes out a twisted corrugation, which un-twists into a simple straight fold. The black arrows indicate surface normals. (b) We describe the global saddle shape of a hypar folded shell by the union of four pieces of ruled surface subject to reflection symmetry. Each corrugation resembles a ruling fiber. A folded corrugation must be twisted to satisfy global compatibility constraint. The circular insets show a projection view looking through the longitudinal axis of a corrugation. (c) Plan and elevation views of a folded corrugation before twisting. The folding angle ρ , and two bending angles θ_1, θ_2 are labeled. (d) The construction of curves ξ and ζ . The black lines show the folded diagonal creases of the hypar origami. (e) The analytical curves that relate the global geometry of a hypar origami measured by kr with local geometry of a corrugation measured by the folding angle ρ , opening angle ψ , and twisting angle γ . Experimental and numerical data are sampled from the scanned and simulated models, respectively.	61
3.3 (a) Alternating asymmetric triangulation. (b) Asymmetric triangulation. The dashed lines indicate the extra pleats introduced by triangulation.	62
3.4 Geometry of corrugations. (a) A folded corrugation before twisting. (b) A folded corrugation after twisting. (c) Twisted configuration of an augmented system considering two adjacent corrugations, where panel $BCFE$ (the middle panel) is shared.	64
3.5 Solution to ODE Eq. (3.46), and its realization. (a) A solution to Eq. (3.46) solved numerically by assuming $\xi(1) = 1$. (b)-(d) By cutting slits on the hypar crease pattern to make it a kirigami, we can realize the solution to Eq. (3.46), which satisfies Eq. (3.29), but breaks the compatibility constraints. (c) Top view of the folded hypar kirigami. Slits are cut along the diagonals. Detailed constriction of the slits are shown in the inset. (d) Side view of the folded hypar kirigami. Diagonal creases approximate the solution of ξ given by Eq. (3.46).	71

3.8	Folding a numerical model of hypar origami. (a) The applied forces and kinematic constraints (red roller supports). Total upward and downward forces are balanced. The numbers are the relative magnitudes of forces normalized by a reference force F_0 . (b)-(d) Frames along the folding process. The folding stops when distance D (as shown in green) becomes 80% of its original length when the sheet is flat (unfolded). (e) The new equilibrium shape after release of folding forces and update of neutral angles of folding hinges. The shape drawn in gray is the same as in (d), which shows the unbalanced configuration of the origami structure before the new equilibrium is found.	78
3.9	Out-of-plane deformations (folding and bending) in terms of deformation angles (in absolute values). The average of k_{blue} and k_{red} interpolated by the blue and red dots are used as an estimation to the quadratic coefficient k in Eq. (3.50).	80
3.10	Snapping of the hypar origami. (a) Snapshots picturing the snapping process of a Mylar-made physical model of thickness $t = 76.2\mu m$ (see Movie S1). We show 4 frames along the process, in which T indicates the frame time relative to the first one. (b) Frames taken from numerical simulation of the snapping process, using the thinner model ($t = 76.2\mu m$) as an example (see Movie S2). To simulate the snapping, we apply forces following the red arrows with the same magnitude. (c) The changing profile of one set of diagonal creases that approximates the curve ξ with varying curvature and projection distance $r (= y)$. (d) Force magnitude (F) vs. displacement (u) plot from numerical analysis, where u is illustrated in (b). (e) Stored energy (U) vs. displacement (u) plot. Contributions from three deformation modes: folding (U_{sprF}), bending (U_{sprB}) and stretching (U_{bar}) are differentiated. (f) The Green-Lagrange strain (E_{11}) in two bar elements. Bar #1 represents a central crease, and bar #2 represents an outermost panel edge, as indicated in (b). Negative values refer to compression.	82

3.11 Multi-stable hypar origami tessellation built from a 2×2 array of hypar origami unit. (a) The crease pattern on a single piece of sheet. (b) The convention of (+) and (-) states for each hypar origami unit. The blue edges are shared edges between adjacent units. (c) Complete chart of the 32 stable states. On the left side, there are 16 states when the middle vertex is in a pop-up state. On the right, the middle vertex is in a pop-down state. On either side, each row lists configurations that are identical to each other after rotations. (d) The 6 unique stable states up to rotational symmetry when the middle vertex is in a pop-up state. (e) The 6 unique stable states up to rotational symmetry when the middle vertex is in a pop-down state. The corresponding pairs of configurations in (d) and (e), as indicated by the double arrows, lead to the same global geometry if one is flipped over (upside down). We can encode each state by 5 symbols, as labeled in (d) and (e). The sign in the parenthesis indicates the state of the middle vertex, and the other four refer to the four hypar origami units. Since the hypar metamaterial is rotationally symmetric, the order of the last four signs does not affect the geometry. Accordingly, when all signs in a code become opposite, the global configuration is flipped over.	83
4.1 Presence and effect of geometric imperfections in origami-based systems. (a) Three origami sheets under the same pressure. We fold the yellow one with the standard Miura pattern, the blue one with a slightly perturbed pattern by randomly perturbing nodal positions, and the red one with a more perturbed pattern. The inset on the upright corner shows the initial configurations. (b) Geometric imperfections can be induced to an origami assemblage by various sources, such as misaligned crease pattern, non-uniform temperature, or swelling/corrosion during service. The gray lines show the ideal design.	87
4.2 Geometry of standard Miura-ori and general degree-4 vertex. (a) Schematic of the Miura-ori unit cell. (b) A 2×2 array of degree-4 origami vertices is not generically rigid foldable. As each vertex possesses single DOF, if we fold ρ_1 of vertex A as input, the rotation transmits along two paths simultaneously: $\rho_1 \rightarrow \rho_3 \rightarrow \rho_5$, and $\rho_1 \rightarrow \rho_2 \rightarrow \rho_4$. If the system is rigid foldable, at vertex D, ρ_4 and ρ_5 must be compatible according to a single DOF. (c) For a generic degree-4 vertex, if the Kawasaki condition is not satisfied (i.e. $\alpha_K > 0$), early contact between two panels prevents the whole origami to be flattened, and some dihedral angles (marked by red crosses) cannot reach zero kinematically.	88
4.3 An illustration of a degree-4 origami vertex. The vectors p_1 to p_4 indicate the spatial directions of the four creases.	90

4.4	Experimental quantification of the effect of geometric imperfections. (a) Bulk stress σ vs. compressive strain ε_x . Each solid line shows the response of a group of samples. The error bars extend to one standard deviation of the measured σ data. The dashed line is the response of ideal Miura-ori according to Eq. (4.1), where k_0^F is obtained by mechanical test on single creases. (b) Snapshots of an unperturbed sample. Each blue polyline outlines a row of lattice lines. (c) Snapshots from experiment of a perturbed sample with $\chi = 0.02a$ under increasing compressive strain. (d) Illustration of the 5-parameter model. The 5 independent parameters ($\varepsilon_{lin}, \sigma_{lin}, \varepsilon_{den}, \sigma_{den}, m$) are fitted by the least squares approach. (e) Fitted E_{lin} and σ_{plt} for different sample groups. The black error bars show standard deviations, and the gray error bars indicate extrema of data. The dashed lines refer to measurements of the reference group. (f)-(g) Mechanical properties (E_{lin}, σ_{plt}) vs. $\ \alpha_K\ ^2$. The black circles refer to the mean of the reference group measurements. The error bars extend to one standard deviation. The gray lines are linear regression with enforced intercept at $\ \alpha_K\ ^2 = 0$. The σ , E_{lin} and σ_{plt} are in units of KPa.	92
4.5	Modeling of random geometric imperfections by random fields of nodal perturbations. At each node, the perturbation is decomposed into x -, y -, and z - directions (denoted as δ_x , δ_y , and δ_z), as we assume no directional preference of the geometric imperfections. The four colored maps demonstrate how ℓ affects spatial correlation between nodal perturbations.	94
4.6	Numerical quantification of the effect of geometric imperfections. Bulk stress σ vs. compressive strain ε_x plots for samples with (a) $\ell = 0$, and (b) $\ell = 6a$. Each solid line shows the mean response of a group of samples and the error bars extend to one standard deviation. (c) Snapshots from numerical simulation of a perturbed sample with $\chi = 0.02a$ and $\ell = 0$. (d)-(h) Fitted E_{lin} (first row) and σ_{plt} (second row) of different groups for different material-associated parameters. The black error bars show standard deviations. The dash lines refer to measurements of the unperturbed Miura folded sheet. The ratio of k_0^B/k_0^F reflects the relative stiffness between bending and folding deformations. As the stretching stiffness remain unchanged, the ratio of $k_0^B/k_{0,pr}^B$ characterizes the relative stiffness between out-of-plane and in-plane deformations, where the reference bending stiffness $k_{0,pr}^B$ is collected from experimental test. For all cases shown in this figure, $\alpha = 60^\circ$ and $\beta_0 = 70^\circ$. The σ , E_{lin} and σ_{plt} are in units of KPa.	96

4.7 Examples of unstable strain softening of some perturbed Miura-ori structures, highlighted by red boxes. For perturbed samples with small χ or large ℓ , this phenomenon is rarely seen. Thus, we believe that instability is caused by relatively large random geometric imperfections. From ((a)) to (c), we raise the level of geometric imperfection by increasing χ . The samples are all taken from the group of data with $k_0^B/k_0^F = 10$, and $k_0^B/k_{0,pr}^B = 1$. The bulk stress σ is in unit of KPa .	97
4.8 Mechanical properties vs. relative imperfection measured as (ℓ/χ) . Each solid dot shows the mean response of a group of samples and the error bars extend to one standard deviation. The black solid line refers to the obtained values from the unperturbed structure. All samples in this figure have $\alpha = 60^\circ$, $\beta_0/2 = 35^\circ$, $k_0^B/k_0^F = 10$ and $k_0^B/k_{0,pr}^B = 1$. The E_{lin} and σ_{plt} are in units of KPa .	98
4.9 Statistics of geometric features. (a) Change of Kawasaki excess ($\ \alpha_K\ $) as χ and ℓ vary, for all samples with $\alpha = 60^\circ$ and $\beta_0/2 = 35^\circ$. The error bars extend to one standard deviation. (c) Linear correlation between $s(\mathbf{J})$ and $\ \alpha_K\ $. Data is obtained from all 11219 numerical simulations.	98
4.10 Mechanical properties vs. the Kawasaki excess. The first row for $E[E_{lin}]$ vs. $E[\ \alpha_K\ ^2]$, and the second row for $E[\sigma_{plt}]$ vs. $E[\ \alpha_K\ ^2]$, where $E[\cdot]$ means the mean (or expected) value. ((a)) demonstrates influence of k_0^B/k_0^F . (b) demonstrates influence of $k_0^B/k_{0,pr}^B$ (equivalent to k_0^B/K_S). In (c), we vary the initial amount of folding (β_0). In (d) we vary the original panel angle α . The coordinate of each dot is determined by the mean (expected) values of E_{lin} (or σ_{plt}) and $\ \alpha_K\ ^2$ for a group of samples. The black circles with $\ \alpha_K\ ^2 = 0$ refer to the mean of the reference group measurements. The gray lines are linear regressions with enforced intercept at $E[\ \alpha_K\ ^2] = 0$. The E_{lin} and σ_{plt} are in units of KPa .	99
4.11 Schematic of the hypothetical deformation process of imperfect origami. (a) The purple pattern indicates the imperfect geometry, and the gray lines indicate the ideal geometry. (b)-(d) Step (i) to (iii). The orange arrows imply the enforced deformation field, which confines the imperfect geometry to the ideal geometry. The pink arrows imply applied forces/displacements on the entire pattern. (e) An imperfect single vertex with angular deficit $\delta_i \alpha_K$. (f) Additional strain energy (density) induced by imperfection when $\varepsilon_x \leq \varepsilon_{lin}$. (g) Additional strain energy induced by imperfection when $\varepsilon_{lin} < \varepsilon_x \leq \varepsilon_{den}$.	100

4.12 Statistics about the key frames of strain (i.e. ε_{lin} and ε_{den}). (a)-(c) The first row is the probability density (i.e. normalized histogram) of ε_{lin} for a group of sample generated by the parameters shown on the top. The bound for ε_{lin} during curve fitting is [0,0.3]. The red vertical line refers to $\varepsilon_{lin,ref}$, while the yellow line refers to $E[\varepsilon_{lin}]$. The second row is the probability density of ε_{den} . The bound for ε_{den} during fitting is [0.4,0.7]. The red vertical line refers to $\varepsilon_{den,ref}$, while the yellow line refers to $E[\varepsilon_{den}]$. The bounds are used to slightly regulate the data. The third row plots $E[\varepsilon_{lin}]$ and $E[\varepsilon_{den}]$ vs. $E[\ \alpha_K\]$.	101
4.13 The Silhouette CAMEO electronic cutter. (a) The Silhouette CAMEO uses a cutting mat to hold the paper flat and use a small blade to make cuts. (b) Samples for resolution test. The left one is by the Universal laser systems PLS4.75, and the right one is by the Silhouette CAMEO. The insets marked by red circles show zoom-in view of the parallel cuts with 0.25mm space. (c) Samples for precision test. The left one is by the Universal laser systems PLS4.75, and the right one is by the Silhouette CAMEO. The measured lengths are indicated in the bottom.	103
4.14 The mechanical testing bed for compression test of origami samples.	105
4.15 Schematics of the compression test.	105
4.16 Tension test on paper material using the Instron machine.	105
4.17 Schematics of the bending and folding test. (a)-(c) Characterization of the bending stiffness of the panels, and (d)-(f) characterization of the folding stiffness of the perforated crease (fold line).	106
4.18 Moment M vs. rotation angle ψ for the panel bending (a) and folding (b) from one sample of each. The measured data is plotted in blue lines, and the red lines represent the linear regressions. From the slope of the red line, the rotational stiffness is obtained.	108
4.19 Purposely induced local deformation concentration by random perturbations. (a) The crease pattern. The purple region represents unperturbed portion. (b) The folded pattern under compression. Notice that the unperturbed region contracts more in the lateral direction than the perturbed portion because of the negative Poisson's ratio of Miura-ori.	110

5.1	(Top) Expanded design space of the Morph pattern (yellow shading) with standard Eggbox (red line) and Miura-ori (blue line) as particular cases. (Middle) Fundamental modes of the Morph pattern: Eggbox mode (left) and Miura mode (right). (Bottom) Configuration space showing transition of the Morph unit cell from one flat-folded state to another. The crease line shown in red morphs from a mountain fold in the Eggbox mode to a valley fold in the Miura mode.	113
5.2	Geometric configuration of the Morph pattern. (a) Schematic of the unit cell with the description of geometric parameters and vertices. (b) The rigid origami configurations of the Morph pattern described in terms of ϕ and ψ for different choices of α considering $\alpha + \beta = 100^\circ$	114
5.3	(a) Geometry of the Morph unit cell. (b), (c), (d) Side views of the unit cell. (b) $\overrightarrow{O_7O_9}$ is normal to the plane $O_1O_4O_7$ as $h_1 = h_2$, i.e., $a \cos \phi_1 = b \cos \phi_2$. (c) $\overrightarrow{O_7O_9}$ is not normal to the plane $O_1O_4O_7$ as $h_1 \neq h_2$ (since $\phi_1 \neq \phi_2$ for $\alpha \neq \beta$). We avoid this case to maintain the orthorhombic nature of the unit cell by making $ \overrightarrow{O_7O_8} \neq \overrightarrow{O_9O_8} $. (d) $\overrightarrow{O_1O_7}$ is normal to the plane $O_1O_2O_3$ as $h_1^* = h_2^* = c \cos(\psi/2)$	115
5.4	In-plane mechanics of the Morph pattern. (b) The Poisson's ratio in stretch (ν_{WL}^s) for different choices of α considering $\alpha + \beta = 100^\circ$. (b) Stretching stiffness in W and L directions for $\alpha = 60^\circ$, $\beta = 40^\circ$. The markers represent numerical results from origami structural analyses using the bar-and-hinge reduced order model. We assume that $a = c = 1$. The solid and dashed lines represent the Eggbox and Miura modes, respectively.	121
5.5	Out-of-plane bending of the Morph. (a), (b) Bent shapes of the pattern in Eggbox and Miura modes respectively obtained using the bar and hinge origami model.	122
5.6	Local coordinate system used to calculate the normals and the angle change for the triangular face $O_1O_2O_3$	123
5.7	Infinitesimal bending of a unit cell and global curvatures of bended pattern. (a) Bending of the Morph pattern in Eggbox mode. Curvatures along both W and L directions are of the same sign. (b) Bending in Miura mode. Curvatures along W and L directions are of opposite sign. (c), (d) Triangular face tilts creating a net angle change across length L in Eggbox and Miura modes, respectively.	126

5.8 (a) Comparison of Poisson's ratio in bending and stretching. (b) Normalized out-of-plane bending stiffness of a Morph unit cell. B_W and B_L represent the bending stiffnesses per unit width along W and L directions respectively. In both the figures, $\alpha = 60^\circ$ and $\beta = 40^\circ$. The dashed lines represent the results in the Miura mode and the solid lines represent the results in the Eggbox mode. The circle and square markers show the numerical results obtained using the bar and hinge model.	131
5.9 Hybrid origami patterns. (a) Alternating strips of Miura (M) and Eggbox (E) modes. (b) Half pattern with strips in Miura (M) mode and other half in Eggbox (E) mode.	135
5.10 The Morph pattern's transformability into various hybrid patterns via the transition state. The hybrid pattern is a composite metamaterial system that can morph into any combination of Miura (denoted by M, shown in green color) and Eggbox (denoted by E, shown in yellow color) modes which have contrasting mechanical properties and therefore is a highly programmable and in-situ tunable metamaterial.	136
5.11 Unit cells of hybrid patterns in the Eggbox and Miura modes. For compatibility, $\psi_e = \psi_m = \psi$ with $\phi_e = \phi_1 + \phi_2$ and $\phi_m = \phi_1 - \phi_2$	137
5.12 Morphing of the hybrid pattern. (a) Creation of hybrid patterns by kinematic bifurcations. (b) Change of Poisson's ratio with respect to varying number of Miura mode strips (n_m) in a hybrid mode with 100×100 unit cells. To prepare the figures, we assume that $\alpha = 60^\circ$, $\beta = 40^\circ$	138
5.13 Hybrid patterns with varying number of Miura strips, n_m , for $n = 6$	139
5.14 In-plane stretching of hybrid patterns. (a), (b) Mode locking phenomenon in which the Miura (M) and Eggbox (E) mode cells cannot change their mode as the deformation takes them away from transition. (c), (d) Deformations that take the Miura and Eggbox mode unit cells towards transition enabling morphability of hybrid patterns.	141

5.15 Mode locking due to extension in L direction when $\nu_{WL}^b > 0$, as depicted in Fig. 5.14(a). (a) The positive global Poisson's ratio implies contraction in the W direction, resulting in decrease of ψ_e and ψ_m . The oppositely signed unit cell Poisson's ratios of the two modes indicates that while ϕ_e increases, ϕ_m decreases, meaning the Miura mode cells are axially contracting, opposite to the global axial deformation. We say that the Miura mode cells with decreasing ϕ_m are locked because such a cell can no longer smoothly transition to its Eggbox mode in a rigid origami motion. (b) Contrasting global and local deformations that occur in hybrid patterns leading to mode locking behavior. The green lines represent the panel diagonals, whose projections provides a clean way of sketching the motions. 142

- | | | |
|-----|--|-----|
| 6.1 | Geometry of a shrimp unit cell. (a) Isometric view. (b) and (c) side views. . | 145 |
| 6.2 | Labels of geometric quantities of a shrimp unit cell. (a) Dihedral folding angles. (b) Vertices. | 146 |
| 6.3 | Configurations space of a Shrimp pattern in terms of ψ' and ϕ . The dashed portion of the curves cannot be reached kinematically under the assumption of rigid origami. | 148 |
| 6.4 | A hypothetical deformation process of a shrimp unit cell and the associated energy states of the system. (a) The change of system energy (U) for a deformed Shrimp pattern, as a summation of bending (U_{sprB}) and folding energy (U_{sprF}). Stretching deformation (and energy) are not considered by the isometry assumption. (b) The idealized configurations of a shrimp unit cell during its deformation. Configuration 0: The initial configuration. Configuration 1: The non-rigid deformed configuration during spanning, when the bending energy in the system reaches maximum. Configuration 2: The after-snapping configuration, we can see that the rare and tail panels are in mirror symmetric with their initial configuration about the panel spanned by O_2 , O_6 and O_{10} | 150 |
| 6.5 | Programmable energy state of a shrimp unit cell. A positive energy difference ΔU indicates that the pattern is bistable. (a), (b), and (c) show how ΔU is affected by geometric parameters (i.e. α_F , α_R , a , d) and material properties (i.e. k_0^B/k_0^F). In (d), we plot the limit surface of the emergence of bistability in the configuration space spanned by α_R , d , k_0^B/k_0^F | 154 |

6.6 Numerical verification of the programmable energy landscape of shrimp unit cell. (a) Boundary conditions for the numerical simulation. Blue arrows are fixed DOF, and the red arrow refers to applied displacement u . (b) Force vs. (normalized) displacement curve. The displacement u is normalized by L_R of each design. We investigated the performance of a shrimp unit cell α_R varies from 45° to 55° . (c) The stored energy vs. (normalized) displacement. (e) Comparison between the analytical estimation of ΔU as formulated in Section 6.3 with the numerically obtained values. When the structure is monostable, ΔU is taken as the difference between the stored energy at $u/L_R = 1$ and $u/L_R = 2$, for the numerical models. (f) The opening of angle ψ' during deformation. We see that ψ' is always smaller than $2\alpha_B (=90^\circ)$.	157
6.7 Sequential snapping of a 3×1 Shrimp pattern tessellation with programmed multi-stability. (a) Geometry and boundary conditions. (b) Force vs. displacement curve, with critical configurations labeled from (1) to (8). (c) Stored energy vs. displacement. Contributions from bending, folding, and stretching of panels are indicated. (d) Side views of the 8 critical configurations during the deformation history.	158
6.8 The double layer technique. We fabricate developable stripes and glue them in two directions to make the non-developable Shrimp pattern. We demonstrate the fabrication of a single unit cell in this figure. The correspondence of panels are shown in (a) and (b), from difference view angles. The designs of developable stripes are shown in (c). (d) A 4×4 patch of Shrimp pattern made using the double layer technique. The sheet material we used is the 63lb premium ICE paper (Durilla Durable Papers, CTI Paper USA, WI).	159
6.9 Shrimp pattern by 3D printing. (a) Procedure to prepare 3D printable solid from geometric data of a Shrimp origami surface. (b) A 3D printed Shrimp pattern using the Selective Laser Sintering (SLS) technology. The sample shown in (b) is printed by selective laser sintering (SLS) technology using a rubbery TPU material.	161
7.1 Preference of larger angle between struts and cables by the objective function. (a) A vertex in the ground structure connecting one member that has already been decided to be a strut (shown with a solid line) and four candidate cable members (shown with dashed lines). For a given compression load in the strut, if cables 3 and 4 are selected as in (b), the sum of tension and the average angle between struts and cables are small. If cables 1 and 2 are selected as in (c), the sum of tension and the average angle between struts and cables are large, which is preferred according to the objective function.	171

7.2	(a) A symmetric planar ground structure. (b) A subset of the ground structure (representation of G) indicated by black solid lines. (c) Another subset of the ground structure (representation of $h_j(G)$) obtained by applying a symmetry operation of the ground structure to the one shown in (b). The structures in (b) and (c) are physically equivalent, as the relative relationships between the nodes and members remain unchanged. (d) An embedded structure that has the same symmetry group as the initial ground structure.	173
7.3	(a) A simple ground structure with 6 nodes and 9 members. (b) The collection of members 1 and 2 in the ground structure. The two members are connected at node B. (c) Members 7 and 8 are contacting each other in the middle, indicating a conflict in space.	179
7.4	Illustration of the Updated Lagrangian formulation for derivation of stiffness matrix of tensegrity member (i.e. a prestressed rod) when only the prestressed state is known.	181
7.5	The ground structure generated within pentagon prism. (a) Geometry of the pentagon prism. (b) The ground structure connecting every pair of nodes, which are located on the vertices of the prism.	185
7.6	The geometry and generation of a twisted prism. (a) The base polygon laid on the top circle B is obtained by rotating the same polygon on the bottom circle A with an angle α . (b) The top view of the twisting of a hexagonal base.	187
7.7	Examples of prismatic tensegrities that are reproduced using the proposed method. Different base polygons are used to generate the twisted prism geometries: (a)-(f). For N -gon based twisted prism, $\alpha = \pi/N$ if N is even, and $\alpha = \pi/2N$ if N is odd. Quantitative date is provided in Table 7.1.	189
7.8	Examples of star-shaped tensegrities that are reproduced using the proposed method. Different base polygons are used to generate the twisted prism geometries: (a)-(c). Compared to the prismatic tensegrities, the initial ground structures have two more nodes that are located at the centroids of the two base polygons.	190
7.9	(a) The geometry and generation of the tower tensegrity. (b) Illustration of the cylindrical restriction zone adopted in this example. Any member in the initial ground structure that passes through this region is removed.	190
7.10	The SVD tower tensegrity. (a) Geometric decomposition of the SVD tower, where the 12 vertices are the nodes used to generate the ground structure. (b) The design obtained using the proposed formulation, which recovers the known form of the SVD tower tensegrity.	191

7.11 Extended examples of tower tensegrity. (a) The basic geometry. (b) The design obtained directly from the ground structure generated with full connectivity in (a). (c) The tensegrity obtained by limiting the length of struts to 2.5, which is in consistent units with the dimension of the geometry. (d) In addition to length limit, a cylindrical restriction zone is applied with $r_{RZ} = 0.3$. (e) Based on (d), by adjusting the overlapping height h_d , a kinematically indeterminate tensegrity design emerges naturally as a result.	192
7.12 Illustration of the ball-shaped restriction zone adopted in this example.	193
7.13 Some known spherical tensegrities that are reproduced. The ground structure of design (a) has a restriction zone with $r_{RZ} = 0.1$, design (b) has a restriction zone with $r_{RZ} = 0.5$, and No restriction zone is used in design (c).	194
7.14 New examples of spherical tensegrities obtained using the proposed method. The radii of the restriction zones as defined in Fig. 7.12 are: (a) $r_{RZ} = 0.20$, (b) $r_{RZ} = 0.65$	195
7.15 A tensegrity that outlines a small rhombicosidodecahedron. (a) Digital rendering of the obtained design, using restriction zone with radius $r_{RZ} = 0.70$. (b) A physical model made of wood struts and 3D printed cables. The cables are printed with a rubber-like material known as Ninja Flex.	196
7.16 A spherical tensegrity optimized from a ground structure generated based on 16 uniformly distributed points on the unit sphere and no restriction zone. (a) Digital rendering of the obtained design. (b) The physical model made of wood struts and rubber band cables.	196
7.17 Other new designs of spherical tensegrities obtained using the proposed method. (a) A dense tensegrity that has 120 nodes uniformly placed on a sphere and restriction zone with radius $r_{RZ} = 0.65$. (b) A Class-2 tensegrity that has a continuous loop of struts.	197
7.18 Design of a Class-1 cylindrical double-layer tensegrity dome. (a) The design domain: $L = 3$, $R_o = 1$, $R_i = 0.7$. The initial ground structure has 54 nodes and 882 members. (b)-(d) Different views of the obtained tensegrity. The design contains 54 nodes, 27 struts, and 153 cables. The dual truss of the tensegrity has 2 first-order mechanisms (KI=2). The tensegrity structure is super-stable.	198
7.19 Different views (a)-(c) of Taubin's heart. The mesh nodes are used to generated the ground structure.	199

- 7.20 Different views (a)-(c) of the tensegrity which outlines the Taubin's heart. The tensegrity contains 53 struts and 312 cables. The lengths of the struts are limited to 1.2, with consistent units to the dimensions of heart surface. Structural analysis shows that the structure is super-stable. 200
- 7.21 (a) The thin black lines shows the flatten cable net. The thick orange lines mark the 12 pieces that are printed separately. (b) The printed pattern pieces. The number on the side of each pattern indicates the number of this pattern embedded in the whole cable net. (c) HYREL 3D printer producing the elastic cable nets. Image courtesy: Rob Felt. 202
- 8.1 Procedure for creating an active tensegrity. Deployment of an active tensegrity is based on the shape recovery property of shape memory polymers (SMP). (a) Schematic of the overall concept and design. (i) The struts, which are programmed to compact shapes, are connected by a network of elastomer cables. (ii) Upon heating, the recovery of the struts to their straight shapes leads to actuation of the structure to a 3D resilient tensegrity structure. To achieve this concept, (iii) the struts are designed to have a tubular shape with a longitudinal slit which are 3D-printed using SMPs; (iv-v) the SMP struts are folded into compact shapes at a temperature that is above the glass transition temperature (T_g) of the SMP; (vi) decreasing the temperature below T_g fixes the struts in the compact shapes, which are then assembled with the elastomer cables (vii), according to the topology of the design to form a loose assembly (i); heating the assembly to a temperature above T_g leads the struts to their original shapes, and thus the constraints from the cables induce prestress. As a consequence, a stable tensegrity structure is obtained. (b) The experimental result shows the deployment process. The scale bars represent 15mm. 207
- 8.2 Failed deployment of a 6-strut spherical tensegrity, due to physical contact between struts, as highlighted by the red circle. As discussed in the main text, when the cables are loose, the folded struts are almost free to move in space. In this example, a strut blocks the recovery of another strut. 209
- 8.3 Deployment of 6-strut spherical tensegrity. (a) Deployment of a spherical tensegrity using the partial folding strategy to improve reliability of deployment. (b) Positioning of three discrete pieces of surfaces into space. (c) Deployment of a continuous surface supported by the active tensegrity to form a tent. The resultant structural system mimics the fundamental structure of vertebrates, with the membrane as skin, elastic cables as muscles, and relatively rigid struts as the skeleton (biomimetics). The scale bars represent 15mm. 210

8.4 Programmed deployment of layered tensegrity structures, using 2 different SMPs for the struts: DM-1 (the dark gray material) and BM (the white material). (a) Programmed deployment sequence of the “2-Layer Tensegrity”. (b) Programmed deployment sequence of the “3-Layer Tensegrity”. The two end layers have struts made with SMP of a lower T_g than the middle layer. The scale bars represent 15mm.	212
8.5 Programmed deployment sequence of the “3-Layer Tensegrity” using 3 different SMPs for the struts: DM-1, DM-2, and BM. The three SMPs have increasing T_g ’s from left to right as shown in the images. The darker the color, the lower the T_g . The scale bars represent 15mm.	213
8.6 Compression test of the deployed tensegrities. (a) Compression test of the deployed “2-Layer Tensegrity” using 2 different SMPs for struts (BM and DM-1). The red line indicates the loading process while the green line indicates the unloading process. According to Fig. 8.7, we estimate the maximal compression in the deployed tensegrity to be 0.12N by the initial slope of the curve. (b) Compression test of the deployed “3-Layer Tensegrity” made with 3 different SMPs (BM, DM-1, and DM-2). The test reveals a maximum compression in the struts around 0.12N. (c) Compression test of the deployed “3-Layer Tensegrity” made with 2 different SMPs (BM and DM-1). Maximal compression in the struts is estimated to be around 0.14N.	214
8.7 The change of tensegrity compression stiffness with respect to prestress level. (a) Illustration of three tensegrity designs. (b) Initial tangent modulus vs. maximum prestress compression forces in struts (i.e. γ).	215
8.8 Design of struts. (a) Schematic of a folded strut with opened cross section. (b) Cross section (A-A) of the struts. (c) Sketch of the critical scenario in the recovery of struts (during the deployment of an active tensegrity), based on observations from the experiments.	216
8.9 Schematic of the cable network design for the “1-Layer Tensegrity” as shown in Fig. 8.7(a).	219
8.10 Comparison of the DMA curves between experimental data and numerical models for three SMP materials used in this research.	221

- 8.11 Properties of the slotted tubular struts via 4D printing. (a) The snapshot images of the free recovery sequence of a strut at 65°C. (b) the predictions from the corresponding FE simulation. (c) The opening angles of the strut during the free recovery and the comparison with FE simulations. The inset shows the definitions of the two opening angles. (d) the critical load of a single strut during uniaxial compression from the experiment and the FE simulation. The inset shows the experimental setup. Considering the boundary condition in the experimental setup, a 0.75 effective length ratio gives the upper bound on the critical buckling load of a single strut. In practical designs, because the joints in our tensegrity are almost free in rotation, 1.0 effective length shall be used. (e) Critical load of a single strut during its recovery. In the experiment, a small initial displacement (1mm) is imposed to prevent the opened cross section from closing. 224
- 8.12 Material properties measured by experiments. (a) Storage modulus (C_s) vs. temperature curves of the three SMPs. (b) Loss tangent ($\tan \delta$) vs. temperature curves of the three SMPs. (c) The stress-strain curve of FilaFlex material at $\sim 25^\circ\text{C}$ 226
- 9.1 Schematic of the design framework to create tensegrity metamaterials. (a) From a (periodic) geometric design to a tensegrity tessellation block. (b)-(d) From tessellation block to tensegrity metamaterials. (b) The tessellation block is directly the unit cell for the bulk assembly, which is named as *dense tessellation*. (c) The tessellation block is first used to sub-assemble a porous unit cell which is re-tessellated into a bulk assembly, called the *porous tessellation*. This particular sub-assembled unit cell leads to truss-like assemblies. (d) The same tessellation block can be sub-assembled into different unit cells, leading to various *porous tessellations*. This particular *porous tessellation* is a honeycomb-like assembly. 233
- 9.2 Effect of periodic boundary condition on the topology of struts. (a) Tessellating Class-1 tessellation block creates nodes connecting multiple struts, which is not desired. The red bars indicate struts. If the struts are placed as shown in (b), the tessellation preserves the tessellation block's Class category – there is no pair of struts connected at one node. (Note: intersections within the length of struts is ignored in this demonstration) (c) Identification of independent groups of nodes for a 4×4 ground structure. Different groups are identified by different colours. The numbers in parenthesis provide the numbers of nodes in different groups. The 4 corner nodes belong to the same group. 236

9.3	Creation of the design domain (i.e. geometry of the tessellation block). (a) Domain unit-cell generation based on convex hulls. The black dots are the nodes used to generate the ground structure for topology optimization. (b) Restriction zone creates holes in the design domain (i.e. the ground structure) by removing all members across the prescribed zone(s). (c) Morphing example: original (un-morphed) tessellation block and morphed tessellation block (in 2×3 assemblies).	238
9.4	Examples of tensegrity metamaterial designs. (a) 3D view of the dense tessellation. (b) 3D view of a porous tessellation. (c) Side view of the dense tessellation. (d) Side view of a porous tessellation.	241
9.5	Tunability of homogenized elastic properties. (a)-(b) Shear mode of the unit cells of the two metamaterials in undeformed and simply sheared configurations: (a) Densely tessellated metamaterial, (b) Porously tessellated metamaterial. (c)-(d) Tunable elastic properties (including elastic modulus D_{11} , D_{13} , D_{44} ; and Poisson's ratio ν_{12}): (c) Densely tessellated metamaterial, (d) Porously tessellated metamaterial. The green lines indicate the limit of prestress that may cause buckling of struts. To the right of the green line, buckling is unlikely to happen.	242
9.6	Schematics of the quasi one-dimensional tensegrity chains with (a) Dense and (b) Porous tensegrity unit cells (shown in shaded rectangles) and their corresponding variation of bandgaps with prestress shown in (e) and (f). (c), (d) Band structure diagrams at a prestress of $(0.05C_C)$ represented by red lines in (e) and (f), respectively. The gray shaded regions illustrate the elastic bandgaps.	251
9.7	Schematics of the quasi two-dimensional tensegrity tessellations with (a) Dense and (b) Porous tensegrity unit cells (shown in shaded rectangles) and their corresponding variation of bandgaps with prestress shown in (e) and (f). (c), (d) Band structure diagrams at a prestress of $(0.05E_C)$ represented by red lines in (e) and (f), respectively. The gray shaded regions illustrate the elastic bandgaps.	252

CHAPTER 1

INTRODUCTION

In recent years, the call for multi-functional structural systems has increased substantially, with potential applications across scales: from deployable outer space structures [1], [2], to transformable multi-role robots [3], [4], and to microstructures of metamaterials [5]–[7]. To achieve various functionalities, the system has to be able to change their behavior on demand, which usually involves programmable physical states, such as geometry, and stress distribution. Some art forms turn out to embed the potential to become multi-functional structural systems. In this thesis, we focus on origami and tensegrity, due to their aesthetic elegance and direct reconfigurability and programmability. In order to position the present work in terms of its contributions, precise definitions associated to origami and tensegrity are needed. Those definitions are provided in *italics* in this introductory chapter, which set the basis for the remainder of the thesis.

Indeed, both origami and tensegrity are not only deeply rooted in art [8]–[10], but also found in nature under various forms [11]–[14], implying their potentially superior performance as multi-functional platforms. Compared to other reconfigurable and programmable structural systems, such as membranes and truss frames, the present understanding of origami and tensegrity is still limited and thus there is room for further investigation, innovation, and creativity.

This thesis investigates how we can apply origami and tensegrity designs to achieve programmable geometries and mechanical properties for applications involving structures and metamaterials, and thus provide insight on rational design of such systems. *In this thesis, we refer to “structures” as stand-alone platforms consisting of a finite assembly of organized elements, such as bridges, robots, and shelters. We define “metamaterials” as artificial materials with engineered microstructure that exhibit unconventional properties*

compared to natural materials. The key concept here is that we can obtain desired and predictable mechanical behavior and geometry by varying the system designs according to certain rules, and hence achieving programmability.

1.1 Origami

Origami is the ancient Japanese paper folding art (see Fig. 1.1), which has become popular all over the world. The Japanese word “origami” can be decomposed into two parts: the first half “ori” refers to folding; and the second half “gami” refers to paper (which is flat). Thus, *the original mathematical definition of origami is restricted to isometric transformation¹ of a simply connected developable surface.* In recent years, advances in origami mathematics and computation technologies brought the design of origami to a new level of complexity [9], [16] (see Fig. 1.2), which also brought origami to the attention of scientists and engineers. In 2012, the National Science Foundation (NSF) launched the “Origami Design for Integration of Self-assembling Systems for Engineering Innovation” (ODISSEI)² program to promote interdisciplinary research on origami. The program sparked a momentum for origami engineering research in the USA and abroad. In origami engineering, the concept of origami is broadened to include also various morphing structures. For example, non-developable thin panel assemblages [5], [7], [17], [18], kirigami [19]–[22], and thick panel folding [23]–[26], are being explored together with classic origami designs. These origami-inspired designs usually preserve one or several features of the classic origami, but also provide improvement in other aspects such as mechanical performance.

The broader impact of origami is ubiquitous. Nowadays, origami is permeating in many active fields of science and engineering, as a rich source of interdisciplinary inspiration for designing multi-functional structures and programmable metamaterials [5]–[7], [18], [28]–[43]. For instance, in aerospace engineering, origami is used to make deployable solar

¹Isometric transformation preserves the intrinsic geometry of a manifold [15]. In the context of origami, isometric transformation indicates that the surface areas of origami panels remain the same during the transformation.

²For more information, visit https://www.nsf.gov/eng/efma/fy12awards_ODISSEI.jsp

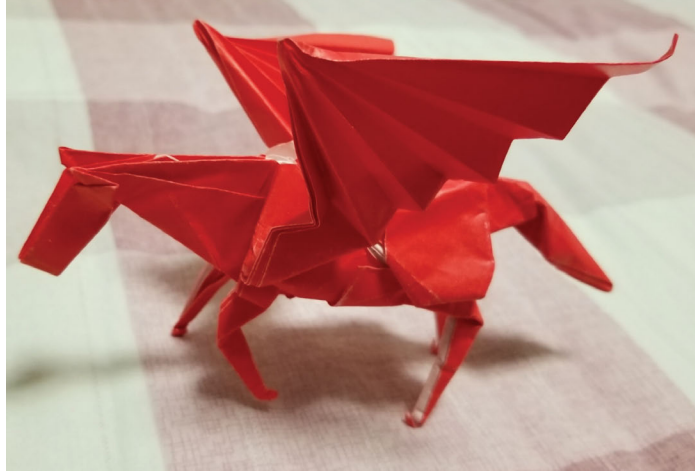


Figure 1.1: Origami Pegasus. Designed by Satoshi Kamiya [27]. Folded by Ke Liu (thesis author).

arrays [44], [45]. Inspired by origami kinematics, a new paradigm of manufacturing has been proposed to fabricate complex shell architectures of single crystal silicon in micro scales [22]. Beyond single layer sheets, origami assemblages have led to novel designs of functional metamaterials [5], [6]. For instance, origami-inspired designs can be used as biomedical devices, such as coronary stent [46]. Moreover, automobiles equipped with origami crashboxes are effective in absorbing energy and thus protecting lives [47].

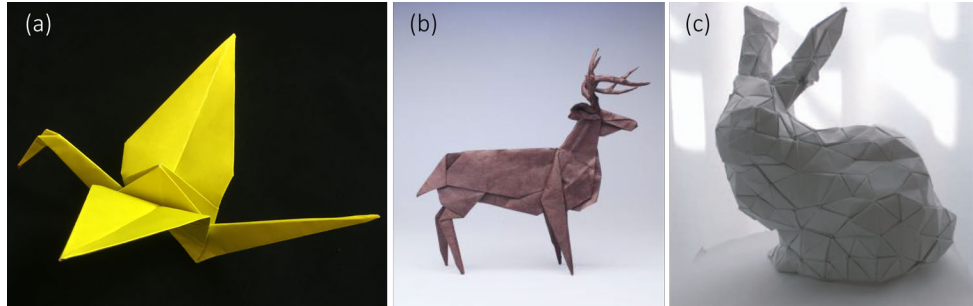


Figure 1.2: Origami art pieces. The later two designs are aided by computational design algorithms. (a) A traditional origami of crane bird, folded by Ke Liu. (b) An origami deer designed by Robert Lang [48]. (c) An origami bunny designed by Tomohiro Tachi [16].

In this thesis, we generalize the concept of origami to any structure composed of 2-dimensional panels that is reconfigurable through flexible (or soft) deformations, but not necessarily isometric. We focus our study to thin origami whose panels are of negligible

thickness that can be assumed as 2-dimensional. We also restrict our scope to origami with straight creases (not curved creases), which means that we are only considering polygonal panels.

For origami systems, we seek for programmable properties through their nonlinear transformations, involving both rigid and non-rigid folding. To understand the rigid and non-rigid folding of origami, we develop a computationally efficient nonlinear structural analysis tool based on reduced order modeling, which is presented in Chapter 2. With the empowering tool in hand, we start our research by investigating how the global geometries and mechanical properties of two existing origami structures, i.e. the pleated hyperbolic paraboloid origami (Chapter 3) and the Miura-ori (Chapter 4), are affected by their pattern designs. Then we propose two new patterns: the “Morph” (Chapter 5) and the “Shrimp” (Chapter 6), and study their folded geometries and mechanical properties. The “Morph” pattern has a non-developable degree-4 unit cell, which expands the design space of the standard Miura-ori and the Eggbox by releasing the constraints on panel angles. The “Shrimp” pattern modifies the “Morph” pattern by breaking connectedness of its configuration space, and thus shows bistable behavior. Compared to the rigid foldable “Morph” pattern, the “Shrimp” pattern combines both features of non-rigid and rigid origami. Although the “Morph” and “Shrimp” patterns introduced in this thesis are new and unlike any other pattern, we remark that the pattern themselves are not as important as the aforementioned unique properties of the patterns are.

1.2 Tensegrity

Snelson [10] referred to tensegrity as the art of “floating compression structures”. According to Fuller [49], the word tensegrity is a contraction of the words “tensile” and “integrity”, which refers to a continuous network of tension. However, historically, tensegrity has not been given a unique technical definition [50], [51] – thus a universal definition does not exist. Although the tensegrity concept is ubiquitous, the actual word is interpreted differently

across fields, such as architecture, engineering, art, mathematics, and biology.

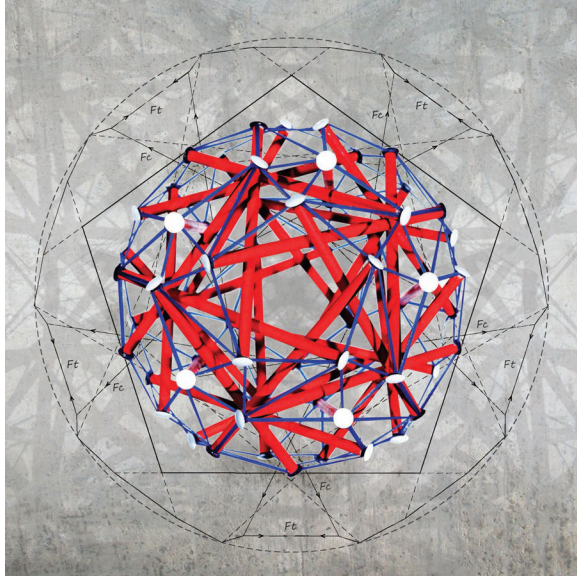


Figure 1.3: A polyhedral tensegrity sculpture. Designed by Ke Liu using a computational optimization algorithm. Struts are in red, made of wood; cables are in blue, which are made of 3D printed rubber-like material.

In the most general definition, the term “tensegrity” encompasses any prestressed structural system that has continuous tensile component, like membranes. For example, in biology, Donald Ingber [13] interpreted tensegrity as the fundamental structure of all living creatures with the characteristic of being prestressed and having a continuous tensile component, such as the cytoskeleton of cells. Classic tensegrities like the sculptures by Snelson [8], align to the definition by Motro [50]: “*A tensegrity system is a system in a stable self-equilibrated state comprising a discontinuous set of compressed components inside a continuum of tensioned components.*” Other definitions can also be found – see reference [52]. Some might insist that a tensegrity must also have infinitesimal mechanisms. In this work, we aim to prompt the application of tensegrity for engineering purposes; therefore, kinematic indeterminacy is not a particular feature of interest in this thesis. *The structures that we design follow the definitions by researchers such as Motro [50], Zhang and Ohsaki [53], and Skelton and de Oliveira [51]. Since we only consider rectilinear members, our designed structures can also be called “strut-tendon” structures, as introduced by Hanaor*

[54]. In addition, we adopt the idea about classification of tensegrity that was proposed by Skelton and others [51], [55] to generalize the concept of tensegrity by relaxing the discontinuity constraint regarding struts. The Class definition sets an upper bound to the number of compressive members (i.e. struts) that can connect at each node of the tensegrity. For example, the iconic “Needle Tower” shown in Fig. 1.4(a) is a Class-1 tensegrity, for which the struts are all isolated. As an example of a Class-2 tensegrity, we cite the work by Moore et al. [56], who designed an active robotic fin for underwater locomotion. For further details about the history and definitions of tensegrity, the readers are referred to the book by Motro [50].

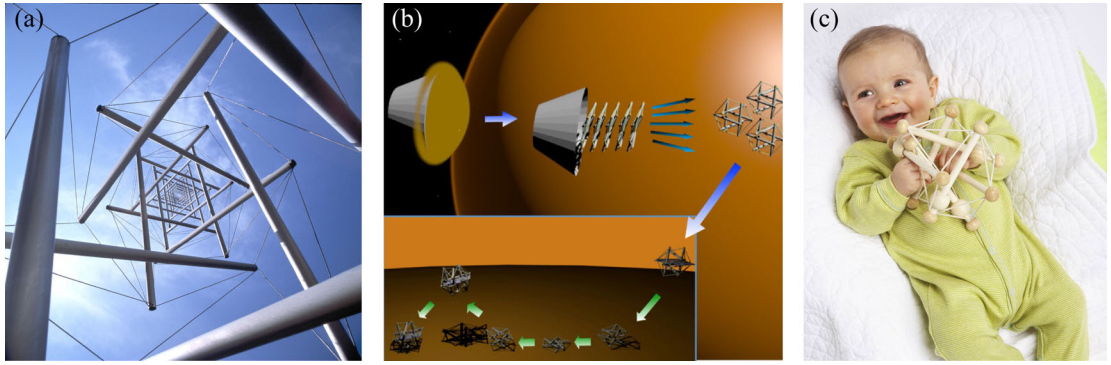


Figure 1.4: Applications of tensegrity structures. (a) The outdoor sculpture “Needle Tower” created by Kenneth Snelson (1968) [8]. (Image courtesy of Kenneth Snelson.) (b) Tensegrity robot design investigated by NASA [1] for outer space missions. (Adapted from [1].) (c) A baby playing with a tensegrity toy. (Image reproduced from [57]. ©2016 Manhattan Toy).

In engineering, tensegrity has been used to make structures that are deployable, actively tunable, and light weight [1], [2], [50], [58], [59]. In this work, we seek for programmable properties of tensegrities by changing their prestress level, which provides an extra dimension of programmability beyond geometry. We first conceptualize a mathematical model of tensegrity design, and propose a mixed integer formulation based on graph theory to effectively design tensegrity structures within arbitrary given geometries (Chapter 7). However, due to the presence of prestress, tensegrity structures pose unique fabrication challenges. In Chapter 8, we use stimuli-responsive materials to achieve programmable deployment of

tensegrity structures with various geometries. Harnessing the programmability provided by prestress, we tessellate tensegrity units to make metamaterials. Our analyses show that tensegrity metamaterials offer tunable effective elastic moduli, Poisson's ratio, and phononic bandgaps by properly changing their prestress levels (Chapter 9).

1.3 Organization of The Thesis

This thesis is divided into two main parts: Part I: Origami, and Part II: Tensegrity. The closure of the work is presented in Part III by means of convergent arguments.

Part I of the thesis comprises Chapter 2 to Chapter 6, which discuss about origami structures. In Chapter 2, a nonlinear formulation based on the bar-and-hinge reduced order model is proposed for structural analysis of non-rigid origami structures involving large deformations and displacements. We implemented the formulation in the software MERLIN [60] and MERLIN2 [61], [62], which are used in the subsequent Chapters as a tool to understand origami mechanics. In Chapter 3, we study the geometry and mechanics of the pleated hyperbolic paraboloid origami, a non-periodic pattern whose geometry remained a “mystery” for decades. In practice, geometric imperfections - resulting from either fabrication errors or distortion during service - may alter the expected behavior of origami systems. Therefore, in Chapter 4, we investigate the influence of geometric imperfections in origami, considering the representative Miura-ori, by combining theoretical, numerical, and experimental analyses. In Chapter 5, we propose a new rigid origami pattern named as the “Morph” pattern, which combines the distinct features of the standard Miura pattern and the Eggbox pattern through morphing. In Chapter 6, we transform some features of the Morph pattern into the so-called “Shrimp” pattern, which displays both rigid and non-rigid behavior at different configurations, and possesses programmable bistability and multi-stability. However, the aforementioned studies focus on perfect geometries and ideal patterns.

Part II of the thesis comprises Chapter 7 to Chapter 9, which discuss about tenseg-

rity structures. In Chapter 7, we propose an optimization formulation to design tensegrity within an arbitrarily given geometry, which is solved by Mixed Integer Linear Programming (MILP). The integer variables are introduced to resolve the discontinuity requirement of compression members (i.e. struts). In Chapter 8, we explore active deployment of tensegrity structure under external stimuli, enabled by shape memory polymers (SMP) struts. In Chapter 9, we modify the formulation proposed in Chapter 7 to design tessellations of tensegrity structures, by introducing periodicity-aware constraints. We further demonstrate that tensegrity tessellations can be used as metamaterials with tunable static and dynamic properties through prestress control.

Typically, for successful applications, a structural system needs to be thoroughly addressed in at least three aspects: design, analysis, and fabrication. Therefore, to improve our understanding of the two structural systems and promote engineering applications, the research presented in this thesis covers the three aspects of both origami and tensegrity. For example, Chapters 5, 6, and 7 mainly focus on the design aspects. Chapters 2 and 3 are mainly about analysis. Chapter 8 focuses on fabrication. Chapter 9 involves both design and analysis. Chapter 4 concerns both analysis and fabrication.

Finally, Part III of the thesis comprises Chapter 10, which summarizes the work through convergent arguments. In addition, potential interdisciplinary extensions of the work are also discussed.

Part I

Origami

CHAPTER 2

NONLINEAR STRUCTURAL ANALYSIS OF NON-RIGID ORIGAMI

Origami-inspired designs possess attractive applications to science and engineering (e.g. deployable, self-assembling, adaptable systems). The special geometric arrangement of panels and creases gives rise to unique mechanical properties of origami, such as reconfigurability, which makes origami designs suitable for tunable structures. However, due to the flexibility of thin sheets, additional soft modes exist in actual origami structures, which influence their behavior. Actual behavior of origami structures usually involves significant geometric nonlinearity, which amplifies the influence of additional soft modes. To investigate the nonlinear mechanics of origami structures with deformable panels, we present a structural engineering approach for simulating the nonlinear response of non-rigid origami structures. We propose a fully nonlinear, displacement-based implicit formulation for constructing static/quasi-static analyses of non-rigid origami structures based on the “bar-and-hinge” models. The formulation itself leads to an efficient and robust numerical implementation. Agreement between real models and numerical simulations demonstrates the ability of the proposed approach to capture key features of origami behavior.

2.1 Introduction

Various approaches have been proposed in order to understand large deformations of origami structures including the folding process. Following rigid origami assumption, belcastro and Hull [63] developed an affine transformation map to describe the folding of a single vertex origami. Tachi [64] extended the idea to simulate the folding of complex origami sheets with arbitrary patterns. Wu and You [65] presented a quaternion-based formulation for rigid origami simulation. For some particular patterns that can be assembled with repeated unit cells, such as the Miura-ori and its deviations [34], [66], closed form equations are

derived to describe any stage along the folding process. However, the aforementioned approaches, based on purely geometric considerations, are applicable only to rigid origami, i.e. they assume that all the panels in an origami structure are rigid surfaces.

Due to the flexibility of thin sheets, origami structures actually gain additional degrees of freedom that come from bending, stretching, and shearing of panels. Thus, rigid origami simulations are not sufficient to reflect the actual behavior of a physical origami structure. Direct modeling of origami structures is possible by means of finite element (FE) analysis with shell elements [67]. It provides detailed information such as stress distribution, but also requires a time-consuming cycle for both modeling and computing, including pre- and post-processing [29], [68]–[70]. Shell elements are usually computationally expensive and have issues associated with numerical artifacts, such as shear and membrane locking [71]–[73]. As the thickness of the origami panels decrease, then specialized approaches are needed [74]. In addition, local instabilities may influence the convergence of the analysis on the global scale. In some instances, the approximate global behavior of an origami structure is of more interest than high-resolution local deformations. In such instances, a simpler and specialized analysis tool is required, which should be able to track global deformations of origami structures, while being less sensitive to local instabilities. This is the main goal of the present work.

A commonly adopted technique to simplify the analysis of origami structures consists of representing an origami structure with a reduced order model. Resch and Christiansen [75] exploited linear elastic rotational hinges for the folding creases, and modeled each panel using a plane stress element. Kumar and Pellegrino [76] used triangulated truss mechanisms to represent origami structures for kinematic path analyses. Evans *et al.* [77] ignored in-plane deformations, but introduced extra diagonal bending lines within each panel to reflect the bending of panels. Tachi [78] used a similar simplification while adopting an iterative strategy to handle large developable transformations. Such simplification was also adopted by Brunck [79].

Schenk and Guest [80], [81] proposed a bar-and-hinge model, where an origami sheet is triangulated to a truss framework with constrained rotational hinges. The basic idea of the model is shown in Fig. 1, considering the Miura-ori as an example. Bars are placed along straight fold lines, and across panels for in-plane stiffness. The rotational hinges are along bars connecting panels to model folding of creases, and along bars across panels to model bending of panels. Such simplified representation is effective for origami structures with quadrilateral panels [37], [82]. A linear elastic formulation in association with the bar-and-hinge model was derived to analyze infinitesimal deformations of origami [80]. Both the bars and the rotations are assigned with constant stiffness. The same discretization scheme has been adopted by Wei *et al.* [35] to simulate bending of the Miura-ori, based on an explicit formulation through time integration without construction of stiffness matrices. Artificial damping is needed to force the structure to come to rest, which is a strategy usually used in computer animation simulating soft surfaces such as cloth [83]. In the bar-and-hinge model, triangular panels may not need to be divided – previous work by Guest and Pellegrino [84] shows the effectiveness of such bar-and-hinge simplification in modeling a triangulated cylindrical pattern.

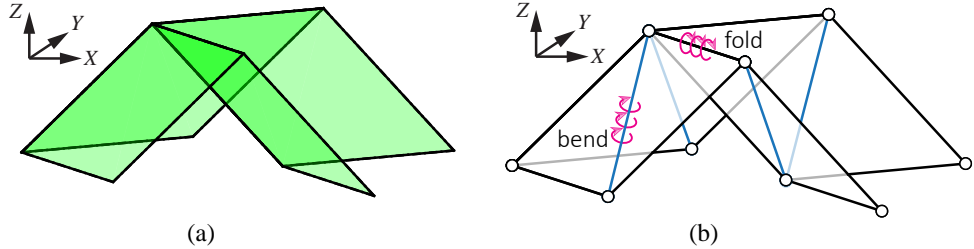


Figure 2.1: (a) The Miura-ori unit cell. (b) A bar-and-hinge model for a unit cell of Miura-ori. The black bars represent creases and boundaries of the origami and the blue bars are added to model in-plane and out-of-plane deformations of the panels (online version in color).

The structural analysis formulation proposed by Schenk and Guest [81] captures well global deformation modes of various origami structures. Based on reference [81], Fuchi *et al.* [85], [86] implemented the linear bar-and-hinge model as the structural analysis mod-

ule for topology optimization of origami structures. Filipov *et al.* [5] used a variation of the model with enriched discretization to analyze mechanical properties of the so-called zipper origami tube. However, the theory associated to the bar-and-hinge simplification has only been developed for infinitesimal deformations, however, for many applications, the attractive feature of origami is its ability to undergo large configurational transformations. Therefore, there is a need for a robust and simple approach that can simulate large deformations and displacements of origami structures - this is the focus of the present work.

In this chapter, we propose a general nonlinear formulation for structural analysis of origami structures associated with arbitrary bar-and-hinge models. The formulation is displacement-based, and considers both geometric and material nonlinearities, building up a fully nonlinear framework for large displacement and large deformation analyses of origami structures. It is more than a straightforward extension of the existing linear formulation [81]. For instance, geometric nonlinearity due to large rotations has to be carefully addressed to avoid singularities which usually do not arise under infinitesimal deformation. The proposed formulation is implicit, which enforces equilibrium at each converged incremental step, thus it is more suitable for static/quasi-static analysis compared to explicit approaches by direct time integration.

The idealization of this work is motivated by the pioneering work of Prof. Richard H. Gallagher on matrix structural analysis [87]–[89] and finite elements [90]. His work paved the way for many developments in the field and thus our numerical formulation of nonlinear mechanics for non-rigid origami is inspired from the fundamental work by Gallagher and his colleagues. The remainder of this chapter is organized as follows. Section 2.2 presents the derivation and associated components of the formulation. Special attention is paid to the geometric terms in the tangent stiffness matrix. Section 2.4 addresses the solution scheme for the nonlinear formulation. Section 2.5 provides numerical examples of origami simulations using the nonlinear bar-and-hinge model. We compare numerical simulations with paper-made models to manifest that the proposed approach is able to capture key features

of the deformation process of origami structures. Conclusions are drawn in Section 2.6. The proposed formulation is implemented by the “MERLIN” and “MERLIN2” software written in MATLAB [60], [61].

2.2 Nonlinear formulation for bar-and-hinge models

From the aforementioned discussion, we adopt a potential energy approach to formulate the nonlinear bar-and-hinge model. This is followed by the finite element implementation of bar elements and rotational spring elements. The treatment of finite rotations is a major aspect of the present work because the classical approach of using trigonometric functions to derive internal force vectors and tangent stiffness matrices fails due to singularities in the gradients of those functions. Thus we propose enhanced formulae based on distance vectors and functions which are free of singularities in their gradients. Next we provide the constitutive relationships for bars and rotational springs. The relevant aspect there is that we transfer the problem of (local) contact to the constitutive model of the rotational springs. These remarks are elaborated upon below.

2.2.1 Principle of stationary potential energy

The potential energy of the bar-and-hinge system, which is assumed to be energy conservative, is only a function of the current configuration, independent of deformation history. Thus, we use the principle of stationary potential energy [91] to derive the equilibrium condition and tangent stiffness matrix, while accounting for both material (constitutive relationship) and geometric nonlinearity. We describe the kinematics by the total Lagrangian approach, taking reference to the initial configuration. The potential energy of the system is comprised of internal strain energy (or stored energy) and external (load) work (V_{ext}). We separate the strain energy into two components: one stored in the bar elements (U_{bar}) and the other stored in the rotational springs (U_{spr}). Thus we have the following expression

for the total potential energy:

$$U = U_{bar} + U_{spr} - V_{ext}. \quad (2.1)$$

The equilibrium of the system is reached when the potential energy is stationary, that is, the first variation of the total potential energy becomes zero. Considering the origami discretization given by the bar-and-hinge model, we obtain the directional derivative of the total potential energy with respect to finite degrees of freedom as:

$$\mathcal{D}U \delta\mathbf{v} = \delta\mathbf{v}^T \mathbf{R} = 0, \quad (2.2)$$

The term \mathcal{D} denotes the directional derivative operator, $\delta\mathbf{v}$ refers to a virtual displacement, and \mathbf{R} denotes the residual force vector. For clarity, let's denote the vector \mathbf{X} as the collection of nodal coordinates in the undeformed configuration, and \mathbf{x} for nodal coordinates in the deformed configuration. The (total) displacement vector \mathbf{u} is defined as $\mathbf{u} = \mathbf{x} - \mathbf{X}$. The nonlinear equilibrium equation can be symbolically assembled as:

$$\mathbf{R}(\mathbf{u}) = \mathbf{T}(\mathbf{u}) - \mathbf{F}(\mathbf{u}) = \mathbf{T}_{bar}(\mathbf{u}) + \mathbf{T}_{spr}(\mathbf{u}) - \mathbf{F}(\mathbf{u}) = \mathbf{0}. \quad (2.3)$$

The vector \mathbf{F} contains the applied forces to the nodes of the bar-and-hinge system, and \mathbf{T} denotes the internal force vector. Linearization of the equilibrium equation (Eq. (2.3)) provides second-order approximation about the total potential energy, which leads to the tangent stiffness matrix, as shown below:

$$\mathcal{D}\mathbf{T} \delta\mathbf{u} = \mathbf{K}\delta\mathbf{u}, \quad (2.4)$$

where $\delta\mathbf{u}$ refers to a small nodal displacement perturbation. Similarly, the tangent stiffness matrix can be decomposed into two contributing terms:

$$\mathbf{K}(\mathbf{u}) = \mathbf{K}_{bar}(\mathbf{u}) + \mathbf{K}_{spr}(\mathbf{u}). \quad (2.5)$$

We elaborate on the internal force vectors and tangent stiffness matrices of each component in the following subsections. The goal is to assemble the internal force vector and tangent stiffness matrix of the whole structure.

2.2.2 Implementation of bar elements

Our constitutive models are hyperelastic because they provide generality to represent a wider variety of constitutive behavior than traditional linear elasticity (adopted in the original bar-and-hinge model). For many materials, linear elastic models do not accurately describe the observed material behavior and thus hyperelasticity provides a means of modeling the stress-strain behavior of such materials – this is helpful to capture the actual behavior of origami sheets made with different materials (such as composites). For instance, we can easily consider materials with different compression and tension stiffness. In addition, the linear elastic constitutive model is not physical under large deformation, which could happen when an origami sheet has high in-plane compliance. In the worst scenario, negative principal stretch could happen with a linear elastic constitutive relationship leading to unphysical response.

The constitutive relationship of a hyperelastic material is governed by a strain energy density function \mathcal{W} [92]. This function is expressed in terms of the Green-Lagrange strain tensor \mathbf{E} and its energy conjugate second Piola-Kirchhoff (P-K) stress tensor \mathbf{S} . We consider linear shape functions for the bar element and then write the strain energy function as a function of nodal displacements. This finite element formulation for nonlinear truss analysis has been extensively studied in previous literature [91], [93], and here it is adapted

to origami assemblages as part of the proposed nonlinear bar-and-hinge model. Below we summarize the finite element formulation for bar elements using matrix notations.

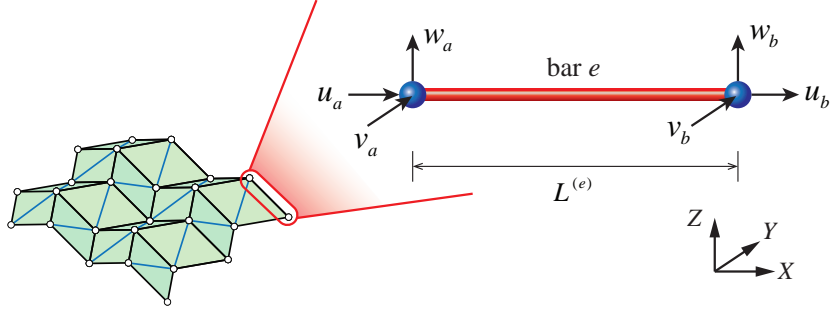


Figure 2.2: Components of a bar element, which is part of an origami assemblage.

Let's assume that the bar element is in its local coordinate, as shown in Fig. 2.2. We denote the area of one bar element as $A^{(e)}$, which is assumed to be constant along the longitudinal direction. The stored energy of a bar element is given by:

$$U_{bar}^{(e)} = \int_0^{L^{(e)}} \mathcal{W} A^{(e)} dX. \quad (2.6)$$

Because bar elements are one-dimensional, we only need to consider one component per stress tensor and strain tensor. Considering a linear shape function, we obtain the one-dimensional Green-Lagrange strain E_{11} as a function of the nodal displacements $\mathbf{u}^{(e)}$ [91], [93]:

$$E_{11} = \mathbf{B}_L \mathbf{u}^{(e)} + \frac{1}{2} \mathbf{u}^{(e)T} \mathbf{B}_{NL} \mathbf{u}^{(e)}, \quad (2.7)$$

where $\mathbf{u}^{(e)} = [u_a, v_a, w_a, u_b, v_b, w_b]^T$ (see Fig. 2.2). The vector \mathbf{B}_L is given by

$$\mathbf{B}_L = \frac{1}{L^{(e)}} \begin{bmatrix} -\mathbf{e}_1 & \mathbf{e}_1 \end{bmatrix}, \quad (2.8)$$

where $\mathbf{e}_1 = [1, 0, 0]$. The matrix \mathbf{B}_{NL} is

$$\mathbf{B}_{NL} = \frac{1}{(L^{(e)})^2} \begin{bmatrix} \mathbf{I}_{3 \times 3} & -\mathbf{I}_{3 \times 3} \\ -\mathbf{I}_{3 \times 3} & \mathbf{I}_{3 \times 3} \end{bmatrix}. \quad (2.9)$$

The matrix $\mathbf{I}_{3 \times 3}$ is the identity matrix of size 3 by 3. Substituting Eq. (2.7) into the derivative of Eq. (2.6), we obtain the internal force vector $\mathbf{T}_{bar}^{(e)}$ for a bar element e [91], [93] as:

$$\mathbf{T}_{bar}^{(e)} = S_{11} A^{(e)} L^{(e)} (\mathbf{B}_L^T + \mathbf{B}_{NL} \mathbf{u}^{(e)}) , \quad (2.10)$$

where S_{11} refers to the one dimensional component of the second P-K stress tensor. Linearization of the internal force vector leads to the component tangent stiffness matrix, which is given by:

$$\mathbf{K}_{bar}^{(e)} = C_{1111} A^{(e)} L^{(e)} (\mathbf{B}_L^T + \mathbf{B}_{NL} \mathbf{u}^{(e)}) (\mathbf{B}_L^T + \mathbf{B}_{NL} \mathbf{u}^{(e)})^T + S_{11} A^{(e)} L^{(e)} \mathbf{B}_{NL}. \quad (2.11)$$

The term C_{1111} is the one dimensional tangent modulus defined as:

$$C_{1111} = \frac{\partial S_{11}}{\partial E_{11}}. \quad (2.12)$$

Expanding the terms of the symmetric element tangent stiffness matrix, we can recognize that $\mathbf{K}_{bar}^{(e)}$ is a summation of several matrices as:

$$\mathbf{K}_{bar}^{(e)} = \mathbf{K}_E^{(e)} + \mathbf{K}_1^{(e)} + \mathbf{K}_2^{(e)} + \mathbf{K}_G^{(e)}. \quad (2.13)$$

where,

$$\mathbf{K}_E^{(e)} = C_{1111} A^{(e)} L^{(e)} \mathbf{B}_L^T \mathbf{B}_L, \quad (2.14)$$

$$\mathbf{K}_1^{(e)} = C_{1111} A^{(e)} L^{(e)} \left((\mathbf{B}_{NL} \mathbf{u}^{(e)}) \mathbf{B}_L + \mathbf{B}_L^T (\mathbf{B}_{NL} \mathbf{u}^{(e)})^T \right), \quad (2.15)$$

$$\mathbf{K}_2^{(e)} = C_{1111} A^{(e)} L^{(e)} (\mathbf{B}_{NL} \mathbf{u}^{(e)}) (\mathbf{B}_{NL} \mathbf{u}^{(e)})^T, \quad (2.16)$$

$$\mathbf{K}_G^{(e)} = S_{11} A^{(e)} L^{(e)} \mathbf{B}_{NL}. \quad (2.17)$$

The matrix $\mathbf{K}_E^{(e)}$ is the linear stiffness matrix, $\mathbf{K}_G^{(e)}$ is the geometric stiffness matrix, and $(\mathbf{K}_1^{(e)} + \mathbf{K}_2^{(e)})$ forms the initial displacement matrix. To assemble the global stiffness ma-

trix, the element stiffness matrix needs to be transformed from its local coordinates to the global coordinates. The resultant matrix, after transformation, can be derived explicitly, where \mathbf{B}_{NL} is invariant and \mathbf{B}_L in global coordinates (i.e. $\tilde{\mathbf{B}}_L$) is composed of the directional cosines of the bar element, that is,

$$\tilde{\mathbf{B}}_L = \frac{1}{L^{(e)}} \begin{bmatrix} -\left(\frac{\mathbf{X}_b - \mathbf{X}_a}{L^{(e)}}\right)^T & \left(\frac{\mathbf{X}_b - \mathbf{X}_a}{L^{(e)}}\right)^T \end{bmatrix}. \quad (2.18)$$

where \mathbf{X}_a and \mathbf{X}_b are the initial global coordinates of nodes a and b , respectively.

2.2.3 Rotational spring elements: basic description

For each rotational hinge that represents either a folding crease or bending diagonal on a panel, its degree of rotation (or bending), measured by the dihedral angle between two planar surfaces, is totally defined by the displacements and original coordinates of nodes. In the bar-and-hinge model, a rotational spring element consists of four neighboring nodes, which forms two triangles, as shown in Fig. 2.3.

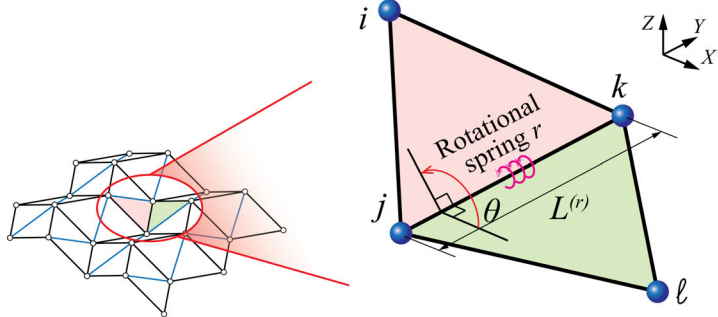


Figure 2.3: Components of a rotational spring element, which is part of an origami assemblage.

We denote the undeformed length of a rotational hinge (axis) as $L^{(r)}$. The rotational spring elements are directly defined based on the nodal coordinates, and thus nodal displacements. Therefore, no shape function is required and, as we directly work in the global coordinates, we do not need to perform any transformation from local to global coordinates or vice versa. We assume that the constitutive relationship for each rotational spring ele-

ment is described by a stored energy function $\mathcal{H} = \mathcal{H}(\theta)$, where θ is the dihedral angle. Thus the total stored energy in a rotational spring element is:

$$U_{spr}^{(r)} = \mathcal{H}(\theta). \quad (2.19)$$

We can define the resistance moment as:

$$M = \frac{\partial \mathcal{H}(\theta)}{\partial \theta}. \quad (2.20)$$

The internal force vector associated with a rotational spring element is obtained as,

$$\mathbf{T}_{spr}^{(r)}(\mathbf{u}) = \tilde{\mathbf{T}}_{spr}^{(r)}(\mathbf{x}) = \frac{d\mathcal{H}}{d\theta} \frac{d\theta}{dx^{(r)}} = M \frac{d\theta}{d\mathbf{x}^{(r)}}. \quad (2.21)$$

The nodal coordinates $\mathbf{x}^{(r)}$ determine the value of the associated dihedral angle. Recalling that $\mathbf{u} = \mathbf{x} - \mathbf{X}$, because \mathbf{X} is constant, derivatives with respect to \mathbf{u} is the same as derivatives with respect to \mathbf{x} . The tangent stiffness matrix of a rotational spring element r is then derived as the derivative of the internal force vector,

$$\mathbf{K}_{spr}^{(r)}(\mathbf{u}) = \tilde{\mathbf{K}}_{spr}^{(r)}(\mathbf{x}) = k \frac{d\theta}{d\mathbf{x}^{(r)}} \otimes \frac{d\theta}{d\mathbf{x}^{(r)}} + M \frac{d^2\theta}{d(\mathbf{x}^{(r)})^2}. \quad (2.22)$$

The symbol “ \otimes ” means the tensor product. The tangent rotational stiffness k is defined by

$$k = \frac{dM}{d\theta}. \quad (2.23)$$

The coupling effect between in-plane behavior (\mathcal{W}) and out-of-plane performance (\mathcal{H}) of origami sheets is not well understood yet. We avoid adding arbitrary and artificial coupling at the current stage by assuming that \mathcal{H} is only a function of θ , and θ will not affect the stiffness of bars (\mathcal{W}). The above formulation generalizes the linear rotational spring model to a nonlinear model, which allows additional flexibilities when accounting for specific

material properties of the panels.

2.2.4 Geometry of rotational spring element: enhanced description

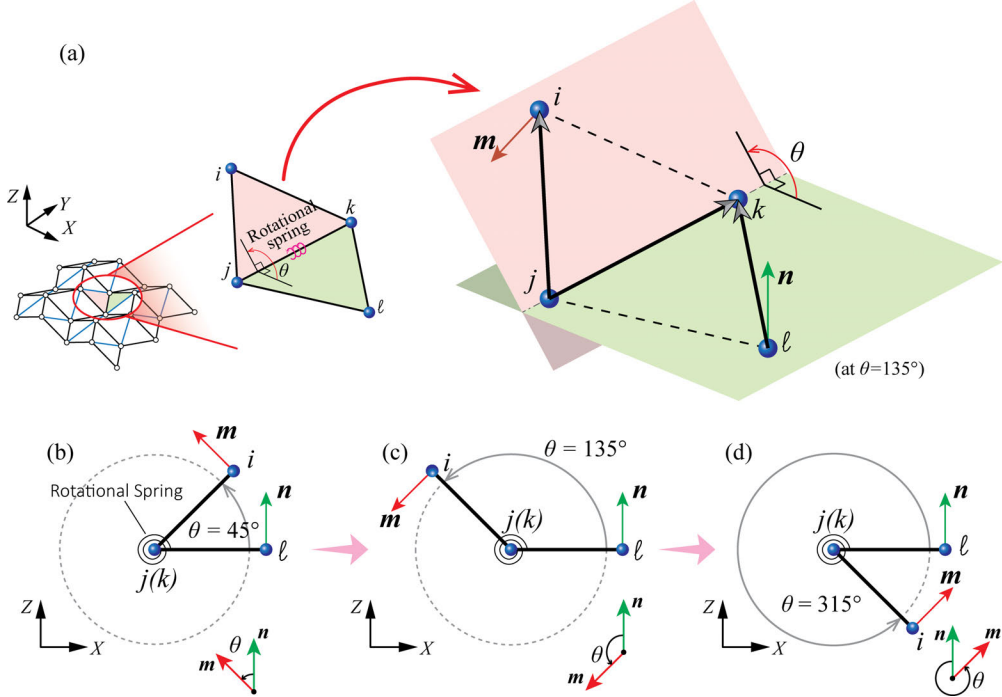


Figure 2.4: (a) Geometry of a rotational spring element. The two triangles lies on two intersecting planes, painted with two different colors. The three space vectors (i.e., $\mathbf{r}_{ij}, \mathbf{r}_{kj}, \mathbf{r}_{\ell k}$), drawn with solid lines are sufficient to define the dihedral angle between the two planes. (b)-(d) An illustration of the consistent assignment for rotation angle θ of a rotational spring element turning from 0 to 2π (360°) .

To complete the formulation of a rotational spring element as defined in Section 2.2.3, we need to obtain the geometric terms, i.e., the dihedral angle and its derivatives with respect to current configuration (same as to nodal displacements). We remark that the common approach of using direct differentiation of trigonometric functions [70], [81] to handle these terms is not sufficient for a robust nonlinear analysis because of the limitations and singularities associated with trigonometric functions. Therefore, in this section, we present the enhanced formulae that will eventually lead to a robust numerical implementation. As shown in Fig. 2.4, the geometry of a rotational spring element consists of four nodes (i, j, k, ℓ), two triangles, and one dihedral angle (θ). The two triangles lie on two intersect-

ing planes. Let's denote a vector connecting any two nodes as:

$$\mathbf{r}_{pq} = \mathbf{x}_p^{(r)} - \mathbf{x}_q^{(r)}, \quad (2.24)$$

where p and q are labels of any pair of nodes. In addition, we define the normal vectors:

$$\mathbf{m} = \mathbf{r}_{ij} \times \mathbf{r}_{kj}, \quad \mathbf{n} = \mathbf{r}_{kj} \times \mathbf{r}_{k\ell}, \quad (2.25)$$

where i, j, k, ℓ are labels of the nodes associated with a rotational spring element as marked in Fig. 2.4. The two vectors \mathbf{m} and \mathbf{n} point to the normal directions of the two intersecting planes. The operator “ \times ” between two vectors means the cross product. In this chapter, repeated indices do not imply summation. Using this notation, the dihedral angle between the two triangles can be determined by

$$\theta = \arccos\left(\frac{\mathbf{m} \cdot \mathbf{n}}{\|\mathbf{m}\| \|\mathbf{n}\|}\right). \quad (2.26)$$

However, this expression is not enough to describe the whole range of rotation, because there is no distinction for angles within the ranges of $[0, \pi)$ and $[\pi, 2\pi)$. Therefore, we introduce the following definition to expand the domain of definition to $[0, 2\pi)$, that is,

$$\theta = \eta \arccos\left(\frac{\mathbf{m} \cdot \mathbf{n}}{\|\mathbf{m}\| \|\mathbf{n}\|}\right) \mod 2\pi, \quad (2.27)$$

where η is a sign indicator defined as,

$$\eta = \begin{cases} \operatorname{sgn}(\mathbf{m} \cdot \mathbf{r}_{k\ell}), & \mathbf{m} \cdot \mathbf{r}_{k\ell} \neq 0; \\ 1, & \mathbf{m} \cdot \mathbf{r}_{k\ell} = 0. \end{cases} \quad (2.28)$$

The symbol “mod” means modulo operation. The exception of $\mathbf{m} \cdot \mathbf{r}_{k\ell} = 0$ happens when the dihedral angle is 0 or π , i.e., the two triangular panels lay on the same plane. Thus

adopting Eq. (2.27), we get a consistent description for all possible rotations of two origami panels if penetration does not happen, that is, from 0 to 2π , as shown in Fig. 2.4(b)-(d).

Such a large range of rotation (θ varying from 0 to 2π) makes it possible for a mountain fold to become a valley and vice-versa. The transition between mountain and valley folds is naturally included in our model. Because our formulation follows an energy approach, it handles both mountain and valley folds in a unified way. For instance, when a mountain fold transitions to a valley fold, it passes through the “flat state,” which corresponds to $\theta = \pi$. Because we define our constitutive model for rotational springs for the range from 0 to 2π , $\theta = \pi$ is a regular state during the rotation process. Thus we do not need any special treatment to handle switching between mountain and valley folds.

Next, we need the first derivative of the rotation angle with respect to nodal coordinates. Differentiation using the chain rule results in formulae that become numerically unstable near the angles 0 and π , because of the sine function in the denominator, as shown in Eq. (2.29) to (2.32):

$$\frac{\partial \theta}{\partial \mathbf{x}_i^{(r)}} = \frac{-1}{\sin(\theta)} \mathbf{r}_{kj} \times \frac{\|\mathbf{m}\|^2 \mathbf{n} - (\mathbf{m} \cdot \mathbf{n}) \mathbf{m}}{\|\mathbf{m}\|^3 \|\mathbf{n}\|}, \quad (2.29)$$

$$\frac{\partial \theta}{\partial \mathbf{x}_\ell^{(r)}} = \frac{-1}{\sin(\theta)} \mathbf{r}_{kj} \times \frac{\|\mathbf{n}\|^2 \mathbf{m} - (\mathbf{n} \cdot \mathbf{m}) \mathbf{n}}{\|\mathbf{n}\|^3 \|\mathbf{m}\|}, \quad (2.30)$$

$$\frac{\partial \theta}{\partial \mathbf{x}_j^{(r)}} = \frac{-1}{\sin(\theta)} \left((\mathbf{r}_{ij} - \mathbf{r}_{kj}) \times \frac{\|\mathbf{m}\|^2 \mathbf{n} - (\mathbf{m} \cdot \mathbf{n}) \mathbf{m}}{\|\mathbf{m}\|^3 \|\mathbf{n}\|} - \mathbf{r}_{kl} \times \frac{\|\mathbf{n}\|^2 \mathbf{m} - (\mathbf{n} \cdot \mathbf{m}) \mathbf{n}}{\|\mathbf{n}\|^3 \|\mathbf{m}\|} \right), \quad (2.31)$$

$$\frac{\partial \theta}{\partial \mathbf{x}_k^{(r)}} = \frac{-1}{\sin(\theta)} \left((\mathbf{r}_{kl} - \mathbf{r}_{kj}) \times \frac{\|\mathbf{n}\|^2 \mathbf{m} - (\mathbf{n} \cdot \mathbf{m}) \mathbf{n}}{\|\mathbf{n}\|^3 \|\mathbf{m}\|} - \mathbf{r}_{ij} \times \frac{\|\mathbf{m}\|^2 \mathbf{n} - (\mathbf{m} \cdot \mathbf{n}) \mathbf{m}}{\|\mathbf{m}\|^3 \|\mathbf{n}\|} \right). \quad (2.32)$$

These expressions contain terms that will reach singularity when $\sin(\theta) = 0$. Theoretically, these formulae have well-defined limits as $\sin(\theta)$ approaches 0, but in numerical computation, such singularities cannot be handled by floating point arithmetic. The use of inverse sine function to define θ leads to the same problem [81].

Therefore, we move from a trigonometric-based approach to an approach based on distance vectors and functions. By means of some simplifying transformations [94], [95], one can obtain equivalent expressions for the gradients, which are free of any singularities in their terms. To accomplish the simplification from Eq. (2.29)-(2.32) to Eq. (2.36)-(2.39), the following vector identity will be used frequently:

$$\mathbf{a} \times (\mathbf{b} \times \mathbf{c}) = (\mathbf{a} \cdot \mathbf{c})\mathbf{b} - (\mathbf{a} \cdot \mathbf{b})\mathbf{c}. \quad (2.33)$$

Following the procedure as described in reference [95], let us first simplify Eq. (2.29) as follows:

$$\begin{aligned} \frac{\partial \theta}{\partial \mathbf{x}_i^{(r)}} &= \frac{-1}{\sin(\theta)} \mathbf{r}_{kj} \times \frac{\|\mathbf{m}\|^2 \mathbf{n} - (\mathbf{m} \cdot \mathbf{n})\mathbf{m}}{\|\mathbf{m}\|^3 \|\mathbf{n}\|} \\ &= \frac{-1}{\sin(\theta)} \mathbf{r}_{kj} \times \left(\frac{\mathbf{m} \times (\mathbf{n} \times \mathbf{m})}{\|\mathbf{m}\|^3 \|\mathbf{n}\|} \right) \\ &= \frac{-1}{\sin(\theta)} \mathbf{r}_{kj} \times \left(\frac{\mathbf{m} \times (-\sin(\theta)\|\mathbf{m}\| \|\mathbf{n}\| \mathbf{r}_{kj})}{\|\mathbf{r}_{kj}\| \|\mathbf{m}\|^3 \|\mathbf{n}\|} \right) \\ &= \frac{\mathbf{r}_{kj} \times \mathbf{m} \times \mathbf{r}_{kj}}{\|\mathbf{r}_{kj}\| \|\mathbf{m}\|^2} \\ &= \frac{\|\mathbf{r}_{kj}\|}{\|\mathbf{m}\|^2} \mathbf{m}. \end{aligned} \quad (2.34)$$

Because Eq. (2.30) has the same structure as (2.29), following the same procedure, Eq. (2.30) can be simplified to Eq. (2.37). Starting with Eq. (2.31) and using Eq. (2.29), we

can obtain Eq. (2.38) by the following transformations:

$$\begin{aligned}
\frac{\partial \theta}{\partial \mathbf{x}_j^{(r)}} &= \frac{-1}{\sin(\theta)} \left((\mathbf{r}_{ij} - \mathbf{r}_{kj}) \times \frac{\|\mathbf{m}\|^2 \mathbf{n} - (\mathbf{m} \cdot \mathbf{n}) \mathbf{m}}{\|\mathbf{m}\|^3 \|\mathbf{n}\|} - \mathbf{r}_{k\ell} \times \frac{\|\mathbf{n}\|^2 \mathbf{m} - (\mathbf{n} \cdot \mathbf{m}) \mathbf{n}}{\|\mathbf{n}\|^3 \|\mathbf{m}\|} \right) \\
&= \frac{-1}{\sin(\theta)} \left(\mathbf{r}_{ij} \times \frac{\mathbf{m} \times (\mathbf{n} \times \mathbf{m})}{\|\mathbf{m}\|^3 \|\mathbf{n}\|} - \mathbf{r}_{k\ell} \times \frac{\mathbf{n} \times (\mathbf{m} \times \mathbf{n})}{\|\mathbf{n}\|^3 \|\mathbf{m}\|} \right) - \frac{\partial \theta}{\partial \mathbf{x}_i^{(r)}} \\
&= -\frac{\mathbf{r}_{ij} \times \mathbf{m} \times (-\mathbf{r}_{kj})}{\|\mathbf{r}_{kj}\| \|\mathbf{m}\|^2} + \frac{\mathbf{r}_{k\ell} \times \mathbf{n} \times \mathbf{r}_{kj}}{\|\mathbf{r}_{kj}\| \|\mathbf{n}\|^2} - \frac{\partial \theta}{\partial \mathbf{x}_i^{(r)}} \\
&= \frac{(\mathbf{r}_{ij} \cdot \mathbf{r}_{kj}) \mathbf{m}}{\|\mathbf{r}_{kj}\| \|\mathbf{m}\|^2} + \frac{(\mathbf{r}_{k\ell} \cdot \mathbf{r}_{kj}) \mathbf{n}}{\|\mathbf{r}_{kj}\| \|\mathbf{n}\|^2} - \frac{\partial \theta}{\partial \mathbf{x}_i^{(r)}} \\
&= \left(\frac{\mathbf{r}_{ij} \cdot \mathbf{r}_{kj}}{\|\mathbf{r}_{kj}\|^2} - 1 \right) \frac{\partial \theta}{\partial \mathbf{x}_i^{(r)}} - \frac{\mathbf{r}_{k\ell} \cdot \mathbf{r}_{kj}}{\|\mathbf{r}_{kj}\|^2} \frac{\partial \theta}{\partial \mathbf{x}_\ell^{(r)}}.
\end{aligned} \tag{2.35}$$

Eventually, we can obtain all the gradient information as:

$$\frac{\partial \theta}{\partial \mathbf{x}_i^{(r)}} = \frac{\|\mathbf{r}_{kj}\|}{\|\mathbf{m}\|^2} \mathbf{m}, \tag{2.36}$$

$$\frac{\partial \theta}{\partial \mathbf{x}_\ell^{(r)}} = -\frac{\|\mathbf{r}_{kj}\|}{\|\mathbf{n}\|^2} \mathbf{n}, \tag{2.37}$$

$$\frac{\partial \theta}{\partial \mathbf{x}_j^{(r)}} = \left(\frac{\mathbf{r}_{ij} \cdot \mathbf{r}_{kj}}{\|\mathbf{r}_{kj}\|^2} - 1 \right) \frac{\partial \theta}{\partial \mathbf{x}_i^{(r)}} - \frac{\mathbf{r}_{k\ell} \cdot \mathbf{r}_{kj}}{\|\mathbf{r}_{kj}\|^2} \frac{\partial \theta}{\partial \mathbf{x}_\ell^{(r)}}, \tag{2.38}$$

$$\frac{\partial \theta}{\partial \mathbf{x}_k^{(r)}} = \left(\frac{\mathbf{r}_{k\ell} \cdot \mathbf{r}_{kj}}{\|\mathbf{r}_{kj}\|^2} - 1 \right) \frac{\partial \theta}{\partial \mathbf{x}_\ell^{(r)}} - \frac{\mathbf{r}_{ij} \cdot \mathbf{r}_{kj}}{\|\mathbf{r}_{kj}\|^2} \frac{\partial \theta}{\partial \mathbf{x}_i^{(r)}}. \tag{2.39}$$

Since Eq. (2.36) to (2.39) eliminate the sine functions in the denominators, they provide more robust and simpler formulae, which dramatically increase the accuracy and efficiency of numerical evaluations.

These simplified gradients also provide physical insight about the internal forces generated by a rotational spring. For example, from Eq. (2.36) and (2.37), we see that the internal force at node i contributed by the rotational spring is always along the direction of \mathbf{m} , and the internal force at node ℓ is always along the direction of \mathbf{n} . The math directly reflects the physics: the torque generated by the rotational spring along axis \mathbf{r}_{kj} results in perpendicular force on each of the two intersecting panels.

By differentiating the above formulae, we obtain the second-order derivative (i.e., the Hessian) of the rotation angle with respect to nodal coordinates, which is used to construct the tangent stiffness matrix associated with a rotational spring element (see Eq. (2.22)). The complete Hessian has 16 blocks of submatrices, where each block is of size 3 by 3, referring to the 3 degrees of freedom (x, y, z) at a node. Among the 16 blocks of submatrices, there are 10 independent blocks due to symmetry. For clarity, let us denote:

$$A = \frac{\mathbf{r}_{ij} \cdot \mathbf{r}_{kj}}{\|\mathbf{r}_{kj}\|^2}, \quad B = \frac{\mathbf{r}_{k\ell} \cdot \mathbf{r}_{kj}}{\|\mathbf{r}_{kj}\|^2}. \quad (2.40)$$

Therefore, we obtain the following relationships:

$$\frac{\partial A}{\partial \mathbf{x}_j^{(r)}} = \frac{1}{\|\mathbf{r}_{kj}\|^2} ((2A - 1) \mathbf{r}_{kj} - \mathbf{r}_{ij}), \quad (2.41)$$

$$\frac{\partial B}{\partial \mathbf{x}_j^{(r)}} = \frac{1}{\|\mathbf{r}_{kj}\|^2} (2B \mathbf{r}_{kj} - \mathbf{r}_{k\ell}), \quad (2.42)$$

$$\frac{\partial A}{\partial \mathbf{x}_k^{(r)}} = \frac{1}{\|\mathbf{r}_{kj}\|^2} (-2A \mathbf{r}_{kj} + \mathbf{r}_{ij}), \quad (2.43)$$

$$\frac{\partial B}{\partial \mathbf{x}_k^{(r)}} = \frac{1}{\|\mathbf{r}_{kj}\|^2} ((1 - 2B) \mathbf{r}_{kj} + \mathbf{r}_{k\ell}). \quad (2.44)$$

In addition, let's define the operator “ \diamond ” as:

$$\mathbf{a} \diamond \mathbf{b} := \mathbf{a} \otimes \mathbf{b} + \mathbf{b} \otimes \mathbf{a}, \quad \forall \mathbf{a}, \mathbf{b} \in \mathbb{R}^3 \quad (2.45)$$

Notice that $\mathbf{a} \diamond \mathbf{b}$ results in a symmetric matrix. Then the 10 independent blocks of the Hessian matrix of the rotation angle with respect to the nodal coordinates are expressed as:

$$\frac{\partial^2 \theta}{\partial (\mathbf{x}_i^{(r)})^2} = -\frac{\|\mathbf{r}_{kj}\|}{\|\mathbf{m}\|^4} (\mathbf{m} \diamond (\mathbf{r}_{kj} \times \mathbf{m})), \quad (2.46)$$

$$\frac{\partial^2 \theta}{\partial (\mathbf{x}_\ell^{(r)})^2} = \frac{\|\mathbf{r}_{kj}\|}{\|\mathbf{n}\|^4} (\mathbf{n} \diamond (\mathbf{r}_{kj} \times \mathbf{n})), \quad (2.47)$$

$$\frac{\partial^2 \theta}{\partial \mathbf{x}_i^{(r)} \mathbf{x}_k^{(r)}} = \frac{\mathbf{m} \otimes \mathbf{r}_{kj}}{\|\mathbf{m}\|^2 \|\mathbf{r}_{kj}\|} + \frac{\|\mathbf{r}_{kj}\|}{\|\mathbf{m}\|^4} (\mathbf{m} \diamond (\mathbf{r}_{ij} \times \mathbf{m})), \quad (2.48)$$

$$\frac{\partial^2 \theta}{\partial \mathbf{x}_\ell^{(r)} \mathbf{x}_j^{(r)}} = \frac{\mathbf{n} \otimes \mathbf{r}_{kj}}{\|\mathbf{n}\|^2 \|\mathbf{r}_{kj}\|} - \frac{\|\mathbf{r}_{kj}\|}{\|\mathbf{n}\|^4} (\mathbf{n} \diamond (\mathbf{r}_{k\ell} \times \mathbf{n})), \quad (2.49)$$

$$\frac{\partial^2 \theta}{\partial \mathbf{x}_i^{(r)} \mathbf{x}_j^{(r)}} = -\frac{\mathbf{m} \otimes \mathbf{r}_{kj}}{\|\mathbf{m}\|^2 \|\mathbf{r}_{kj}\|} + \frac{\|\mathbf{r}_{kj}\|}{\|\mathbf{m}\|^4} (\mathbf{m} \diamond ((\mathbf{r}_{kj} - \mathbf{r}_{ij}) \times \mathbf{m})), \quad (2.50)$$

$$\frac{\partial^2 \theta}{\partial \mathbf{x}_\ell^{(r)} \mathbf{x}_k^{(r)}} = -\frac{\mathbf{n} \otimes \mathbf{r}_{kj}}{\|\mathbf{n}\|^2 \|\mathbf{r}_{kj}\|} - \frac{\|\mathbf{r}_{kj}\|}{\|\mathbf{n}\|^4} (\mathbf{n} \diamond ((\mathbf{r}_{kj} - \mathbf{r}_{k\ell}) \times \mathbf{n})), \quad (2.51)$$

$$\frac{\partial^2 \theta}{(\partial \mathbf{x}_j^{(r)})^2} = \frac{\partial \theta}{\partial \mathbf{x}_i^{(r)}} \otimes \frac{\partial A}{\partial \mathbf{x}_j^{(r)}} + (A-1) \frac{\partial^2 \theta}{\partial \mathbf{x}_i^{(r)} \mathbf{x}_j^{(r)}} - \left(\frac{\partial \theta}{\partial \mathbf{x}_\ell^{(r)}} \otimes \frac{\partial B}{\partial \mathbf{x}_j^{(r)}} + B \frac{\partial^2 \theta}{\partial \mathbf{x}_\ell^{(r)} \mathbf{x}_j^{(r)}} \right), \quad (2.52)$$

$$\frac{\partial^2 \theta}{\partial \mathbf{x}_j^{(r)} \partial \mathbf{x}_k^{(r)}} = \frac{\partial \theta}{\partial \mathbf{x}_i^{(r)}} \otimes \frac{\partial A}{\partial \mathbf{x}_k^{(r)}} + (A-1) \frac{\partial^2 \theta}{\partial \mathbf{x}_i^{(r)} \mathbf{x}_k^{(r)}} - \left(\frac{\partial \theta}{\partial \mathbf{x}_\ell^{(r)}} \otimes \frac{\partial B}{\partial \mathbf{x}_k^{(r)}} + B \frac{\partial^2 \theta}{\partial \mathbf{x}_\ell^{(r)} \mathbf{x}_k^{(r)}} \right), \quad (2.53)$$

$$\frac{\partial^2 \theta}{(\partial \mathbf{x}_k^{(r)})^2} = \frac{\partial \theta}{\partial \mathbf{x}_\ell^{(r)}} \otimes \frac{\partial B}{\partial \mathbf{x}_k^{(r)}} + (B-1) \frac{\partial^2 \theta}{\partial \mathbf{x}_\ell^{(r)} \mathbf{x}_k^{(r)}} - \left(\frac{\partial \theta}{\partial \mathbf{x}_i^{(r)}} \otimes \frac{\partial A}{\partial \mathbf{x}_k^{(r)}} + A \frac{\partial^2 \theta}{\partial \mathbf{x}_i^{(r)} \mathbf{x}_k^{(r)}} \right), \quad (2.54)$$

$$\frac{\partial^2 \theta}{\partial \mathbf{x}_\ell^{(r)} \mathbf{x}_i^{(r)}} = \mathbf{0}_{3 \times 3}. \quad (2.55)$$

The symbol $\mathbf{0}_{3 \times 3}$ means a 3×3 zero matrix. Due to symmetry, the other 6 blocks of the Hessian matrix can be completed with the following identities:

$$\begin{aligned} \frac{\partial^2 \theta}{\partial \mathbf{x}_k^{(r)} \mathbf{x}_i^{(r)}} &= \left(\frac{\partial^2 \theta}{\partial \mathbf{x}_i^{(r)} \mathbf{x}_k^{(r)}} \right)^T, & \frac{\partial^2 \theta}{\partial \mathbf{x}_j^{(r)} \mathbf{x}_\ell^{(r)}} &= \left(\frac{\partial^2 \theta}{\partial \mathbf{x}_\ell^{(r)} \mathbf{x}_j^{(r)}} \right)^T, \\ \frac{\partial^2 \theta}{\partial \mathbf{x}_j^{(r)} \mathbf{x}_i^{(r)}} &= \left(\frac{\partial^2 \theta}{\partial \mathbf{x}_i^{(r)} \mathbf{x}_j^{(r)}} \right)^T, & \frac{\partial^2 \theta}{\partial \mathbf{x}_k^{(r)} \mathbf{x}_j^{(r)}} &= \left(\frac{\partial^2 \theta}{\partial \mathbf{x}_j^{(r)} \mathbf{x}_k^{(r)}} \right)^T, \\ \frac{\partial^2 \theta}{\partial \mathbf{x}_i^{(r)} \mathbf{x}_\ell^{(r)}} &= \left(\frac{\partial^2 \theta}{\partial \mathbf{x}_\ell^{(r)} \mathbf{x}_i^{(r)}} \right)^T, & \frac{\partial^2 \theta}{\partial \mathbf{x}_k^{(r)} \mathbf{x}_\ell^{(r)}} &= \left(\frac{\partial^2 \theta}{\partial \mathbf{x}_\ell^{(r)} \mathbf{x}_k^{(r)}} \right)^T. \end{aligned} \quad (2.56)$$

The terms shown above are not completely simplified, but they are good enough for numerical computation because they are free of any singularity.

2.2.5 Verification using finite differences

The correctness of the derived terms in Section 2.2.4 are verified by the finite difference (FD) method. We take an example of a single rotational spring element (whose geometry is the same as in later Section 2.5.1). Let θ rotate from 0 to 2π . We adopt the central difference formula [96] with a step size of $\delta\theta = 10^{-6}$. In the approximation of the gradient $\nabla\theta$, the dihedral angles are computed using Eq. (2.27). In the approximation of the Hessian matrix H , the gradient is computed using Eq. (2.36)-(2.39). The entries of the gradient vector and Hessian matrix are approximated one-by-one. We define the following measures of differences:

$$\Delta_g = \max_i |(\nabla\theta)_i - (\nabla\theta)_i^{FD}|, \quad (2.57)$$

$$\Delta_H = \max_{i,j} |H_{ij} - H_{ij}^{FD}|, \quad (2.58)$$

where a quantity with superscript FD means that it is computed using the finite difference approximation, otherwise, it is computed using the derived analytical formula. The differences are plotted in Fig. 2.5 with respect to the dihedral angle θ . Notice that due to the ill-conditioning of the inverse cosine function near $\theta = 0$ and π [96], the finite difference approximations for the gradient become inaccurate near those angles. As a consequence, we find a comparably larger difference between the analytical value and the finite difference approximation for the gradient near 0 and π than for other angles. In general the two approaches yield almost identical results for both the gradient and the Hessian, which verifies the correctness of the analytical derivations.

2.2.6 Constitutive relationships for bars

As discussed in Section 2.2.2, the bars behave hyperelastically in our formulation. We use the Ogden constitutive model [92] for the numerical examples. In this section, we look at the implementation of the Ogden model in the nonlinear bar-and-hinge model. In the Ogden model, the strain energy density \mathcal{W} is expressed in terms of the principal stretches

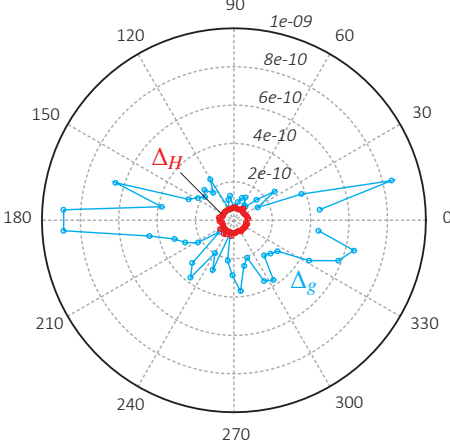


Figure 2.5: The difference between the analytical expressions and finite difference approximations versus the rotation angle θ (in degree) for a single rotational spring element - see Section 2.5.1 and Fig. 2.10.

as:

$$\mathcal{W}(\mathbf{E}) = \hat{\mathcal{W}}(\lambda_1, \lambda_2, \lambda_3) = \sum_{j=1}^N \frac{\mu_j}{\alpha_j^{OG}} \left(\lambda_1^{\alpha_j^{OG}} + \lambda_2^{\alpha_j^{OG}} + \lambda_3^{\alpha_j^{OG}} - 3 \right), \quad (2.59)$$

where λ_j denotes the principal stretches and N , μ_j and α_j^{OG} are the material constants. For one dimensional bar elements, the material is either under uniaxial tension or compression. Thus, only the principal stretch λ_1 is relevant. Starting from the identity $\lambda_1 = \sqrt{2E_{11} + 1}$ [93] and applying the chain rule, the 2nd Piola-Kirchhoff stress is given by

$$S_{11} = \frac{\partial W}{\partial E_{11}} = \frac{\partial \hat{W}}{\partial \lambda_1} \frac{d\lambda_1}{dE_{11}} = \sum_{j=1}^N \mu_j \lambda_1^{\alpha_j^{OG}-2}. \quad (2.60)$$

Accordingly, the tangent modulus in Eq. (2.11) is derived as

$$C_{1111} = \frac{\partial S_{11}}{\partial E_{11}} = \frac{\partial S_{11}}{\partial \lambda_1} \frac{d\lambda_1}{dE_{11}} = \sum_{j=1}^N \mu_j (\alpha_j^{OG} - 2) \lambda_1^{\alpha_j^{OG}-4}. \quad (2.61)$$

Since the undeformed configuration is in a stress-free state (i.e. $S_{11} = 0$), we have the constraint for μ_j as

$$S_{11} = \sum_{j=1}^N \mu_j = 0. \quad (2.62)$$

Then we obtain the tangent modulus

$$C_{1111}(\lambda_1 = 1) = C_0 = \sum_{j=1}^N \mu_j \alpha_j^{OG}. \quad (2.63)$$

Taking the special case with $N = 2$, we determine all of the material constants by providing α_1^{OG} , α_2^{OG} and the initial tangent modulus C_0 , which is typically known as the Young's modulus. An advantage of the Ogden model is that it can represent a range of hyperelastic behavior by fine-tuning a few parameters [92], [97]. For example, there are three Ogden material models shown in Fig. 2.6. Ogden-1 material with parameters $\alpha_1^{OG} = 5$ and $\alpha_2^{OG} = 1$ behaves similar to linear elastic material under small strain. Ogden-2 material is stiffer in compression than tension, while Ogden-3 material is stiffer in tension than compression. We will use constitutive models Ogden-1 and Ogden-2 in the numerical examples.

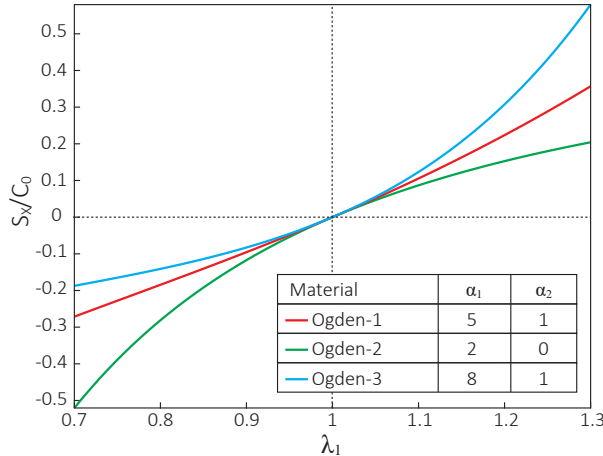


Figure 2.6: Different hyperelastic material models in uniaxial strain based on the Ogden model. The plot shows normalized (2nd P-K) stress vs. principal stretch (λ_1).

2.2.7 Constitutive relationships for rotational springs

In the literature, rotational hinges in origami structures are usually supposed to be linear elastic [70], [75], [77], [81]. Therefore, following the notation in Section 2.2.3, the explicit

expression for the moment (M) generated by the linear elastic rotational spring is given as,

$$M = L^{(r)}k(\theta - \theta_0). \quad (2.64)$$

where k is the rotational stiffness modulus per unit length along the axis (referring to undeformed configuration). The angle θ_0 is the neutral angle, when the rotational spring is at a stress-free state. There are two main limitations of the linear model. First, the linear constitutive law allows only one adjustable parameter, which is the constant tangent stiffness k . Hence, this model has limited tunability and adaptivity. Second, the linear model does not consider the possibility of local penetration, that is when one origami panel is rotating while passing through the adjacent joint panels. These two drawbacks encourage us to seek new constitutive laws that could provide richer tunability and better physical agreement.

In this section, we introduce a nonlinear constitutive law enhanced based on the linear elastic model, which assumes that the rotational springs have constant stiffness in most range of its rotation, while exhibit excessive stiffness when the panels are locally close to contact. The expression for M is given as:

$$M = \begin{cases} L^{(r)}k_0(\theta_1 - \theta_0) + (2k_0\theta_1/\pi) \tan\left(\frac{\pi(\theta-\theta_1)}{2\theta_1}\right), & 0 < \theta < \theta_1; \\ L^{(r)}k_0(\theta - \theta_0), & \theta_1 \leq \theta \leq \theta_2; \\ L^{(r)}k_0(\theta_2 - \theta_0) + (2k_0(2\pi - \theta_2)/\pi) \tan\left(\frac{\pi(\theta-\theta_2)}{4\pi-2\theta_2}\right), & \theta_2 < \theta < 2\pi. \end{cases} \quad (2.65)$$

The constitutive relationship is designed to have a continuous tangent rotational stiffness k for $\theta \in (0, 2\pi)$, as shown below:

$$k = \begin{cases} L^{(r)}k_0 \sec^2\left(\frac{\pi(\theta-\theta_1)}{2\theta_1}\right), & 0 < \theta < \theta_1; \\ L^{(r)}k_0, & \theta_1 \leq \theta \leq \theta_2; \\ L^{(r)}k_0 \sec^2\left(\frac{\pi(\theta-\theta_2)}{4\pi-2\theta_2}\right), & \theta_2 < \theta < 2\pi. \end{cases} \quad (2.66)$$

Extremely high stiffness occurs when the dihedral angle approaches 0 or 2π , and thus prevents the local penetration of panels. The physics is clearly indicated by the fact that,

$$\text{as } \theta \rightarrow 0 \implies k \rightarrow \infty, \quad \text{and} \quad \text{as } \theta \rightarrow 2\pi \implies k \rightarrow \infty. \quad (2.67)$$

The parameters θ_1 and θ_2 can be related to the thickness of the panels. By observation, thicker panels lead to an earlier increase of stiffness when two adjacent panels are close to contact, thus θ_1 and θ_2 should be closer to π (i.e. the flat state). From a practical point of view, θ_1 and θ_2 shall not be too close to 0 and 2π respectively, because then a numerical solver may skip sharp increases of stiffness and continue to rotate allowing penetration. Fig. 2.7 demonstrates the constitutive relationship of rotational springs described by the enriched linear model. Both the bending and folding of origami structures may be treated using the same rotational spring constitutive model with different linear stiffness k_0 .

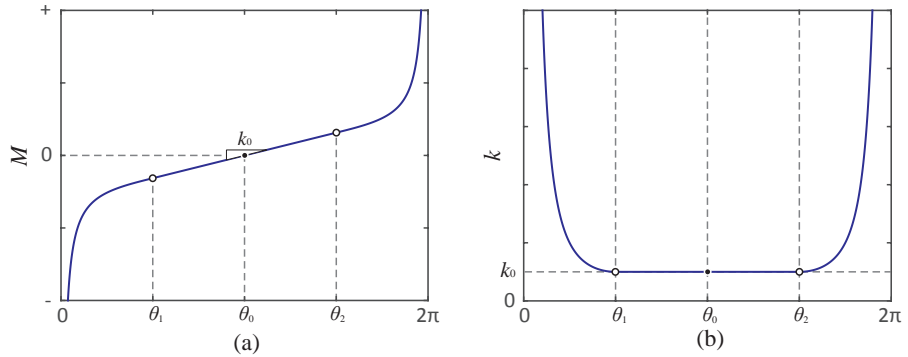


Figure 2.7: Proposed nonlinear elastic constitutive model of rotational springs, with consideration of local contact. (a) dihedral angle vs. moment per unit length M , and (b) dihedral angle vs. tangent rotational stiffness k . The parameters k_0 , θ_1 and θ_2 are tunable. The neutral angle θ_0 yields the relaxed state with $M = 0$.

For the bending rotational springs, a special nonlinear model is derived based on continuum thin shell theory [98]. This model considers scaling effect of ridge singularity [98], [99], and has been verified with shell element based FE analysis. In this model, the resis-

tance moment of the hinge is derived to be [98]:

$$M = L^{(r)} k_0^B (\theta - \theta_0)^{4/3}, \quad (2.68)$$

where k_0^B denotes the bending stiffness constant. The rotational modulus k_0^B is derived to be [5], [98]:

$$k_0^B = \frac{C_0 h^3}{12(1 - \nu^2)L_D} \left(\frac{L_D}{t} \right)^{1/3}, \quad (2.69)$$

where L_D is the total length of the diagonal on which the bending hinge lies, t refers to the thickness of sheet, and ν is the Poisson's ratio of the sheet material. This model does not consider potential self contact of panels, which however, is unlikely to occur for bending hinges.

The folding rotational modulus k_0^F can be determined by (1) experiments, (2) direct ratio compared to k_0^B , (3) or through a scalable formula [98]. The scalable formula is suitable when the origami sheets are elastic continuum thin shells. Following the scalable formula,

$$k_0^F = 1/(1/k_l + 1/k_m), \quad (2.70)$$

where,

$$k_l = \frac{C_0 t^3}{12(1 - \nu^2)L^*}, \quad k_m = 0.55 \frac{C_0 t^3}{12(1 - \nu^2)L^{(r)}} \left(\frac{L^{(r)}}{t} \right)^{1/3}. \quad (2.71)$$

The parameter L^* is known as the length scale factor (in units of length).

2.3 Discretization schemes

Bar-and-hinge approaches are mesh-dependent by design, and thus it is crucial to choose a representative triangulation scheme for origami structures. Currently, there are two types of triangulation schemes that differ by how they discretized quadrilateral panels. One is the N4B5 scheme, which simply divide a quadrilateral panel by one of its diagonals, discretizing it into two triangles. The other is the N5B8 scheme, which adds an extra interior node

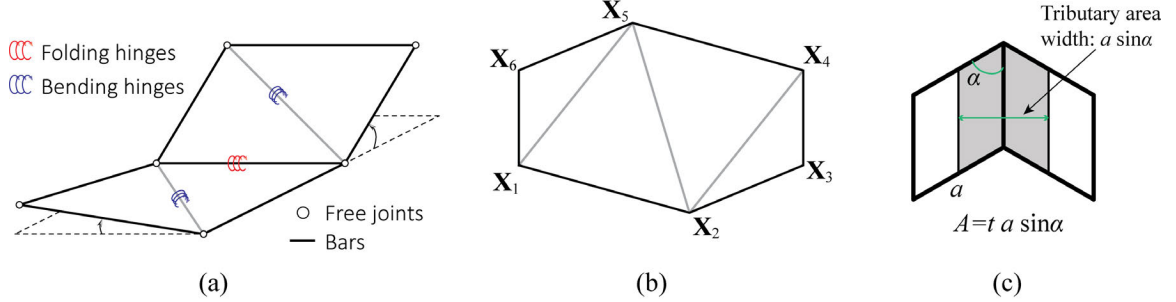


Figure 2.8: (a) Illustration of a N4B5 model. (b) A hexagonal origami panel triangulated by the generalized N4B5 scheme. (c) The tributary area of a bar element, used to approximate the areas of bars.

within each quadrilateral panel. Since the extra node is not a member of the initial input geometry, it is similar to what is known as a “Steiner point” in computational geometry [100]. The extra interior node divides a quadrilateral into four triangles. Triangular panels are not further discretized by both schemes. In this section, we review the basic concepts of these two schemes and generalize them to the triangulation of convex polygonal origami panels, as non-convex panels rarely appear in origami patterns.

2.3.1 The N4B5 scheme and its generalization to polygonal panels

The N4B5 discretization scheme is most commonly adopted for reduced-order modeling of origami structures with quadrilateral panels [5], [6], which divides each quadrilateral panel into two triangles by its shorter diagonal, as demonstrated in Fig. 2.8(a). If we assume that the panel bending stiffness is the same per unit length along both diagonals, then shorter diagonals are easier to bend and thus require lower energy.

To extend this idea to the discretization of polygonal panels, we progressively bisect a polygon by the shortest diagonals until the original polygon is triangulated, which can be efficiently achieved using a divide and conquer algorithm [96]. In the example shown in Fig. 2.8(b), we first bisect hexagon 1-2-3-4-5-6 by its shortest diagonal 1-5 (could also be 2-4), dividing the hexagon into one triangle and one pentagon. Then we divide the pentagon 1-2-3-4-5 by its shortest diagonal 2-4. Finally, we divide the quadrilateral 1-2-4-5

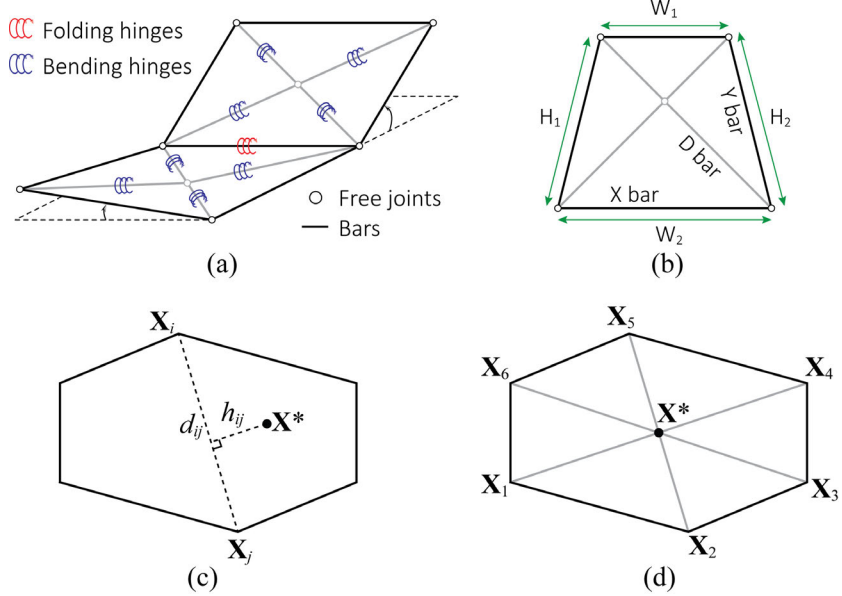


Figure 2.9: (a) Illustration of a N5B8 model. (b) Discretization of a single quadrilateral panel. (c) Illustration for d_{ij} and h_{ij} . (d) Triangulation by the generalized N4B5 scheme.

by its shortest diagonal 2-5 to finish the triangulation. The area of the bars can be assigned using a simple rule based on tributary areas, as demonstrated in Fig. 2.8(c).

The major advantage of the generalized N4B5 scheme is its simplicity. For certain origami patterns, such as the Miura-ori with only parallelogram panels, its accuracy is also satisfactory [101]. However, ambiguity arises when multiple diagonals of a panel are of the same length.

2.3.2 The N5B8 scheme and its generalization to polygonal panels

As illustrated in Fig. 2.9(a), the N5B8 triangulation scheme adds an interior node at the intersection of the two diagonals of a quadrilateral panel, dividing it into four triangles, hence there are 5 nodes and 8 bars belong to each panel. The N5B8 scheme allows the discrete model to capture more realistic doubly curved out-of-plane deformations and isotropic in-plane behaviors of thin panels, potentially yielding higher resolution than the N4B5 scheme [98].

To extend the N5B8 discretization scheme to a polygonal panel, a interior node that

simultaneously locates on all of the diagonals would be ideal because origami panels usually display concentrated bending curvatures along their diagonals [37], [98]. However, in general, it is impossible to find such an interior node within an arbitrarily shaped polygonal panel except quadrilateral ones. Here we propose to pursue a point that has the shortest overall (weighted) distance to all diagonals of a convex polygon by solving the following optimization problem:

$$\mathbf{X}^* = \operatorname{argmin}_{\mathbf{X}} \sum_{|j-i|>1} \frac{h_{ij}}{d_{ij}}, \quad (2.72)$$

where

$$d_{ij} = \|\mathbf{X}_i - \mathbf{X}_j\|, \quad \text{and} \quad h_{ij} = \frac{\|(\mathbf{X}_i - \mathbf{X}^*) \times (\mathbf{X}_j - \mathbf{X}^*)\|}{d_{ij}}. \quad (2.73)$$

Geometrically, d_{ij} is the length of the diagonal $i-j$, and h_{ij} is the distance from the interior node (i.e. \mathbf{X}^*) to the diagonal $i-j$ (see Fig. 2.9(c)). The measure of (h_{ij}/d_{ij}) is a weighted distance that favours shorter diagonals because they are more likely to bend than longer ones, judged by the scaled stiffness of bending ridges [82], [98]. Notice that, for quadrilateral panels, the optimal solution for \mathbf{X}^* by formula (2.72) is simply the intersection point of the two diagonals, and thus the extended scheme is consistent with the previous N5B8 model. In the example shown in Fig. 2.9(d), the optimal interior node for the hexagon (same as in Fig. 2.8(b)) is at the common intersection of three diagonals.

To recover the in-plane Poisson's effect of origami panels, the original N5B8 model [98] provides formulas for assigning bar areas based on rectangular panels. Denoting ν as the material's Poisson's ratio, the member areas are defined as [98]:

$$\bar{A}_X = h \frac{\bar{H}^2 - \nu \bar{W}^2}{2\bar{H}(1 - \nu^2)}, \quad (2.74)$$

$$\bar{A}_Y = h \frac{\bar{W}^2 - \nu \bar{H}^2}{2\bar{W}(1 - \nu^2)}, \quad (2.75)$$

$$\bar{A}_D = h \frac{\nu(\bar{H}^2 + \bar{W}^2)^{3/2}}{2\bar{H}\bar{W}(1 - \nu^2)}, \quad (2.76)$$

where $\bar{W} = (W_1 + W_2)/2$, $\bar{H} = (H_1 + H_2)/2$, and the subscripts X, Y, D label different bars, as illustrated in Fig. 2.9(b).

Realizing that it is difficult to account for the Poisson effect for polygonal and triangular panels, we propose to assign the bar areas such that they preserves the (linear elastic) strain energy of a continuous panel (of any shape) under uniform in-plane dilation assuming plane stress state. For a polygonal panel of thickness t and polygon area A_S , we assign a uniform area A for all bars belonging to this panel by:

$$A = \frac{2A_S t}{(1 - \nu) \sum_i L_i}, \quad (2.77)$$

where $\sum_i L_i$ is the total length of bars, and ν denotes the Poisson's ratio. When applied to rectangular panels, the results are similar to those calculated by the existing formulas [98], which is satisfactory as an estimation tool.

2.4 Solution algorithms for nonlinear analysis

2.4.1 Force loading

Origami structures are typically subject to highly geometric nonlinearity, however, conventional Newton-Raphson method is unable to capture the equilibrium path beyond limit points [91], [93], [102], [103]. Thus to achieve a successful nonlinear analysis of the structure, we need a suitable solution scheme. Here we utilize the modified generalized displacement control method (MGDCM) [104], a kind of arc-length method, as the solver. The MGDCM method has shown its advantages in tracking complicated solution paths of nonlinear problems compared to the standard generalized displacement control method (GDCM) [105]. The method can follow the equilibrium paths with snap-through and snap-back behaviors, and we will verify this using the numerical examples.

The MGDCM solves the equilibrium equation $\mathbf{R}(\mathbf{u}, \lambda) = \mathbf{T}(\mathbf{u}) - \lambda \mathbf{F}$, following an incremental-iterative procedure. The parameter λ is known as the load factor that controls

the magnitude of the external loads. The algorithm is summarized in Algorithm 1.

Algorithm 1 Modified Generalized Displacement Control Method (MGDCM)

```

1:  $\mathbf{u}^{1,0} \leftarrow \mathbf{0}$ ,  $\lambda^{1,0} \leftarrow 0$                                 ▷ Initialization
2: for  $i = 1$  to a specified increment number do
3:    $k \leftarrow 0$ 
4:   while  $\|\Delta\mathbf{u}^{i,k}\| > tol$  do
5:      $k \leftarrow k + 1$ 
6:      $\mathbf{T}^{i,k-1} \leftarrow \mathbf{T}(\mathbf{u}^{i,k-1})$ ,  $\mathbf{K}^{i,k-1} \leftarrow \mathbf{K}(\mathbf{u}^{i,k-1})$ 
7:      $\mathbf{R}^{i,k-1} \leftarrow \lambda^{i,k-1} \mathbf{F} - \mathbf{T}^{i,k-1}$ 
           ▷ Compute internal forces, tangent stiffness matrix and residual vector
8:     Solve  $\mathbf{K}^{i,k-1} \Delta\hat{\mathbf{u}}^{i,k} = \mathbf{F}$ ,  $\mathbf{K}^{i,k-1} \Delta\check{\mathbf{u}}^{i,k} = \mathbf{R}^{i,k-1}$ 
9:     Determine  $\Delta\lambda^{i,k}$ 
10:     $\Delta\mathbf{u}^{i,k} \leftarrow \Delta\lambda^{i,k} \Delta\hat{\mathbf{u}}^{i,k} + \Delta\check{\mathbf{u}}^{i,k}$           ▷ Notice for  $k = 1$ ,  $\Delta\check{\mathbf{u}}^{i,1} = \mathbf{0}$ 
11:     $\mathbf{u}^{i,k} \leftarrow \mathbf{u}^{i,k-1} + \Delta\mathbf{u}^{i,k}$ ,  $\lambda^{i,k} \leftarrow \lambda^{i,k-1} + \Delta\lambda^{i,k}$  ▷ Compute iterative update
12:   end while
13: end for

```

In the k -th iteration of the i -th increment, the load factor increment $\Delta\lambda^{i,k}$ is determined by [104]:

$$\Delta\lambda^{i,k} = \begin{cases} \overline{\Delta\lambda}, & i = 1, k = 1; \\ - (\Delta\hat{\mathbf{u}}^{1,1} \cdot \Delta\check{\mathbf{u}}^{i,k}) / (\Delta\hat{\mathbf{u}}^{1,1} \cdot \Delta\hat{\mathbf{u}}^{i,k}), & i = 1, k > 1; \\ \pm \overline{\Delta\lambda} |(\Delta\hat{\mathbf{u}}^{1,1} \cdot \Delta\hat{\mathbf{u}}^{1,1}) / (\Delta\hat{\mathbf{u}}^{i,1} \cdot \Delta\hat{\mathbf{u}}^{i,1})|^{1/2}, & i > 1, k = 1; \\ - (\Delta\hat{\mathbf{u}}^{i,1} \cdot \Delta\check{\mathbf{u}}^{i,k}) / (\Delta\hat{\mathbf{u}}^{i,1} \cdot \Delta\hat{\mathbf{u}}^{i,k}), & i > 1, k > 1. \end{cases} \quad (2.78)$$

The sign of the load factor increment in the third expression of Eq. (2.78) is determined by $\text{sgn}(\Delta\hat{\mathbf{u}}_1^{i-1} \cdot \Delta\hat{\mathbf{u}}^{i,1})$. The parameter $\overline{\Delta\lambda}$ is the prescribed initial load factor. Typically, the choice of $\overline{\Delta\lambda}$ can play a major role in arc-length methods, and usually small values are good for capturing complex nonlinear behaviors. Sometimes, even a slight change in the initial load factor may lead to poor convergence. However, the MGDCM is not very sensitive to the value of the initial load factor, which means that we can get convergent solutions for a relatively wide range of $\overline{\Delta\lambda}$ [104].

2.4.2 Displacement loading

In the case of displacement loading, we denote the displacement load as \mathbf{u}_p , which is imposed on some DOF of the system marked as p . Some other DOF (denoted as r) are fixed to provide support to the structure, and the corresponding displacement is \mathbf{u}_r , which is always a zero vector. The other DOF in the system are free to move, denoted as f . Therefore, we partition the displacement field of the system into three groups: \mathbf{u}_p , \mathbf{u}_r , \mathbf{u}_f . Among the three, \mathbf{u}_p and \mathbf{u}_r are boundary conditions and thus have fixed values. Notice that \mathbf{u}_p is fixed but nonzero, while \mathbf{u}_r is fixed to a zero vector.

We can also divide the internal force vector \mathbf{T} into three parts by their corresponding DOF: \mathbf{T}_r , \mathbf{T}_p , and \mathbf{T}_f . In an equilibrium state of the system, $\mathbf{T}_f = \mathbf{0}$ while the other two parts shall not be zero. The reaction forces of the supports are equal to $-\mathbf{T}_r$, and the external forces required to achieve the prescribed displacement \mathbf{u}_p are given by $-\mathbf{T}_p$. After a displacement load \mathbf{u}_p is applied, our goal is to find a proper \mathbf{u}_f , such that $\mathbf{T}_f(\mathbf{u}) = \mathbf{0}$, that is, all the internal free nodes are balanced.

We use numerical algorithm to solve the nonlinear equation of $\mathbf{T}_f(\mathbf{u}) = \mathbf{0}$. A large displacement load cannot be applied at once, otherwise a numerical algorithm would likely fail to converge. Hence, we divide the total displacement load into small increments. At each increment, we solve for the equilibrium using a damped Newton-Raphson method iteratively. Let i be the increment number, and j be the iteration number, marked as $\mathbf{u}^{i,j}$. The prescribed amount of displacement load is \mathbf{u}_p , and the small displacement load applied at increment i is $\beta^i \mathbf{u}_p$. We note that when one or more partitions of \mathbf{u} (i.e. \mathbf{u}_p , \mathbf{u}_f and \mathbf{u}_r) are changed, \mathbf{u} shall update accordingly with the other components remain the same. We summarize the algorithm in Algorithm 2. The parameters β^0 , tol , j_{max} , and $N_{att,max}$ are predefined with values equal to 0.002, 10^{-6} , 50, and 5, respectively. The incremental step size β^i and damping factor v are updated based on heuristic rules.

Algorithm 2 Large Displacement Load Solver

```
1:  $\mathbf{u}^{0,0} \leftarrow \mathbf{0}$ ,  $i \leftarrow 1$ ,  $\beta^1 \leftarrow \beta^0$ ,  $v = 1$ ,  $N_{att} \leftarrow 0$ 
2: while  $\sum_i \beta^i < 1$  do
3:    $\mathbf{u}_p^{i,0} \leftarrow \mathbf{u}_p^{i-1,0} + \beta^i \mathbf{u}_p$ 
4:    $j \leftarrow 0$ ,  $err \leftarrow 1$ 
5:   while  $err > tol$  do
6:      $j \leftarrow j + 1$ 
7:      $\mathbf{T}^{i,j-1} \leftarrow \mathbf{T}(\mathbf{u}^{i,j-1})$ ,  $\mathbf{K}^{i,j-1} \leftarrow \mathbf{K}(\mathbf{u}^{i,j-1})$ 
8:      $\mathbf{R}^{i,j-1} \leftarrow -\mathbf{T}^{i,j-1}$ 
9:     Solve  $\mathbf{K}_{ff}^{i,j-1} \Delta \mathbf{u}_f^{i,j-1} = \mathbf{R}_f^{i,j-1}$ 
10:     $\mathbf{u}_f^{i,j} \leftarrow \mathbf{u}_f^{i,j-1} + v \Delta \mathbf{u}_f^{i,j-1}$ 
11:     $err \leftarrow \|\Delta \mathbf{u}_f^{i,j-1}\|$ 
12:   end while
13:   if  $j > (j_{max}/(v + 1))$  then
14:      $N_{att} \leftarrow N_{att} + 1$ 
15:     if  $N_{att} < N_{att,max}$  then
16:        $\beta^i \leftarrow 0.5 \beta^{i-1}$ 
17:     else
18:        $\beta^i \leftarrow 1.5 \max(1, \beta^{i-1})$ 
19:        $v \leftarrow 0.75v$ 
20:     end if
21:   else
22:      $v = 1$ ,  $N_{att} \leftarrow 0$ 
23:      $i \leftarrow i + 1$ 
24:     if  $\beta_i < 1$  then
25:        $\beta^i \leftarrow \min(1.1 \beta^{i-1}, \beta^0)$ 
26:     else
27:        $\beta^i \leftarrow \max(0.9 \beta^{i-1}, \beta^0)$ 
28:     end if
29:   end if
30: end while
```

2.5 Origami simulations

In this section, the nonlinear bar-and-hinge model is applied to structural analyses of various origami structures. The examples start with a simple folding mechanism which is composed of two triangular panels with a single joint line. The numerical results are compared with analytical solutions to verify the implementation of the formulation. It is then followed by analyses of the well-known Miura-ori, under different boundary conditions. The simulations are compared with experiments on actual paper-made models. We also simulate the multi-stable behavior of a helical origami tower structure, known as the Kresling pattern [106], [107]. The aforementioned examples are conducted adopting the N4B5 scheme, using the “MERLIN” [60] software. In the last example, we use “MERLIN2” [61] to analyze a non-periodic origami structure under displacement load adopting the N5B8 model. Computational time is provided to roughly show the efficiency of the software¹.

2.5.1 A simple fold

The first example comprises the necessary components for a rotational spring element to exist, namely, four nodes, two triangular panels and one folding crease. The geometry and boundary conditions of the structure are depicted in Fig. 2.10(a). One of the panels is totally fixed on the ground, and the other rotates about the crease line driven by a vertical force applied at the free node D. Based on the bar-and-hinge simplification, the model is composed of one rotational hinge and five bars. To verify the accuracy of the implementation, the numerical solution is compared with analytical derivations.

The initial configuration is assigned with a dihedral angle at $\theta = 135^\circ$, and the rotational spring has a neutral angle at $\theta_0 = 210^\circ$. The values are chosen arbitrarily in order to make a fair evaluation of the accuracy of the numerical implementation. The rotational spring uses the constitutive law introduced in Section 2.2.7, with $\theta_1 = 90^\circ$, $\theta_2 = 210^\circ$ and $k_0 = 1$.

¹For reference, the MATLAB implementation was executed on a desktop computer equipped with Intel Xeon CPU (8 cores, 3.0 GHz).

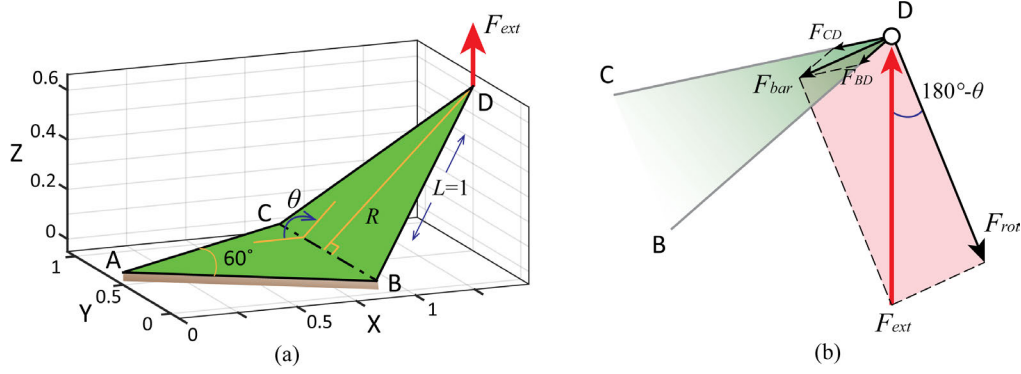


Figure 2.10: The simple fold example. (a) Geometry and boundary conditions. (b) Force diagram at node D.

The panels are assumed to be rigid, thus numerically, the bars are assigned a large value for the initial tangent stiffness with $C_0 = 10^{10}$ to asymptotically approach infinite stiffness. The material constitutive relationship for the bar elements follows the pair of parameters: $\alpha_1^{OG} = 2$, $\alpha_2^{OG} = 0$ (i.e. Neo-Hookean material model, as shown in Fig. 2.6), and member areas are assumed to be 10^{-4} . Based on the current setting, the analysis starts from a non-equilibrium state. Guided by the force diagram at node D shown in Fig. 2.10(b), the magnitude of the applied force can be derived as a function of the angle θ ,

$$F_{ext} = \frac{F_{rot}}{\cos(\pi - \theta)} = \frac{M(\theta)}{L \sin(\pi/3) \cos(\theta)}. \quad (2.79)$$

The force F_{rot} induced by the rotational spring is always orthogonal to the rotating panel (i.e., the plane of BCD). Notice that at the initial configuration, the value of F_{ext} is negative when in equilibrium, meaning that it needs to point upwards. Due to the symmetry of the structure and boundary conditions, the internal forces in bars BD and CD are of the same magnitude. Therefore $F_{BD}(= F_{CD})$ can be calculated as:

$$F_{BD} = \frac{F_{rot} \tan(\theta)}{2 \sin(\pi/3)} = \frac{M(\theta)}{L \sin^2(\pi/3)}. \quad (2.80)$$

The comparisons shown in Fig. 2.11 present great agreement between the numerical and analytical solutions. This verification example serves as a reference for other simulations.

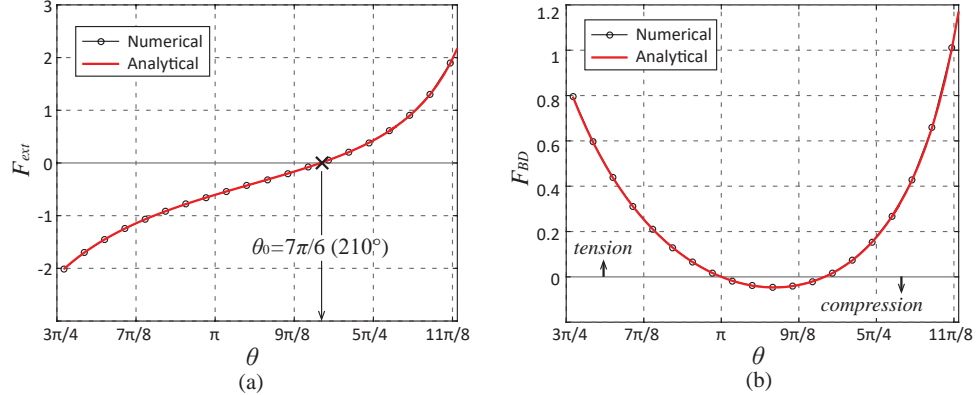


Figure 2.11: (a) Equilibrium path, F_{ext} versus θ . (b) F_{BD} versus θ .

2.5.2 Folding and bending of Miura-ori

Miura-ori is one of the most famous patterns in origami engineering and has been studied extensively [6], [37], [66], [108]. This example, as a verification of the proposed nonlinear formulation, compares existing theoretical analyses of Miura-ori [35], [80] with our numerical simulations. A Miura-ori can be configured by a few geometric parameters: a , b , and α , as shown in Fig. 2.12. In this example, we assign the following values: $a = 0.02$, $b = 0.02$, and $\alpha = 60^\circ$. The material properties are determined by the following parameters: folding stiffness $k_0^F = 0.1$, bar element area $A = 1 \times 10^{-5}$, and Ogden model parameters $\alpha_1^{OG} = 5$, $\alpha_2^{OG} = 1$, i.e., material Ogden-1 as shown in Fig. 2.6. Because the theoretical predictions [35], [80] are derived without considering surface contact, we do not apply local collision penalty in this example, so we set $\theta_1 = 0^\circ$, $\theta_2 = 360^\circ$. In the compressed folding test, we adopt bending stiffness $k_0^B = 10^4$ and stretching stiffness $C_0 = 10^{10}$. For the bending test, i.e., non-rigid Miura-ori case, we reduce the bending stiffness and stretching stiffness to $k_0^B = 1$ and $C_0 = 10^8$, respectively.

The ratio k_0^B/k_0^F is a key parameter that determines whether an origami is close to a mechanism (rigid origami) or not. For example, when $k_0^B/k_0^F \rightarrow \infty$, we approach a situation where rigid panels are connected by compliant hinges (rigid origami). When $k_0^B/k_0^F \rightarrow 1$, the panel and the fold have the same stiffness (e.g. origami sheet folded from

a single material such as metal) [81]. In this example, we use two values for k_0^B/k_0^F . In the folding simulation, we choose a relative large ratio ($k_0^B/k_0^F = 10^5$), such that the origami structure is asymptotically rigid. In bending simulation, a smaller ratio ($k_0^B/k_0^F = 10$) is used to simulate a non-rigid origami in which panel bending cannot be neglected.

Rigid Miura-ori: folding

First, we look at the folding kinematics of Miura-ori. The in-plane stiffness and the tangential Poisson's ratio [35], [80], [109] of Miura-ori have been derived analytically based on the rigid origami assumption, with linear elastic rotational stiffness for the folding hinges [35], [80]. If our proposed formulation is correct, then it should be able to asymptotically simulate rigid origami by assigning large panel bending stiffness and stretching stiffness, i.e. k^B and C_0 . Applying in-plane compression forces the Miura-ori to fold. We restrict the displacements of nodes at the left end ($x = 0$) to the yz -plane, and fix the node at $(x, y, z) = (0, 0, 0)$ in all three directions. The ground nodes ($z = 0$) to the right end are not allowed to translate in the z direction. Then we apply uniform forces of unit magnitude to all the nodes at the right-end, towards the left (i.e., $-x$ direction). Fig. 2.12(c) shows a side view of the boundary condition.

The in-plane compression starts from an almost flat state. We compare the load-displacement curve and tangential Poisson's ratio curve, obtained by the numerical method with the analytical predictions in [35]. The tangential Poisson's ratio describes the Poisson's ratio of a material at an infinitesimal deformation limit, deviating from the current deformed configuration [35], [80]. The ratio is defined as follows:

$$\nu_{LW} = -\frac{dW/W}{dL/L} = -\frac{L}{W} \frac{dW}{dL}. \quad (2.81)$$

where \mathcal{W} and L are the bulk dimensions of a Miura-ori as depicted in Fig. 2.13(b). Other measures of the effect might be used to consider the large deformation nature of origami,

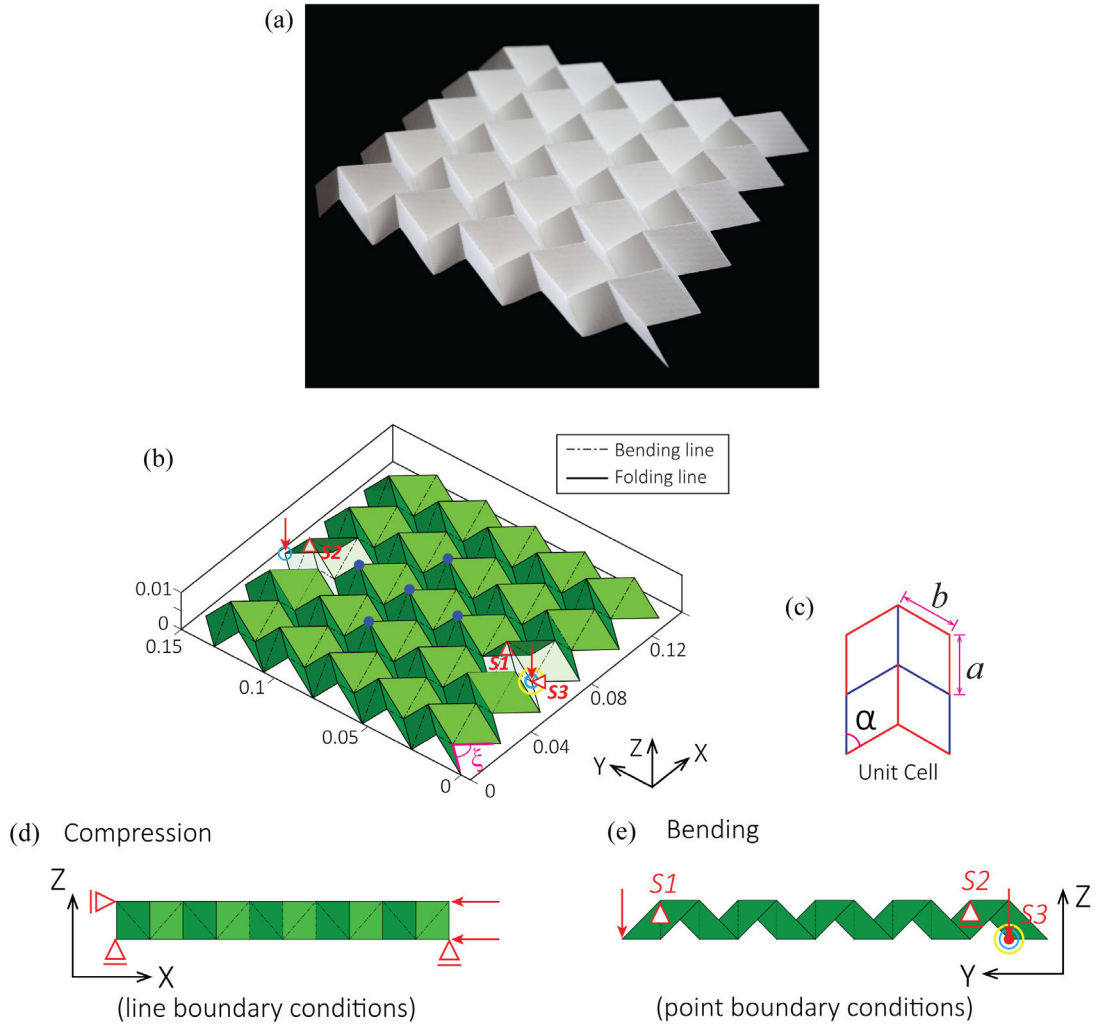


Figure 2.12: (a) Paper-made Miura-ori model. (b) An isometric view of the initial configuration of the numerical model and boundary conditions for the bending simulation. The angle ξ between two edges is used to specify the initial configuration of a Miura-ori, which equals 118.27° for the compression simulation and 90° for the bending simulation. In the bending simulation, support S_1 restricts displacements in x , y , z directions; S_2 fixes x , z directions; S_3 confines only x translations. Unit forces are applied toward the $-z$ direction on nodes marked with blue circles. Displacement u is measured at one of the loading nodes as the z -displacement, marked with a yellow circle (same node as S_3). The blue dots show the nodes that are used to approximate the global principal curvatures near the center of the origami sheet. (c) A flattened unit cell of the Miura-ori. We take $a = 0.02$, $b = 0.02$, and $\alpha = 60^\circ$ for the simulations. (d) Illustration of the boundary conditions in the compression simulation from a side view. (e) Side view of the boundary conditions for the bending simulation.

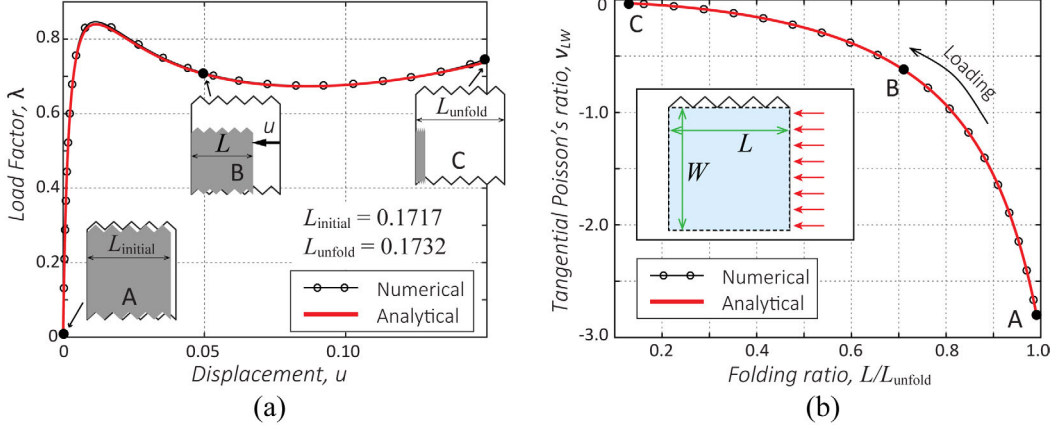


Figure 2.13: Compressed folding of Miura-ori. The in-plane compression starts from an almost flat state (i.e. at L_{initial}). (a) Equilibrium path, displacement versus load factor (λ). The insets demonstrate the folded shapes along the compression process. The black profiles in the three insets outline the unfolded planar pattern. (b) In-plane tangential Poisson's ratio ν_{LW} versus folding ratio (L/L_{unfold}). The analytical solutions are obtained based on the formulae presented in reference [35].

such as the Poisson function [110], [111]. Here we adopt the same tangential Poisson's ratio definition as used for the theoretical predictions to show that our proposed formulation is able to asymptotically capture the correct kinematics of rigid origami. The theoretical Poisson's ratio for a Miura-ori is given as [35], [80]:

$$\nu_{LW} = -\tan^2(\xi/2), \quad (2.82)$$

where angle ξ is illustrated in Fig. 2.12(e). We plot the tangential Poisson's ratio with respect to the folding ratio (i.e. L/L_{unfold} as shown in Fig. 2.13) of the Miura-ori, which equals to 1 when the origami is fully flat, and 0 when fully folded. To get the numerical approximation, we first interpolate the discrete values of \mathcal{W} and L at all load steps to a continuous function using cubic splines, and then compute the Poisson's ratio using Eq. (2.81). A very good agreement is observed as shown in Fig. 2.13.

Non-rigid Miura-ori: bending

When the Miura-ori has non-rigid panels, it can present global out-of-plane deformations, bending anticlastically into a saddle-shaped configuration. An elegant theoretical derivation by Wei *et al.* [35] shows that the Poisson's ratio of Miura-ori for in-plane and out-of-plane infinitesimal deformation have equal magnitude, but opposite signs. The derivation for bending Poisson's ratio is made with the assumption that there are periodic small deformations of unit cells. For a large global bending deformation, the unit cells of Miura-ori actually deform non-uniformly throughout the sheet [35], [80]. Therefore, the applicable range of this analytical expression for the bending Poisson's ratio is limited. The proposed numerical approach provides a way to numerically predict the global bending behavior of Miura-ori under large deformation. Because the bending Poisson's ratio is not well-defined for large deformation case, we instead compute the coupling ratio of the two principal curvatures of the sheet, i.e. $-\kappa_x/\kappa_y$, as shown in Fig. 2.14. For small deformations, this coupling ratio equals the bending Poisson's ratio as defined in [35]. We adopt the values of input parameters for the compression test, except reduced bending stiffness and stretching stiffness ($k_0^B = 1$ and $C_0 = 10^8$), in order to represent non-rigid panels. Boundary conditions are shown in Fig. 2.12(d) and (e).

In the bending simulation, the Miura-ori is initially partially folded. The computation takes about 7 seconds with $\overline{\Delta\lambda} = 0.03$. The analysis successfully predicts the saddle-shaped deformation of the Miura-ori. The load-displacement curve is shown in Fig. 2.14(a). The coupling ratio ($-\kappa_x/\kappa_y$) is interpolated near the center of the sheet using 5 nodes on the upper surface as marked with blue dots in Fig. 2.12(e). When the deformation is small (at point "A"), the ratio is close to 1.0, agreeing with the analytical prediction. As the deformation gets larger, the unit cells deform heterogeneously and the coupling ratio increases. The deformation is compared with the paper-made model, as demonstrated in Fig. 2.14(b), which yields a qualitatively good agreement.

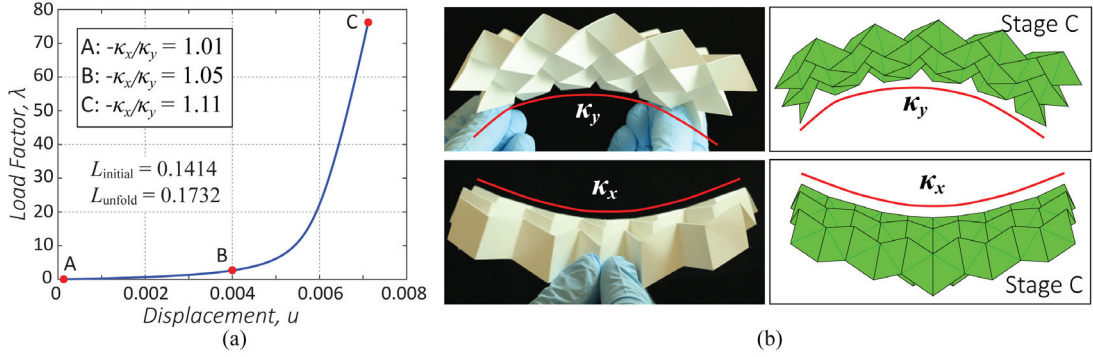


Figure 2.14: Bending of Miura-ori. (a) Equilibrium path, displacement u versus load factor λ . Displacement u is measured at one of the loading nodes as the z -displacement, as shown in Fig. 2.12. (b) Two views of the final state (at point “C”) of the bended Miura-ori, with pictures of both the paper model and the numerical model.

2.5.3 Pop-through defect of Miura-ori: bistability

Miura sheets may display a local bistable behavior. Silverberg *et al.* [37] named such behavior as “pop-through defects,” and studied their influence on the mechanical properties of Miura-ori structures. Fig. 2.15(a) shows a regular configuration of Miura-ori, while on the side, Fig. 2.15(b) shows a Miura-ori with a central unit cell in the “pop-through” state. The “pop-through” state can be achieved by applying a vertical force to a vertex until the unit cell pops into another mechanically stable state. The soft bending of panels is the main contributor to this phenomenon [37].

The deformation process that forms a “pop-through” state has not been investigated yet, and thus it is the subject of this study. We consider a Miura-ori structure with the same geometry as the previous example presented in Section 2.5.2. The Ogden-1 material model is used for bar elements. Other material related parameters are: $k_0^F = 0.1$, $k_0^B = 1$, $C_0 = 1 \times 10^8$, $A = 1 \times 10^{-5}$. We consider contact of adjacent panels by setting $\theta_1 = 45^\circ$, $\theta_2 = 315^\circ$. The initial state and boundary conditions are shown in Fig. 2.15(b). The initial load factor is $\overline{\Delta\lambda} = 0.06$ and the computational time is around 11 seconds. Fig. 2.16 shows the equilibrium path and different deformations under various magnitudes of loading. The corresponding configuration at point “C” is the stable pop-through state when the structure

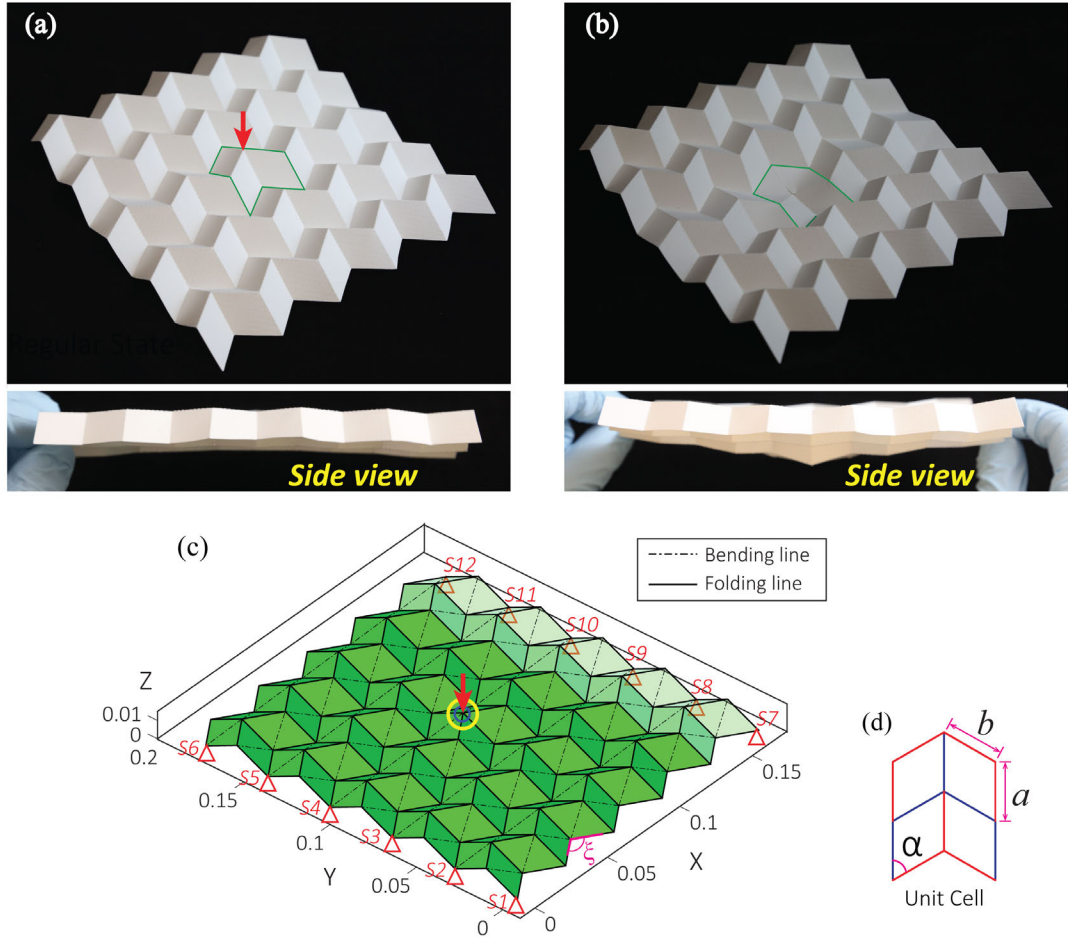


Figure 2.15: The Miura-ori “pop-through defect”. (a) The paper-made Miura-ori model in a regular partially folded configuration. (b) The Miura-ori model in the “pop-through” state, which is a stable configuration. (c) The numerical model and boundary conditions for simulation. The angle ξ is 112.61° . Support $S1$ fixes displacements in x , y , z directions, $S2$ - $S6$ fix displacements in x , z directions, and $S7$ fixes y , z displacements. From $S8$ to $S12$, restrictions only apply in z direction. Load is applied as a unit force toward the $-z$ direction on the node marked with blue circle. Displacement u is the z -displacement measured at the loading node – also marked with yellow circle. (d) A flattened unit cell of the Miura-ori. We take $a = 0.02$, $b = 0.02$, and $\alpha = 60^\circ$.

is in self-equilibrium. The numerical simulation approximately reproduce the formation of the “pop-through defect” of the paper-made model. Under the given load, the Miura-ori presents a typical curve of bistability with snap-through behavior [91], [102], as indicated in Fig. 2.16.

2.5.4 Multi-stability of the Kresling pattern

The Kresling pattern [106] is a type of cylindrical shell origami that has multi-stable behavior [112]. The nodes of the Kresling pattern lie on the intersection of two sets of helices (longitudinal) and one set of circles (transverse). A commercial company has used the idea of Kresling pattern to fabricate foldable wine bags as shown in Fig. 2.17(a), which forms stable structures in both a folded and deployed state [107]. In this example, we look at the equilibrium path of such multi-stable behavior using the proposed nonlinear bar-and-hinge model.

According to Cai *et al.* [112], the multi-stability of this structure is due to the change of lengths of the creases. In other words, the multi-stability behavior comes from panel stretching, instead of panel bending as in the previous example. The numerical model has three layers, capturing a portion of the origami wine bag. We assign $k_0^F = 1 \times 10^{-3}$, $\theta_1 = 45^\circ$, $\theta_2 = 315^\circ$, and $C_0 = 5 \times 10^7$ as the basic material properties. The Ogden-1 material model is used for bar elements. The folding stiffness is very small because we observe that the folding creases of the physical model (i.e. the origami wine bag as shown in Fig. 2.17(a)) are quite soft. The cross-sectional areas of the bar elements are 10^{-5} . This pattern has only triangular panels and they are not further discretized in the bar-and-hinge model. Therefore, there is no bending hinges. The boundary conditions for the simulations are shown in Fig. 2.17(b). The bottom of the tower is fixed on the ground in all directions.

The investigation is conducted by applying uniform unit compression forces on the top nodes. An initial load factor $\overline{\Delta\lambda} = 0.032$ is used. The execution time of the analysis is 4 seconds. The equilibrium path shown in Fig. 2.17(c) draws the downward displacement

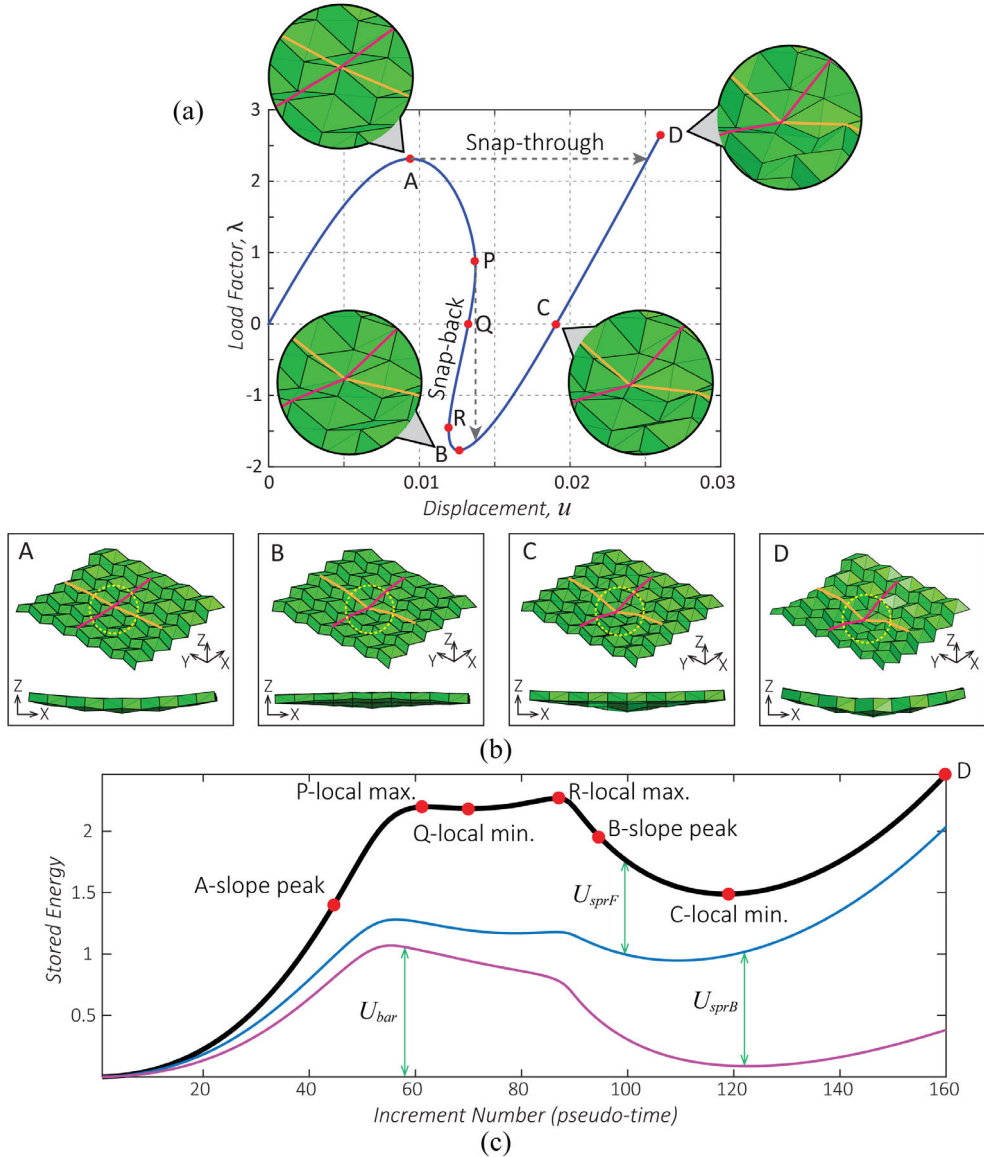


Figure 2.16: Quantitative measurements. (a) Equilibrium path, u versus λ , during the deformation process of a “pop-through defect” on Miura-ori. The insets show zoom-in views of the deformed Miura-ori near the central region. Reference of these insets to the global configuration is illustrated in (b). (b) Several key frames of deformed configurations along the simulation, corresponding to the 4 points (“A” to “D”) on the equilibrium path. At stage C, the corresponding configuration is in a stable state, and the digital rendering shows a similar configuration to the physical model shown in Fig. 2.15(b). The yellow dashed circles mark the zoom-in regions for insets in (a). (c) Change of stored energy breakdown in the system throughout the deformation history. Critical states are marked by red dots and corresponds to (b).

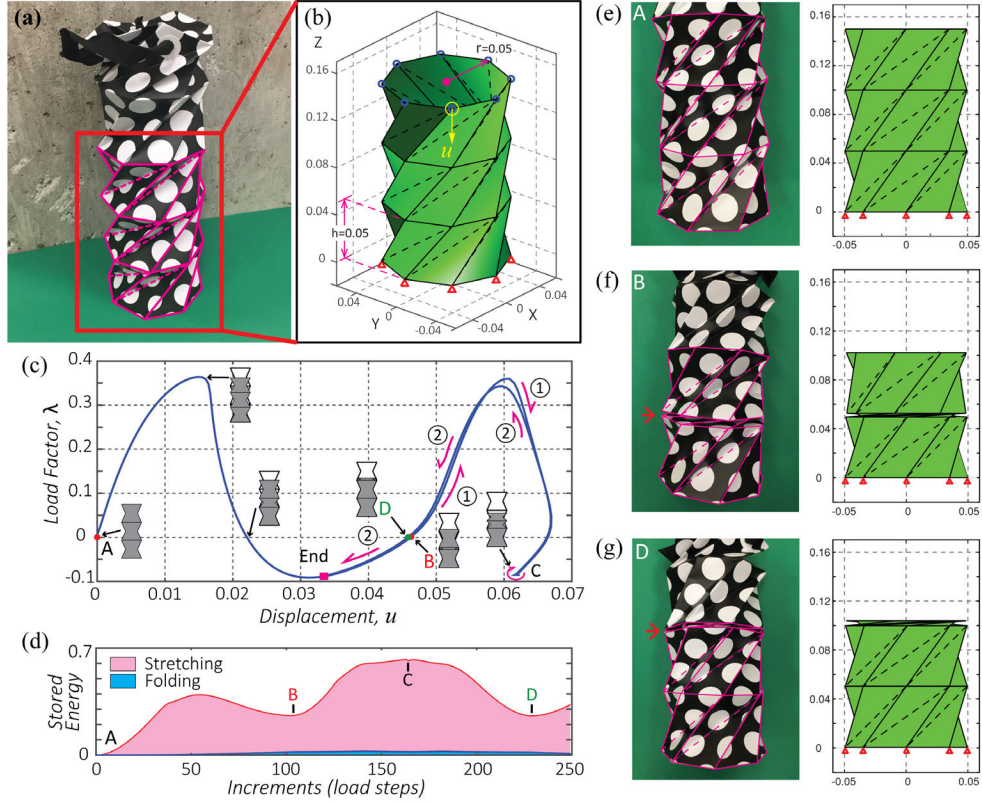


Figure 2.17: The multi-stable Kresling origami tower. (a) An origami wine bag that has the shape of Kresling pattern with 8 sides. (b) Geometry and boundary conditions of the numerical model. Each layer of the tower has a height of $h = 0.05$. On each layer, the cross sectional outline, which is a regular octagon, is placed inside a circle of radius $r = 0.05$. Supports are indicated by red triangles, all of which restrict displacement in x , y , z directions. Unit forces are applied at nodes circled in blue to the $-z$ direction. Displacement u is measured as the z -displacement of the node marked with a yellow circle. (c) Equilibrium path, u versus λ . The insets illustrate the global deformation of the origami at different points on the equilibrium path. At point “C”, we can see that the top and middle layer have equal chance to collapse, thus C refers to a bifurcation point. (d) Stored energy profile along the simulation process. States A, B and C refer to three local minima on the profile. Energy contributions from stretching deformation and folding deformation are distinguished by different colors. There is no bending deformation considered in this simulation. (e)-(g) Stable configurations along the path (at points “A”, “B” and “C”) are demonstrated using side views. We present both key frames from the numerical simulation and corresponding physical model configurations.

of a top node versus the value of load factor. This diagram can be seen as a projection of the multi-dimensional equilibrium path onto the specific plane of u and λ . It is interesting that the equilibrium path makes a U-turn at point “C”, and then traces a path of almost identical projection as previously passed route, but actually, the two almost overlapping paths refer to completely different deformations, as illustrated in Fig. 2.17(c) with the insets and Figs. 2.17(e) to (g). For example, coincident points B and D, on the first and second passes respectively, refer to different stable states of the origami structure, as shown in Figs. 2.17(f) and (g). At point “B”, the middle layer is fully folded, while at point “D”, the middle layer re-opens. From the stored energy diagram, we can clearly see that B and D are two different local minima. The distribution of stored energy verifies that for such an origami structure, the non-rigid behavior comes mostly from the stretching deformation of the panels.

We note here that such multi-stable structures typically have many bifurcation points and branches on the equilibrium paths, however, the solution solver (MGDCM) would only pick one of the many branches. The choice of which branch to trace for the solver depends on many factors, including the value of the initial load factor $\bar{\Delta\lambda}$. In general, the choice of branching appears to be arbitrary. Despite this insufficiency of the nonlinear solver, this example indicates that our nonlinear formulation is able to present the full picture of the deformation spaces of multi-stable origami structures, since we (at least) captured two equilibrium states other than the initial configuration in this example. Numerical techniques for bifurcation analysis [93] may allow us to guide the nonlinear solver to follow a specific branch of the equilibrium paths, which is a possible improvement of the current nonlinear bar-and-hinge model.

Guest and Pellegrino [84], [113], [114] investigated (numerically and experimentally) a multi-stable triangulated cylinder, which has a similar geometry as the Kresling pattern, but whose nodes are at the intersections of three helices, meaning that the transverse edges form helices instead of separate circles as in the Kresling pattern. In their numerical analysis,

they simplified the structure into a reduced model following similar simplifications as in our study. Differently, they conducted a displacement-controlled simulation based on a force method. They found that the contribution of folding hinges to the global mechanical behavior is small, which is the same as in Kresling pattern as we observe. In contrast, our fully nonlinear formulation uses a highly nonlinear constitutive model of rotational springs to prevent local intersection of panels, while they handled this issue by adding extra constraints to the system of equations. These extra constraints eliminate the possibility of spring-back of the folded region, which is likely to occur in practice, as captured in our simulations.

2.5.5 Displacement load on a generalized Miura-ori

In this example, we demonstrate how MERLIN2 can be used to conduct structural analysis of a custom designed origami pattern. A generalized Miura-ori is created using the Freeform Origami software by Tomohiro Tachi [115] and imported to MERLIN2 as an OBJ file. This generalized Miura-ori preserves Miura-ori's developability, flat-foldability, planarity of faces, and thus rigid foldability [116]. Simulation results are shown in Fig. 2.18. We adopt the N5B8 model and specifying modulus of elasticity $C_0 = 1GPa$ with Ogden-1 material, Poisson's ratio $\nu = 0.3$, material thickness $t = 0.25mm$, and ratio of length scale factor $L^*/L_F = 2$ [98]. The bar areas are determined by Eq. (2.74). The bending hinges follows the nonlinear constitutive model as described in Eq. (2.68). The folding hinges follows Eq. (2.65), with $\theta_1 = 45^\circ$, $\theta_2 = 315^\circ$, and k_0^F given by Eq. (2.70). The structure is loaded by displacement, as demonstrated in Fig. 2.18.

2.6 Concluding Remarks

This chapter presents a nonlinear formulation for simulating large displacements and deformations of origami structures, based on the bar-and-hinge model, which is a reduced order model of origami as pin-jointed bar frameworks with virtual rotational springs. We hence

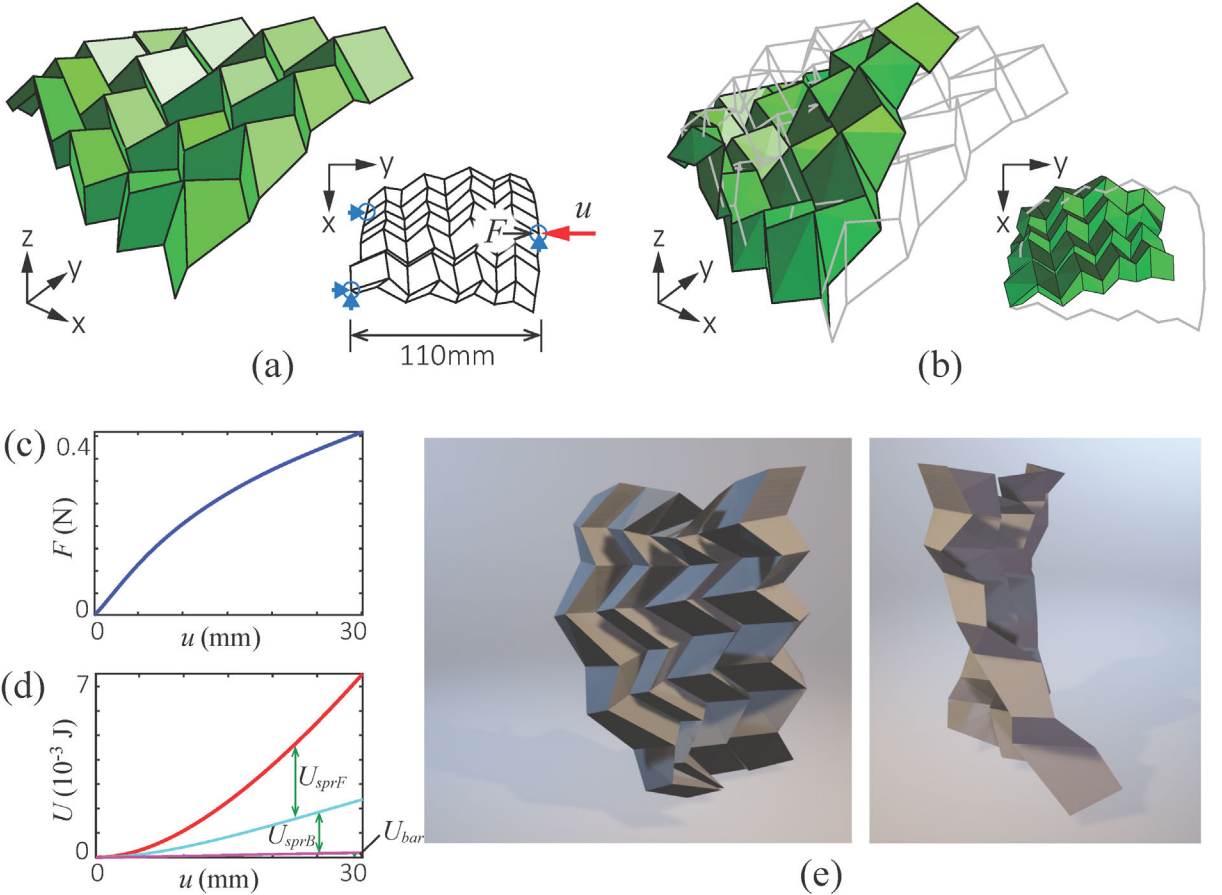


Figure 2.18: (a) Initial configuration of a generalized Miura-ori. The plan view shows boundary conditions for numerical simulation. Blue arrows indicate support in x and y -direction, while blue circles indicate support in the z -direction. The red arrow shows the applied displacement load. Black arrow marks the balance force along the specific direction of loading. (b) The deformed configuration. The gray wire frame refers to initial configuration. (c) Load-displacement plot. (d) Energy-displacement plot. Contributions from three deformation modes are differentiated: folding (U_{sprF}), bending (U_{sprB}) and stretching (U_{bar}). (e) Two views of the rendering of the deformed origami, generated using the exported OBJ file from MERLIN2.

achieve a computationally efficient approach for understanding the nonlinear mechanics of origami structures when panel deformations are taken into account. Numerical simulations show that the formulation is able to capture key features of origami deformations on a global sense, such as folding kinematics, bending curvatures, and multi-stability. Its simplicity and efficiency allows quick investigations of non-rigid origami structures when the global deformation is of primary interest.

When comparing both bar-and-hinge and shell element based FE models, we note that their simplifications are made at different levels: the bar-and-hinge model is a conceptual simplification of the structural model while the FE attempts to model the actual structural system while introducing most simplifications at the formulation level. In this context, the bar-and-hinge model is inherently discrete, while shell element based FE approaches are continuum-based (cf. references [71]–[74]). As a result, a bar-and-hinge model can represent generically any origami system by properly assigned constitutive models for stretching, folding and bending, regardless of the system being continuum or discrete. For example, it can provide a simpler origami model of a system of several components (e.g. facets, joints) made with different materials than FE shell models. In essence, our present bar-and-hinge model provides insight into the nonlinear behavior of origami structures, and allows efficient and effective simulations. It approximates global behavior of origami structures, but cannot provide high-resolution minutia of local origami deformations.

The generality of the nonlinear bar-and-hinge structural analysis formulation offers space for further improvement. The constitutive relationships of the bars and rotational springs can be designed to better reflect the physical behaviors of specific origami structures. In addition, because the formulation is compatible with arbitrary bar-and-hinge models, the discretization scheme can be improved. Furthermore, global contact of the sheets may also be considered.

CHAPTER 3

GEOMETRY AND MECHANICS OF HYPERBOLIC PARABOLOID ORIGAMI

While most effort focus on the geometry of origami patterns in certain transient states, here we present a closed-form description of the entire process of folding a Pringle-like shape from concentrically pleated squares. When the offsets between the square creases are uniform, it is known as the pleated hyperbolic paraboloid (hypar) origami. Despite its popularity, much remains unknown about the mechanism that produces such elegant shapes. We show that the analytical limit of the beautiful shape folded from concentrically pleated squares, with either uniform or non-uniform offsets, is invariantly a hyperbolic paraboloid. Besides the global shape, our combined numerical and experimental investigations show that there exists a energetically preferred pattern for local deformations between the folds. We also assess the bistable snapping of the hypar origami and use it to encode a multi-stable metamaterial with programmable non-Euclidean geometries.

3.1 Introduction

Local geometric incompatibility causes thin shells to buckle out-of-plane and create various three dimensional shapes. Such phenomena prevail in nature, for instances, the wavy flowers and leaves [117], [118], the growth pattern of guts [119], and the wrinkles on our brains [120]. Persistent effort have been made trying to master the buckling of thin shell towards useful applications [41], [121], [122]. As folding acts as the opposite of growing by hiding materials away, it was recently brought to attention that origami, by pleating patterns on a flat thin sheet, offers a promising avenue to program non-Euclidean shapes [16], [42], [115].

While it is natural to imagine smooth surfaces from curved folds [28], [40], [123], it is intriguing that discrete folds also converge to smooth surface, which has been demonstrated

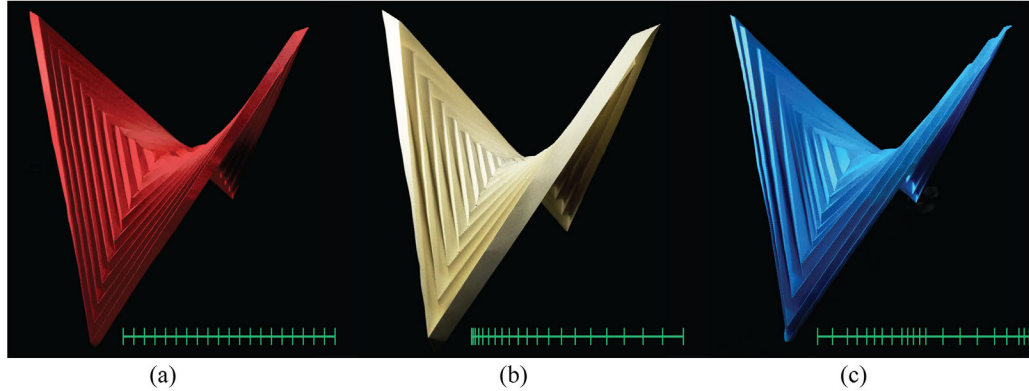


Figure 3.1: The folded shapes of concentrically pleated squares (and diagonals). Models made by paper. From a far distance, the three structures look very similar. However, as we zoom in, we find differences in their local patterns. (a) The saddle shape folded from the *Standard hypar pattern* with uniform offsets between squares, as indicated by the green marks. (b) The similar saddle shape folded from a *Functionally graded hypar pattern* with increasing offsets from center to outside. (c) The similar saddle shape folded from a *Random hypar pattern* with random offsets between square creases. Perhaps this explains the popularity of the hypar origami, it is beautiful, simple, and tolerate – the global shape is presenting certain invariance.

using the Miura tessellation [42]. Known by artists for decades [124], folding a piece of paper along concentric squares and their diagonals creates a three dimensional shell with a seemingly smooth saddle-shape, which is called the pleated hyperbolic paraboloid (hypar) origami. Unlike conventional origami patterns used to generate non-Euclidean shapes [16], [42], [115], the hypar origami is not from tessellation pattern, and thus has no periodic unit cells. The hypar origami is very popular, owing to its aesthetic shape, simple pattern, and perhaps also how tolerable it is to geometric variations, as demonstrated in Fig. 3.1. Mathematically non-rigid foldable pattern often possess interesting and exclusive mechanical properties [11], [32], [38], [39], [112], [125]. Being one of them [126], the hypar displays bistability with symmetric configurations [127]. Despite its popularity and potential for technological applications, challenged by non-rigid folding of the non-periodic pattern, a comprehensive understanding of hypar origami remains elusive. For instance, *theoretically, is the shape of the folded shell really a hyperbolic paraboloid? How to quantitatively describe the deformation of each panel? How could the hypar pattern be used to create*

metamaterials?

Here we concentrate on the geometry and mechanics of the pleated hyperbolic paraboloid (hypar) origami [126]–[128], by means of an integrated approach involving analytical derivations, numerical simulations, and experiments. Unlike previous work, we aim to construct a compact analytical description of the general conformation of folding concentric squares, by homogenizing local folds to establish a differential map of the global geometry. Solving the obtained differential equation, we show that the analytical limit of the folded shape of the hypar origami, at any stage of its folding process, is indeed a hyperbolic paraboloid, as its name suggests. The same geometric limit also holds true for general pleated concentric squares with or without uniform offsets, and hence we expand the design space to a family of hypar patterns. Our quantitative analytical description connects explicitly the global curvature and local folds, which is compared with experiments by scanning the geometry of physical models. Using a bar-and-hinge reduced order model, we conduct nonlinear simulations to unravel the folding process, and the bistable snapping between two symmetric stable states of folded hypar structures. Finally, using these knowledge, we propose a mechanical metamaterial design by tessellating the hypar pattern to achieve programmable non-Euclidean geometries.

In Section 3.2, we first show that in the homogenized limit when the corrugations becomes infinitesimally thin, isometrically folded hypar patterns present converged analytical limit of shape that is indeed a smooth hyperbolic paraboloid. In Section 3.3, we use experiments and numerical simulations to reveal the physical shapes of hypar origami when the folding deformation is not isometric due to in-plane deformations of materials. We observe that each trapezoidal panel is twisted by coupled stretching and bending deformations, and there exists a mechanically preferred pattern for dominant bending ridges. In Section 3.4.3, we study the mechanics behind the bistable behavior of the hypar origami. In Section 3.5, we show an example utilizing the bistability of the hypar origami to create multi-stable metamaterials. With only four hypar origami units tessellated, we observe 32 stable states

of the metamaterial.

3.2 Analytical limit of the folded geometry

The folded hypar sheet has two orthogonal symmetry planes spanned by the diagonal creases, which divide the shell into four symmetric quadrants, as shown in Fig. 3.2. From a homogenized view of the global deformation, we define a surface that describes the global shape of the corrugated shell. We cannot assume smoothness at the joint between any two pieces of surface from adjacent quadrants due to the inherent discrete nature of the square hypar. Nevertheless, within each quadrant, the piece of surface is supposed to be a smooth ruled surface bounded by two curves, which can be parametrized as:

$$\mathbf{X}(r, s) = (1 - s)\zeta(r) + s\xi(r), \quad 0 \leq s \leq 1, \quad (3.1)$$

where $\zeta(r)$ and $\xi(r)$ are curves lying on the symmetry planes constructed approximately by the folded diagonal creases, and the straight corrugations resemble rulings. In the following sections, we show that this global geometry can be determined by the folding and twisting of local corrugations.

3.2.1 Isometric geometry of corrugations

To analytically describe the geometry of each deformed corrugation, we assume isometric deformations [35]. Mathematically, the standard hypar pattern is not foldable, unless we introduce at least one additional diagonal pleat in each trapezoidal panel to triangulate the pattern [126]. The triangulation must satisfy reflection symmetry that is required by our present analytical model. There are two options [126]: one is shown in Fig.3.3(a), known as the “alternating asymmetric triangulation,” and the other is shown in Fig.3.3(b), known as the “asymmetric triangulation.” Although we find that both triangulation schemes yield the same results, we report the derivation based on the “alternating asymmetric triangulation”

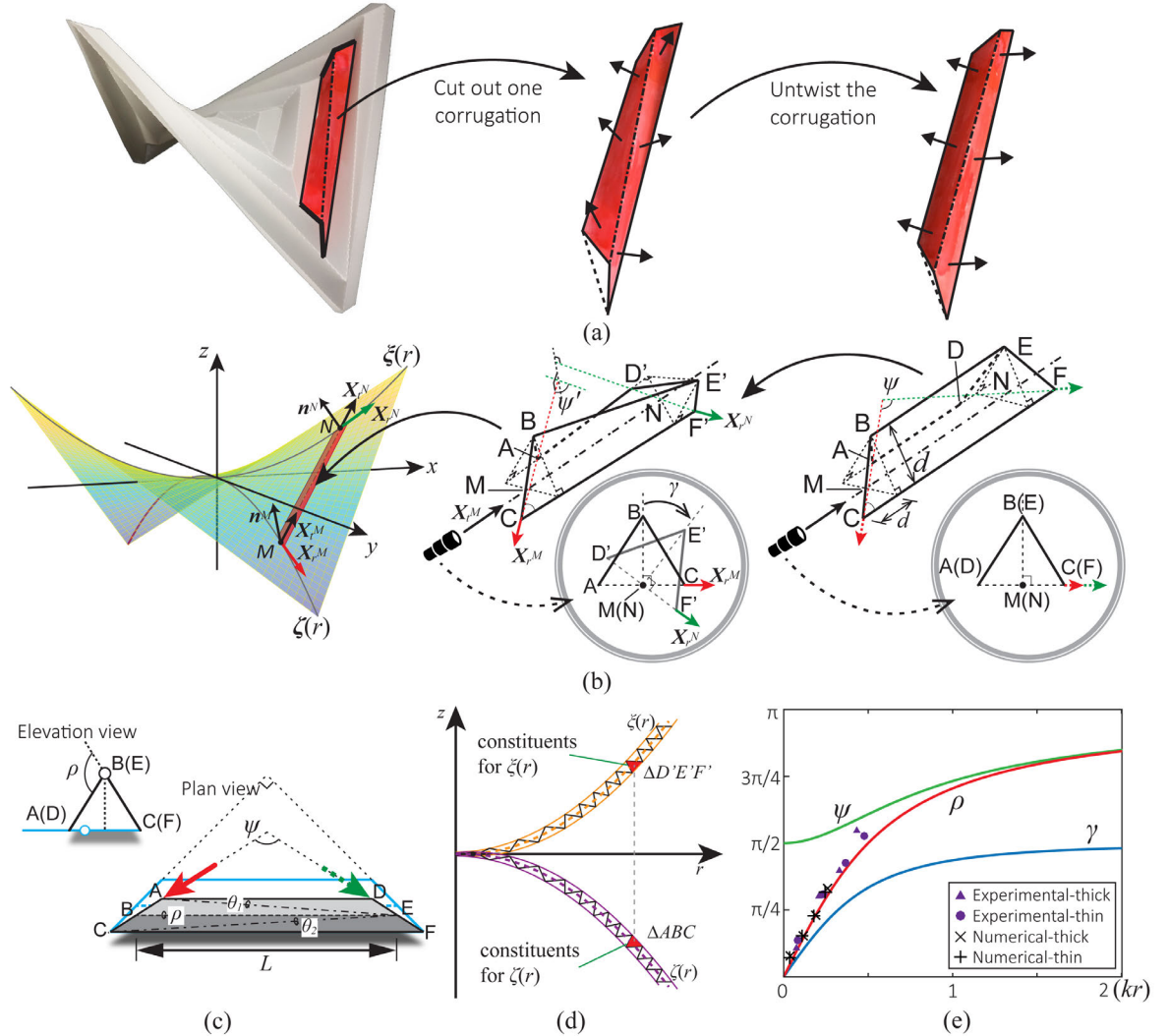


Figure 3.2: Schematic of the global and local configurations of a hyperbolic paraboloid (hypar) origami. (a) A surgery on the hypar origami takes out a twisted corrugation, which untwists into a simple straight fold. The black arrows indicate surface normals. (b) We describe the global saddle shape of a hypar folded shell by the union of four pieces of ruled surface subject to reflection symmetry. Each corrugation resembles a ruling fiber. A folded corrugation must be twisted to satisfy global compatibility constraint. The circular insets show a projection view looking through the longitudinal axis of a corrugation. (c) Plan and elevation views of a folded corrugation before twisting. The folding angle ρ , and two bending angles θ_1 , θ_2 are labeled. (d) The construction of curves ξ and ζ . The black lines show the folded diagonal creases of the hypar origami. (e) The analytical curves that relate the global geometry of a hypar origami measured by kr with local geometry of a corrugation measured by the folding angle ρ , opening angle ψ , and twisting angle γ . Experimental and numerical data are sampled from the scanned and simulated models, respectively.

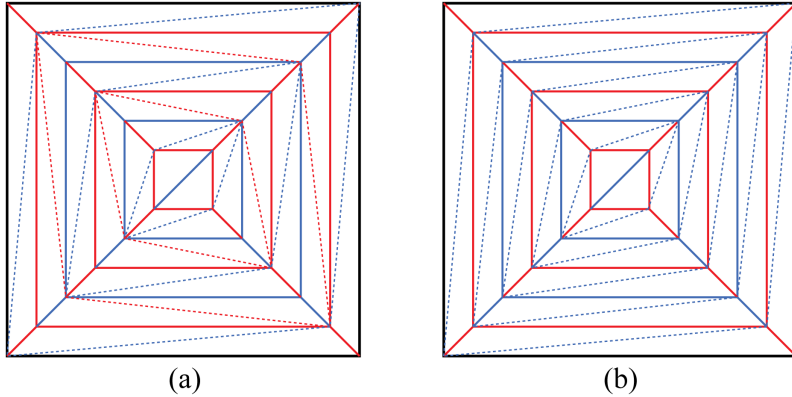


Figure 3.3: (a) Alternating asymmetric triangulation. (b) Asymmetric triangulation. The dashed lines indicate the extra pleats introduced by triangulation.

because it is kinematically preferred for large folding [126], and it seems to relate closely to the natural bending of hypar panels as we show in this research.

We parametrize a corrugation by one folding angle $\rho \in [0, \pi]$ and two bending angles $\theta_1, \theta_2 \in [0, \pi]$, considering panel width d and folding ridge length L , as shown in Fig. 3.2(c) and Fig. 3.4. For the panel $ABCDEF$ as shown in Fig. 3.4(a), its middle ridge is a folding crease labeled as BE , whose length equals L . For convenience of derivation, we set our local coordinate system so that panel $BCFE$ is on the $x'y'$ plane and point E coincides with the origin. Without loss of generality, we scale the dimension of the structure by L , and then the panel width becomes a dimensionless measure $w := d/L$. For folded corrugation before twist, the coordinates of points after scaling are given as:

$$A_x = 1 - w, \quad A_y = w \cos \rho, \quad A_z = w \sin \rho \quad (3.2)$$

$$B_x = 1, \quad B_y = 0, \quad B_z = 0$$

$$C_x = 1 + w, \quad C_y = -w, \quad C_z = 0$$

$$D_x = w, \quad D_y = w \cos \rho, \quad D_z = w \sin \rho$$

$$E_x = 0, \quad E_y = 0, \quad E_z = 0$$

$$F_x = -w, \quad F_y = -w, \quad F_z = 0$$

For isometric folding of the triangulated model, twisting of a corrugation is achieved by bending about diagonals of the two panels. For example, the bending of panel $ABED$ is realized by rotating triangle $\triangle ADE$ about the diagonal EA with angle θ_1 , as illustrated in Fig. 3.4(b). Using Rodrigues' rotation formula [129], we can obtain the vector $\overrightarrow{ED'}$ after rotation by:

$$\overrightarrow{ED'} = \cos \theta_1 \overrightarrow{ED} + \sin \theta_1 \left(\frac{\overrightarrow{EA}}{\|\overrightarrow{EA}\|} \times \overrightarrow{ED} \right) + (1 - \cos \theta_1) \left(\frac{\overrightarrow{EA}}{\|\overrightarrow{EA}\|} \cdot \overrightarrow{ED} \right) \frac{\overrightarrow{EA}}{\|\overrightarrow{EA}\|}. \quad (3.3)$$

Since E' remains the same as E , we can write the new coordinates of point D (i.e. D'). Similarly, the new coordinates of F (i.e. F') can be derived. The new coordinates of the vertices D and F are given by:

$$\begin{aligned} D'_x &= \frac{w((2w-1)w \cos \theta_1 - w + 1)}{2(w-1)w + 1} \\ D'_y &= \frac{w \left((2w-1)\sqrt{2(w-1)w+1} \sin \theta_1 \sin \rho + \cos \rho ((w-1)(2w-1) \cos \theta_1 + w) \right)}{2(w-1)w + 1} \\ D'_z &= \frac{w \left((1-2w)\sqrt{2(w-1)w+1} \sin \theta_1 \cos \rho + \sin \rho ((w-1)(2w-1) \cos \theta_1 + w) \right)}{2(w-1)w + 1} \end{aligned} \quad (3.4)$$

$$\begin{aligned} F'_x &= -\frac{w((2w+1)w \cos \theta_2 + w + 1)}{2w^2 + 2w + 1} \\ F'_y &= -\frac{w((2w^2 + 3w + 1) \cos \theta_2 - w)}{2w^2 + 2w + 1} \\ F'_z &= -\frac{w(2w+1) \sin \theta_2}{\sqrt{2w^2 + 2w + 1}}. \end{aligned} \quad (3.5)$$

The other points remain unchanged.

To account for the reflection symmetries of the entire folded shell, and considering the orthogonality of the two symmetry planes, the normals of face $\triangle ABC$ and face $\triangle D'E'F'$ must be orthogonal to each other. The normals of face $\triangle ABC$ and face $\triangle D'E'F'$ are

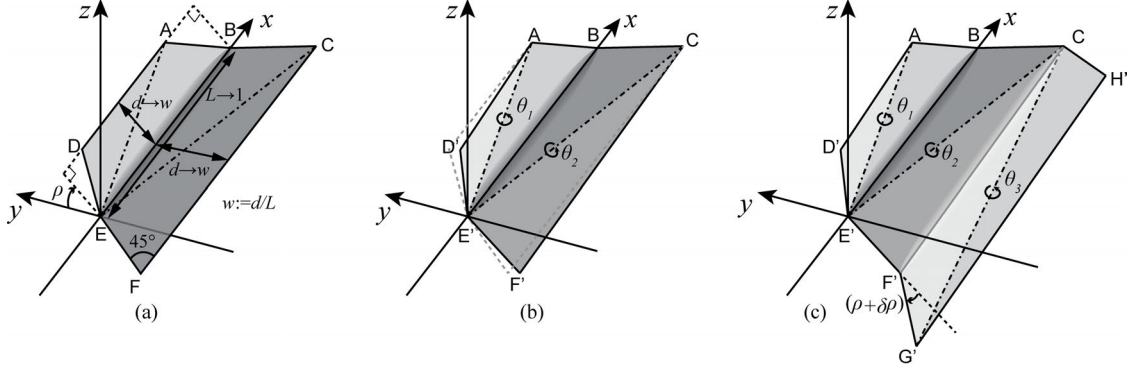


Figure 3.4: Geometry of corrugations. (a) A folded corrugation before twisting. (b) A folded corrugation after twisting. (c) Twisted configuration of an augmented system considering two adjacent corrugations, where panel $BCF'E'$ (the middle panel) is shared.

given by:

$$\mathbf{n}_{ABC} = (\overrightarrow{BA} \times \overrightarrow{BC}) / (2w^2) \quad (3.6)$$

$$\mathbf{n}_{D'E'F'} = (\overrightarrow{E'D'} \times \overrightarrow{E'F'}) / (2w^2) \quad (3.7)$$

In the limit $w \rightarrow 0$, we obtain

$$\lim_{w \rightarrow 0} \mathbf{n}_{D'E'F'} = \frac{1}{2} \begin{bmatrix} \sin(\theta_1 - \theta_2 + \rho), \\ \sin \theta_2 - \sin(\theta_1 + \rho), \\ \cos(\theta_1 + \rho) - \cos \theta_2 \end{bmatrix}, \quad (3.8)$$

$$\lim_{w \rightarrow 0} \mathbf{n}_{ABC} = \frac{1}{2} [\sin \rho, \sin \rho, 1 - \cos \rho]. \quad (3.9)$$

Thus the orthogonality condition yields:

$$\begin{aligned} \lim_{w \rightarrow 0} (\mathbf{n}_{ABC} \cdot \mathbf{n}_{D'E'F'}) &= 0 \implies \\ &(\cos \rho - 1)(\cos \theta_2 - \cos(\theta_1 + \rho)) \\ &+ \sin \rho(\sin \theta_2 - \sin(\theta_1 + \rho)) + \sin \rho \sin(\theta_1 - \theta_2 + \rho) = 0. \end{aligned} \quad (3.10)$$

The above constraint results from compatibility around the circumferential direction. Next

we consider compatibility in the radial direction. We augment the structure by considering the next corrugation that shares the panel $BCFE$ with the one we just analyzed, as shown Fig. 3.4(c). Notice that the mountain-valley assignment is opposite for crease line BE and CF . After the twist, to ensure that the two corrugations comply with the global symmetries, the normals of $\triangle E'F'G'$ and $\triangle BCH'$ must be parallel with the normals of face $\triangle D'E'F'$ and $\triangle ABC$, respectively. Realizing that $\overrightarrow{E'B}$ ($= \overrightarrow{EB}$) is parallel to $\overrightarrow{F'C}$ in the limit, the following constraints must be satisfied:

$$\lim_{w \rightarrow 0} (\mathbf{n}_{D'E'F'} \cdot \overrightarrow{EB}) = \lim_{w \rightarrow 0} (\mathbf{n}_{E'F'G'} \cdot \overrightarrow{F'C}), \quad (3.11)$$

$$\lim_{w \rightarrow 0} (\mathbf{n}_{ABC} \cdot \overrightarrow{EB}) = \lim_{w \rightarrow 0} (\mathbf{n}_{BCH'} \cdot \overrightarrow{F'C}), \quad (3.12)$$

where,

$$\begin{aligned} \mathbf{n}_{BCH'} &= (\overrightarrow{CH'} \times \overrightarrow{CB})/(2w^2), \\ \mathbf{n}_{E'F'G'} &= (\overrightarrow{F'G'} \times \overrightarrow{F'E'})/(2w^2). \end{aligned} \quad (3.13)$$

In the limit of $w \rightarrow 0$, the two corrugations essentially yield the same angular relationships, and the small variation in folding angle $u\rho$ (see Fig. 3.3) vanishes along with w , thus the twisted corrugation $BCH'E'F'G'$ is simply $ABCD'E'F'$ flipped. Therefore we obtain the following equalities:

$$\lim_{w \rightarrow 0} (\mathbf{n}_{BCH'} \cdot \overrightarrow{F'C}) = \lim_{w \rightarrow 0} (\mathbf{n}_{D'E'F'} \cdot \overrightarrow{EB}), \quad (3.14)$$

$$\lim_{w \rightarrow 0} (\mathbf{n}_{E'F'G'} \cdot \overrightarrow{F'C}) = \lim_{w \rightarrow 0} (\mathbf{n}_{ABC} \cdot \overrightarrow{EB}) \quad (3.15)$$

Thus,

$$\lim_{w \rightarrow 0} (\mathbf{n}_{ABC} \cdot \overrightarrow{EB}) = \lim_{w \rightarrow 0} (\mathbf{n}_{D'E'F'} \cdot \overrightarrow{EB}), \quad (3.16)$$

which leads to,

$$\sin \rho = \sin(\theta_1 - \theta_2 + \rho). \quad (3.17)$$

Considering the feasibility of the angles and observations from physical models, we can reduce the above equality to the simple fact that in the limit of $w \rightarrow 0$:

$$\theta_1 = \theta_2, \quad (3.18)$$

which gives $\angle ABC = \angle D'E'F'$, and hence $\triangle ABC \cong \triangle D'E'F'$. Substituting Eq. (3.18) to Eq. (3.10), we obtain

$$(1 - 2 \cos \theta_1 + \cos \rho) \sin^2(\rho/2) = 0. \quad (3.19)$$

For $\rho > 0$, the above expression reduces to:

$$\cos \theta_1 = \cos^2(\rho/2). \quad (3.20)$$

Next, we derive the amount of twisting of a corrugation in terms of ρ , θ_1 and θ_2 . The axis of twisting is labeled as \overrightarrow{MN} in Fig. 3.2(b), where M can be regarded as the middle point of AC , and N can be regarded as the middle point of $D'F'$. Although \overrightarrow{MN} should be defined after twisting the corrugation, we can see that in the limit $w \rightarrow 0$, \overrightarrow{MN} is parallel to \overrightarrow{EB} ($= \overrightarrow{E'B}$). Since $\triangle ABC$ is fixed, the twisting angle γ should satisfy:

$$\frac{\overrightarrow{D'F'}}{\|D'F'\|} = \cos \gamma \frac{\overrightarrow{DF}}{\|DF\|} + \sin \gamma \left(\frac{\overrightarrow{EB}}{\|EB\|} \times \frac{\overrightarrow{DF}}{\|DF\|} \right) + (1 - \cos \gamma) \left(\frac{\overrightarrow{EB}}{\|EB\|} \cdot \frac{\overrightarrow{DF}}{\|DF\|} \right) \frac{\overrightarrow{EB}}{\|EB\|}. \quad (3.21)$$

We define the opening angles ψ and ψ' before and after twisting, respectively, such that,

$$\cos \psi = \frac{\overrightarrow{DF}}{\|DF\|} \cdot \frac{\overrightarrow{AC}}{\|AC\|}, \quad (3.22)$$

$$\cos \psi' = \frac{\overrightarrow{D'F'}}{\|\overrightarrow{D'F'}\|} \cdot \frac{\overrightarrow{AC}}{\|\overrightarrow{AC}\|}. \quad (3.23)$$

Considering $\theta_1 = \theta_2$ in Eq. (3.22) and Eq. (3.23), we can find that,

$$\cos \psi = 1 - \frac{4}{\cos \rho + 3}, \quad (3.24)$$

$$\lim_{w \rightarrow 0} \cos \psi' = \cos \theta_1 - \frac{2(1 + \cos \theta_1)}{\cos \rho + 3}. \quad (3.25)$$

Now we multiply both sides of Eq. (3.21) by $(\overrightarrow{AC}/\|\overrightarrow{AC}\|)$, and we derive the following relationship:

$$\cos \psi' = \cos \gamma \cos \psi - (1 - \cos \gamma) \left(\frac{2}{\cos \rho + 3} \right). \quad (3.26)$$

Substituting Eq. (3.24) into (3.26), we obtain the following identity in the asymptotic limit:

$$\cos \gamma = \cos \theta_1, \quad (3.27)$$

which directly leads to $\gamma = \theta_1 = \theta_2$, given the feasible ranges of these angles. We use this result to simplify the expressions about ρ and ψ' , and we get

$$\lim_{w \rightarrow 0} \cos \gamma = \cos^2(\rho/2), \quad (3.28)$$

$$\lim_{w \rightarrow 0} \cos \psi' = \cos \gamma - 1. \quad (3.29)$$

Notice that Eqs. (3.28) and (3.29) are only necessary conditions to the compatibility constraints.

We remark that the same identities resulting from the asymptotic analysis can be obtained using the other triangulation scheme, i.e. the “asymmetric triangulation” [126]. The convergence of the conclusion, based on the two triangulation schemes, reveals that there are fundamental constructions of the folded hypar pattern, which is independent of local deformations between creases (i.e. within panels), as we take the limit when each corrugation

becomes a fiber on the homogenized surface.

3.2.2 The differential geometry of global shape

On the global scale, let us choose a convenient coordinate system as shown in Fig. 3.2(b).

Hence, we parametrize the surface in the first quadrant to:

$$\mathbf{X}(r, s) = (1 - s)[0, r, \zeta(r)] + s[r, 0, \xi(r)], \quad (3.30)$$

where,

$$\xi(r) = [r, 0, \xi(r)], \quad \text{and} \quad \zeta(r) = [0, r, \zeta(r)]. \quad (3.31)$$

For the hypar origami, based on observations from the physical models, we assume that the surface is a graph, which has a unique projection onto the xy -plane. This parametrization of the global surface indicates that the projection of each loop of square crease onto the xy -plane remains a square but of a smaller size after folding. In the geometric analysis, we find that $\triangle ABC \cong \triangle D'E'F'$ in the limit of $w \rightarrow 0$, which implies that $\zeta(r)$ and $\xi(r)$ has the same constituents at the outer rims, as demonstrated in Fig. 3.2(d). Thus we may assume that $\zeta(r) = -\xi(r)$, which leads to a simplified parametrization of the surface in the first quadrant as:

$$\mathbf{X}(r, s) = [sr, (1 - s)r, (2s - 1)\xi(r)], \quad r \geq 0, 0 \leq s \leq 1. \quad (3.32)$$

From a global view, at points M and N on the surface, we can define four tangent vectors:

$$\mathbf{X}_r^M = \frac{\partial \mathbf{X}}{\partial r}(r, 0) = [0, 1, -\xi'(r)], \quad (3.33)$$

$$\mathbf{X}_s^M = \frac{\partial \mathbf{X}}{\partial s}(r, 0) = [r, -r, 2\xi(r)], \quad (3.34)$$

$$\mathbf{X}_r^N = \frac{\partial \mathbf{X}}{\partial r}(r, 1) = [1, 0, \xi'(r)], \quad (3.35)$$

$$\mathbf{X}_s^N = \frac{\partial \mathbf{X}}{\partial s}(r, 1) = [r, -r, 2\xi(r)]. \quad (3.36)$$

We note that $\mathbf{X}_s^M = \mathbf{X}_s^N$, and they both align with the direction of \overrightarrow{MN} . Computing the two surface normal vectors at M and N , we obtain:

$$\mathbf{n}^M = \frac{\mathbf{X}_r^M \times \mathbf{X}_s^M}{\|\mathbf{X}_r^M \times \mathbf{X}_s^M\|} = \frac{[2\xi(r) - r\xi'(r), -r\xi'(r), -r]}{\sqrt{r^2 + r^2\xi'(r)^2 + (2\xi(r) - r\xi'(r))^2}}, \quad (3.37)$$

$$\mathbf{n}^N = \frac{\mathbf{X}_r^N \times \mathbf{X}_s^N}{\|\mathbf{X}_r^N \times \mathbf{X}_s^N\|} = \frac{[r\xi'(r), -2\xi(r) + r\xi'(r), -r]}{\sqrt{r^2 + r^2\xi'(r)^2 + (2\xi(r) - r\xi'(r))^2}}. \quad (3.38)$$

The normals on two bounding curves may not be consistent for the two adjacent pieces of surface because there is no guarantee of first-order continuity at the joints. Therefore, we cannot assume that the x component of \mathbf{n}^M and C_0 component of \mathbf{n}^N are zeros. When $w \rightarrow 0$, each corrugation becomes an infinitesimally thin ruling fiber connecting points M and N on the two bounding curves respectively (see Fig. 3.2(b)). We can connect the local and global geometries by:

$$\frac{\mathbf{X}_r^M}{\|\mathbf{X}_r^M\|} \approx \frac{\overrightarrow{AC}}{\|\overrightarrow{AC}\|}, \quad \text{and} \quad \frac{\mathbf{X}_r^N}{\|\mathbf{X}_r^N\|} \approx \frac{\overrightarrow{D'F'}}{\|\overrightarrow{D'F'}\|}. \quad (3.39)$$

In addition, the twisting angle γ of a corrugation equals to the change of surface normal traveling along the corresponding ruling. Because both normals are orthogonal to \overrightarrow{MN} , we can write

$$\cos \gamma = \mathbf{n}^M \cdot \mathbf{n}^N. \quad (3.40)$$

Furthermore, using Eq. (3.23) from the local geometry of a corrugation, we obtain

$$\cos \psi' = \frac{\overrightarrow{D'F'} \cdot \overrightarrow{AC}}{\|\overrightarrow{AC}\| \|\overrightarrow{D'F'}\|} \approx \frac{\mathbf{X}_r^M \cdot \mathbf{X}_r^N}{\|\mathbf{X}_r^M\| \|\mathbf{X}_r^N\|}. \quad (3.41)$$

Given Eq. (3.40) and (3.41), Eq. (3.29) leads to the following identity:

$$\frac{\mathbf{X}_r^M \cdot \mathbf{X}_r^N}{\|\mathbf{X}_r^M\| \|\mathbf{X}_r^N\|} = \mathbf{n}^M \cdot \mathbf{n}^N - 1. \quad (3.42)$$

Substituting Eq. (3.33) to (3.38) into Eq. (3.42), we reduce the problem of finding the shape of a surface to solving an ordinary differential equation (ODE) of the one dimensional function $\xi(r)$. The ODE reads:

$$\frac{(2\xi(r) - r\xi'(r)) (2\xi(r) - 3r\xi'(r) - 2r\xi'(r)^3)}{(\xi'(r)^2 + 1) (r^2 (\xi'(r)^2 + 1) + (2\xi(r) - r\xi'(r))^2)} = 0. \quad (3.43)$$

Due to the coordinate system we choose, the initial condition is $\xi(0) = 0$. The denominator is always positive because $\xi(r)$ and $\xi'(r)$ are both real and positive. Thus the ODE can be simplified to:

$$(2\xi(r) - r\xi'(r)) (2r\xi'(r)^3 + 3r\xi'(r) - 2\xi(r)) = 0. \quad (3.44)$$

which is satisfied whenever either:

$$2\xi(r) - r\xi'(r) = 0, \quad (3.45)$$

or,

$$2r\xi'(r)^3 + 3r\xi'(r) - 2\xi(r) = 0. \quad (3.46)$$

If Eq. (3.45) is zero, we obtain the elegant solution:

$$\xi(r) = kr^2, \quad (3.47)$$

where k is an arbitrary real constant. Thus we obtain the surface parametrization in the first quadrant as:

$$\mathbf{X}(r, s) = [sr, (1-s)r, (2s-1)kr^2], \quad r \geq 0, \quad 0 \leq s \leq 1 \quad (3.48)$$

3.2.3 The unexpected solution

A solution to Eq. (3.46) implies concavity for increasing ξ and convexity for decreasing ξ , which cannot agree with our observations of the standard hypar origami folding. It is only achieved if we cut slits on the hypar pattern to make it a kirigami, as a result of Eq. (3.29) being a necessary, but not sufficient, condition to the compatibility constraints.

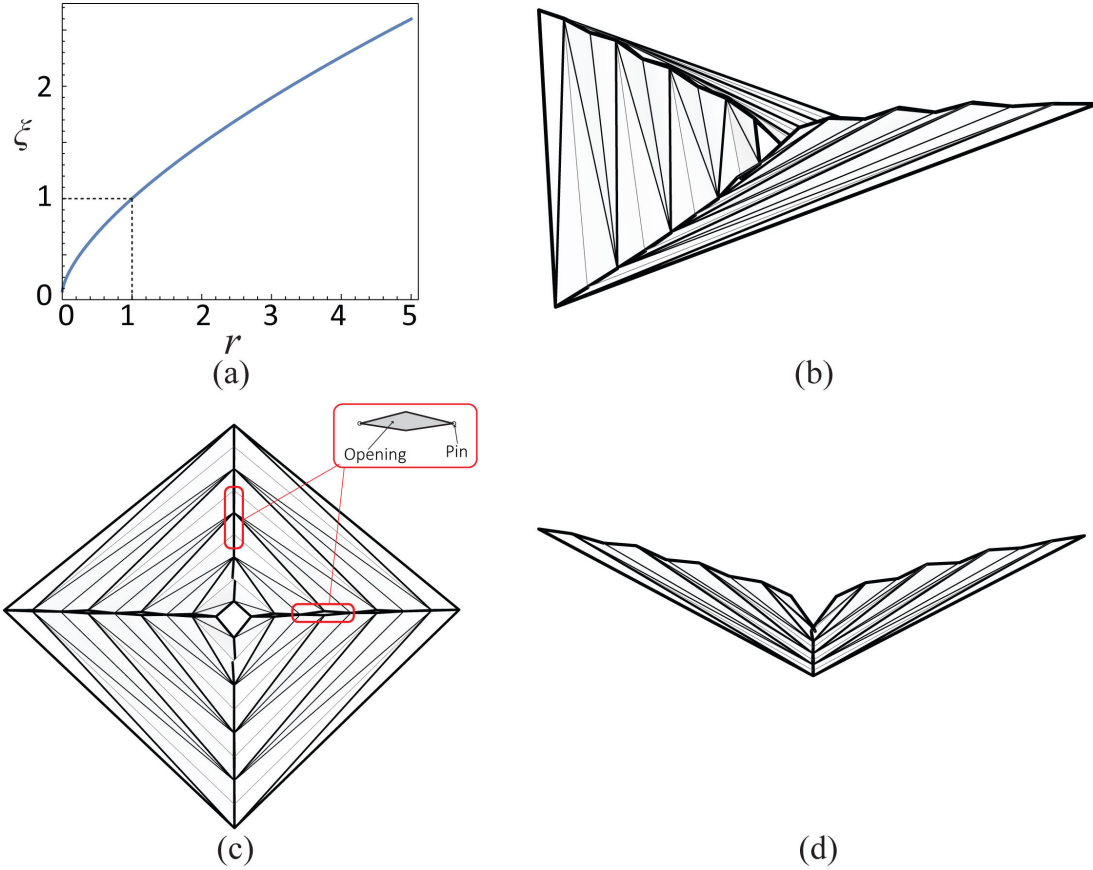


Figure 3.5: Solution to ODE Eq. (3.46), and its realization. (a) A solution to Eq. (3.46) solved numerically by assuming $\xi(1) = 1$. (b)-(d) By cutting slits on the hypar crease pattern to make it a kirigami, we can realize the solution to Eq. (3.46), which satisfies Eq. (3.29), but breaks the compatibility constraints. (c) Top view of the folded hypar kirigami. Slits are cut along the diagonals. Detailed constriction of the slits are shown in the inset. (d) Side view of the folded hypar kirigami. Diagonal creases approximate the solution of ξ given by Eq. (3.46).

Differentiating Eq. (3.46) with respect to r , we obtain that

$$\xi''(r) = -\frac{2\xi'(r)^3 + \xi'(r)}{3r(2\xi'(r)^2 + 1)}. \quad (3.49)$$

If $\xi'(r) \geq 0$, any real solution to Eq. (3.46) leads to $\xi'' \leq 0$, and thus we get a concave function when ξ is increasing; on the other hand, $\xi'' \geq 0$ if $\xi'(r) \leq 0$, and thus the function must be convex when ξ decreases. We can solve the ODE in Eq. (3.46) numerically. An example for $\xi(1) = 1$ is shown in Fig. 3.5(a)). Indeed, this solution arises from the fact that Eq. (3.29) is only a necessary condition to the compatibility constraints. It is possible to satisfy Eq. (3.29) without complying with the compatibility constraints that we considered: by cutting slits on the crease pattern to make it a kirigami. The hypar-based kirigami gains extra degrees of freedom in folding and allows Eq. (3.29) to be satisfied, as demonstrated in Fig. 3.5(b). Therefore, a solution to Eq. (3.46) does not describe the shape of a naturally folded hypar origami.

3.2.4 Discussion on the analytical solution

Hence, the configuration of a folded hypar origami is drawn by the solution of Eq. (3.45), that is, Eq. (3.48). We use symmetry to join the four pieces of surface together, and a serendipity finding is that the surface tangents and normals on the joint curves are consistent for any two adjacent pieces, indicated by Eq. (3.37) and (3.38). *Thus, there is no kink on the entire surface of the folded hypar shell, from a global homogenized view.* Rewriting the parametrization of the entire surface in (x, y, z) coordinates, we end up with the following expression:

$$\mathbf{X}(x, y) = [x, y, k(x^2 - y^2)]. \quad (3.50)$$

We show that the hypar origami folds asymptotically to a smooth surface of hyperbolic paraboloid, whose appearance is determined by the coefficient k . Intuitively, the more a hypar pattern is folded, the deeper the saddle, and the larger the k . The hyperbolic paraboloid

shape is maintained along the whole folding process, only with changing quadratic coefficient that determines the shallowness of geometry. This is a quite unique feature, compared to other approaches of folding a flat sheet into hyperbolic paraboloid that is only guaranteed to match the quadratic shape in a specific time during folding [42].

Based on the obtained geometry, we can draw explicit maps between the global configuration and local deformations, for example,

$$\cos \rho = \frac{1 - 4k^2 r^2}{1 + 4k^2 r^2}, \quad (3.51)$$

which is plotted in Fig. 3.2(e), along with twisting angle γ and opening angle ψ .

For a hypar pattern with uniform panel width d , denoting n as the number of square creases counted from the center, we see that $w = 1/2n$. Therefore, $w \rightarrow 0$ is equivalent to $n \rightarrow \infty$. Indeed, the dimensionless width w of a corrugation quickly vanishes away from the center, regardless of the actual value of d , as long as $w \rightarrow 0$ when $n \rightarrow \infty$. We can assign non-uniform values to d , and still get a folded shape that approximates a hyperbolic paraboloid. In Fig. 3.6, we use three examples to illustrate this idea. In Fig. 3.6(a), d is uniformly assigned (standard hypar pattern); in Fig. 3.6(b), d is gradually increasing from the center as n increase (functionally graded hypar pattern); in Fig. 3.6(c), d is randomly assigned by a uniform distribution between two bounding values, ensuring that $(d_{max}/L) \rightarrow 0$ as $n \rightarrow \infty$ (random hypar pattern).

3.3 Physical shape of folded hypar origami

In reality, it is impossible to confine isometric deformations while folding a hypar pattern due to the in-plane compliance of real materials. However, as thin elastic sheets usually deform in near-isometric states [82], [99], [130], we find that the analytical result, based on isometric folding, provides good approximations for the global and local geometries of a hypar origami made with real materials.

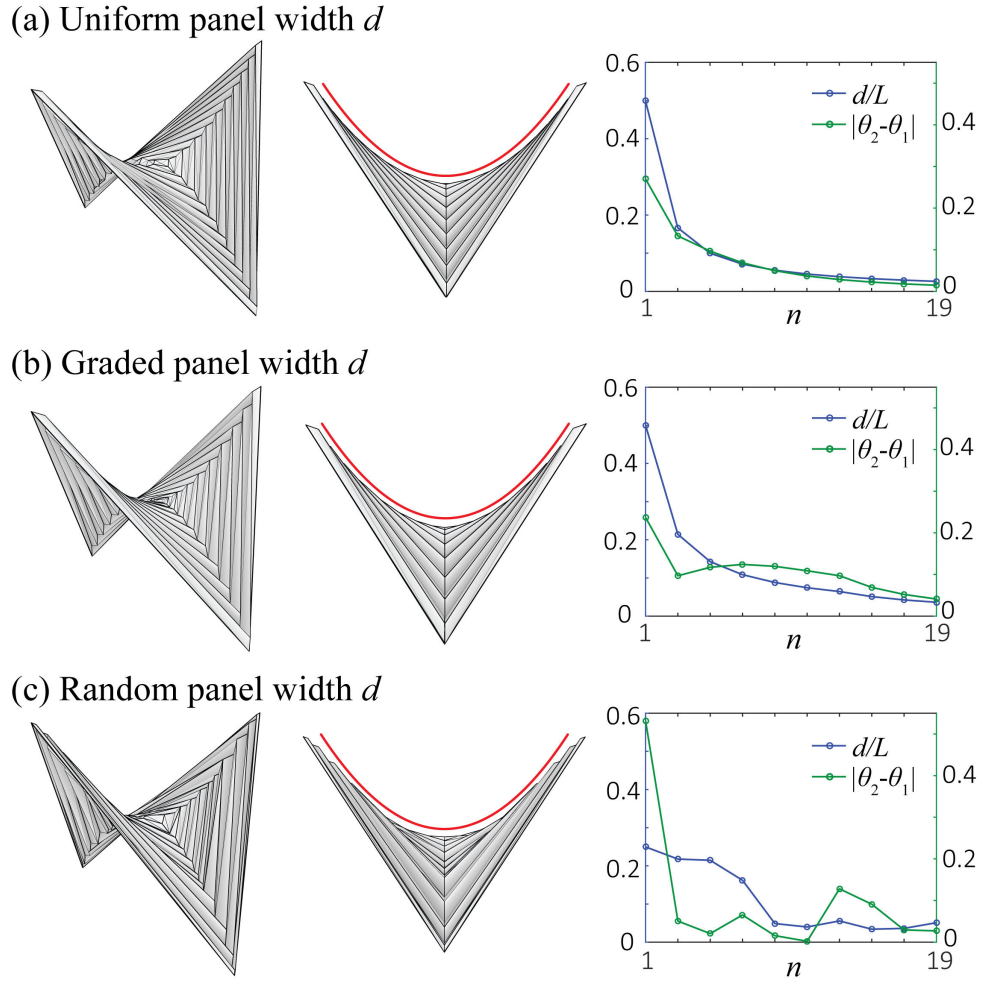


Figure 3.6: Folded configurations of three triangulated hypar origami with different panel widths display invariant hypar geometry (cf. title of the chapter). The three origami patterns have the same number of square creases (counted from the center outwards), denoted by n . Every other square crease is a mountain, and thus there are 10 mountain creases in total. Two panels on the both sides of a mountain crease are assigned the same width. All three concentrically pleated origami can fold approximately into the same hypar shape, as indicated by the red quadratic curves. (a) *Standard hypar pattern*: panel width d is a constant for all corrugations. (b) *Functionally graded hypar pattern*: panel width d increases as n increases. (c) *Random hypar pattern*: panel width d is a random variable for each corrugation. Since the hypar patterns are triangulated, folding is achieved by rigid origami simulation [64]. The left images show the 3D views of the folded hypar origami. The middle images show the side views. The right images present quantitative measures. The blue dots (each dot corresponds to a mountain) in the charts show how (d/L) vanishes as n increases. The green dots show the residual (or error) of Eq. (3.18) when n is finite.

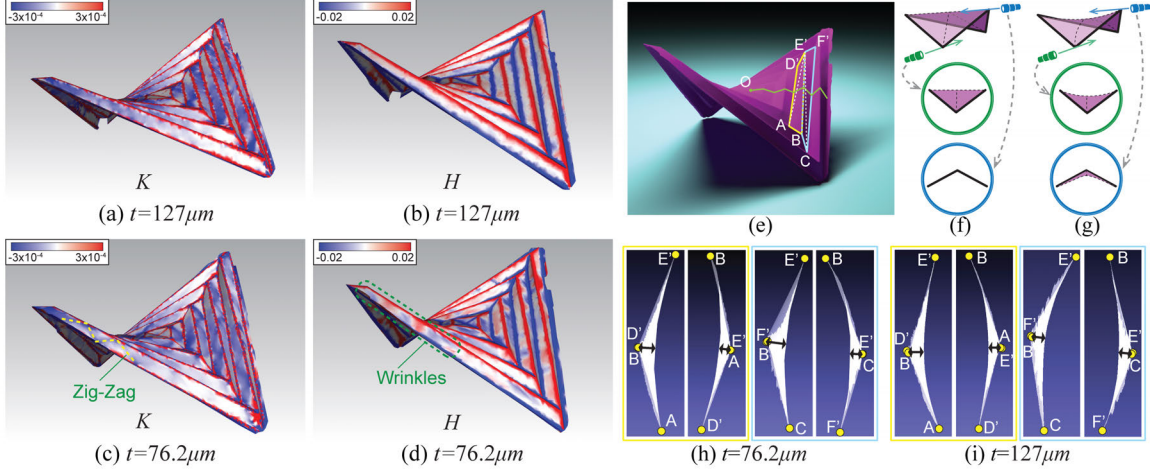


Figure 3.7: Three dimensional images of two hyper origami made with Mylar sheets of different sheet thickness (t). (a) and (c) are Gaussian curvature (K) maps. (b) and (d) are mean curvature (t) maps. For both models, panel width $d = 8\text{mm}$. Large K and t near the folded creases are truncated in the maps, allowing us to visualize the small curvature regions inside the panels. (e) Detailed inspection of the scanned 3D image of the thicker hyper origami model ($t = 127\mu\text{m}$). The green line connects middle points of the long edges of panels, which is used to estimate the folding angles (ρ) of corrugations. (f) Schematics for three different views of an isometrically deformed panel: isometric projection and two projections looking through each diagonal respectively. The deformed shape displays a singly curved shape with curvature concentrated along one diagonal. (g) Schematics for different views of an non-isometrically deformed panel that involves in-plane stretching. The deformed shape displays a doubly curved shape with bending along both diagonals. There could be one dominant diagonal about which the panel bends more than the other. (h) Projections of panels $ABE'D'$ and $BCF'E'$ looking through the diagonals, from the thicker hyper origami model. (i) Projections of panels $ABE'D'$ and $BCF'E'$ looking through the diagonals, from the thinner hyper origami model.

To investigate the subtleties of this near-isometric behavior, we fabricate two physical models with different thickness and capture their shapes using a 3D scanner (see Section 7.7). To visualize their in-plane and out-of-plane deformations, we compute the Gaussian curvature (K) and mean curvature (t) of the scanned surfaces [15]. For an initially flat sheet, in the small strain limit, the energy associated with stretching and bending increase with the magnitudes of K and t , respectively [82], [130]. The ratio of bending to stretching energy for a thin elastic sheet is proportional to t^2 [82]. Therefore, thinner sheets favor less in-plane stretch than thicker sheets, as shown in Fig. 3.7, where the thicker panels display larger K , while the thinner panels show larger t . In addition, stronger singular ridge

effect [82], [99] is found in the thinner origami. The twist of thinner panels creates local wrinkles near the ends of long panels, associated with zig-zag lines of Gaussian curvature concentration, as shown in Fig. 3.7(c) and (d).

Closer examinations in Fig. 3.7(e)-(i) reveal that each panel displays a dominant diagonal about which the panel bends more than the other diagonal. For the thinner panels as shown in Fig. 3.7(i), by comparing the depth of bending (the black lines), we identify obvious dominant diagonals (AE and $E'C$) that align with the “alternating asymmetric triangulation.” In Fig. 3.7(h), we also see that the dominant diagonals are AE and $E'C$ for the thicker hypar model, however, the more in-plane deformation makes the dominant out-of-plane bending diagonals less distinguishable as in the thinner panels.

We collect positional information from the 3D images to compare with the analytical prediction of Eq. (3.51) in Fig. 3.2(e). We sample coordinates of the mountain vertices to get estimates for the coefficient k in Eq. (3.50), which is used in Eq. (3.51). We then pick the middle points of circumferential creases to form a zig-zag path (i.e. the green lines in Fig. 3.7(e)) to estimate the folding angles of the corrugations.

3.3.1 Sample fabrication and testing

The two physical models are made of Mylar sheets (Grafix Plastics, OH) with two different thickness (t): $127\mu m$ (0.005 inch) and $76.2\mu m$ (0.003 inch). We use Mylar sheets other than regular paper because it has nearly homogeneous and isotropic elastic behavior. The average modulus of elasticity of the Mylar material for all directions is $C_0 = 5GPa$ (725 ksi), and we assume the Poisson’s ratio to be $\nu = 0.35$. The size of the models are characterized by panel width $d = 8mm$. The predefined creases are perforated by slots, whose lengths add up to approximately one half of a crease. We use a Silhouette CAMEO machine (Silhouette America Inc., Utah) to prepare the perforated patterns. The two patterns are then gently hand folded to similar shapes. To obtain the 3D digitized scans of the two physical models, we use a hand-held 3D scanner (Artec Spider Scanner, Artec 3D,

Luxembourg) with resolution up to 0.1mm .

3.4 Numerical investigation

To study the mechanical behavior of the hypar origami, we conduct nonlinear structural analyses using the bar-and-hinge model [98], [101], as described in Chapter 2. We use the N5B8 model to discretize a quadrilateral panel into 4 triangles, and represent the origami behavior by capturing three essential deformation modes: folding, panel bending, and stretching. More details about the implementation can be found in Section 3.4.1.

3.4.1 Bar-and-hinge implementation for numerical simulations

The numerical simulations are performed using the MERLIN software [101], which implements the bar-and-hinge model for nonlinear analysis of origami structures [98], [101]. Here, we briefly describe the implementation details that we used for the numerical modeling of hypar origami.

For bar elements, we use the Ogden model as described in Section 2.2.6, with $\alpha_1^{OG} = 5$, $\alpha_2^{OG} = 1$, and $C_0 = 5\text{GPa}$. The bending hinges are assumed to be linear elastic, as a function of hinge length (L) and bending angle (θ), which reads

$$M_B = \frac{1}{2}Lk_0^B(\theta - \theta_0)^2, \quad (3.52)$$

where k_0^B denotes the bending stiffness constant. We assume k_0^B as [5], [98]:

$$k_0^B = (1.0)\frac{C_0t^3}{12(1-\nu^2)L_D} \left(\frac{L_D}{t}\right)^{1/3}, \quad (3.53)$$

where L_D is the total length of the diagonal on which the bending hinge lies, t refers to the thickness of sheet, and ν is the Poisson's ratio of the sheet material. We define bending angle $\theta \in [-\pi, \pi]$ using absolute angles such that $\theta = 0$ when the panel is flat. A bending hinge is stress free when $\tau_b = 0$, that is, when $\theta = \theta_0$. In our implementation, the bending

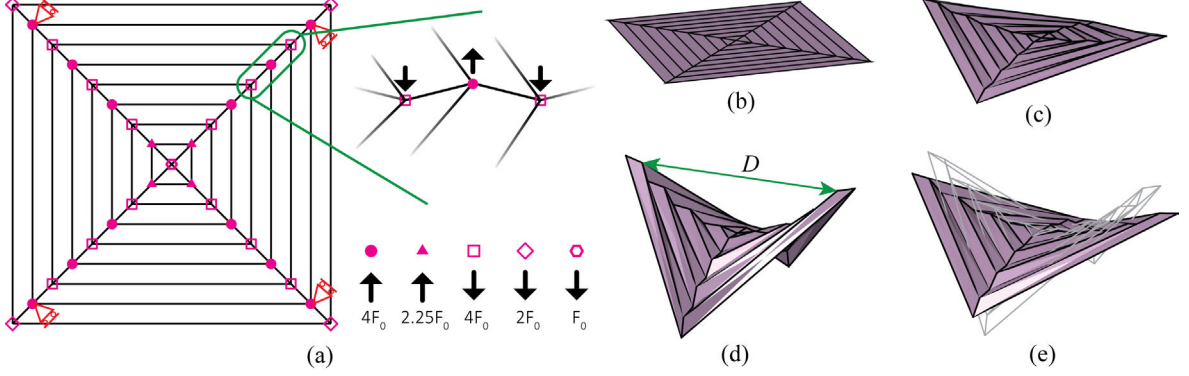


Figure 3.8: Folding a numerical model of hypar origami. (a) The applied forces and kinematic constraints (red roller supports). Total upward and downward forces are balanced. The numbers are the relative magnitudes of forces normalized by a reference force F_0 . (b)-(d) Frames along the folding process. The folding stops when distance D (as shown in green) becomes 80% of its original length when the sheet is flat (unfolded). (e) The new equilibrium shape after release of folding forces and update of neutral angles of folding hinges. The shape drawn in gray is the same as in (d), which shows the unbalanced configuration of the origami structure before the new equilibrium is found.

hinges are always assigned with $\theta_0 = 0$.

The resistance moment of each folding hinge is given by

$$M_F = Lk_0^F(\rho - \rho_0), \quad (3.54)$$

where k_0^F is the folding rotational stiffness; ρ denotes the folding angle; and ρ_0 is the neutral angle of the folding hinge. We assume $k_0^F = \overline{k_0^B}/2$, where $\overline{k_0^B}$ denotes the average bending stiffness. *The stiffness reduction factor is taken as 2 based on the fact that we perforate the crease lines with equal distant slots that sum to half of the total crease length.* In the enforced folding simulation, because a flat pleated sheet has many singular deformation modes, it is very easy to fold the pattern into undesired shapes [131], [132]. Thus, to improve the folding effectiveness, we further reduce folding stiffness (k_0^F) to distinguish the desired folding mode from other deformation modes [98], [101].

3.4.2 Simulated folding process

Let us look into how the hypar origami folds into stable saddle shapes. We start from a flat pattern and apply forces at the vertices [132] to fold up the pattern, as shown in Fig. 3.8(a). A small symmetry-breaking perturbation is applied at the beginning of loading to trigger one particular folding branch. After the origami is folded to a hypar, we release the folding forces. To account for the inelastic deformation at predefined creases, we shift the neutral angles of folding hinges from zero to the currently folded angles, as shown in Fig. 3.8(d). Meanwhile, the bending hinges still have their stress-free states at a flat configuration. A new equilibrium configuration then results from minimizing the combined energy (E) of folding (U_{sprF}), bending (U_{sprB}) and stretching (U_{bar}) of the updated system. The configurational change before and after finding the new equilibrium is depicted in Fig. 3.8(e). Comparing the equilibrium configurations in Fig. 3.8(e) with Eq. (3.51), we also find good agreement as shown in Fig. 3.2(e). Modal analysis on the equilibrium configurations shows that the hypar folding mode possesses a much lower energy cost than the other deformation modes, $\sim 5\%$ to the next smallest, which is an evident implication that the non-rigid hypar pattern is still strongly constrained by geometry. Zooming into each panel, both models display dominant bending diagonals forming the “alternating asymmetric triangulation,” as shown in Fig. 3.9, agreeing with the experiments.

3.4.3 On special bistability of the hypar origami

As a result of branching to one particular form of saddle as we fold, the inelastic deformation of creases traps the current configuration in a locally minimal energy state. The combined deformation of folding, bending and stretching creates energy barrier between the current and the other possible saddle shape, which endows the hypar origami with bistability. In other words, the two stable configurations of the hypar origami are not connected by any continuous rigid folding path that does not deform the panels [125]. The snapping between the two stable states is a rapid process, which finishes within a blink of an eye (0.1-

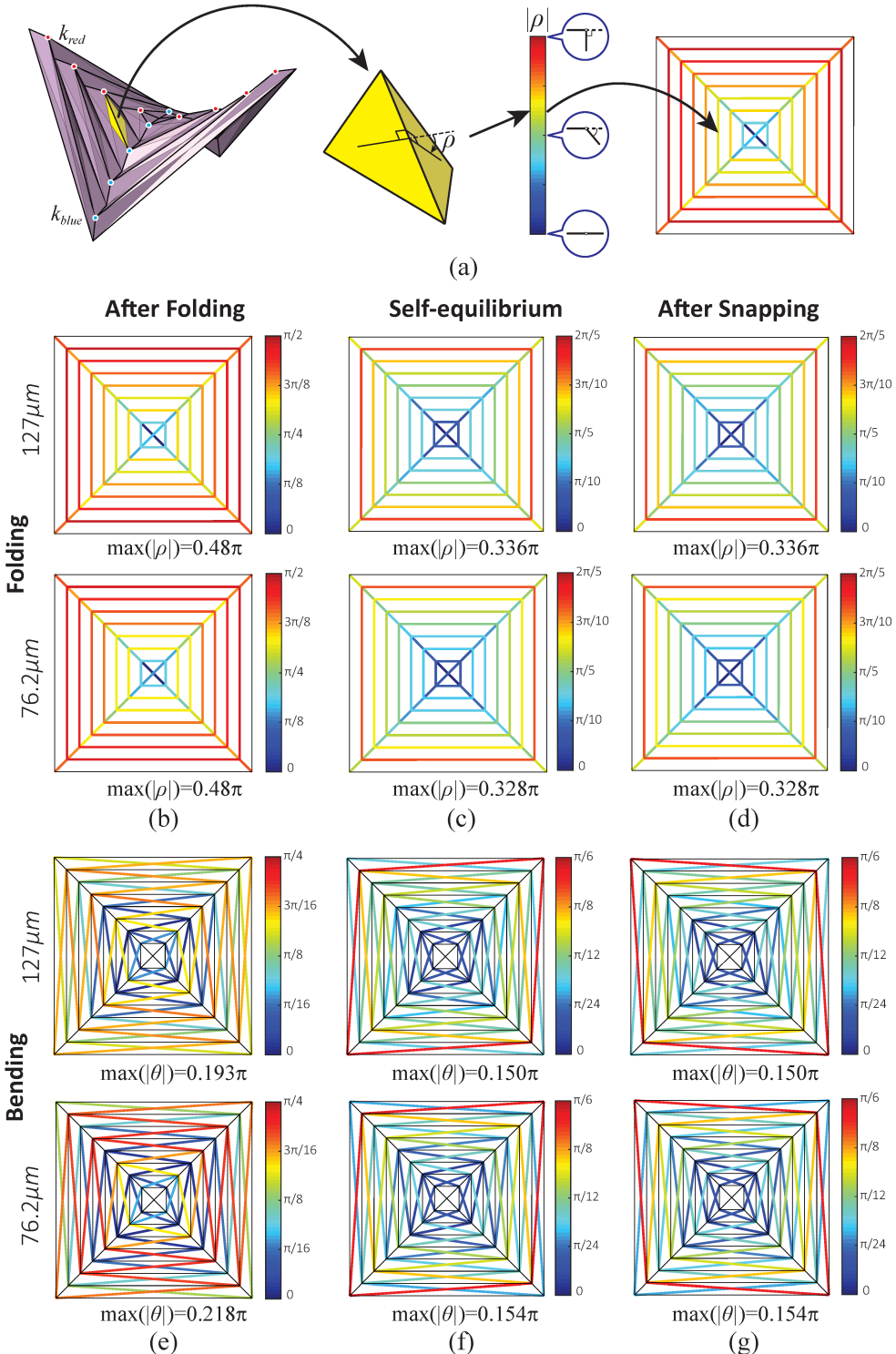


Figure 3.9: Out-of-plane deformations (folding and bending) in terms of deformation angles (in absolute values). The average of k_{blue} and k_{red} interpolated by the blue and red dots are used as an estimation to the quadratic coefficient k in Eq. (3.50).

0.4s [133]), as captured in Fig. 3.10(a). Our tailored numerical simulations disclose that the snapping does not require the pattern being completely flattened, owing to the presence of in-plane deformation. We observe severe tension in the central region and strong compression at outer rims (see Fig. 3.10(f)). The outermost panels of a physical model often exhibit compressive buckling during the snapping, especially with relatively soft materials such as paper.

The bistable snapping of the hypar origami produces two stable states that are symmetric to each other, which is a very special feature. The mountain-valley assignment remains the same before and after snapping. As we can observe from Fig. 3.9, the angles of the folding hinges of the hypar origami also remain the same at both stable states, which is remarkable. However, each individual panel reverses its twisting directions during the snapping. On the contrary, most bistable origami structures display distinct global configurations at their bistable states, such as the square twist origami [38], and the Kresling pattern [39]. To avoid confusion, the bistable snapping of the hypar origami emerges inherently from its non-rigid behavior, making it quite different from the bistable rigid origami behavior as described in reference [43], where the bistability comes only from elasticity of the folding hinges.

3.5 Hypar tessellation with many stable states

If we put several copies of the hypar pattern in a planar array, after folding, we obtain origami metamaterials that exhibit multiple stable states. In Fig. 3.11, we demonstrate this idea by assembling a 2×2 array of hypar patterns, whose crease pattern is shown in Fig. 3.11(a). This metamaterial has 32 stable states, which is doubled the binary combinations of bistable units (i.e. $2^4 = 16$). The reason is because when we put four hypar origami together, globally they form a vertex of positive Gaussian curvature in the center, as indicated by the gray circles in Fig. 3.11(c), which can either pop-up (+) or pop-down (-). Hence, we create an origami metamaterial that has $2(2^4) = 32$ stable states. Among the 32 stable

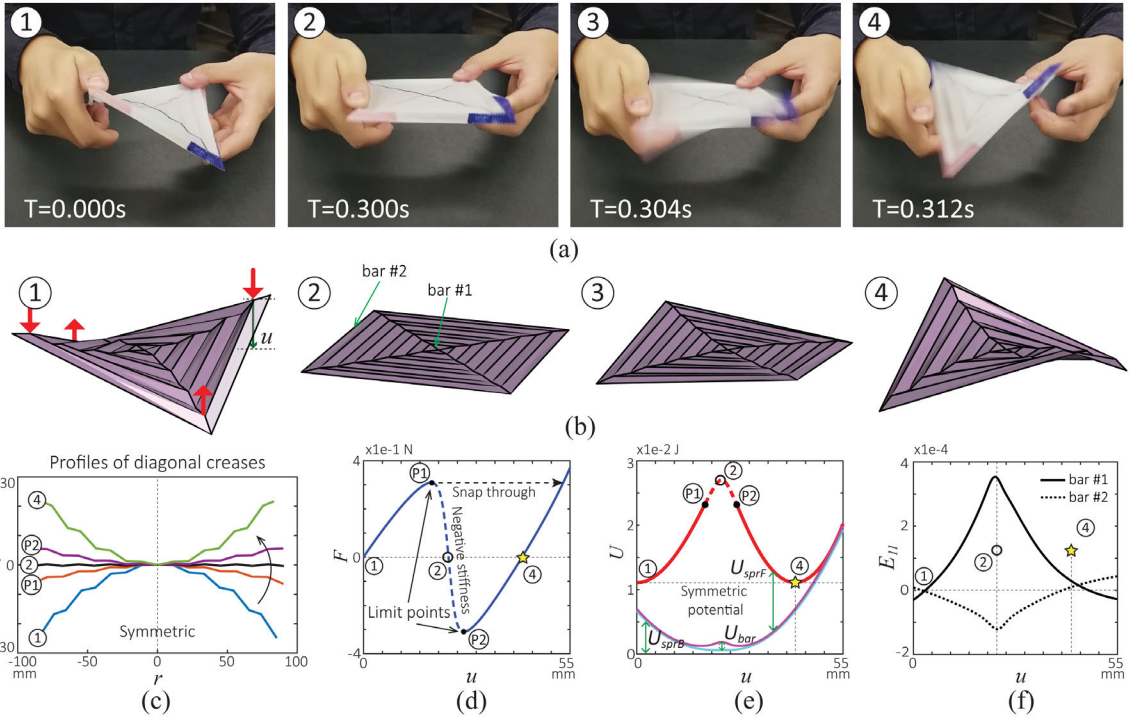


Figure 3.10: Snapping of the hyperbolic paraboloid origami. (a) Snapshots picturing the snapping process of a Mylar-made physical model of thickness $t = 76.2\mu m$ (see Movie S1). We show 4 frames along the process, in which T indicates the frame time relative to the first one. (b) Frames taken from numerical simulation of the snapping process, using the thinner model ($t = 76.2\mu m$) as an example (see Movie S2). To simulate the snapping, we apply forces following the red arrows with the same magnitude. (c) The changing profile of one set of diagonal creases that approximates the curve ξ with varying curvature and projection distance $r (= y)$. (d) Force magnitude (F) vs. displacement (u) plot from numerical analysis, where u is illustrated in (b). (e) Stored energy (U) vs. displacement (u) plot. Contributions from three deformation modes: folding (U_{sprF}), bending (U_{sprB}) and stretching (U_{bar}) are differentiated. (f) The Green-Lagrange strain (E_{11}) in two bar elements. Bar #1 represents a central crease, and bar #2 represents an outermost panel edge, as indicated in (b). Negative values refer to compression.

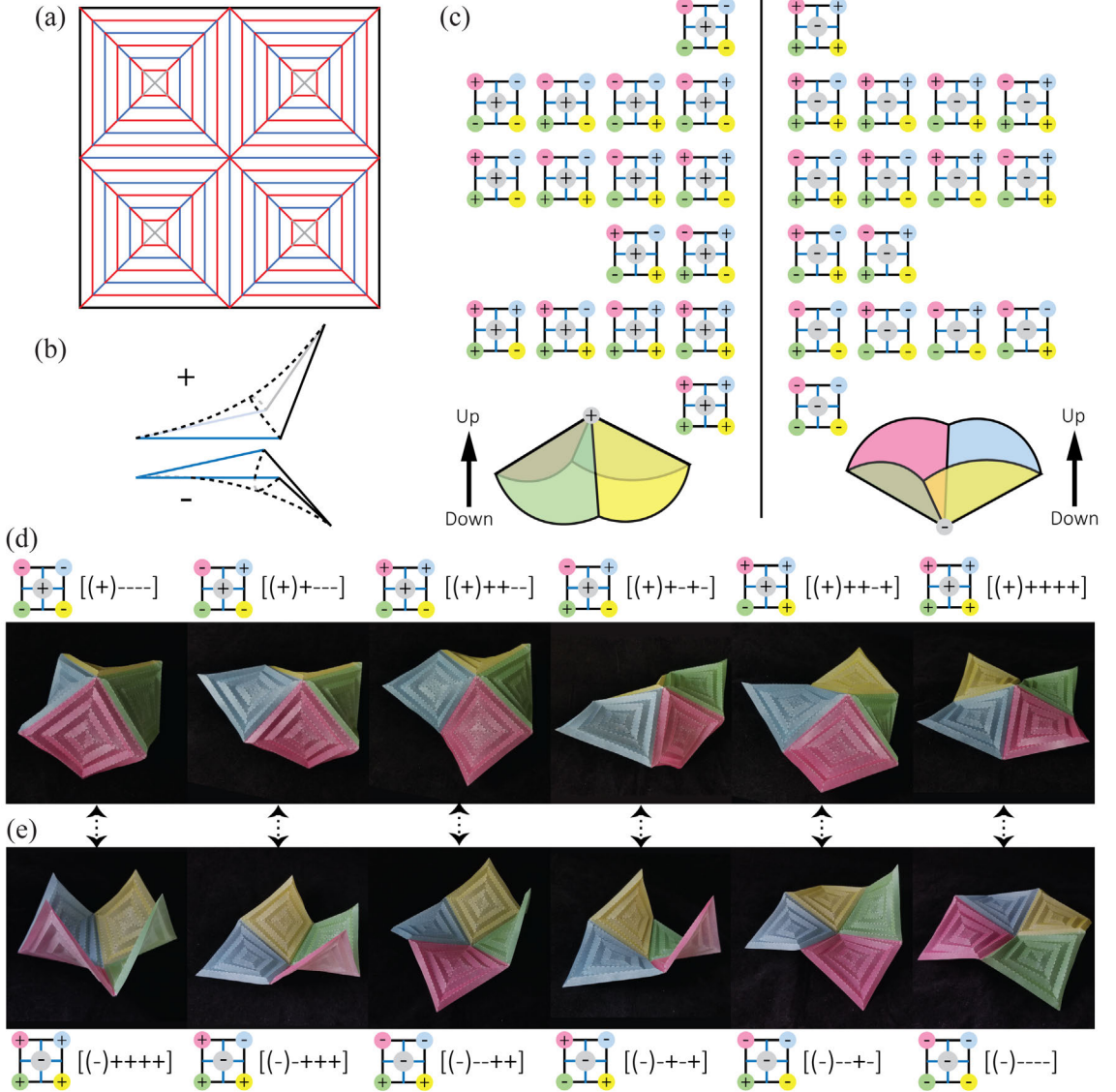


Figure 3.11: Multi-stable hyper origami tessellation built from a 2×2 array of hyper origami unit. (a) The crease pattern on a single piece of sheet. (b) The convention of (+) and (-) states for each hyper origami unit. The blue edges are shared edges between adjacent units. (c) Complete chart of the 32 stable states. On the left side, there are 16 states when the middle vertex is in a pop-up state. On the right, the middle vertex is in a pop-down state. On either side, each row lists configurations that are identical to each other after rotations. (d) The 6 unique stable states up to rotational symmetry when the middle vertex is in a pop-up state. (e) The 6 unique stable states up to rotational symmetry when the middle vertex is in a pop-down state. The corresponding pairs of configurations in (d) and (e), as indicated by the double arrows, lead to the same global geometry if one is flipped over (upside down). We can encode each state by 5 symbols, as labeled in (d) and (e). The sign in the parenthesis indicates the state of the middle vertex, and the other four refer to the four hyper origami units. Since the hyper metamaterial is rotationally symmetric, the order of the last four signs does not affect the geometry. Accordingly, when all signs in a code become opposite, the global configuration is flipped over.

states, 12 of them are unique up to rotational symmetry, and 6 of them are distinct in terms of approximate global shape. This idea can lead to programmable metamaterials, which may have important applications in energy trapping [134], and micro electronic devices [41].

3.6 Concluding Remarks

Our study of non-rigid foldable hypar origami shows that folding concentrically pleated squares produces shapes that asymptotically approach smooth hyperbolic paraboloids. Such a global saddle shape is strongly constrained by geometry, and quite robust to some variations of the crease pattern (see Fig. 3.6). Implied by our study, a unique feature of the hypar origami is that throughout its folding process, the folded geometry is always a hyperbolic paraboloid, except for different shallowness, which can be very useful for optical applications [135]. Ruled by both geometry and mechanics, the local deformation of panels appear as a twisted shape with a dominant bending ridge that exhibit concentrated curvatures. We observe that the bistability of the hypar origami leads to an ultrafast snapping behavior. Our study proposes an analytical framework of homogenizing local folds to establish differential map of the global geometry, which can be used as a basis to investigate other corrugated origami shells, such as concentrically pleated patterns with polygonal outlines. Furthermore, we provide insight into the bistability of the non-rigid hypar pattern, with an example in its use as a bistable constituent in a multi-stable metamaterial. In fact, recent papers [136], [137] have pointed out an observable paradigm shift, away from avoiding instabilities to harnessing instabilities, which could be explored with the hypar origami. In summary, we offer an example of bistability and snapping behavior that emerge inherently from the geometry of folding.

CHAPTER 4

BIG INFLUENCE OF SMALL IMPERFECTIONS IN ORIGAMI ASSEMBLAGES

Imperfection plays a profound role in shaping the behavior of materials, including metamaterials with exotic properties. Origami demonstrates great theoretical potential for creating such materials. However, most studies so far have focused on origami metamaterials with ideal patterns, possessing perfect symmetry and periodicity. In practice, geometric imperfections - resulting from either fabrication errors or distortion during service - break symmetry and/or periodicity of the origami metamaterials, and thus may alter their expected behavior. Therefore, to bridge theory and practice, a better understanding of how imperfections affect the mechanical behavior of origami metamaterials is crucial. This paper investigates the influence of geometric imperfections on the nonlinear compressive response of the representative Miura-ori pattern, which serves as the fundamental building block for many metamaterial designs. Interestingly, geometric imperfections increase the materials compressive stiffness and strength. Moreover, it is intriguing that, the residual of an origami design constraint, given by the famous Kawasaki theorem, strongly correlates with the stiffness and strength of imperfect origami metamaterials.

4.1 Introduction

Mechanical metamaterials exhibit exotic behaviors that are unusual for conventional materials [138]–[141]. Their exclusive properties and functionalities arise from carefully architected microscopic structures, for which origami is a rich source of inspiration [5]–[7], [20], [30], [35]–[37], [42], [43], [70], [142], [143]. Origami-inspired metamaterial designs are able to produce negative Poissons ratio [5], [6], [30], [35], [70], programmable thermal expansion [36], and tunable chirality [143]. However, there is still a gap between theory and practice. A fundamental question that is not yet well understood, is how robust the

predicted behavior of these geometric systems are, and how they may change properties when there are imperfections in the system, which are inevitable in reality, as illustrated in Fig. 4.1. Recently, the “pop-through defect” in Miura-ori, which causes large change of geometry, was shown to significantly affect the stiffness of Miura-folded sheets, towards either stiffening or softening [37]. In this research, we study the influence of small geometric imperfections on mechanical properties of the Miura-ori pattern, which, together with its variants, is perhaps the most adopted pattern for origami-based metamaterial designs [5], [6], [20], [30], [35]–[37], [42], [43], [70], [142], [143].

To motivate our study, let us fold three Miura-ori with different degrees of misalignment in the crease patterns. Since the perturbations are small, the three origami structures do not show any obvious difference initially. However, if we align them and apply a constant pressure, their responses deviate significantly, as shown in Fig. 4.1(a). Typically, small geometric imperfections in lattice and thin-walled cellular materials reduce the materials stiffness and strength [138], [144]–[147]. As opposed to the common behavior of other mechanical metamaterials, we see that small geometric imperfections seem to increase the stiffness of Miura folded sheets.

4.2 Theoretical consideration on the impact of geometric imperfections

Several origami patterns have been used in engineering applications [41], [148] - among them the Miura-ori has been most adopted, and thus it is emphasized in this work. A standard Miura pattern is composed of identical parallelogram panels, defined by side lengths a , b , and vertex angle α , as shown in Fig. 4.2(a). Such a pattern admits a single degree-of-freedom (DOF) rigid folding mechanism, which can be parametrized by the folding angle β (or θ). The two dihedral angles β and θ are related by $\sin^2(\beta/2) = \sin^2(\theta/2)[\cos^2 \alpha + \sin^2 \alpha \sin^2(\beta/2)]$ [6], [35]. Ideally, when subject to compression, a Miura-ori structure should deform only at the folding creases, which is known as rigid origami behavior. If we assign rotational stiffness k_0^F to the folding creases, the reaction

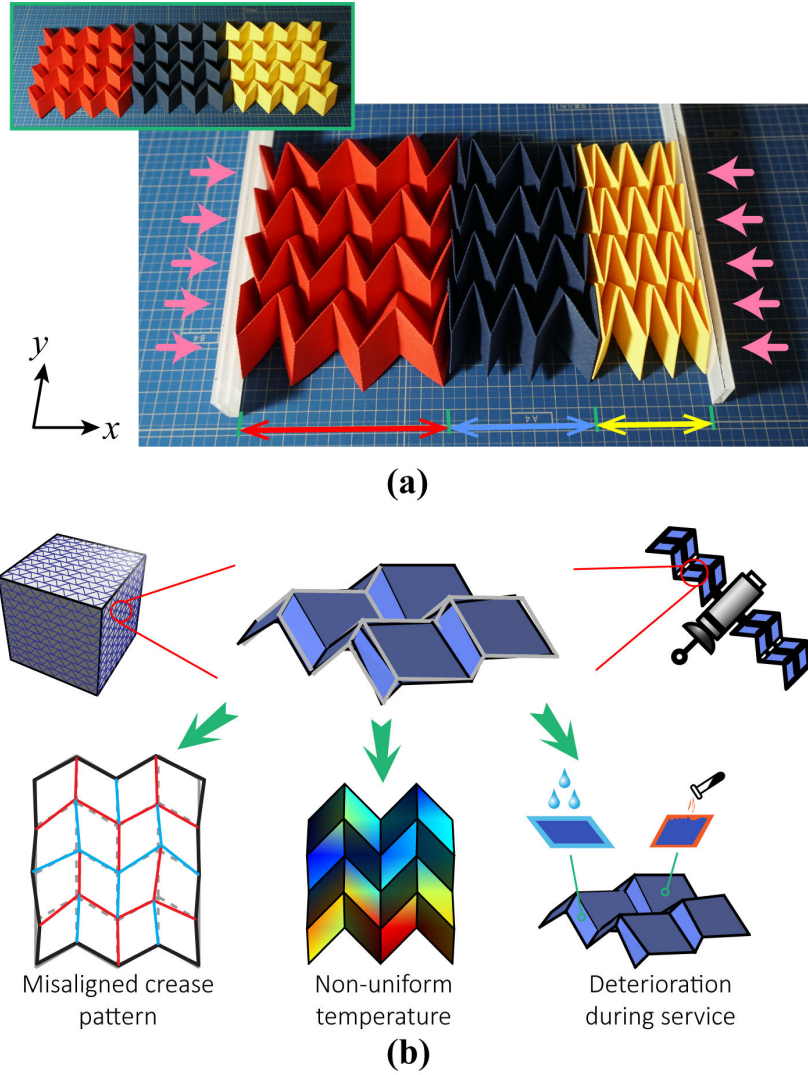


Figure 4.1: Presence and effect of geometric imperfections in origami-based systems. (a) Three origami sheets under the same pressure. We fold the yellow one with the standard Miura pattern, the blue one with a slightly perturbed pattern by randomly perturbing nodal positions, and the red one with a more perturbed pattern. The inset on the upright corner shows the initial configurations. (b) Geometric imperfections can be induced to an origami assemblage by various sources, such as misaligned crease pattern, non-uniform temperature, or swelling/corrosion during service. The gray lines show the ideal design.

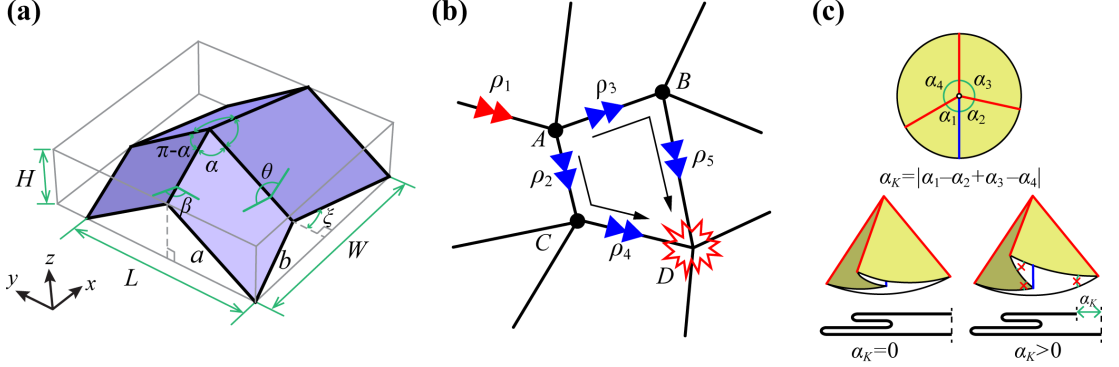


Figure 4.2: Geometry of standard Miura-ori and general degree-4 vertex. (a) Schematic of the Miura-ori unit cell. (b) A 2×2 array of degree-4 origami vertices is not generically rigid foldable. As each vertex possesses single DOF, if we fold ρ_1 of vertex A as input, the rotation transmits along two paths simultaneously: $\rho_1 \rightarrow \rho_3 \rightarrow \rho_5$, and $\rho_1 \rightarrow \rho_2 \rightarrow \rho_4$. If the system is rigid foldable, at vertex D, ρ_4 and ρ_5 must be compatible according to a single DOF. (c) For a generic degree-4 vertex, if the Kawasaki condition is not satisfied (i.e. $\alpha_K > 0$), early contact between two panels prevents the whole origami to be flattened, and some dihedral angles (marked by red crosses) cannot reach zero kinematically.

force (along W -direction) of a Miura-ori unit cell is derived as [35]:

$$f_x = 2k_0^F \frac{a(\theta - \theta_0) \cos^2(\xi/2) + b(\beta - \beta_0) \cos \alpha}{b \cos^2(\xi/2) \sin \alpha \cos(\theta/2)} \quad (4.1)$$

where $\xi = 2 \sin^{-1}[\sin \alpha \sin(\theta/2)]$, and β_0 and θ_0 define the initial configuration.

Rigid foldability and flat foldability are geometric properties that may directly impact the mechanical properties of an origami structure. A rigid foldable origami transforms by deforming only the folding creases and leaving the panels undeformed [149], [150]. On the other hand, flat foldability describes whether an origami can be completely folded such that all panels can lay on the same plane if ignoring their thickness.

An ideal Miura-ori satisfies both rigid foldability and flat foldability. The linearized first-order rigid foldability is determined by the singularity of a folding compatibility matrix \mathbf{J} [20], [64]. The kernel of the column space of \mathbf{J} contains the rigid folding mechanisms, while the kernel of its row space are states of self-stress [125], [151]. The difference between the number of rows and columns of \mathbf{J} gives the generic DOF (topologically pro-

tected [151]) for a two-dimensional $M \times N$ array of degree-4 unit cells, counted as:

$$\text{GDOF} = 4(M + N) - 4MN - 3. \quad (4.2)$$

When both M and N are greater than 1, GDOF becomes a negative value, thus the singularity of \mathbf{J} relies on the geometry of the system. Consequently, an origami assemblage with more than a 2×2 array of degree-4 vertices are not inherently rigid foldable [20], [150] (cf. Fig. 4.2(b)). Origami patterns that are rigidly foldable but not flat foldable would lock themselves kinematically during a folding process due to contact of panels [34], [142]. Locally, for a single vertex, the Kawasaki theorem gives the necessary and sufficient condition for flat foldability [149], [152]. For a degree-4 vertex, if we define the Kawasaki excess [152] as $\alpha_K = |\alpha_1 - \alpha_2 + \alpha_3 - \alpha_4|$ (see Fig. 4.2(c)), the Kawasaki theorem states that flat foldability is equivalent to $\alpha_K = 0$. For a multi-vertex assemblage, we can assemble the vertex-wise α_K into a vector $\boldsymbol{\alpha}_K$. We can define the Kawasaki excess of an multi-vertex assemblage as the $L2$ -norm of the Kawasaki excess vector $\|\boldsymbol{\alpha}_K\|$. It is sufficient that when $\|\boldsymbol{\alpha}_K\|$ becomes nonzero, the assemblage loses global flat foldability. The presence of random geometric imperfections most likely eliminates both rigid and flat foldability.

4.2.1 First-order rigid foldability

This section briefly reviews the derivation of the folding compatibility matrix \mathbf{J} . At a single origami vertex, let $\mathbf{p}_i = [p_i^x, p_i^y, p_i^z]$ be the space direction of crease i , and ρ_i be the associated relative rotation between two adjacent panels along the axis of \mathbf{p}_i (see Fig. 4.3). If there are n creases connected to one vertex, there is a loop condition requires that [63], [115], [153]

$$\mathbf{O} := \mathbf{R}(\mathbf{p}_1, \rho_1) \mathbf{R}(\mathbf{p}_2, \rho_2) \dots \mathbf{R}(\mathbf{p}_{n-1}, \rho_{n-1}) \mathbf{R}(\mathbf{p}_n, \rho_n) = \mathbf{I}, \quad (4.3)$$

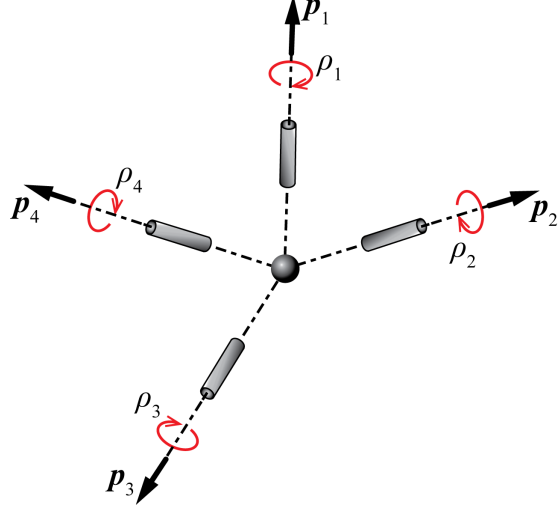


Figure 4.3: An illustration of a degree-4 origami vertex. The vectors \mathbf{p}_1 to \mathbf{p}_4 indicate the spatial directions of the four creases.

where $\mathbf{R}(\mathbf{p}_i, \rho_i)$ is a rotation matrix depending on \mathbf{p}_i and ρ_i of size 3×3 . Using Rodrigues' rotational formula, $\mathbf{R}(\mathbf{p}_i, \rho_i)$ is defined as:

$$\mathbf{R}(\mathbf{p}_i, \rho_i) = \mathbf{I} + \sin \rho_i [\mathbf{p}_i]_{\times} + (1 - \cos \rho_i) [\mathbf{p}_i]_{\times}^2, \quad (4.4)$$

where,

$$[\mathbf{p}_i]_{\times} := \begin{bmatrix} 0 & -p_i^z & p_i^y \\ p_i^z & 0 & -p_i^x \\ -p_i^y & p_i^x & 0 \end{bmatrix}. \quad (4.5)$$

A continuously varying assignment of \mathbf{p}_i and ρ_i results in a rigid foldable origami vertex.

Linearizing Eq. (4.3) at $\mathbf{O} = \mathbf{I}$ (and hence $\boldsymbol{\rho} = \mathbf{0}$), we obtain [153]:

$$\mathbf{O} = \mathbf{I} + \sum_{i=1}^n \frac{\partial \mathbf{O}}{\partial \rho_i} \Big|_{\boldsymbol{\rho}=\mathbf{0}} \delta \rho_i + H.O.T. \quad (4.6)$$

It is derived in reference [153] that:

$$\frac{\partial \mathbf{O}}{\partial \rho_i} \Big|_{\boldsymbol{\rho}=\mathbf{0}} = [\mathbf{p}_i]_{\times}. \quad (4.7)$$

Therefore, the first-order foldability of a single vertex is obtained by setting the second term of Eq. (4.6) equal to zero:

$$\sum_{i=1}^n \frac{\partial \mathbf{O}}{\partial \rho_i} \Big|_{\boldsymbol{\rho}=0} \delta \rho_i = \sum_{i=1}^n \delta \rho_i [\mathbf{p}_i]_\times = \mathbf{0}_{3 \times 3}. \quad (4.8)$$

Since each $[\mathbf{p}_i]_\times$ has only three independent components, Eq. (4.8) is equivalent to [115], [153]:

$$\sum_{i=1}^n \delta \rho_i \mathbf{p}_i = \mathbf{0}_{3 \times 1}. \quad (4.9)$$

For a multi-vertex origami pattern, Eq. (4.9) need to be assembled over all vertices and holes [64], [115], which gives the linear system of equations $\mathbf{J}\delta\boldsymbol{\rho} = \mathbf{0}$, where \mathbf{J} contains information from \mathbf{p}_i 's.

4.3 Results and Discussion

In practice, owing to the compliance of materials, kinematically unfoldable imperfect origami assemblages can still be folded with panel bending and stretching [101]. The aforementioned motivational example clearly suggests that geometric imperfections affect the mechanical behavior of Miura folded sheets. As the functionality of origami-based structures and metamaterials mainly arise from large folding deformations, here we emphasize the nonlinear response of imperfect Miura folded sheet under compressive folding.

4.3.1 Experimental Quantification

To quantitatively examine the mechanical consequences of geometric imperfections, we manufacture 4×4 Miura folded sheets with different degrees of imperfection for mechanical test. The imperfections are induced to the planar crease pattern by random in-plane nodal perturbations. At each node, the perturbations along x - and y -direction are sampled independently from a Gaussian distribution $N(0, \chi)$, with zero mean and standard deviation χ . Four representative χ 's are used to prepare four groups of perturbed patterns:

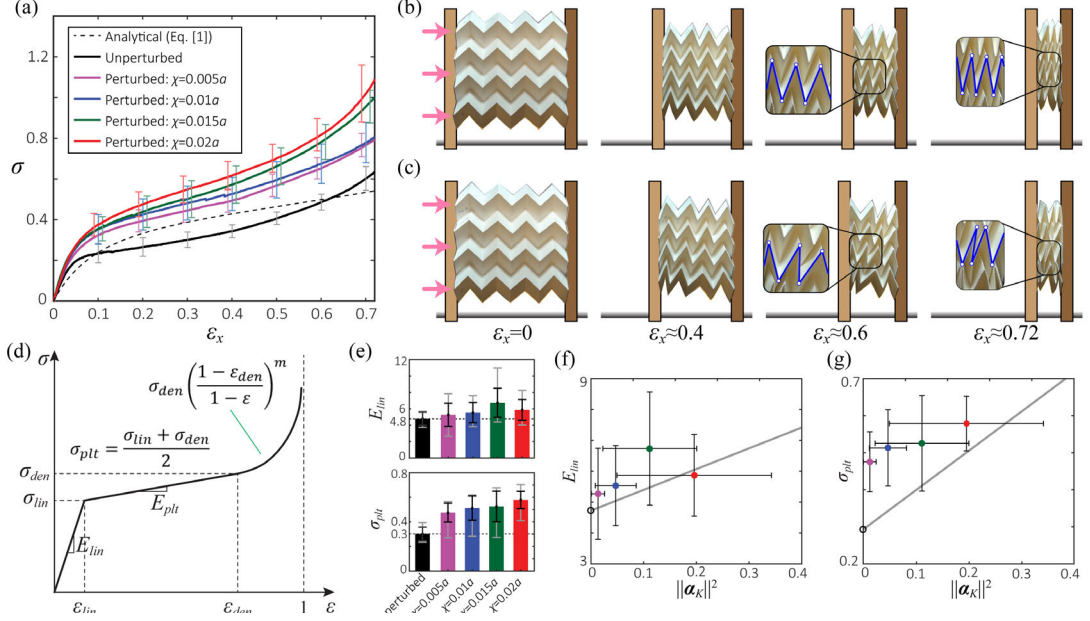


Figure 4.4: Experimental quantification of the effect of geometric imperfections. (a) Bulk stress σ vs. compressive strain ε_x . Each solid line shows the response of a group of samples. The error bars extend to one standard deviation of the measured σ data. The dashed line is the response of ideal Miura-ori according to Eq. (4.1), where k_0^F is obtained by mechanical test on single creases. (b) Snapshots of an unperturbed sample. Each blue polyline outlines a row of lattice lines. (c) Snapshots from experiment of a perturbed sample with $\chi = 0.02a$ under increasing compressive strain. (d) Illustration of the 5-parameter model. The 5 independent parameters ($\varepsilon_{lin}, \sigma_{lin}, \varepsilon_{den}, \sigma_{den}, m$) are fitted by the least squares approach. (e) Fitted E_{lin} and σ_{plt} for different sample groups. The black error bars show standard deviations, and the gray error bars indicate extrema of data. The dashed lines refer to measurements of the reference group. (f)-(g) Mechanical properties (E_{lin}, σ_{plt}) vs. $\|\alpha_K\|^2$. The black circles refer to the mean of the reference group measurements. The error bars extend to one standard deviation. The gray lines are linear regression with enforced intercept at $\|\alpha_K\|^2 = 0$. The σ, E_{lin} and σ_{plt} are in units of KPa.

$$\chi = 0.005a, \chi = 0.01a, \chi = 0.015a, \text{ and } \chi = 0.02a.$$

The samples are compressed uniaxially along the x -direction (see Fig. 4.2(a)). The performance of the samples is recorded by the compressive strain ($\varepsilon_x = \Delta W/W_0$) and bulk stress ($\sigma = F/H_0 L_0$), where F is the measured force, and H_0, L_0 , and W_0 are dimensions of the initial configuration. As shown in Fig. 4.4, all samples behave almost linearly up to a small strain ($\sim 5\%$). The structures continue to deform at a slowly increasing stress for a large range of deformation, until the stress rises with increasing slope. This behavior is similar to the Ashby-Gibson model for general cellular materials [154], but the plateau

stage of the Miura-ori samples display a linear slope. Hence, we propose a 5-parameter phenomenological model (see Fig. 4.4(d)), to summarize the experimental data into simple parameters for ease of comparison. We focus on the fitted Young's modulus E_{lin} and the average plateau stress σ_{plt} as two representative measurements that may be interpreted as “stiffness” and “strength.” The reference group of unperturbed samples reports mean of $E_{lin} = 4.8\text{KPa}$ and $\sigma_{plt} = 0.3\text{KPa}$. As χ increases from 0.005a to 0.02a, the samples become stiffer and stronger with mean of E_{lin} increasing up to 39% and mean of σ_{plt} increasing up to 95%.

Besides the difference of global response between the perturbed and the unperturbed samples, significant difference is spotted at the local level. The unit cells of the unperturbed pattern uniformly deform with lattice lines remaining relative ordered and periodic, as shown in Fig. 4.4(b). The perturbed samples, however, display heterogeneous deformation among unit cells, with severely distorted lattice lines, as shown in Fig. 4.4(c), especially under higher compressive strains.

Our experiments reveal that geometric imperfections positively correlate to the stiffness (E_{lin}) and strength (σ_{plt}) of Miura-folded sheets. However, the variability of mechanical performance present in the experimental data not only comes from geometric variability, but also material-associated variability, which distracts our focus on geometric imperfections. The main source of material-associated variability comes from the constitutive behavior of folding hinges, indicated by mechanical test on single crease behavior (see Section 4.5.4). This influence is noticeable with the unperturbed samples. Despite the small geometric error induced during the perforation process, the crease pattern of the unperturbed samples are identical. However, the constitutive relations show relatively large variation at the beginning of loading process, and the variation reduces as ε_x becomes large (see Fig. 4.4(a)). This trend is different from the perturbed samples for which the variation becomes larger and larger during the loading process due to random geometric imperfections. Therefore, it appears that the material-associated variability is most significant under

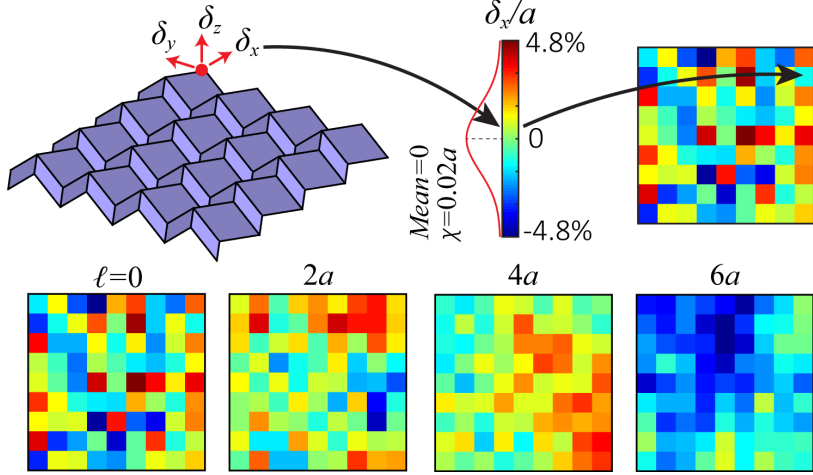


Figure 4.5: Modeling of random geometric imperfections by random fields of nodal perturbations. At each node, the perturbation is decomposed into x -, y -, and z - directions (denoted as δ_x , δ_y , and δ_z), as we assume no directional preference of the geometric imperfections. The four colored maps demonstrate how ℓ affects spatial correlation between nodal perturbations.

small deformation. This uncertainty may explain why the mean of E_{lin} of the perturbed samples with $\chi = 0.015a$ is larger than the mean of samples with $\chi = 0.02a$.

4.3.2 Numerical Quantification

To focus on the effect of geometric imperfections and exclude material-associated variability, we perform numerical analysis with the elastic bar-and-hinge reduced order models. The bar-and-hinge model represents the behavior of an origami structure by triangulated bar frame with constrained rotational hinges, capturing three essential deformation modes of origami structures: in-plane stretching, folding, and panel bending (see Fig. 4.5(b)). With only a few degrees of freedom, the bar-and-hinge model predicts surprisingly well the overall mechanical behavior of origami structures [5]–[7], [101]. Therefore, owing to its generality and computational efficiency, we use the bar-and-hinge model for our nonlinear numerical analysis.

The numerical simulations are performed using the MERLIN software [101], using formulation explained in Chapter 2. We apply displacement load to compress the Miura-ori

models. The sample size of each group with a certain combination of χ and ℓ is adaptively determined to allow the estimated mean of σ_{lin} 's to have 95% confidence within $\pm 10\%$ error. We generated 12400 perturbed samples and obtained 11219 converged results. The constitutive model for bars following the Ogden model, with areas assigned using the tributary area strategy, as described in Section 2.2.6 and 2.3.1. The constitutive model for bending and folding follows the enhanced linear model as described in Section 2.2.7. In this work, we assume that $\theta_1 = \pi/4$ and $\theta_2 = 7\pi/4$. The bending and folding hinges are distinguished by different values of the linear stiffness k_0 . In the numerical simulations, we assign k_0^B to the bending hinges, which is calculated based on the prescribed ratio of $k_0^B/k_{0,paper}^B$, where $k_{0,paper}$ is measured from experiments of paper-made samples, elaborated in Section 4.5.4. The linear folding stiffness k_0^F is calculated based on prescribed ratios of k_0^B/k_0^F .

With numerical models, we can assign constant material properties and control precisely the distribution of imperfections. Without the process of folding, we configure the numerical models directly in 3D, in order to reproduce the general presence of imperfections, with examples shown in Fig. 4.1(b). Some types of imperfections, such as distortion induced by non-uniform thermal effect, may display strong spatial correlation. We use spatially correlated random fields [155] to generate the nodal perturbations. The random perturbations follow zero-mean Gaussian fields with the exponential covariance function [156] characterized by standard deviation χ and correlation length ℓ :

$$C(\mathbf{X}_i, \mathbf{X}_j) = \chi^2 \exp\left(-\frac{\|\mathbf{X}_j - \mathbf{X}_i\|}{\ell}\right), \quad (4.10)$$

where $\|\mathbf{X}_j - \mathbf{X}_i\|$ is the Euclidean distance between two nodes i and j . Larger ℓ indicates stronger spatial correlation between random nodal perturbations, as demonstrated in Fig. 4.5(a). In particular, for the experimental samples, the imposed perturbations follow random fields with $\ell = 0$. Therefore, the numerical analyses are used to generalize our study,

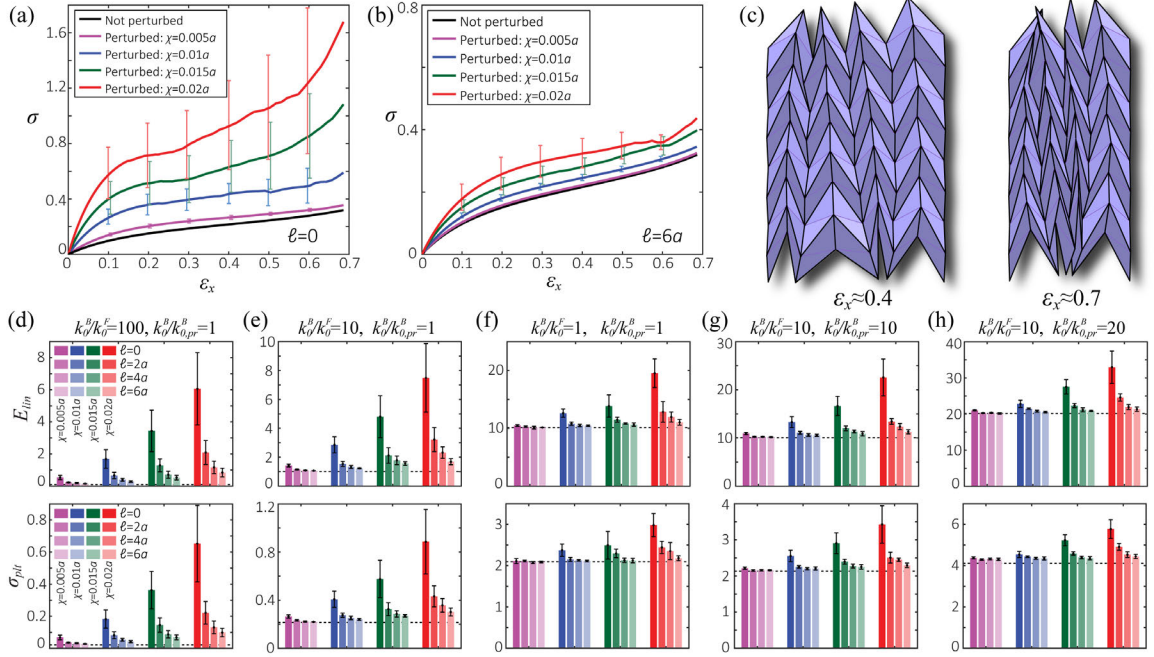


Figure 4.6: Numerical quantification of the effect of geometric imperfections. Bulk stress σ vs. compressive strain ε_x plots for samples with (a) $\ell = 0$, and (b) $\ell = 6a$. Each solid line shows the mean response of a group of samples and the error bars extend to one standard deviation. (c) Snapshots from numerical simulation of a perturbed sample with $\chi = 0.02a$ and $\ell = 0$. (d)-(h) Fitted E_{lin} (first row) and σ_{plt} (second row) of different groups for different material-associated parameters. The black error bars show standard deviations. The dash lines refer to measurements of the unperturbed Miura folded sheet. The ratio of k_0^B/k_0^F reflects the relative stiffness between bending and folding deformations. As the stretching stiffness remain unchanged, the ratio of $k_0^B/k_{0,pr}^B$ characterizes the relative stiffness between out-of-plane and in-plane deformations, where the reference bending stiffness $k_{0,pr}^B$ is collected from experimental test. For all cases shown in this figure, $\alpha = 60^\circ$ and $\beta_0 = 70^\circ$. The σ , E_{lin} and σ_{plt} are in units of KPa.

and they are not designed to reproduce the experimental data.

A uniform displacement load is applied to compress the partially folded numerical samples, mimicking the experiments. We prepare in total 16 groups of perturbed samples with 4 different χ 's and 4 different ℓ 's. As shown in Fig. 4.6(a), the strain-stress curves of the numerical models display very similar trend as the physical samples. The deformation of perturbed numerical samples also display obvious local disorder, as shown in Fig. 4.6(c). In Fig. 4.6(d)-(h), we look into the influence of material-associated properties on the effect of imperfections, by comparing E_{lin} and σ_{plt} . We see that sample groups with relatively

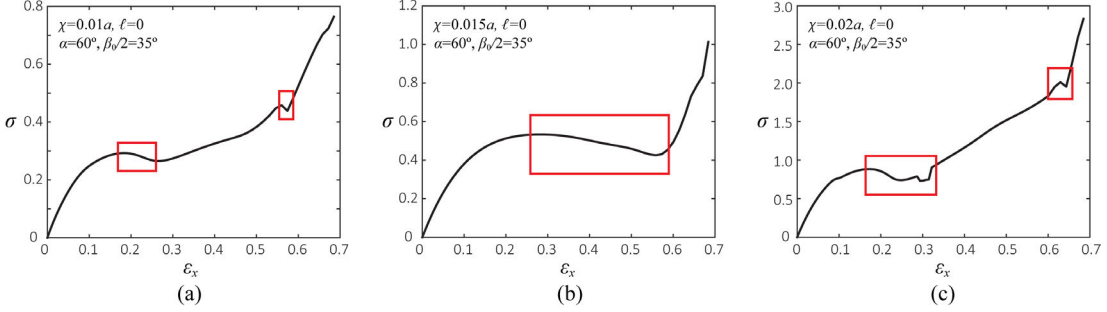


Figure 4.7: Examples of unstable strain softening of some perturbed Miura-ori structures, highlighted by red boxes. For perturbed samples with small χ or large ℓ , this phenomenon is rarely seen. Thus, we believe that instability is caused by relatively large random geometric imperfections. From ((a)) to (c), we raise the level of geometric imperfection by increasing χ . The samples are all taken from the group of data with $k_0^B/k_0^F = 10$, and $k_0^B/k_{0,pr}^B = 1$. The bulk stress σ is in unit of KPa .

larger mean of E_{lin} also possess relatively larger σ_{plt} . Relatively large degree of imperfections may lead to instability, as we observe strain softening from the σ - ε_x curves of some samples as shown in Fig. 4.7. In addition, we found no significant change of bulk in-plane Poisson's ratio due to imperfections.

4.4 Correlation with Geometric Design Constraints

The spatial correlation between nodal perturbations notably mitigates the effect of imperfections (see Fig. 4.6), indicating that what alters the response are indeed the relative imperfections between nodes. Therefore, we seek for simple measures that could reflect relative imperfections. We first compare how the mechanical properties varies with respect to relative imperfection measured as (ℓ/χ) , as shown in Fig. 4.8. However, this measure of relative imperfection leads to ambiguity when $\ell = 0$, as we can see there are multiple points on the line of $\ell = 0$. Therefore, a better measure need to be defined.

The Kawasaki excess (i.e. $\|\alpha_K\|$) and the smallest singular value of \mathbf{J} (i.e. $s(\mathbf{J})$) become suitable candidates. For small imperfections as investigated in this research, $s(\mathbf{J})$ and $\|\alpha_K\|$ are found linearly correlated to each other (see Fig. 4.9(a)), and thus we may focus only on the Kawasaki excess. As shown in Fig. 4.9(b), the norm of Kawasaki excess

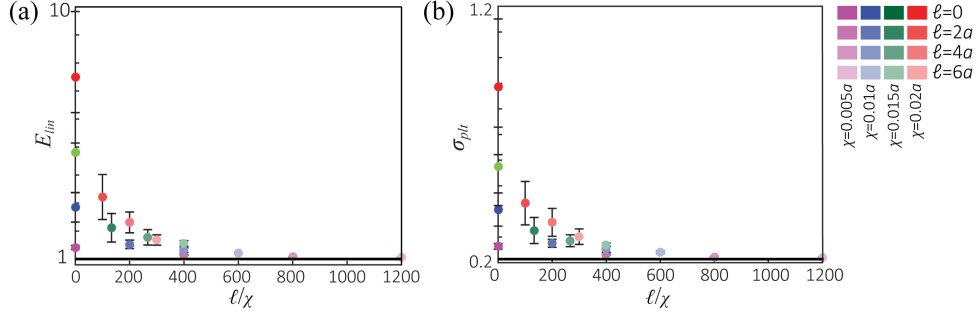


Figure 4.8: Mechanical properties vs. relative imperfection measured as (ℓ/χ) . Each solid dot shows the mean response of a group of samples and the error bars extend to one standard deviation. The black solid line refers to the obtained values from the unperturbed structure. All samples in this figure have $\alpha = 60^\circ$, $\beta_0/2 = 35^\circ$, $k_0^B/k_0^F = 10$ and $k_0^B/k_{0,pr}^B = 1$. The E_{lin} and σ_{plt} are in units of KPa.

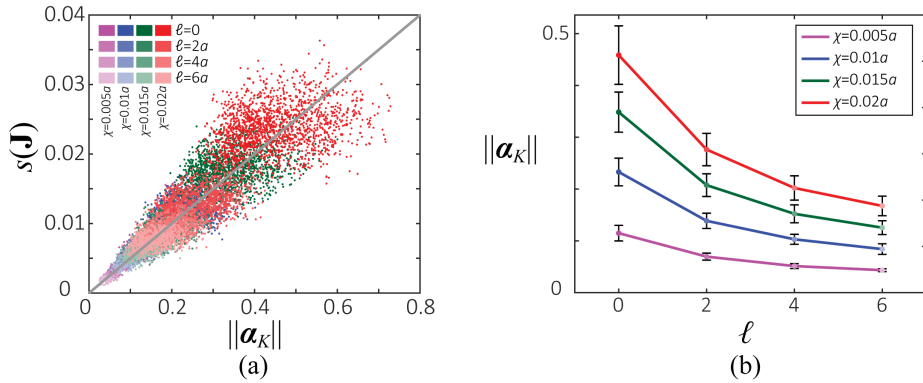


Figure 4.9: Statistics of geometric features. (a) Change of Kawasaki excess ($\|\boldsymbol{\alpha}_K\|$) as χ and ℓ vary, for all samples with $\alpha = 60^\circ$ and $\beta_0/2 = 35^\circ$. The error bars extend to one standard deviation. (c) Linear correlation between $s(\mathbf{J})$ and $\|\boldsymbol{\alpha}_K\|$. Data is obtained from all 11219 numerical simulations.

vector increases as the standard deviation χ of perturbations increases, and decreases as the correlation length ℓ increases, which shows similar trend as the mechanical properties E_{lin} and σ_{plt} . Indeed, we find that both E_{lin} and σ_{plt} are correlated linearly with $\|\boldsymbol{\alpha}_K\|^2$. A hypothetical explanation is provided in Section 4.4.1.

We plot the expected values of E_{lin} and σ_{plt} with respect to $\|\boldsymbol{\alpha}_K\|^2$ in Fig. 4.10 for different combinations of material-associated properties and geometric features. Each slope in Fig. 4.10 implies the sensitivity of the mechanical property of a certain group of samples with respect to $\|\boldsymbol{\alpha}_K\|^2$. We observe that geometric features impose a much stronger influence on the slopes than material-associated properties. In addition, as expected, the relative

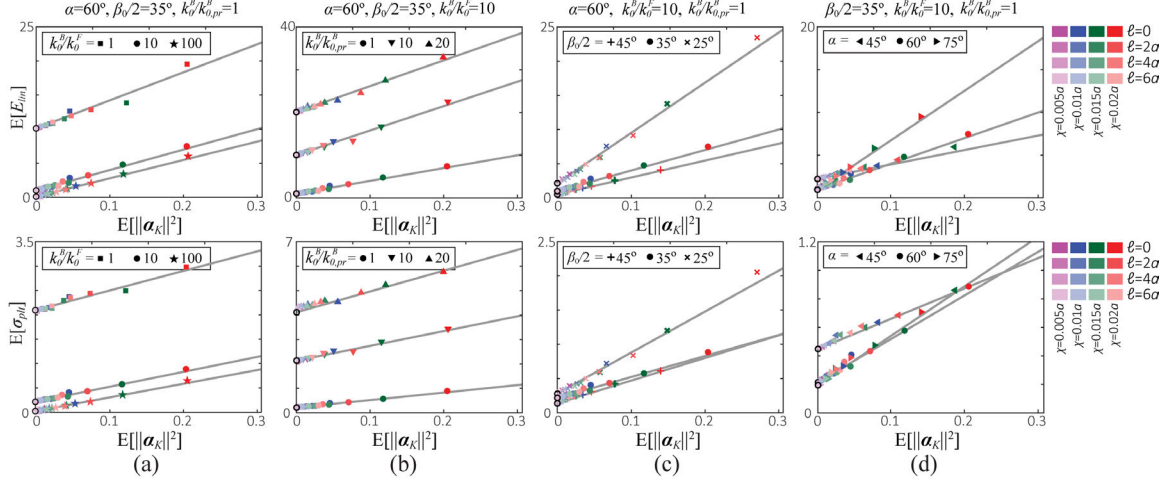


Figure 4.10: Mechanical properties vs. the Kawasaki excess. The first row for $E[E_{lin}]$ vs. $E[\|\boldsymbol{\alpha}_K\|^2]$, and the second row for $E[\sigma_{plt}]$ vs. $E[\|\boldsymbol{\alpha}_K\|^2]$, where $E[\cdot]$ means the mean (or expected) value. ((a)) demonstrates influence of k_0^B/k_0^F . (b) demonstrates influence of $k_0^B/k_{0,pr}^B$ (equivalent to k_0^B/K_S). In (c), we vary the initial amount of folding (β_0). In (d) we vary the original panel angle α . The coordinate of each dot is determined by the mean (expected) values of E_{lin} (or σ_{plt}) and $\|\boldsymbol{\alpha}_K\|^2$ for a group of samples. The black circles with $\|\boldsymbol{\alpha}_K\|^2 = 0$ refer to the mean of the reference group measurements. The gray lines are linear regressions with enforced intercept at $E[\|\boldsymbol{\alpha}_K\|^2] = 0$. The E_{lin} and σ_{plt} are in units of KPa .

significance of sensitivities are consistent for both E_{lin} and σ_{plt} . For example, in the two plots of Fig. 4.10(d), the samples with $\alpha = 75^\circ$ are most sensitive, and the samples with $\alpha = 45^\circ$ are least sensitive to $\|\boldsymbol{\alpha}_K\|^2$, for both E_{lin} and σ_{plt} . For the experimental samples, E_{lin} and σ_{plt} also exhibit approximately linear correlation with $\|\boldsymbol{\alpha}_K\|^2$, as shown in Fig. 4.4(f)-(g), with discrepancy that is likely owing to material-associated variabilities.

4.4.1 Hypothesis for the correlation between Kawasaki excess and mechanical properties

To make sense of the linear correlation between E_{lin} (or σ_{plt}) and $\boldsymbol{\alpha}_K$, we consider the following deformation procedure to achieve a certain amount of compressive folding (see Fig. 4.11(a)-(d)): (i) enforce the geometry of the distorted panels to the standard panel shapes by in-plane deformation; (ii) compress the origami structure by pure folding; (iii) release the in-plane strains and allow the structure to find new equilibrium between folding, bending and stretching. In step (ii), the structure deforms following the same kinematics

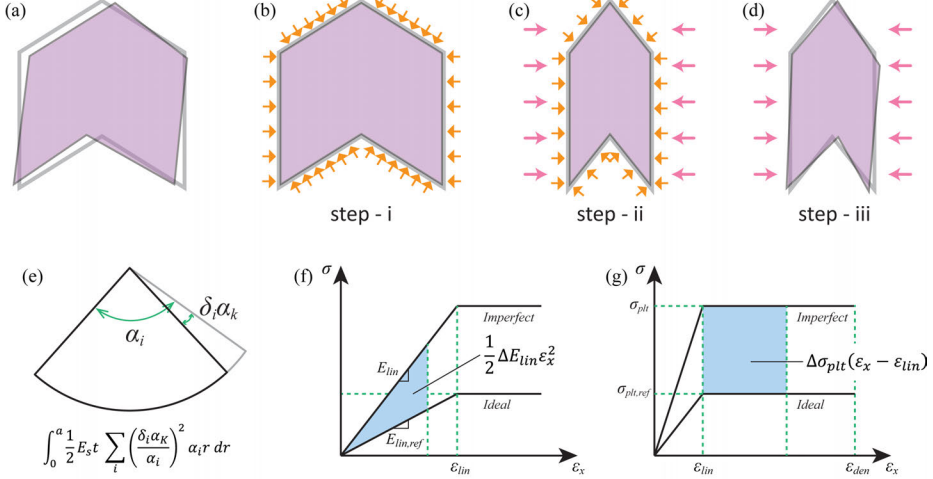


Figure 4.11: Schematic of the hypothetical deformation process of imperfect origami. (a) The purple pattern indicates the imperfect geometry, and the gray lines indicate the ideal geometry. (b)-(d) Step (i) to (iii). The orange arrows imply the enforced deformation field, which confines the imperfect geometry to the ideal geometry. The pink arrows imply applied forces/displacements on the entire pattern. (e) An imperfect single vertex with angular deficit $\delta_i \alpha_K$. (f) Additional strain energy (density) induced by imperfection when $\varepsilon_x \leq \varepsilon_{lin}$. (g) Additional strain energy induced by imperfection when $\varepsilon_{lin} < \varepsilon_x \leq \varepsilon_{den}$.

as an ideal origami system, thus the extra strain energy in the system after this step comes from the deformation in step (i). In step (iii), finding the new balance leads to a lower or equal energy state. Considering continuum panels with small imperfection, we may approximate the extra strain energy compared to the ideal pattern around a vertex k as,

$$\Delta U_k \approx \eta_k \int_0^a \frac{1}{2} E_{st} t \sum_i \left(\frac{(\delta_i \alpha_K)^2 r}{\alpha_i} \right) dr, \quad (4.11)$$

where t is the thickness of panels, and $(\delta_i \alpha_K)$ is the angular excess or deficit of each panel angle i around vertex k (see Fig. 4.11(e)). The adjustment factor η_k is a factor depending on both material and geometric properties of the system, such as K_B/K_S , K_B/K_F , and folding angles between panels, etc. In Eq. (4.11), α_K , δ_i , and η_k are random variables. We may assume that δ_i and η_k are independent from α_K . Taking expectation ($E[\cdot]$) of both

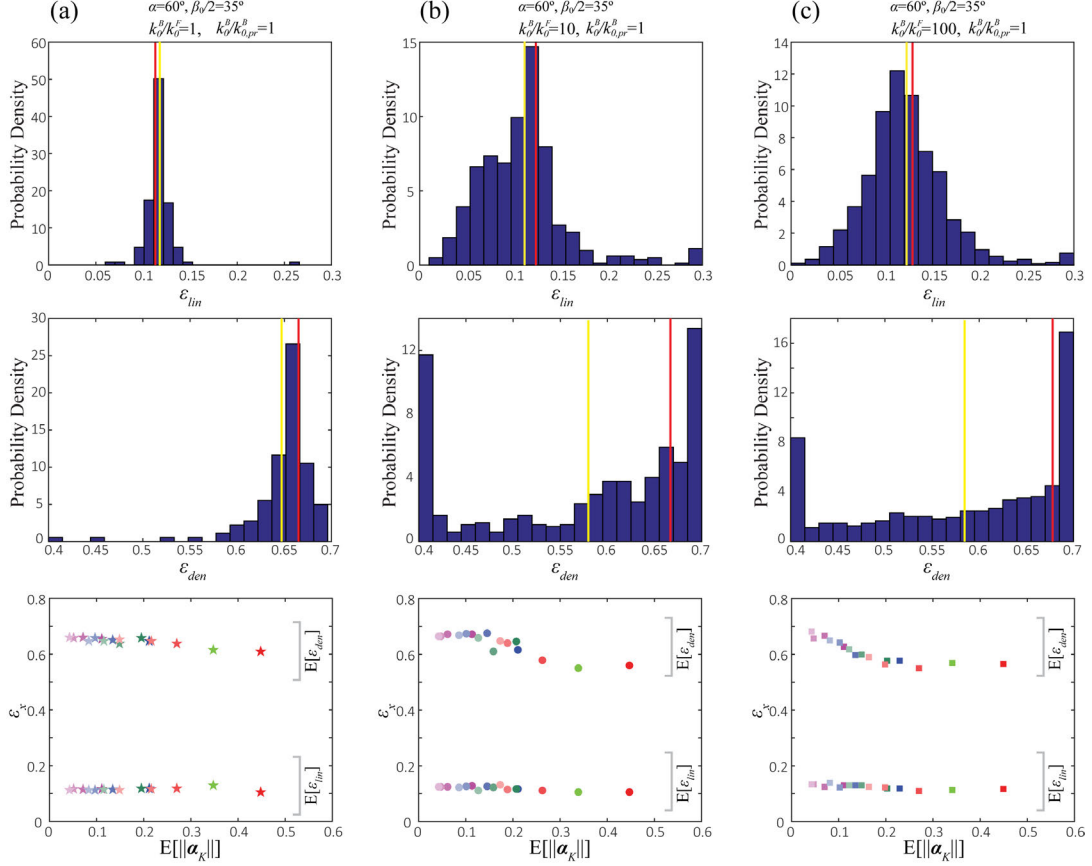


Figure 4.12: Statistics about the key frames of strain (i.e. ε_{lin} and ε_{den}). (a)-(c) The first row is the probability density (i.e. normalized histogram) of ε_{lin} for a group of sample generated by the parameters shown on the top. The bound for ε_{lin} during curve fitting is [0,0.3]. The red vertical line refers to $\varepsilon_{lin,ref}$, while the yellow line refers to $E[\varepsilon_{lin}]$. The second row is the probability density of ε_{den} . The bound for ε_{den} during fitting is [0.4,0.7]. The red vertical line refers to $\varepsilon_{den,ref}$, while the yellow line refers to $E[\varepsilon_{den}]$. The bounds are used to slightly regulate the data. The third row plots $E[\varepsilon_{lin}]$ and $E[\varepsilon_{den}]$ vs. $E[||\alpha_K||]$.

sides of Eq. (4.11), we can obtain that:

$$E[\Delta U_k] \approx E[\alpha_K^2] E \left[\eta_k \int_0^a \frac{1}{2} E_{st} \sum_i \left(\frac{\delta_i^2 r}{\alpha_i} \right) dr \right] \propto E[\alpha_K^2]. \quad (4.12)$$

The actual deformation of imperfect origami assemblages are more complex than the aforementioned three steps. Nevertheless, assuming elasticity, the simplified procedure helps to reveal the linear correlation between ΔU_k and α_K^2 . Since Eq. (4.12) applies to all

vertices within an origami assemblage, we can take a sum over a finite number of k , which leads to:

$$\sum_k E[\Delta U_k] = E \left[\sum_k \Delta U_k \right] \propto \sum_k E[\alpha_K^2] = E[\|\alpha_K\|^2], \quad (4.13)$$

where $\sum_k \Delta U_k$ is the global (total) strain energy difference.

Denoting $\Delta E_{lin} = E_{lin} - E_{lin,ref}$, for $\varepsilon_x \leq \varepsilon_{lin}$, on the global scale we obtain:

$$\frac{1}{2} E[\Delta E_{lin}] \varepsilon_x^2 \approx E \left[\frac{\sum_k \Delta U_k}{W_0 H_0 L_0} \right] = \frac{E[\sum_k \Delta U_k]}{W_0 H_0 L_0}, \quad (4.14)$$

where $W_0 H_0 L_0$ is the initial volume of the origami assemblage, and $E_{lin,ref}$ is obtained from the reference pattern without geometric imperfections (see Fig. 4.11(f)). Therefore, we may conclude that for a group of samples with the same geometric feature and material-associated properties, under random geometric imperfections, $E[\Delta E_{lin}] \propto E[\|\alpha_K\|^2]$. We actually observe that the mean value of ε_{lin} is always very close to the reference $\varepsilon_{lin,ref}$ of the ideal sample (i.e. $E[\varepsilon_{lin}] \approx \varepsilon_{lin,ref}$), as shown in Fig. 4.12(a), and ε_{lin} appears to be independent of $\|\alpha_K\|$.

Similarly, when $\varepsilon_{lin} < \varepsilon_x \leq \varepsilon_{den}$, we have:

$$E[\Delta \sigma_{plt}(\varepsilon_x - \varepsilon_{lin})] \approx E \left[\frac{\sum_k \Delta U_k}{W_0 H_0 L_0} - \frac{1}{2} \Delta E_{lin} \varepsilon_{lin}^2 \right] = \frac{E[\sum_k \Delta U_k]}{W_0 H_0 L_0} - \frac{1}{2} E[\Delta E_{lin} \varepsilon_{lin}^2]. \quad (4.15)$$

where $\Delta \sigma_{plt} = \sigma_{plt} - \sigma_{plt,ref}$ (see Fig. 4.11(g)). Based on observation, we may assume that ε_{lin} is independent of $\|\alpha_K\|$, ΔE_{lin} , and $\Delta \sigma_{plt}$. Now we can derive that:

$$\begin{aligned} E[\Delta \sigma_{plt}(\varepsilon_x - \varepsilon_{lin})] &= E[\Delta \sigma_{plt}](\varepsilon_x - E[\varepsilon_{lin}]) \approx E[\Delta \sigma_{plt}](\varepsilon_x - \varepsilon_{lin,ref}) \\ &= \frac{E[\sum_k \Delta U_k]}{W_0 H_0 L_0} - \frac{1}{2} E[\Delta E_{lin}] E[\varepsilon_{lin}^2], \end{aligned} \quad (4.16)$$

which suggests that $E[\Delta \sigma_{plt}] \propto E[\|\alpha_K\|^2]$. Notice that the the global strain energy difference $\sum_k \Delta U_k$ has different values in Eq. (4.14) and Eq. (4.15), because η_k 's depend

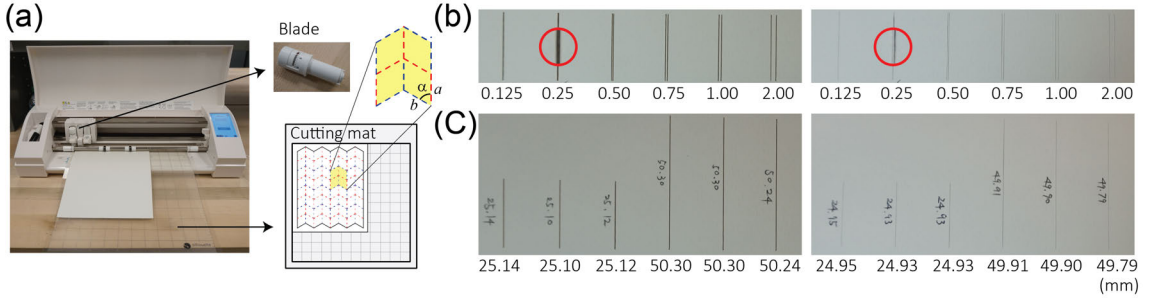


Figure 4.13: The Silhouette CAMEO electronic cutter. (a) The Silhouette CAMEO uses a cutting mat to hold the paper flat and use a small blade to make cuts. (b) Samples for resolution test. The left one is by the Universal laser systems PLS4.75, and the right one is by the Silhouette CAMEO. The insets marked by red circles show zoom-in view of the parallel cuts with 0.25mm space. (c) Samples for precision test. The left one is by the Universal laser systems PLS4.75, and the right one is by the Silhouette CAMEO. The measured lengths are indicated in the bottom.

on ε_x . For large compressive strain, and when $K_B/K_F \geq 10$, we observe that in general $E[\varepsilon_{den}] < \varepsilon_{den,ref}$ (see Fig. 4.12(b)), and appears to reduce as $\|\alpha_K\|$ increases (see Fig. 4.12(c)).

4.5 Materials and Methods

4.5.1 Sample fabrication

The crease patterns for the samples were generated by a MATLAB program. We use the same crease pattern for the 6 samples of the reference group. For each standard deviation of random perturbation, a group of 12 different crease patterns were generated. For all experimental samples, we set $a = b = 25\text{mm}$ and $\alpha = 60^\circ$. An electronic cutting machine (Silhouette CAMEO, Silhouette America) is used to fabricate the samples from 160g/m² paper (Mi-Teintes, Canson). Creases were patterned by cutting perforated lines with equal lengths of material and gaps. All samples are then folded by hand, according to the same folding procedure. Samples were first folded to approximately 20% of initial extension before mechanical testing, and then unfolded to obtain a stable partially folded configuration with width of $W_0 = 152\text{mm}$.

We compare the cutting resolution and precision of the Silhouette CAMEO (Silhouette America) with the PLS4.75 laser cutting system (Universal laser systems). To test the resolution, we make pairs of parallel cuts with gap distances varying from 0.125mm to 2mm (see Fig. 4.13(b)). We find that both cutters are only able to distinguish the two lines when the gap is of 0.25mm width, which is about the thickness of the paper. However, the Silhouette CAMEO leaves clearer gap in between because it does not burn out materials like the laser cutter. To test the precision, we cut straight lines with specified length of 25mm and 50mm. For each length we make three cuts, and measure the length of cuts using a caliper (Fig. 4.13(b)). The laser cutter over cuts, while the Silhouette CAMEO under cuts, but the error is slightly smaller with the Silhouette CAMEO. Another advantage of the Silhouette CAMEO is that it uses an adhesive cutting mat to provide support to the paper and hold it flat during cutting. However, for the laser cutter, the paper is loosely placed on a honeycomb grid, and thus the paper may be curved or warped. When the paper is not flat, the laser beam does not cut precisely straight lines.

4.5.2 Miura-ori Compression test

A custom-built mechanical testing bed was used to measure the mechanical properties of Miura-ori samples under compression. Samples were placed on the testing bed between two steel plates with a distance of 152mm. One of the plates is fixed and mounted on a high-sensitivity load cell; the other is controlled by a stepper motor to apply prescribed displacement load. All samples are subject to a displacement load of 110mm with speed of 1 mm/s. The displacement and force data were simultaneously recorded by a custom LabVIEW program, and stored for later analysis.

4.5.3 Stretching stiffness

To obtain the Young's modulus (C_S) of the paper, we used an Instron model 5566 equipped with a 30kN load cell to perform a tensile test on five samples (see Fig. 4.16). The samples

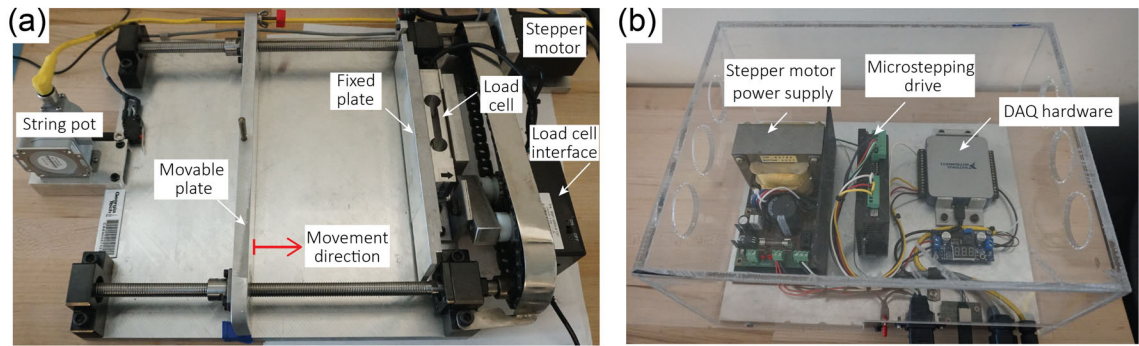


Figure 4.14: The mechanical testing bed for compression test of origami samples.

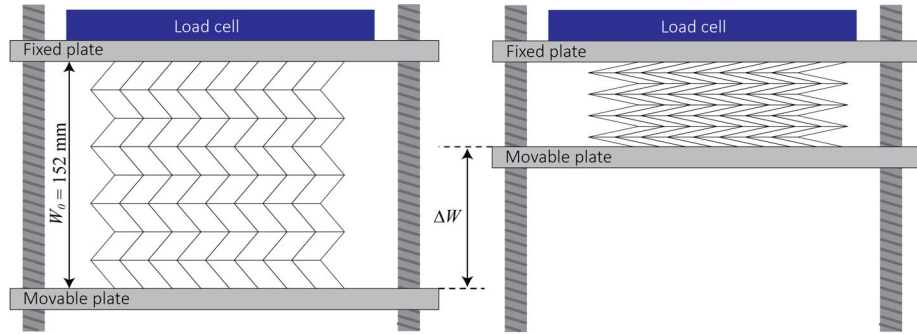


Figure 4.15: Schematics of the compression test.

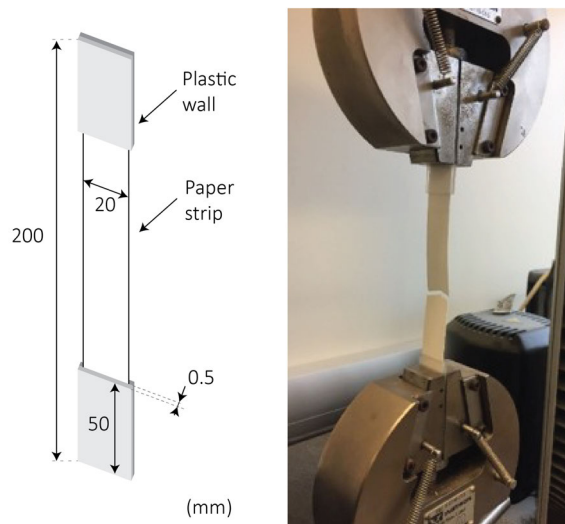


Figure 4.16: Tension test on paper material using the Instron machine.

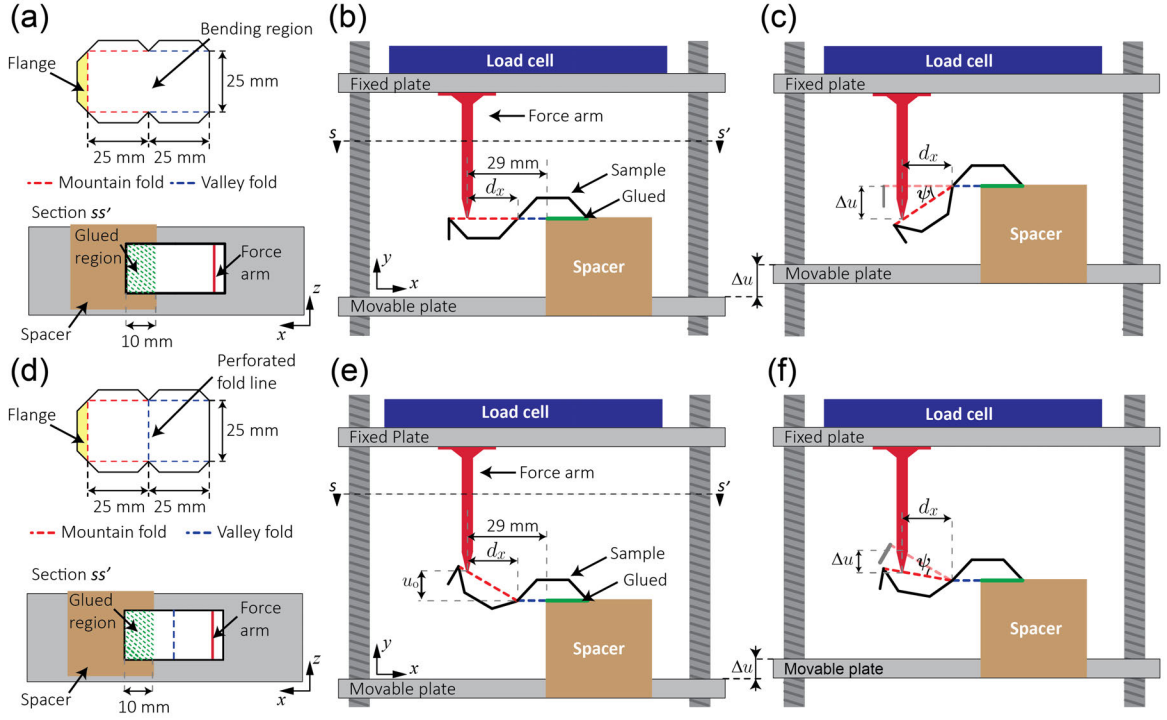


Figure 4.17: Schematics of the bending and folding test. (a)-(c) Characterization of the bending stiffness of the panels, and (d)-(f) characterization of the folding stiffness of the perforated crease (fold line).

tested are made of 160g/m Canson Mi-Teintes paper. Each sample has a dimension of 20mm×100mm with thickness of 0.24mm. From those tests, we take the mean of the results and obtained $C_S=1219.43$ MPa. The data is collected in Table. 4.1.

4.5.4 Folding and bending stiffness

To characterize the bending stiffness of the origami panels ($k_{0,pr}^B$), we prototype five paper-made rectangular panels (50mm×25mm) surrounded by folded flanges that resemble the presence of the neighboring panels in an origami system, as shown in Fig. 4.17(a). The arrangement of the flanges lead to localized bending line, similar to the deformed origami panels [98]. In a similar fashion, we also prototype five samples to characterize the folding stiffness of the paper creases ($k_{0,pr}^F$). Each sample has two square panels of dimension 25mm×25mm, jointed by a perforated crease line (see Fig. 4.17(d)). The crease lines are first folded completely and then released to a neutral angle prior to the test.

The samples are tested using an adapted setup of the custom-built mechanical testing bed, as shown in Fig. 4.17. First, we attach a spacer to the movable plate. This spacer holds the sample, while leaving clearance for the free end of the sample to displace freely in space to some extent. Second, we mount a 3D-printed force arm to the fixed plate with its center offset 29 mm from the spacer edge. This arm transmits the reaction force from the sample to the load cell. Fig. 4.17(b) and (e) show the initial setup of the tests to measure bending stiffness and folding stiffness, respectively. Fig. 4.17(c) and (f) depict intermediary scenarios during the test. The moment (M) at the crease/bending lines and the rotational angle (ψ) is calculated as follows:

$$M = Fd_x, \quad \psi = \tan^{-1} \left(\frac{u_0}{d_x} \right) - \tan^{-1} \left(\frac{u_0 - \Delta u}{d_x} \right), \quad (4.17)$$

where d_x is the distance between the crease/bending line and the force arm (i.e., $d_x = 19$ mm), F is the measured forces from load cell, and u_0 is the initial distance between the force arm and the spacer in the y -direction. For the measurements of bending stiffness, $u_0 = 0$, while for the folding stiffness, we see different initial neutral angles after a complete fold. In such cases, u_0 was measured for each sample based on where the force arm touches the sample. Fig. 4.18 shows the moment-rotation diagrams of one bending test and one folding test. The measured rotational stiffness from all samples are collected in Table 4.1, with coefficients of determination (i.e. R_B^2 and R_F^2) included. The mean of rotational stiffness is then normalized by the bending/folding line length (i.e., 25mm) to obtain the rotational stiffness per length, and we obtain: $k_{0,pr}^B = 0.23$ (N·mm)/mm/rad, and $k_{0,pr}^F = 0.036$ (N·mm)/mm/rad. The ratio between the bending and folding stiffness for the particular paper material used in the experiments is approximately $k_{0,pr}^B/k_{0,pr}^F = 6.4$.

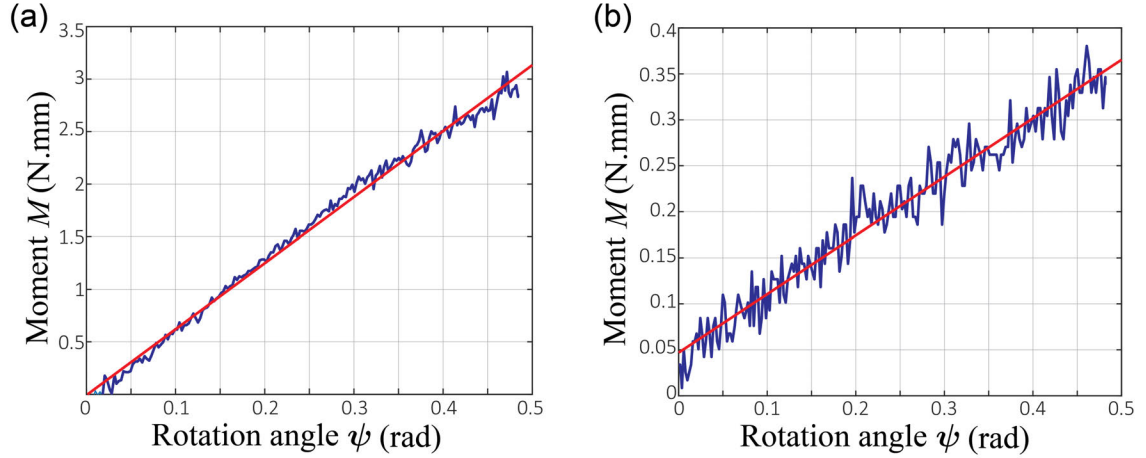


Figure 4.18: Moment M vs. rotation angle ψ for the panel bending (a) and folding (b) from one sample of each. The measured data is plotted in blue lines, and the red lines represent the linear regressions. From the slope of the red line, the rotational stiffness is obtained.

Table 4.1: Paper Material Properties

C_S (MPa)	k_0^B ((N·mm)/mm/rad)	R_B^2	k_0^F ((N·mm)/mm/rad)	R_F^2
1313.317	0.2513	0.9934	0.0375	0.9226
1114.336	0.2078	0.9693	0.0322	0.9280
1287.007	0.2465	0.9923	0.0225	0.9520
1201.944	0.2141	0.9858	0.0434	0.9621
1180.504	0.2194	0.9930	0.0445	0.9489
Average				
1219.428	0.2278	0.9868	0.0366	0.9427

4.6 Concluding Remarks

Small geometric imperfections alter the mechanical performance of origami assemblages, as has been systematically demonstrated. In this work, we conduct experimental and numerical analyses to reveal that small geometric imperfections may significantly increase the compressive stiffness and strength of Miura folded sheets. More importantly, we find that the change of mechanical properties is mainly due to the relative imperfect positioning between origami vertices, as the Young's modulus ($E[E_{lin}]$) and average plateau stress ($E[\sigma_{plt}]$) increase linearly according to the residual norm of the Kawasaki excess. Geometric imperfections usually exist in a random manner, and thus greatly amplify variabilities of the mechanical properties of origami assemblages, which is in general undesirable, and has to be considered cautiously. However, for applications such as energy storage and dissipation [148], [157], geometric imperfections may be beneficial as they raise stored energy (i.e. area below the $\sigma-\varepsilon_x$ curve) of the origami assemblage. Other applications include self-deployable structures by removing selected panels of misaligned patterns [20]. Furthermore, we can exploit random geometric imperfections to purposely modify the behavior of origami systems. For example, we can introduce unevenly distributed imperfections to achieve functionally graded stiffness (like Fig. 4.1(b)), or create designated local deformations, as shown in Fig. 4.19.

Our current work focuses on the compressive behavior of geometrically imperfect Miura-ori. Moving forward, much work remains to be done, for instance, investigating the effect of geometric imperfections for other deformation modes and patterns, in order to bring the theoretical advantages of origami to reality.

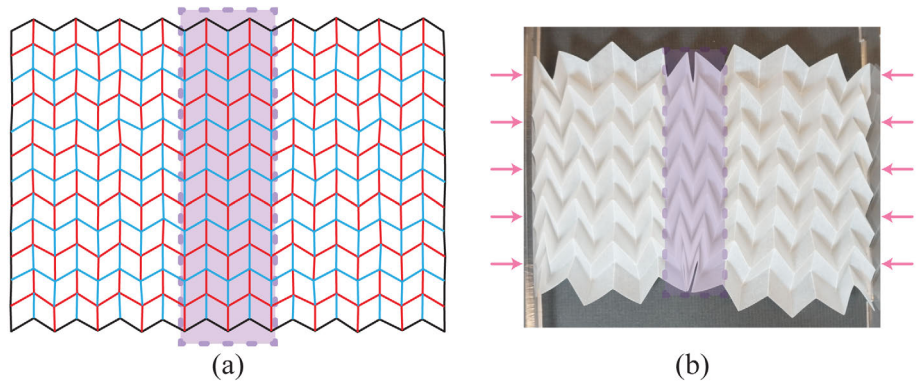


Figure 4.19: Purposely induced local deformation concentration by random perturbations. (a) The crease pattern. The purple region represents unperturbed portion. (b) The folded pattern under compression. Notice that the unperturbed region contracts more in the lateral direction than the perturbed portion because of the negative Poisson's ratio of Miura-ori.

CHAPTER 5

GEOMETRIC MECHANICS OF THE MORPH PATTERN

Exploring the configurational space of specific origami patterns (e.g. Miura-Ori, Eggbox) has led to major advances in science and technology. To augment the origami design space, we present a pattern, named *Morph*, that combines the features of its parent patterns. We introduce a four-vertex origami cell that morphs continuously between a Miura mode and an Eggbox mode, forming a homotopy class of configurations. This is achieved by changing Mountain/Valley assignment of one of the creases, leading to a smooth switch through a wide range of negative and positive Poisson’s ratios. We present elegant analytical expressions of Poisson’s ratios for both in-plane stretching and out-of-plane bending, and find that they are equal in magnitude and opposite in sign. Further, we show that by combining compatible unit cells in each of the aforementioned modes through kinematic bifurcation, we can create hybrid origami patterns that display unique properties such as topological mode-locking (irreversible morphing under stretch by synchronized engagement of aligned panels in the Miura mode) and tunable switching of Poisson’s ratio.

5.1 Introduction

Origami’s reconfigurability are encoded in their crease patterns. In this work, we propose a new periodic origami pattern, named the “Morph”, with a non-developable degree-4 unit cell that allows a certain crease to switch its mountain/valley assignment, leading to exclusive properties such as arbitrarily tunable Poisson’s ratio that spans from positive to negative, and topological mode locking.

Owing to their special geometries, origami metamaterials usually display interesting behavior [6], [19], [35], [70]. For instance, the Miura-ori exhibits a negative Poisson’s ratio under in-plane deformations [35], and the standard Eggbox pattern has a positive Poisson’s

ratio [17], [80]. As our proposed new design morphs continuously between a Miura-like mode and an Eggbox-like mode, it behaves as a single material possessing both positive and negative Poisson’s ratio. The Poisson’s ratio switching is an enticing phenomenon that has only been found recently for a few mechanical metamaterial designs, including nanoplates [158], reentrant origami tube assemblage [30], bistable auxetics [159], kirigami structures [21] and soft networks [160]. Compared to other designs, the Morph excels on having a wider tunable range of Poisson’s ratio, theoretically from negative infinity to positive infinity. In addition, as we assemble the unit cells of the Morph to form tessellated two-dimensional sheets, by harnessing kinematic bifurcation, we find an interesting arrangement that takes advantage of the fact that each unit cell can stay in either Miura or Eggbox mode, which leads to hybrid patterns.

In their most general form as shown in Fig. 5.1, the panel angles α and β of the Morph pattern are two independent geometric parameters, thereby enriching the origami design space, unlike the standard cases such as Eggbox ($\beta = \alpha$) or Miura-ori ($\beta = \pi - \alpha$) whose vertex geometry is dictated by just a single parameter α . Additionally, for $\alpha \neq \beta$, the degree-4 non-developability feature that the Morph shares with the standard Eggbox makes it a generalization of the basic patterns. Theoretically, the Poisson’s ratio of the Morph pattern sweeps the whole spectrum of real numbers as it morphs from one flat-folded state to the Eggbox mode, to the Miura mode, and to another flat-folded state, as shown in Fig. 5.1. The red crease in Fig. 5.1 changes its mountain/valley assignment as it *transitions* from Eggbox mode to the Miura mode, which is made possible owing to the fact that $\beta < \alpha$. By contrast, the standard Eggbox or Miura-ori patterns do not allow any crease to switch its mountain/valley assignment.

5.2 Geometry and configuration space of the Morph pattern

To parametrize the rigid origami behavior of the Morph unit cell, we define angles ϕ, ψ as the angles between opposing crease lines and denote the dihedral angles between the

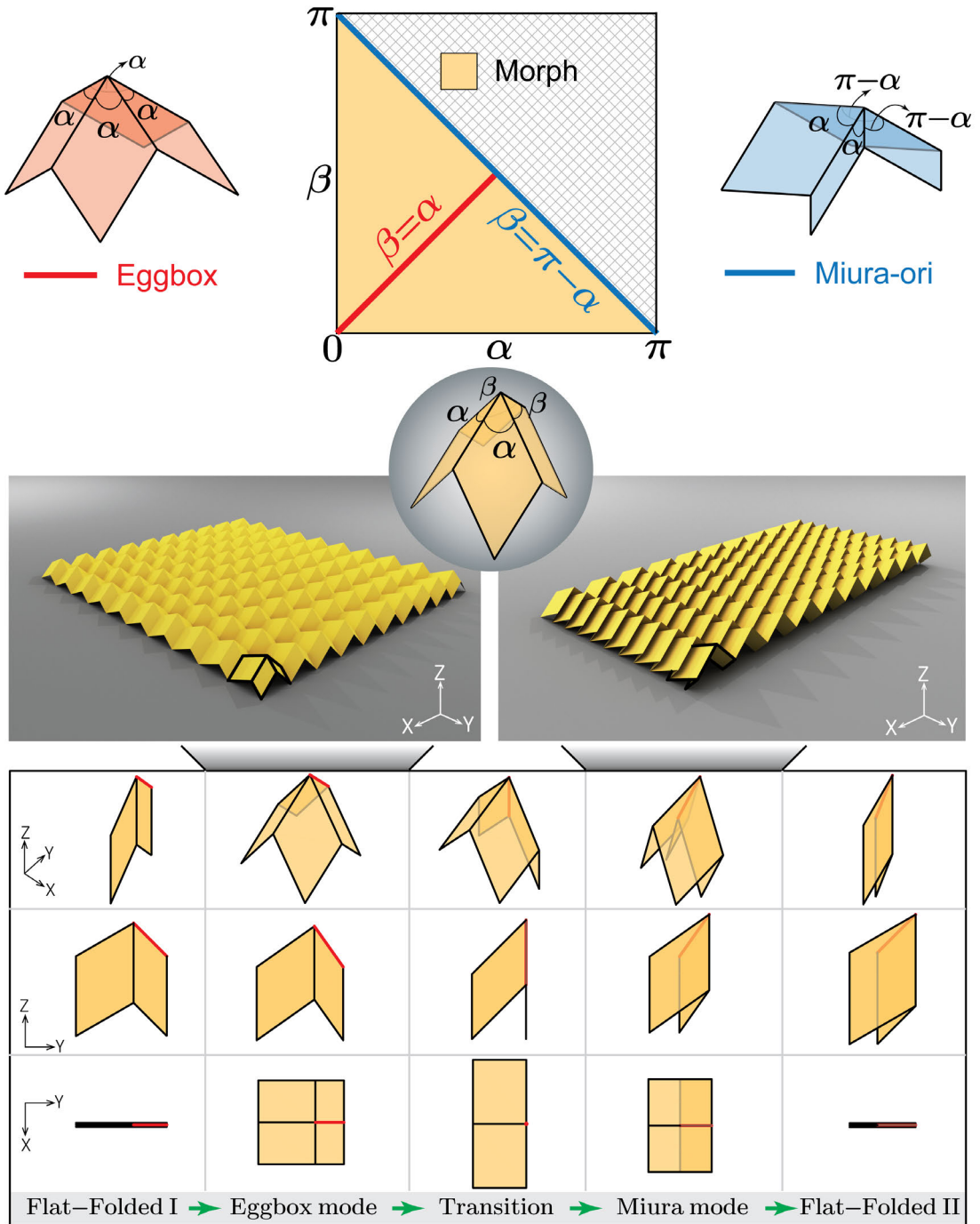


Figure 5.1: (Top) Expanded design space of the Morph pattern (yellow shading) with standard Eggbox (red line) and Miura-ori (blue line) as particular cases. (Middle) Fundamental modes of the Morph pattern: Eggbox mode (left) and Miura mode (right). (Bottom) Configuration space showing transition of the Morph unit cell from one flat-folded state to another. The crease line shown in red morphs from a mountain fold in the Eggbox mode to a valley fold in the Miura mode.

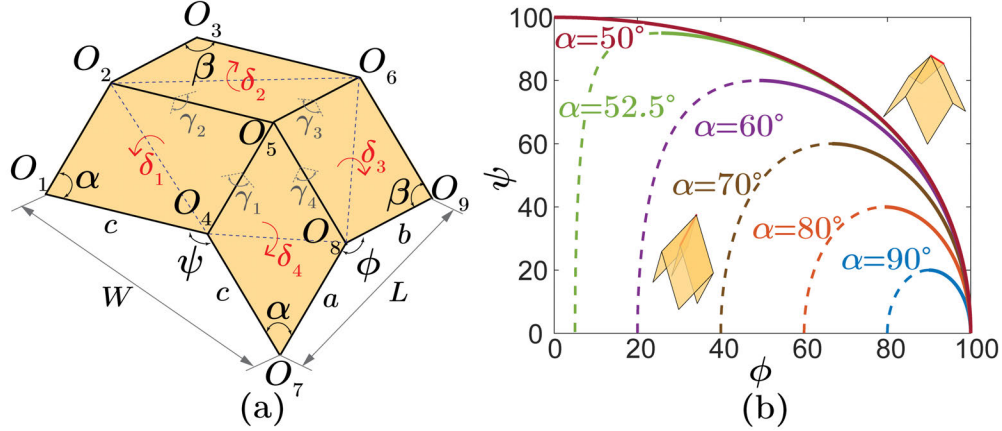


Figure 5.2: Geometric configuration of the Morph pattern. (a) Schematic of the unit cell with the description of geometric parameters and vertices. (b) The rigid origami configurations of the Morph pattern described in terms of ϕ and ψ for different choices of α considering $\alpha + \beta = 100^\circ$.

panels as $\gamma_1, \gamma_2, \gamma_3, \gamma_4$, as shown in Fig. 5.2(a). The unit cell has a degree-4 vertex, and thus it is a single degree of freedom system. The dihedral angles are related to one another and to ϕ, ψ . The panel shapes are given by the angles α, β and edge lengths a, b, c . The nine vertices of the unit cell are numbered from O_1 to O_9 .

Without loss of generality, we assume $\alpha > \beta$, which makes the $\overrightarrow{O_5O_6}$ crease to be the one that switches between mountain/valley, as indicated by the red line shown in Fig. 5.3(a). As shown in Fig. 5.3, to protect the orthorhombic feature of the unit cell, the edge lengths of adjacent panels need to be unequal (but related) except when they have the same panel angles. Hence, the edge lengths $|\overrightarrow{O_1O_4}|$ and $|\overrightarrow{O_7O_4}|$ are equal to c as they belong to panels with the same angle α . On the other hand, $|\overrightarrow{O_7O_8}|$ and $|\overrightarrow{O_9O_8}|$ cannot be equal when $\alpha \neq \beta$. As a consequence of, the Morph pattern has only one plane of symmetry (unlike the two-fold symmetric nature of the standard Eggbox).

The relation between the unequal edge lengths a, b can be obtained as follows. Fig. 5.3(b) and (c) show the side views of the unit cell. When $h_1 (= a|\cos\phi_1|)$ and $h_2 (= b|\cos\phi_2|)$ are equal, $\overrightarrow{O_7O_9}$ is normal to the planes $O_1O_4O_7$ and $O_3O_6O_9$ which ensures that the unit cell

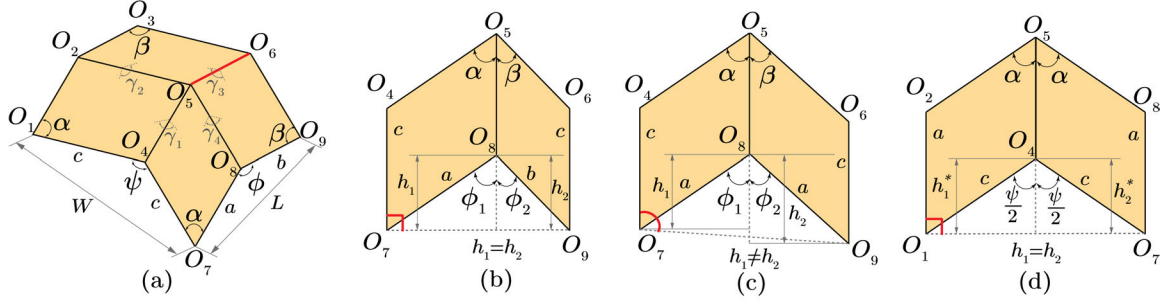


Figure 5.3: (a) Geometry of the Morph unit cell. (b), (c), (d) Side views of the unit cell. (b) $\overrightarrow{O_7O_9}$ is normal to the plane $O_1O_4O_7$ as $h_1 = h_2$, i.e., $a \cos \phi_1 = b \cos \phi_2$. (c) $\overrightarrow{O_7O_9}$ is not normal to the plane $O_1O_4O_7$ as $h_1 \neq h_2$ (since $\phi_1 \neq \phi_2$ for $\alpha \neq \beta$). We avoid this case to maintain the orthorhombic nature of the unit cell by making $|O_7O_8| \neq |O_9O_8|$. (d) $\overrightarrow{O_1O_7}$ is normal to the plane $O_1O_2O_3$ as $h_1^* = h_2^* = c \cos(\psi/2)$.

is orthorhombic. However, this is not true when $h_1 \neq h_2$. Hence, for $h_1 = h_2$, we have,

$$\frac{a}{b} = \left| \frac{\cos \phi_2}{\cos \phi_1} \right|. \quad (5.1)$$

Using spherical trigonometry of vertex O_5 , we have,

$$\cos \alpha = \cos \frac{\psi}{2} \cos \phi_1, \quad (5.2)$$

$$\cos \beta = \cos \frac{\psi}{2} \cos \phi_2. \quad (5.3)$$

This is true due to the plane of symmetry that bisects the dihedral angles γ_1, γ_3 and therefore angle ψ . Combining the above two equations, we get,

$$\frac{\cos \phi_2}{\cos \phi_1} = \frac{\cos \beta}{\cos \alpha}. \quad (5.4)$$

Finally, from Eq. 5.1 and 5.4, we get,

$$\frac{a}{b} = \left| \frac{\cos \beta}{\cos \alpha} \right|. \quad (5.5)$$

Consequently, in order to ensure that the triangular faces $(O_1O_2O_3, O_3O_6O_9, O_1O_4O_7,$

$O_7O_8O_9$) are all orthogonal to the base of the unit cell ($O_1O_7O_9O_3$), we only consider geometries with $b|\cos\beta| = a|\cos\alpha|$ so that,

$$b = a \left| \frac{\cos\alpha}{\cos\beta} \right| \quad (5.6)$$

The length L and width W of the unit cell are given by,

$$W = 2c \sin \frac{\psi}{2}, \quad (5.7)$$

$$L = \sqrt{a^2 + b^2 - 2ab \cos\phi}. \quad (5.8)$$

The folded state of the system is given by any of ϕ , ψ or the dihedral angles γ_1 , γ_2 , γ_3 , γ_4 all of which can be related to one another through the following equations obtained using the spherical law of cosines at vertex O_5 :

$$\cos\psi = \cos^2\alpha + \sin^2\alpha \cos\gamma_1 \quad (5.9)$$

$$\cos\psi = \cos^2\beta + \sin^2\beta \cos\gamma_3 \quad (5.10)$$

$$\cos\phi = \cos\alpha \cos\beta + \sin\alpha \sin\beta \cos\gamma_2 \quad (5.11)$$

$$\cos\phi = \cos\alpha \cos\beta + \sin\alpha \sin\beta \cos\gamma_4 \quad (5.12)$$

The configuration space that describes the morphing between Eggbox and Miura modes is understood in terms of the relation between ϕ and ψ . While $0 \leq \gamma_1 < \pi$, the ability of the crease O_5O_6 to switch between mountain and valley allows γ_3 to vary from 0 to 2π . In the flat-folded state I, $\phi = \phi_{max} = \alpha + \beta$ and $\gamma_3 = 0$. For $0 < \gamma_3 < \pi$, the unit cell is in Eggbox mode and O_5O_6 is a mountain crease. As γ_3 passes through π , O_5O_6 transitions from a mountain to a valley crease and the panels on either side of O_5O_6 become coplanar. In the transition state, angle ψ also reaches its maximum $\psi_{max} = 2\beta$. For $\pi < \gamma_3 < 2\pi$, the unit cell is in Miura mode and O_5O_6 is a valley crease. Finally, as $\gamma_3 \rightarrow 2\pi$, the unit cell approaches the flat-folded II state with $\phi = \phi_{min} = \alpha - \beta$.

From Eq. (5.11) and (5.12), we have $\gamma_2 = \gamma_4$ indicating the presence of a plane of symmetry $O_4O_5O_6$ which bisects the dihedral angles γ_1 and γ_3 . Using spherical trigonometry at vertex O_5 , the spherical law of cosines gives,

$$\cos \beta = \cos \alpha \cos \phi + \sin \alpha \sin \phi \cos \left(\frac{\gamma_1}{2} \right) \quad (5.13)$$

$$\cos \alpha = \cos \beta \cos \phi + \sin \beta \sin \phi \cos \left(\frac{\gamma_3}{2} \right) \quad (5.14)$$

Let us define two intermediate variables:

$$\xi = \cos \beta - \cos \alpha \cos \phi = \sin \alpha \sin \phi \cos(\gamma_1/2), \quad (5.15)$$

$$\zeta = \cos \alpha - \cos \beta \cos \phi = \sin \beta \sin \phi \cos(\gamma_3/2). \quad (5.16)$$

This gives us,

$$\cos \gamma_1 = \left(\frac{2\xi^2}{\sin^2 \alpha \sin^2 \phi} - 1 \right) \quad (5.17)$$

Combining the above equations with Eq. (5.9), we get,

$$\cos \psi = \cos 2\alpha + \frac{2\xi^2}{\sin^2 \phi}, \quad (5.18)$$

which is presented for various choices of panel angles in Fig. 5.2(b). We can observe that as $\alpha \rightarrow \beta$, the Miura mode vanishes.

5.2.1 Poisson's ratio

We define the (tangential) Poisson's ratio for in-plane stretching as the tangential ratio of the orthogonal strains measured by the change of width W and length L of a unit cell [6], [35], which is:

$$\nu_{WL}^s = -\frac{\epsilon_W}{\epsilon_L} = -\frac{dW/W}{dL/L} = -\frac{L}{W} \frac{dW}{dL} = -\frac{L}{W} \left(\frac{dW/d\psi}{dL/d\phi} \right) \frac{d\psi}{d\phi}. \quad (5.19)$$

From Eq. (5.18), we can obtain that:

$$\frac{d\psi}{d\phi} = -\frac{4(\cos \beta - \cos \alpha \cos \phi)(\cos \alpha - \cos \beta \cos \phi)}{\sin \psi \sin^3 \phi} = -\frac{4\xi\zeta}{\sin \psi \sin^3 \phi} \quad (5.20)$$

From Eq. (5.15), $\xi > 0$ since, $\phi < \pi$ and $\gamma_1 < \pi$ throughout the configurational space. Hence, the sign of the above derivative depends only on the sign of ζ . For $\gamma_3 > \pi$ (Miura mode), $\zeta < 0$, making $d\psi/d\phi > 0$. The analytical expression for the in-plane Poisson's ratio when stretching in the **L** direction is derived as,

$$\nu_{WL}^s = -\frac{dW/W}{dL/L} = \frac{4c^2L^2}{a^2W^2} \left| \frac{\cos \beta}{\cos \alpha} \right| \frac{\xi\zeta}{\sin^4 \phi}. \quad (5.21)$$

As plotted in Fig. 5.4(a), it is clear that the stretching Poisson's ratio is negative in the Miura mode and positive in the Eggbox mode, with a smooth transition near 0. Theoretically ν_{WL}^s approaches $-\infty$ or $+\infty$ in the two flat-folded limits, thereby leading to a wide range of tunability. We note that, since, W^2/c^2 and L^2/a^2 do not depend on the length dimensions of the unit cell, the Poisson's ratio of the unit cell depends only on α , β and ϕ making it a purely geometric quantity that is also independent of length scale of the pattern.

5.2.2 In-plane linear stiffness

Folding of the Morph pattern results in planar kinematics that keeps the global configuration of an assemblage staying flat. If we assign elasticity to the folding hinges, we can obtain the in-plane stiffness of the assemblage. We look at the stiffness of a single unit cell here (essentially one vertex with 4 folding hinges). Let the energy per unit length in the rotational hinges be given by $\mathcal{E}(\gamma_i) = \frac{1}{2}k_0^F(\gamma_i - \gamma_{i,0})^2$ for $i = 1, 2, 3, 4$, where, $\gamma_{i,0}$ denotes the neutral angles in the undeformed configuration and k_0^F is the folding stiffness constant per unit length associated with the rotational hinges. Due to symmetry, $\gamma_2 = \gamma_4$, and we

have the total energy of the unit cell in stretch given by,

$$\begin{aligned} U_s &= a\mathcal{E}(\gamma_1) + b\mathcal{E}(\gamma_3) + 2c\mathcal{E}(\gamma_2) \\ &= \frac{k_0^F}{2} [a(\gamma_1 - \gamma_{1,0})^2 + b(\gamma_3 - \gamma_{3,0})^2 + 2c(\gamma_2 - \gamma_{2,0})^2] \end{aligned} \quad (5.22)$$

As the in-plane deformation of the unit cell can be described using a single degree of freedom, γ_3 and γ_2 can be expressed in terms of γ_1 and we can evaluate the derivatives of the energy as:

$$\frac{d^2U_s}{dW^2} = \frac{d^2U_s}{d\gamma_1^2} \left(\frac{dW}{d\gamma_1} \right)^{-2} - \frac{dU_s}{d\gamma_1} \frac{d^2W}{d\gamma_1^2} \left(\frac{dW}{d\gamma_1} \right)^{-3} \quad (5.23)$$

$$\frac{d^2U_s}{dL^2} = \frac{d^2U_s}{d\gamma_1^2} \left(\frac{dL}{d\gamma_1} \right)^{-2} - \frac{dU_s}{d\gamma_1} \frac{d^2L}{d\gamma_1^2} \left(\frac{dL}{d\gamma_1} \right)^{-3} \quad (5.24)$$

We can derive that,

$$\frac{dU_s}{d\gamma_1} = a\mathcal{E}'(\gamma_1) + b\mathcal{E}'(\gamma_3) \left(\frac{d\gamma_3}{d\gamma_1} \right) + 2c\mathcal{E}'(\gamma_2) \left(\frac{d\gamma_2}{d\gamma_1} \right) \quad (5.25)$$

$$\begin{aligned} \frac{d^2U_s}{d\gamma_1^2} &= a\mathcal{E}''(\gamma_1) + b\mathcal{E}''(\gamma_3) \left(\frac{d\gamma_3}{d\gamma_1} \right)^2 + 2c\mathcal{E}''(\gamma_2) \left(\frac{d\gamma_2}{d\gamma_1} \right)^2 + \\ &\quad b\mathcal{E}'(\gamma_3) \left(\frac{d^2\gamma_3}{d\gamma_1^2} \right) + 2c\mathcal{E}'(\gamma_2) \left(\frac{d^2\gamma_2}{d\gamma_1^2} \right) \end{aligned} \quad (5.26)$$

where, $\mathcal{E}'(\gamma_i) = k_0^F(\gamma_i - \gamma_{i,0})$ and $\mathcal{E}''(\gamma_i) = k_0^F$. Noting that, $dU_s/d\gamma_1|_{\gamma_1=\gamma_{1,0}} = 0$, we define the stiffness along **W** and **L** directions as follows:

$$K_W = \frac{d^2U_s}{dW^2} \Big|_{\gamma_1=\gamma_{1,0}} = \frac{d^2U_s}{d\gamma_1^2} \Big|_{\gamma_1=\gamma_{1,0}} \left(\frac{dW}{d\gamma_1} \Big|_{\gamma_1=\gamma_{1,0}} \right)^{-2} \quad (5.27)$$

$$K_L = \frac{d^2U_s}{dL^2} \Big|_{\gamma_1=\gamma_{1,0}} = \frac{d^2U_s}{d\gamma_1^2} \Big|_{\gamma_1=\gamma_{1,0}} \left(\frac{dL}{d\gamma_1} \Big|_{\gamma_1=\gamma_{1,0}} \right)^{-2} \quad (5.28)$$

We have,

$$\frac{d^2U_s}{d\gamma_1^2} \Big|_{\gamma_1=\gamma_{1,0}} = ak_0^F + bk_0^F \left(\frac{d\gamma_3}{d\gamma_1} \Big|_{\gamma_1=\gamma_{1,0}} \right)^2 + 2ck_0^F \left(\frac{d\gamma_2}{d\gamma_1} \Big|_{\gamma_1=\gamma_{1,0}} \right)^2 \quad (5.29)$$

One can derive,

$$\frac{d\gamma_3}{d\gamma_1} \Big|_{\gamma_1=\gamma_{1,0}} = \frac{\cos \beta - \cos \alpha \cos \phi_0}{\cos \alpha - \cos \beta \cos \phi_0} \quad (5.30)$$

$$\frac{d\gamma_2}{d\gamma_1} \Big|_{\gamma_1=\gamma_{1,0}} = \frac{-\sin^2 \phi_0}{2(\cos \alpha - \cos \beta \cos \phi_0)} \quad (5.31)$$

$$\frac{dW}{d\gamma_1} \Big|_{\gamma_1=\gamma_{1,0}} = \frac{c(\cos \beta - \cos \alpha \cos \phi_0)}{\sin \phi_0} \quad (5.32)$$

$$\frac{dL}{d\gamma_1} \Big|_{\gamma_1=\gamma_{1,0}} = \frac{-ab \sin \alpha \sin \beta \sin \gamma_{2,0} \sin^2 \phi_0}{2L_0(\cos \alpha - \cos \beta \cos \phi_0)} \quad (5.33)$$

where, ϕ_0 , L_0 correspond to ϕ and L respectively when $\gamma_i = \gamma_{i,0}$. By combining Eq. (5.29) with Eq. (5.27) and (5.28), we have,

$$K_W = ak_0^F \left(\frac{d\gamma_1}{dW} \Big|_{\gamma_1=\gamma_{1,0}} \right)^2 + bk_0^F \left(\frac{d\gamma_3}{dW} \Big|_{\gamma_1=\gamma_{1,0}} \right)^2 + 2ck_0^F \left(\frac{d\gamma_2}{dW} \Big|_{\gamma_1=\gamma_{1,0}} \right)^2, \quad (5.34)$$

$$K_L = ak_0^F \left(\frac{d\gamma_1}{dL} \Big|_{\gamma_1=\gamma_{1,0}} \right)^2 + bk_0^F \left(\frac{d\gamma_3}{dL} \Big|_{\gamma_1=\gamma_{1,0}} \right)^2 + 2ck_0^F \left(\frac{d\gamma_2}{dL} \Big|_{\gamma_1=\gamma_{1,0}} \right)^2 \quad (5.35)$$

The normalized stiffnesses are obtained as K_W/k_0^F and K_L/k_0^F .

For standard Eggbox, by using, $a = b = c$ and $\alpha = \beta$ in the above equations, we get:

$$K_W = \frac{2k_0^F}{a} \left(\frac{\cos^2 \frac{\phi}{2} + \cos^2 \frac{\psi}{2}}{\sin^2 \frac{\phi}{2} \cos^4 \frac{\psi}{2}} \right) \quad (5.36)$$

$$K_L = \frac{2k_0^F}{a} \left(\frac{\cos^2 \frac{\phi}{2} + \cos^2 \frac{\psi}{2}}{\sin^2 \frac{\psi}{2} \cos^4 \frac{\phi}{2}} \right) \quad (5.37)$$

As shown in Fig. 5.4(b), the in-plane stiffness in the **W** direction (denoted by K_W) is minimum at flat-folded states and reaches maximum at the transition state. Interestingly, while K_L is maximal at flat-folded states, it is only close to minimum at the transition but

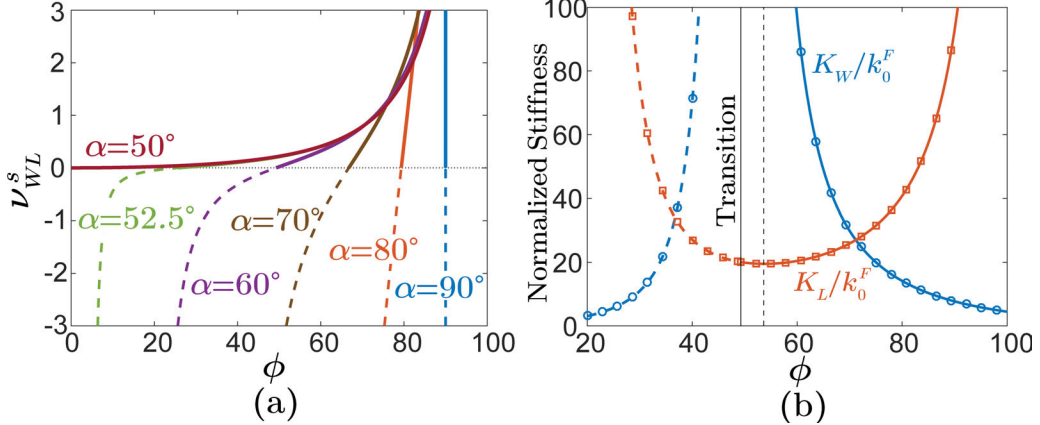


Figure 5.4: In-plane mechanics of the Morph pattern. (b) The Poisson’s ratio in stretch (ν_{WL}^s) for different choices of α considering $\alpha + \beta = 100^\circ$. (b) Stretching stiffness in W and L directions for $\alpha = 60^\circ$, $\beta = 40^\circ$. The markers represent numerical results from origami structural analyses using the bar-and-hinge reduced order model. We assume that $a = c = 1$. The solid and dashed lines represent the Eggbox and Miura modes, respectively.

slightly away towards the Eggbox mode.

5.3 Out-of-plane bending of the Morph pattern

As revealed in previous research [6], [17], [35], kinematically 1-DOF origami pattern may experience out-of-plane deformation other than pure (in-plane) folding, if compliance of panels is taken into consideration. Accordingly, we define the Poisson’s ratio in bending as the ratio of principal curvatures ($\nu_{WL}^b = -\kappa_W/\kappa_L$) and find that the Morph pattern features a saddle shaped geometry in the Miura mode, and a dome shape geometry in the Eggbox mode (see Fig. 5.5(a) and (b)). It is intriguing that the Morph pattern exhibits distinct Poisson’s ratio in stretching and bending, similar to what have been found, separately, with the standard Miura-ori and the standard Eggbox patterns. Here we show that, just like its two extreme cases [17], [35], the Morph pattern display Poisson’s ratio with opposite sign but equal magnitude in stretching and bending. We can analytically calculate the principal bending curvatures by allowing each panel of the origami pattern to bend along one of its diagonal [35], under the assumption of infinitesimal deformation.

We introduce infinitesimal rotations $\delta_1, \delta_2, \delta_3, \delta_4$, as shown in Fig. 5.2(a) to provide

further degrees of freedom to the system that simulates bending of panels. Hence, there are in total 4 extra DOF being added, yet isometric deformation is still ensured.

5.3.1 Coordinate system, vertices and normals

We take out two panels for ease of study. As shown in Fig. 5.6, we assume a coordinate system with origin at vertex O_5 and x -axis along the fold line $\overrightarrow{O_2O_5}$. The xy -plane is assumed to coincide with panel $O_1O_2O_5O_4$ and z -axis is obtained by the right hand rule. The coordinates of all the vertices in this system can be obtained in terms of the panel edge lengths (a, b, c), the panel angles (α, β) and the dihedral angles ($\gamma_i, i = 1, 2, 3, 4$) using the Rodrigues' rotation formula for finite rotations:

$$\vec{v}_{rot} = \vec{v} \cos \eta + (\hat{\mathbf{p}} \times \vec{v}) \sin \eta + \hat{\mathbf{p}}(\hat{\mathbf{p}} \cdot \vec{v})(1 - \cos \eta) \quad (5.38)$$

where, \vec{v}_{rot} is obtained by rotating a vector \vec{v} about axis of rotation $\hat{\mathbf{p}}$ by an angle η using the right hand rule. Using this formula, the coordinates of vertices on the triangular face $O_1O_2O_3$ are obtained as:

$$O_2 = (-c, 0, 0) \quad (5.39)$$

$$O_1 = (-c - a \cos \alpha, -a \sin \alpha, 0) \quad (5.40)$$

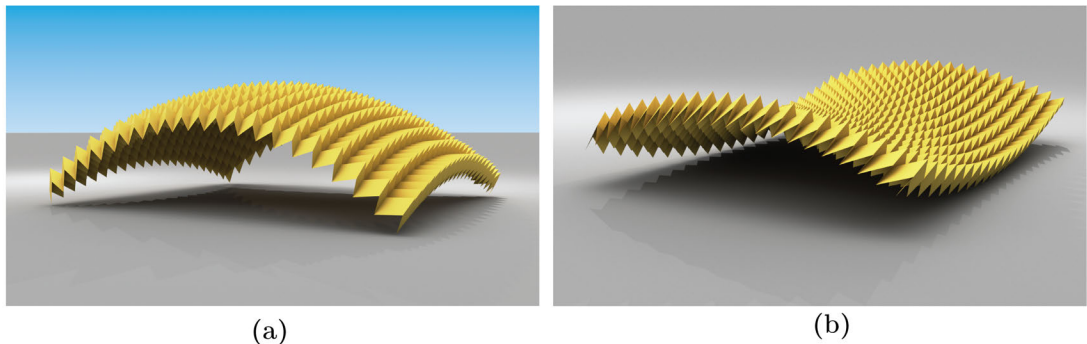


Figure 5.5: Out-of-plane bending of the Morph. (a), (b) Bent shapes of the pattern in Eggbox and Miura modes respectively obtained using the bar and hinge origami model.

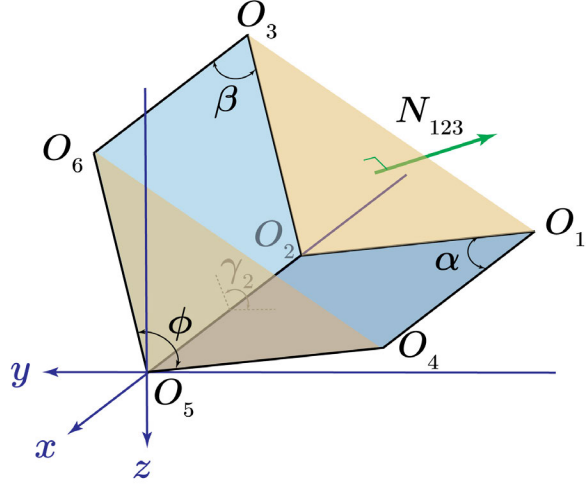


Figure 5.6: Local coordinate system used to calculate the normals and the angle change for the triangular face $O_1O_2O_3$.

$$O_3 = (-c - b \cos \beta, -b \cos \gamma_2 \sin \beta, -b \sin \gamma_2 \sin \beta) \quad (5.41)$$

Using linearized Rodrigues' rotation formula, the coordinates of O_1 and O_3 after applying the infinitesimal rotations δ_1 (about $\overrightarrow{O_2O_4}$) and δ_2 (about $\overrightarrow{O_6O_2}$) are obtained as,

$$O'_1 = (-c - a \cos \alpha, -a \sin \alpha, -(ac \sin \alpha) \frac{\delta_1}{\ell_1}) \quad (5.42)$$

$$\begin{aligned} O'_3 = & (-c - b \cos \beta, \\ & -b \cos \gamma_2 \sin \beta - (cb \sin \gamma_2 \sin \beta) \frac{\delta_2}{\ell_2}, \\ & -b \sin \gamma_2 \sin \beta + (cb \cos \gamma_2 \sin \beta) \frac{\delta_2}{\ell_2}) \end{aligned} \quad (5.43)$$

The normals of the triangular face $O_1O_2O_3$ before and after bending are calculated as

$$\begin{aligned} \mathbf{N}_{123} &= \overrightarrow{O_2O_3} \times \overrightarrow{O_2O_1} \\ &= -ab \left[\sin \alpha \sin \gamma_2 \sin \beta \right] \hat{\mathbf{i}} + ab \left[\cos \alpha \sin \gamma_2 \sin \beta \right] \hat{\mathbf{j}} \\ &\quad - ab \left[\cos \alpha \cos \gamma_2 \sin \beta - \sin \alpha \cos \beta \right] \hat{\mathbf{k}} \end{aligned} \quad (5.44)$$

$$\begin{aligned}
\mathbf{N}'_{123} &= \overrightarrow{O_2 O_3} \times \overrightarrow{O_2 O_1} \\
&= -ab \left[\sin \alpha \sin \gamma_2 \sin \beta - (c \sin \alpha \cos \gamma_2 \sin \beta) \left(\frac{\delta_2}{\ell_2} + \frac{\delta_1}{\ell_1} \right) \right] \hat{\mathbf{i}} \\
&\quad + ab \left[\cos \alpha \sin \gamma_2 \sin \beta - (c \cos \alpha \cos \gamma_2 \sin \beta) \frac{\delta_2}{\ell_2} - (c \sin \alpha \cos \beta) \frac{\delta_1}{\ell_1} \right] \hat{\mathbf{j}} \\
&\quad - ab \left[\cos \alpha \cos \gamma_2 \sin \beta - \sin \alpha \cos \beta + (c \cos \alpha \sin \gamma_2 \sin \beta) \frac{\delta_2}{\ell_2} \right] \hat{\mathbf{k}}
\end{aligned} \tag{5.45}$$

where, $\hat{\mathbf{i}}, \hat{\mathbf{j}}, \hat{\mathbf{k}}$ are the unit vectors along the x, y, z axes.

5.3.2 Constraints on bending rotations

The bending of the tessellation preserves the orthogonality of the unit cell (i.e. $\mathbf{L} \cdot \mathbf{W} = 0$). Hence, we enforce the constraint that the normals of the triangular faces ($O_1 O_2 O_3, O_3 O_6 O_9, O_1 O_4 O_7, O_7 O_8 O_9$) before and after panel bending are orthogonal to their respective base edges. We impose,

$$(\mathbf{N}'_{123} - \mathbf{N}_{123}) \cdot \overrightarrow{O_1 O_3} = \Delta \mathbf{N}_{123} \cdot \overrightarrow{O_1 O_3} = 0 \tag{5.46}$$

since, $\mathbf{N}_{123} \perp \overrightarrow{O_1 O_3}$. After evaluating the above constraint, we arrive at a relation between the panel bending rotations δ_1 and δ_2 (since, \mathbf{N}'_{123} only depends on the rotations δ_1, δ_2):

$$\frac{\delta_2}{\ell_2} b \zeta = \frac{\delta_1}{\ell_1} a \xi \tag{5.47}$$

Using the above mentioned procedure for the other triangular faces and the relation between a and b (Eq. 5.6), we have the following constraints on the bending rotations:

$$\frac{\delta_2}{\ell_2} |\cos \alpha| \zeta = \frac{\delta_1}{\ell_1} |\cos \beta| \xi \tag{5.48}$$

$$\frac{\delta_4}{\ell_4} |\cos \beta| \xi = \frac{\delta_3}{\ell_3} |\cos \alpha| \zeta \tag{5.49}$$

$$\frac{\delta_1}{\ell_1} = \frac{\delta_4}{\ell_4} \tag{5.50}$$

$$\frac{\delta_3}{\ell_3} = \frac{\delta_2}{\ell_2} \quad (5.51)$$

It can be easily verified that the above rotations are a compatible set with a single degree of freedom associated with bending of the panels i.e. choosing any one rotation independently will define a unique bending configuration of the unit cell. Additionally, it can be also be verified that these rotations satisfy the tessellation boundary conditions, i.e. $\angle O'_1O_2O'_3 = \angle O'_7O_8O'_9$ and $\angle O'_1O_4O'_7 = \angle O'_3O_6O'_9$

5.3.3 Bending curvatures

We define the curvatures along each of the orthogonal directions $\mathbf{L} = \overrightarrow{O_1O_3}$ and $\mathbf{W} = \overrightarrow{O_1O_7}$ as the relative tilt of the triangular faces across the unit cell length in the respective directions, as shown in Fig. 5.7. The curvature along \mathbf{L} direction is given by,

$$\kappa_L = \frac{\operatorname{sgn}[(\mathbf{n} \times \mathbf{L}) \cdot (\mathbf{N}'_{369} \times \mathbf{N}_{369})]|\theta_{369}| - \operatorname{sgn}[(\mathbf{n} \times \mathbf{L}) \cdot (\mathbf{N}'_{147} \times \mathbf{N}_{147})]|\theta_{147}|}{L} \quad (5.52)$$

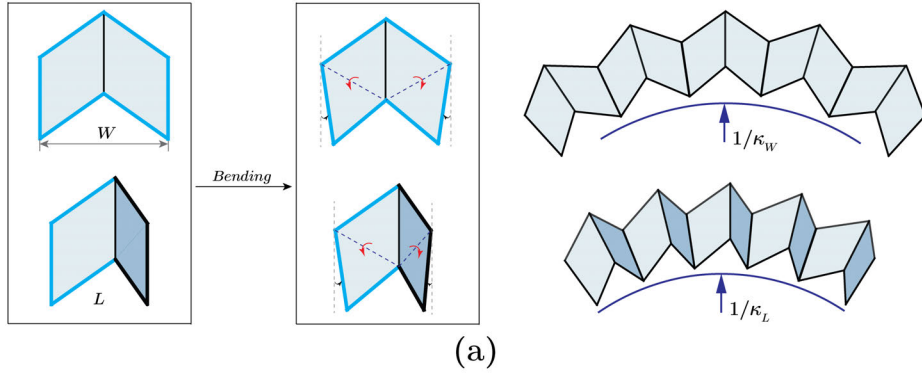
The curvature along \mathbf{W} direction is given by,

$$\kappa_W = \frac{\operatorname{sgn}[(\mathbf{n} \times \mathbf{W}) \cdot (\mathbf{N}'_{789} \times \mathbf{N}_{789})]|\theta_{789}| - \operatorname{sgn}[(\mathbf{n} \times \mathbf{W}) \cdot (\mathbf{N}'_{123} \times \mathbf{N}_{123})]|\theta_{123}|}{W} \quad (5.53)$$

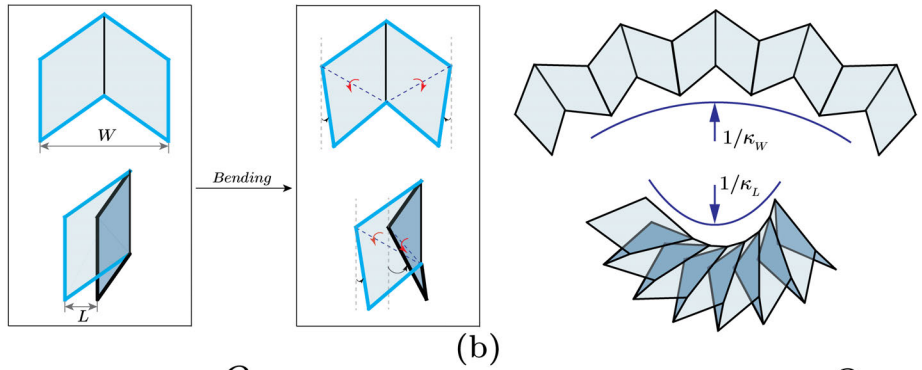
where, $\mathbf{n} = \mathbf{W} \times \mathbf{L}$, $|\theta_{123}|$, $|\theta_{789}|$, $|\theta_{147}|$, and $|\theta_{369}|$ are the respective angles between the normals \mathbf{N}_{123} , \mathbf{N}_{789} , \mathbf{N}_{147} , and \mathbf{N}_{369} and \mathbf{N}'_{123} , \mathbf{N}'_{789} , \mathbf{N}'_{147} , and \mathbf{N}'_{369} . The angle between the face normals before and after bending represents the slope (or angle change) of each of the curves formed by the unit cells along the tessellation directions.

The angle change between the above normals can be calculated through their vector cross product. We have,

$$(\mathbf{N}'_{123} \times \mathbf{N}_{123}) \frac{\cos^2 \beta}{ca^4 \cos^2 \alpha} = \left[\cos \alpha \zeta \left(\frac{\delta_2}{\ell_2} \right) + \cos \beta (\cos \alpha \cos \phi - \cos \beta) \left(\frac{\delta_1}{\ell_1} \right) \right] \hat{\mathbf{i}}$$



(a)



(b)

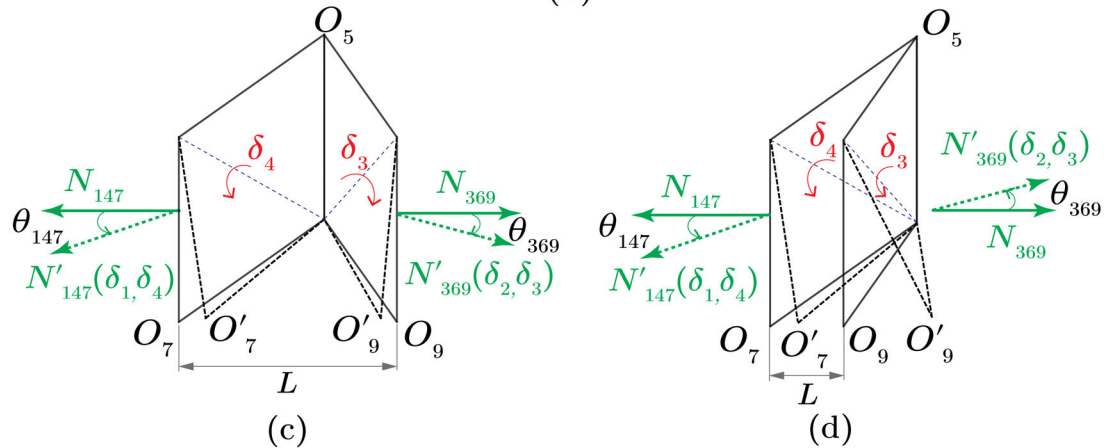


Figure 5.7: Infinitesimal bending of a unit cell and global curvatures of bended pattern. (a) Bending of the Morph pattern in Eggbox mode. Curvatures along both W and L directions are of the same sign. (b) Bending in Miura mode. Curvatures along W and L directions are of opposite sign. (c), (d) Triangular face tilts creating a net angle change across length L in Eggbox and Miura modes, respectively.

$$\begin{aligned}
& + \left[\sin \alpha \zeta \left(\frac{\delta_2}{\ell_2} \right) + \frac{(\cos \phi - \cos \alpha \cos \beta)(\cos \alpha \cos \phi - \cos \beta)}{\sin \alpha} \left(\frac{\delta_1}{\ell_1} \right) \right] \hat{\mathbf{j}} \\
& + \left[\sin \gamma_2 \sin \beta (\cos \alpha \cos \phi - \cos \beta) \left(\frac{\delta_1}{\ell_1} \right) \right] \hat{\mathbf{k}}
\end{aligned} \quad (5.54)$$

This gives us,

$$|\mathbf{N}'_{123} \times \mathbf{N}_{123}|^2 \left[\frac{\cos^2 \beta}{ca^4 \cos^2 \alpha} \right]^2 = \left(\frac{\delta_2}{\ell_2} \right)^2 \zeta^2 + \left(\frac{\delta_1}{\ell_1} \right)^2 \xi^2 - 2 \left(\frac{\delta_2}{\ell_2} \right) \left(\frac{\delta_1}{\ell_1} \right) \zeta \xi \cos \phi \quad (5.55)$$

Using the constraint on bending rotations that relates δ_2 and δ_1 (Eq. (5.48)), the above expression can be simplified as,

$$\begin{aligned}
|\mathbf{N}'_{123} \times \mathbf{N}_{123}|^2 \left[\frac{\cos^2 \beta}{ca^4 \cos^2 \alpha} \right]^2 &= \left(\frac{\delta_1}{\ell_1} \right)^2 \xi^2 \left[\frac{\cos^2 \beta}{\cos^2 \alpha} + 1 - 2 \frac{\cos \beta}{\cos \alpha} \cos \phi \right] \\
&= \left(\frac{\delta_1}{\ell_1} \right)^2 \xi^2 \frac{L^2}{b^2} \quad (\text{Using Eq. (5.6) and (5.8)})
\end{aligned} \quad (5.56)$$

This gives us,

$$|\mathbf{N}'_{123} \times \mathbf{N}_{123}| = a^2 b^2 c \frac{|\delta_1|}{\ell_1} |\xi| \frac{L}{b} \quad (5.57)$$

Finally, noting that $|\mathbf{N}_{123}| = ab \sin \phi$, the angle change for the triangular face $O_1 O_2 O_3$ is given by

$$|\theta_{123}| \approx \frac{|\mathbf{N}_{123} \times \mathbf{N}'_{123}|}{|\mathbf{N}_{123}|^2} = \frac{cL|\xi|}{b \sin^2 \phi} \frac{|\delta_1|}{\ell_1} \quad (5.58)$$

In order to obtain the angle changes for each of the other triangular faces after bending, we conveniently choose a coordinate system that is oriented such that the x -axis is along the fold line that is connected to the triangular face and passing through O_5 and the xy -plane to coincide with one of the panels connected to the triangular face. This will allow us to perform a similar calculation as above and produce the following result:

$$\begin{aligned}
\left[\frac{|\mathbf{N}'_{789} \times \mathbf{N}_{789}|}{a^2 b^2 c} \right]^2 &= \left(\frac{\delta_3}{\ell_3} \right)^2 \zeta^2 + \left(\frac{\delta_4}{\ell_4} \right)^2 \xi^2 - 2 \left(\frac{\delta_3}{\ell_3} \right) \left(\frac{\delta_4}{\ell_4} \right) \zeta \xi \cos \phi \\
\left[\frac{|\mathbf{N}'_{147} \times \mathbf{N}_{147}|}{c^4 a} \right]^2 &= \left(\frac{\delta_1}{\ell_1} \right)^2 \cos^2 \alpha (1 - \cos \psi)^2 + \left(\frac{\delta_4}{\ell_4} \right)^2 \cos^2 \alpha (1 - \cos \psi)^2
\end{aligned} \quad (5.59)$$

$$- 2\left(\frac{\delta_1}{\ell_1}\right)\left(\frac{\delta_4}{\ell_4}\right) \cos^2 \alpha (1 - \cos \psi)^2 \cos \psi \quad (5.60)$$

$$\begin{aligned} \left[\frac{|\mathbf{N}'_{369} \times \mathbf{N}_{369}|}{c^4 b} \right]^2 &= \left(\frac{\delta_3}{\ell_3}\right)^2 \cos^2 \beta (1 - \cos \psi)^2 + \left(\frac{\delta_2}{\ell_2}\right)^2 \cos^2 \beta (1 - \cos \psi)^2 \\ &\quad - 2\left(\frac{\delta_3}{\ell_3}\right)\left(\frac{\delta_2}{\ell_2}\right) \cos^2 \beta (1 - \cos \psi)^2 \cos \psi \end{aligned} \quad (5.61)$$

Simplifying the above expressions using constraint Eq. (5.48), (5.49), (5.50), (5.51), and noting that $|\mathbf{N}_{789}| = ab \sin \phi$, $|\mathbf{N}_{147}| = c^2 \sin \psi$, $|\mathbf{N}_{369}| = c^2 \sin \psi$, we can derive the following expressions for the angle changes

$$|\theta_{123}| \approx \frac{|\mathbf{N}_{123} \times \mathbf{N}'_{123}|}{|\mathbf{N}_{123}|^2} = \frac{cL\xi}{b \sin^2 \phi} \frac{|\delta_1|}{\ell_1} \quad (5.62)$$

$$|\theta_{789}| \approx \frac{|\mathbf{N}_{789} \times \mathbf{N}'_{789}|}{|\mathbf{N}_{789}|^2} = \frac{cL\xi}{b \sin^2 \phi} \frac{|\delta_1|}{\ell_1} \quad (5.63)$$

$$|\theta_{147}| \approx \frac{|\mathbf{N}_{147} \times \mathbf{N}'_{147}|}{|\mathbf{N}_{147}|^2} = \frac{aW \cos \alpha (1 - \cos \psi)}{c \sin^2 \psi} \frac{|\delta_1|}{\ell_1} \quad (5.64)$$

$$|\theta_{369}| \approx \frac{|\mathbf{N}_{369} \times \mathbf{N}'_{369}|}{|\mathbf{N}_{369}|^2} = \frac{aW \cos \beta (1 - \cos \psi)}{c \sin^2 \psi} \frac{\xi}{|\zeta|} \frac{|\delta_1|}{\ell_1} \quad (5.65)$$

The above expressions indicate that $|\theta_{123}| = |\theta_{789}|$ which is consistent with the presence of the plane of symmetry $O_4O_5O_6$. The symmetry also makes the expression for κ_W to be independent of whether the system is in Eggbox or Miura mode. However, that is not the case for the curvature κ_L . The normals \mathbf{N}'_{147} , \mathbf{N}'_{369} depend only on rotations δ_1 , δ_4 and δ_2 , δ_3 respectively. From Eq. 5.49 (or 5.48), δ_4 (or δ_1) and δ_3 (or δ_2) have the same sign for Eggbox mode and opposite sign for Miura mode. This is because, as noted before, from Eq. (5.13), $\xi \geq 0$ (since $\gamma_1 \leq \pi$) throughout the configurational space and from Eq. (5.14) $\zeta < 0$ when $\gamma_3 > \pi$. This makes the angle changes for faces $O_1O_4O_7$ and $O_3O_6O_9$ to have opposite sign for Eggbox mode and same sign for Miura mode.

To calculate the curvatures, we consider the two cases depending on whether $\gamma_3 < \pi$ (Eggbox mode) or $\gamma_3 > \pi$ (Miura mode).

Case-1: $\gamma_3 < \pi \implies \zeta > 0$ (Eggbox mode)

$$\begin{aligned}\kappa_L &= -\frac{|\theta_{369}| + |\theta_{147}|}{L} \operatorname{sgn}(\delta_1) \\ &= -\frac{aW(1 - \cos \psi)}{cL \sin^2 \psi} \frac{(\cos^2 \alpha + \cos^2 \beta - 2 \cos \alpha \cos \beta \cos \phi)}{\zeta} \frac{|\delta_1|}{\ell_1} \operatorname{sgn}(\delta_1)\end{aligned}\quad (5.66)$$

$$\kappa_W = -\frac{|\theta_{789}| + |\theta_{123}|}{W} \operatorname{sgn}(\delta_1) = -\frac{2cL\xi}{bW \sin^2 \phi} \frac{|\delta_1|}{\ell_1} \operatorname{sgn}(\delta_1) \quad (5.67)$$

Case-2: $\gamma_3 > \pi \implies \zeta < 0$ (Miura mode)

$$\begin{aligned}\kappa_L &= \frac{|\theta_{369}| - |\theta_{147}|}{L} \operatorname{sgn}(\delta_1) \\ &= -\frac{aW(1 - \cos \psi)}{cL \sin^2 \psi} \frac{(\cos^2 \alpha + \cos^2 \beta - 2 \cos \alpha \cos \beta \cos \phi)}{\zeta} \frac{|\delta_1|}{\ell_1} \operatorname{sgn}(\delta_1)\end{aligned}\quad (5.68)$$

$$\kappa_W = -\frac{|\theta_{789}| + |\theta_{123}|}{W} \operatorname{sgn}(\delta_1) = -\frac{2cL\xi}{bW \sin^2 \phi} \frac{|\delta_1|}{\ell_1} \operatorname{sgn}(\delta_1) \quad (5.69)$$

We note that the curvatures κ_L in both the cases are of opposite sign due to the change in sign of ζ . However, the analytical expressions for the curvatures in both the cases are the same irrespective of the configuration change from Eggbox to Miura mode.

5.3.4 Poisson's ratio in bending

The Poisson's ratio in bending ν_{WL}^b is defined as the ratio of curvatures in W and L directions [6], [35]. Using Eq. (5.6) and (5.18) to simplify the above expressions of the curvatures, we can calculate the bending Poisson's ratio as,

$$\begin{aligned}\nu_{WL}^b &= -\kappa_W / \kappa_L \\ &= -\frac{2cL\xi}{aW(1 - \cos \psi)} \frac{\zeta}{(\cos^2 \alpha + \cos^2 \beta - 2 \cos \alpha \cos \beta \cos \phi)} \frac{cL \sin^2 \psi}{bW \sin^2 \phi} \\ &= -\frac{2c^2 L^2 \xi}{a^2 W^2 (1 - \cos \psi)} \frac{\zeta}{(\cos^2 \frac{\psi}{2} \sin^2 \phi)} \left| \frac{\cos \beta}{\cos \alpha} \right| \frac{\sin^2 \psi}{\sin^2 \phi} \\ &= -\frac{4c^2 L^2}{a^2 W^2} \left| \frac{\cos \beta}{\cos \alpha} \right| \frac{\xi \zeta}{\sin^4 \phi}\end{aligned}\quad (5.70)$$

This shows that for the Morph, $\nu_{WL}^s = -\nu_{WL}^b$ (see Fig. 5.8(a)), a remarkable property first shown in the case of standard Miura-ori tessellation by [35]. This geometric property holds in both Eggbox and Miura modes and is independent of the material properties and length scale of the system. Clearly, the remarkable result of $\nu_{WL}^b = -\nu_{WL}^s$ [6], [17], [35] also holds true for the Morph pattern. The above expression reduces to standard Miura-ori and Eggbox as two particular cases for appropriate choice of panel angles α and β , as elaborated in Section 5.4 and 5.5.

5.3.5 Out-of-plane bending stiffness

The bending energy per unit cell is given by,

$$U_b = \frac{1}{2}WL B_W \kappa_W^2 = \frac{1}{2}WL B_L \kappa_L^2 \quad (5.71)$$

where B_W and B_L are the bending stiffness of the tessellation per unit width in **W** and **L** directions respectively. But, as discussed before, the bending is assumed to be solely due to the bending of the four panels. Hence, we can also write,

$$U_b = \ell_1 \mathcal{F}(\delta_1) + \ell_2 \mathcal{F}(\delta_2) + \ell_3 \mathcal{F}(\delta_3) + \ell_4 \mathcal{F}(\delta_4) \quad (5.72)$$

where, $\mathcal{F}(\delta_i) = \frac{1}{2}k_0^B \delta_i^2$ is the energy per unit length along the bending lines which are modeled as bending rotational hinges across panel diagonals and k_0^B is the stiffness constant associated with those hinges. Since, $\ell_1 = \ell_4$, $\ell_3 = \ell_2$ for the Morph, we have, $\delta_1 = \delta_4$, $\delta_3 = \delta_2$ using Eq. (5.50), and (5.51). Thus, we obtain that:

$$U_b = k_0^B (\ell_1 \delta_1^2 + \ell_3 \delta_3^2) \quad (5.73)$$

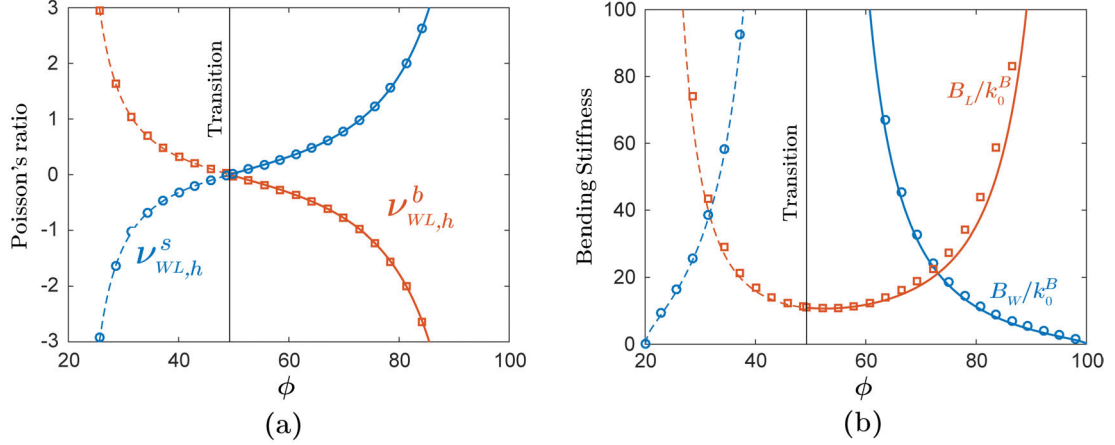


Figure 5.8: (a) Comparison of Poisson's ratio in bending and stretching. (b) Normalized out-of-plane bending stiffness of a Morph unit cell. B_W and B_L represent the bending stiffnesses per unit width along **W** and **L** directions respectively. In both the figures, $\alpha = 60^\circ$ and $\beta = 40^\circ$. The dashed lines represent the results in the Miura mode and the solid lines represent the results in the Eggbox mode. The circle and square markers show the numerical results obtained using the bar and hinge model.

Now, applying Eq. (5.48), we have,

$$U_b = k_0^B \frac{\delta_1^2}{\ell_1^2} \left[\frac{\ell_1^3 \cos^2 \alpha \zeta^2 + \ell_3^3 \cos^2 \beta \xi^2}{\cos^2 \alpha \zeta^2} \right] \quad (5.74)$$

Comparing Eq. (5.71) and (5.74), and using the expressions for curvatures from previous sub-section, we get the analytical expressions for the bending stiffnesses as given below,

$$B_W = \frac{k_0^B b^2 W \sin^4 \phi}{2c^2 L^3 \cos^2 \alpha} \left[\frac{\ell_1^3 \cos^2 \alpha \zeta^2 + \ell_3^3 \cos^2 \beta \xi^2}{\xi^2 \zeta^2} \right] \quad (5.75)$$

$$B_L = \frac{2k_0^B a^2 c^2 (1 + \cos \psi)^2}{W^3 L^3 \cos^2 \beta} \left[\frac{\ell_1^3 \cos^2 \alpha \zeta^2 + \ell_3^3 \cos^2 \beta \xi^2}{\cos^2 \alpha \cos^2 \beta} \right] \quad (5.76)$$

The bending stiffnesses are related to bending Poisson's ratio as $(\nu_{WL}^b)^2 = B_L/B_W$. This can be easily observed by comparing Eq. (5.71) and (5.70). The above analytical expressions are plotted in Fig. 5.8(b). For numerical simulation of bending we consider a pattern with 21×21 cells and calculate curvatures from unit cells at the center of the system. The moments are applied in a way similar to that followed by [35].

By performing numerical simulation using the reduced order bar-and-hinge model [5], [6], [101], we find that the analytical model agrees well with the numerical simulations with very small discrepancies, which further strengthens the assumption that infinitesimal rotations about panel diagonals are sufficient to characterize first order bending response of the Morph pattern.

5.4 Recovery of standard Eggbox relationships from the Morph pattern

In this section, we show that, all the results derived for the Morph pattern can be reduced to the special case of standard Eggbox that has been well studied in the literature [17], by setting $\beta = \alpha$ and $a = b$. From Eq. (5.18), the relation between ϕ and ψ becomes:

$$\begin{aligned} \cos^2 \frac{\psi}{2} &= \frac{\cos^2 \alpha + \cos^2 \beta - 2 \cos \alpha \cos \beta \cos \phi}{\sin^2 \phi} \\ &= 2 \cos^2 \alpha \frac{(1 - \cos \phi)}{1 - \cos^2 \phi} \\ &= \frac{\cos^2 \alpha}{\cos^2 \frac{\phi}{2}} \\ \implies \cos \frac{\phi}{2} \cos \frac{\psi}{2} &= \cos \alpha \end{aligned} \tag{5.77}$$

Since, for standard Eggbox, $L = 2a \sin \frac{\phi}{2}$ and $W = 2c \sin \frac{\psi}{2}$, then we have,

$$\begin{aligned} \nu_{WL}^s &= \frac{4c^2 L^2}{a^2 W^2} \left| \frac{\cos \beta}{\cos \alpha} \right| \frac{\xi \zeta}{\sin^4 \phi} \\ &= \frac{\sin^2 \frac{\phi}{2}}{\sin^2 \frac{\psi}{2}} \frac{4 \cos^2 \alpha (1 - \cos \phi)^2}{(1 - \cos^2 \phi)^2} \\ &= \frac{\sin^2 \frac{\phi}{2}}{\sin^2 \frac{\psi}{2}} \frac{\cos^2 \frac{\phi}{2} \cos^2 \frac{\psi}{2}}{\cos^4 \frac{\phi}{2}} = \frac{\tan^2 \frac{\phi}{2}}{\tan^2 \frac{\psi}{2}} \\ \implies \nu_{WL}^s &= \frac{\tan^2 \frac{\phi}{2}}{\tan^2 \frac{\psi}{2}} \end{aligned} \tag{5.78}$$

which is in agreement with the expression previously derived by [6], [17].

Next, we obtain the expressions for bending curvatures from Eqs. (5.66), and (5.67).

$$\begin{aligned}
\kappa_L &= -\frac{aW(1-\cos\psi)}{cL\sin^2\psi} \frac{(\cos^2\alpha + \cos^2\beta - 2\cos\alpha\cos\beta\cos\phi)}{\zeta} \frac{|\delta_1|}{\ell_1} \text{sgn}(\delta_1) \\
&= -\frac{\sin\frac{\psi}{2}}{\sin\frac{\phi}{2}} \frac{2\cos\alpha(1-\cos\phi)}{(1+\cos\psi)(1-\cos\phi)} \frac{|\delta_1|}{\ell_1} \text{sgn}(\delta_1) \\
&= -\frac{\tan\frac{\psi}{2}}{\tan\frac{\phi}{2}} \frac{|\delta_1|}{\ell_1} \text{sgn}(\delta_1)
\end{aligned} \tag{5.79}$$

$$\begin{aligned}
\kappa_W &= -\frac{2cL\xi}{bW\sin^2\phi} \frac{|\delta_1|}{\ell_1} \text{sgn}(\delta_1) \\
&= -\frac{2\sin\frac{\phi}{2}}{\sin\frac{\psi}{2}} \frac{2\cos\alpha}{(1+\cos\phi)} \frac{|\delta_1|}{\ell_1} \text{sgn}(\delta_1) \\
&= -\frac{\tan\frac{\phi}{2}}{\tan\frac{\psi}{2}} \frac{|\delta_1|}{\ell_1} \text{sgn}(\delta_1)
\end{aligned} \tag{5.80}$$

The bending Poisson's ratio is now obtained as,

$$\nu_{WL}^b = -\kappa_W/\kappa_L = -\frac{\tan^2\frac{\phi}{2}}{\tan^2\frac{\psi}{2}} \tag{5.81}$$

These results are in agreement with what have been derived previously for bending of standard Eggbox [17].

5.5 Recovery of standard Miura-ori relationships from the Morph pattern

In this section, we show that, all the results derived for the Morph pattern can be reduced to the special case of standard Miura-ori that has been well studied in the literature, by setting $\beta = \pi - \alpha$ and $a = b$. From Eq. (5.18), the relation between ϕ and ψ becomes:

$$\begin{aligned}
\cos^2\frac{\psi}{2} &= \frac{\cos^2\alpha + \cos^2\beta - 2\cos\alpha\cos\beta\cos\phi}{\sin^2\phi} \\
&= 2\cos^2\alpha \frac{(1+\cos\phi)}{1-\cos^2\phi}
\end{aligned}$$

$$\begin{aligned}
&= \frac{\cos^2 \alpha}{\sin^2 \frac{\phi}{2}} \\
\implies \sin \frac{\phi}{2} \cos \frac{\psi}{2} &= |\cos \alpha| \tag{5.82}
\end{aligned}$$

Since, for standard Miura-ori, $L = 2a \sin \frac{\phi}{2}$ and $W = 2c \sin \frac{\psi}{2}$, we have,

$$\begin{aligned}
\nu_{WL}^s &= \frac{4c^2 L^2}{a^2 W^2} \left| \frac{\cos \beta}{\cos \alpha} \right| \frac{\xi \zeta}{\sin^4 \phi} \\
&= -\frac{\sin^2 \frac{\phi}{2}}{\sin^2 \frac{\psi}{2}} \frac{4 \cos^2 \alpha (1 + \cos \phi)^2}{(1 - \cos^2 \phi)^2} \\
&= -\frac{\sin^2 \frac{\phi}{2}}{\sin^2 \frac{\psi}{2}} \frac{\sin^2 \frac{\phi}{2} \cos^2 \frac{\psi}{2}}{\sin^4 \frac{\phi}{2}} = -\cot^2 \frac{\psi}{2} \\
\implies \nu_{WL}^s &= -\cot^2 \frac{\psi}{2} \tag{5.83}
\end{aligned}$$

which is in agreement with the expressions previously derived in references [6], [35].

Next, we obtain the expressions for bending curvatures from Eq. (5.66) and (5.67).

$$\begin{aligned}
\kappa_L &= -\frac{aW(1 - \cos \psi)}{cL \sin^2 \psi} \frac{(\cos^2 \alpha + \cos^2 \beta - 2 \cos \alpha \cos \beta \cos \phi)}{\zeta} \frac{|\delta_1|}{\ell_1} \operatorname{sgn}(\delta_1) \\
&= -\frac{\sin \frac{\psi}{2}}{\sin \frac{\phi}{2}} \frac{2 \cos \alpha (1 + \cos \phi)}{(1 + \cos \psi)(1 + \cos \phi)} \frac{|\delta_1|}{\ell_1} \operatorname{sgn}(\delta_1) \\
&= -\frac{\sin \frac{\psi}{2}}{\sin \frac{\phi}{2}} \frac{2 \cos \alpha}{(1 + \cos \psi)} \frac{|\delta_1|}{\ell_1} \operatorname{sgn}(\delta_1) \tag{5.84}
\end{aligned}$$

$$\begin{aligned}
\kappa_W &= -\frac{2cL\xi}{bW \sin^2 \phi} \frac{|\delta_1|}{\ell_1} \operatorname{sgn}(\delta_1) \\
&= \frac{\sin \frac{\phi}{2}}{\sin \frac{\psi}{2}} \frac{2 \cos \alpha}{(1 - \cos \phi)} \frac{|\delta_1|}{\ell_1} \operatorname{sgn}(\delta_1) \tag{5.85}
\end{aligned}$$

The bending Poisson's ratio is now obtained as,

$$\nu_{WL}^b = -\kappa_W / \kappa_L = \cot^2 \frac{\psi}{2} \tag{5.86}$$

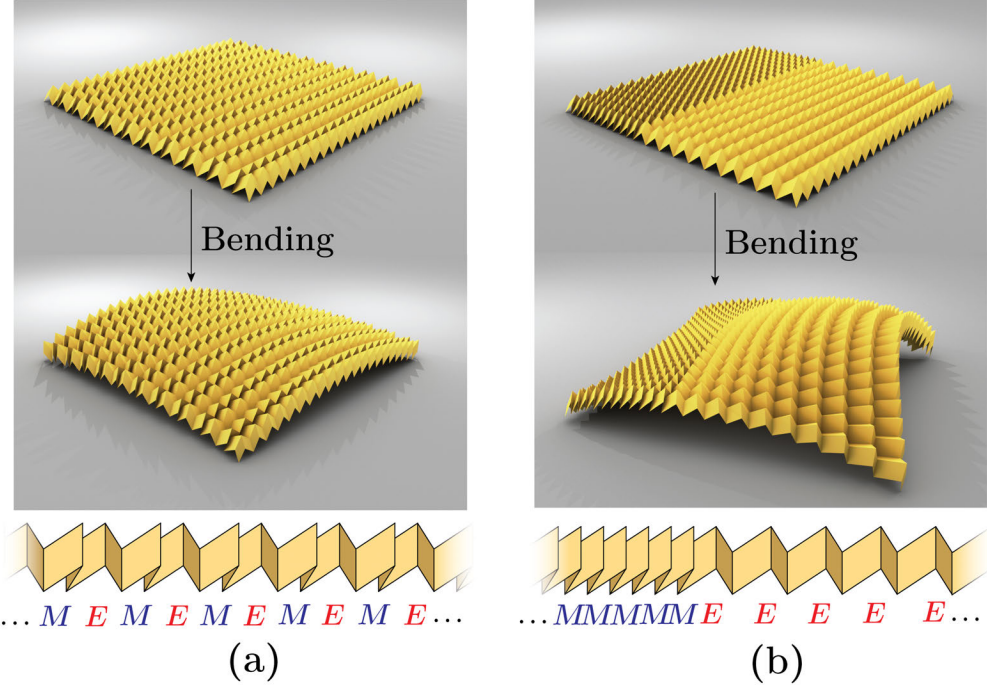


Figure 5.9: Hybrid origami patterns. (a) Alternating strips of Miura (M) and Eggbox (E) modes. (b) Half pattern with strips in Miura (M) mode and other half in Eggbox (E) mode.

These results are in agreement with that obtained by [35] for bending of standard Miura-ori.

5.6 Hybrid patterns

Owing to the mode switching feature, the Morph unit cells do not have to be tessellated with uniform configuration. It is kinematically admissible to couple Morph unit cells into a hybrid pattern, such that there are both Miura-mode cells and Eggbox mode cells in one tessellation, as demonstrated in Fig. 5.9 (a) and (b).

The hybrid patterns exhibit interesting behavior in bending due to the combined action from Miura and Eggbox mode cells. For example, a hybrid pattern with alternating Miura and Eggbox mode strips bends into a dome shape that is close to part of a cylinder (Fig. 5.9(a)), whereas that with a set a of Miura mode strips adjacent to one another bends into a complex geometry that has both saddle and dome shapes Fig. 5.9(b). Such complex geometries with both positive and negative Gaussian curvatures were previously only

obtained by tailoring the geometry of origami design [42], but not by deformation.

5.6.1 Configuration space of hybrid patterns

The rigid foldability between various hybrid patterns is only possible when all unit cells are first brought to the transition state (see Fig. 5.10). The feasibility of such a hybrid system

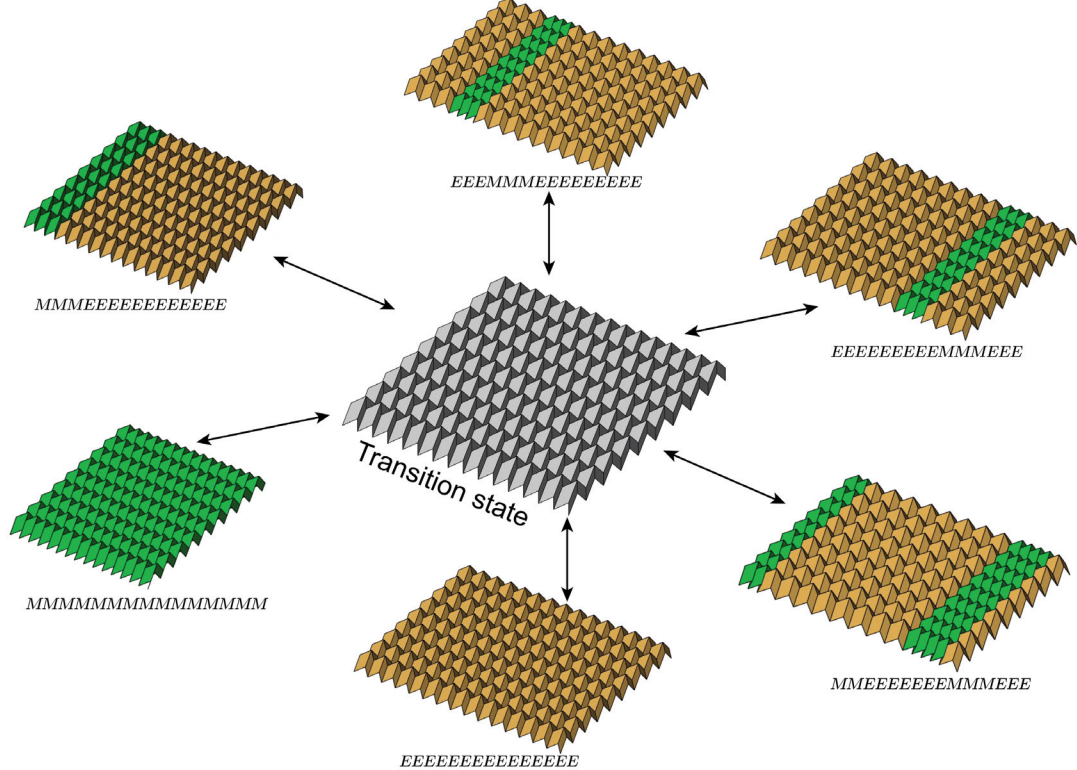


Figure 5.10: The Morph pattern's transformability into various hybrid patterns via the transition state. The hybrid pattern is a composite metamaterial system that can morph into any combination of Miura (denoted by M, shown in green color) and Eggbox (denoted by E, shown in yellow color) modes which have contrasting mechanical properties and therefore is a highly programmable and in-situ tunable metamaterial.

can be understood by noting that in Fig. 5.2(b), a given angle ψ can correspond to two possible ϕ 's, in either the Eggbox mode or the Miura mode, which are denoted as ϕ_e or ϕ_m , respectively. From Fig. 5.11, we can see that $\phi_e = \phi_1 + \phi_2$ and $\phi_m = \phi_1 - \phi_2$. In order to place the Eggbox and Miura mode unit cells adjacent to each other, they should meet the compatibility condition that $\psi_e = \psi_m = \psi$.

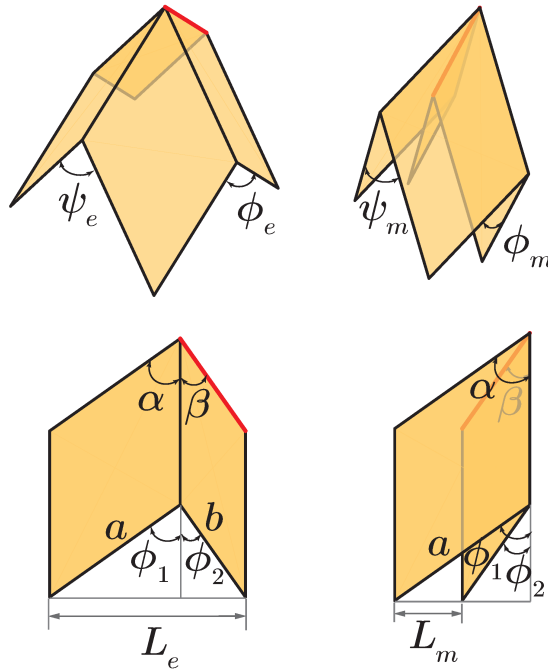


Figure 5.11: Unit cells of hybrid patterns in the Eggbox and Miura modes. For compatibility, $\psi_e = \psi_m = \psi$ with $\phi_e = \phi_1 + \phi_2$ and $\phi_m = \phi_1 - \phi_2$.

Orthogonality of the unit cell gives,

$$\frac{b}{a} = \frac{\cos \alpha}{\cos \beta} = \frac{\cos \phi_1}{\cos \phi_2} \quad (5.87)$$

where, $\phi_1 \rightarrow \alpha$ and $\phi_2 \rightarrow \beta$ in the limit of approaching the flat-folded states. Also, from Eq. (5.8) and (5.18), we have,

$$\cos \frac{\psi}{2} = \frac{L \cos \alpha}{b \sin \phi} = \frac{L \cos \beta}{a \sin \phi} \quad (5.88)$$

We can also show that, $\sin \phi = \sin(\phi_1 \pm \phi_2) = L \cos \phi_1 / b = L \cos \phi_2 / a$. Using these relations, we can calculate ϕ_1 and ϕ_2 for a given ψ as,

$$\cos \phi_1 = \frac{\cos \alpha}{\cos \frac{\psi}{2}} \quad (5.89)$$

$$\cos \phi_2 = \frac{\cos \beta}{\cos \frac{\psi}{2}} \quad (5.90)$$

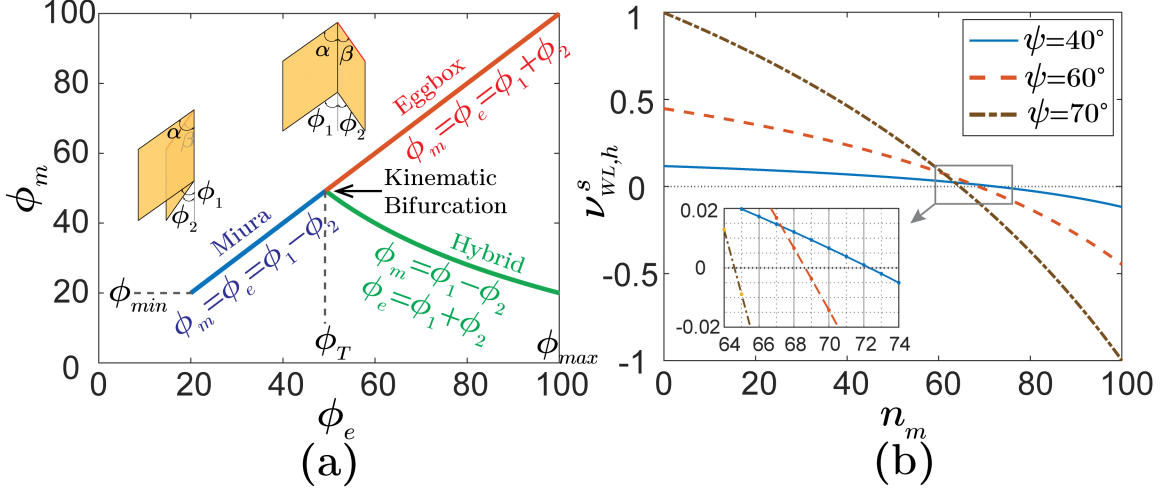


Figure 5.12: Morphing of the hybrid pattern. (a) Creation of hybrid patterns by kinematic bifurcations. (b) Change of Poisson's ratio with respect to varying number of Miura mode strips (n_m) in a hybrid mode with 100×100 unit cells. To prepare the figures, we assume that $\alpha = 60^\circ$, $\beta = 40^\circ$.

from which $\phi_e = \phi_1 + \phi_2$ and $\phi_m = \phi_1 - \phi_2$ can be calculated. In Fig. 5.12(a), we show that one can smoothly deform a homogeneous Morph pattern to a hybrid pattern using rigid origami motion (no panel bending).

5.6.2 In-plane Poisson's ratio of hybrid patterns

Depending on the coupling mode of the hybrid pattern, the tessellated sheet exhibits a different Poisson's ratio ($\nu_{WL,h}^s$), as shown in Fig. 5.12(b). There exists a transition point when $\nu_{WL,h}^s$ varies from positive to negative, which however, is not when the number of Miura mode and Eggbox mode strips are the same, due to unequal contributions from both the modes. We consider a system with 100×100 cells and increase the number of Miura mode cells (in strips) along the L direction (denoted as n_m) from 0 to 100 (see Fig. 5.12(b)). For a given pattern, the switching of Poisson's ratio can be tuned to occur at different fold angles by smoothly modifying the number of Miura mode strips in the system, which renders the Morph pattern reprogrammable.

We define the length and width of the pattern of $n \times n$ unit cells as, $L' = n_e L_e + n_m L_m$

and $W' = nW$ respectively, where, $n = n_e + n_m$ with n_e denoting number of Eggbox mode strips and n_m denoting the number of Miura mode strips (see Fig. 5.13). The unit cell lengths in the two modes are given by,

$$L_e^2 = a^2 + b^2 - 2ab \cos \phi_e \quad (5.91)$$

$$L_m^2 = a^2 + b^2 - 2ab \cos \phi_m \quad (5.92)$$

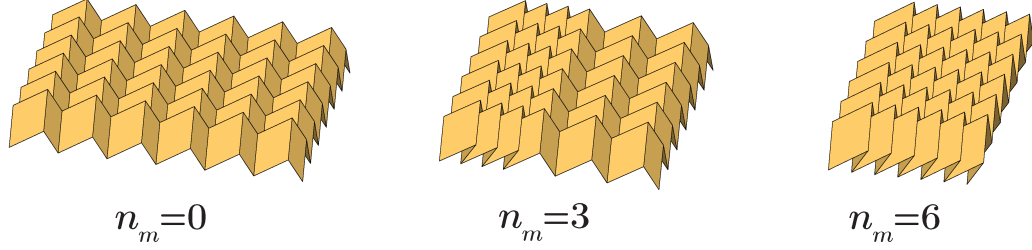


Figure 5.13: Hybrid patterns with varying number of Miura strips, n_m , for $n = 6$.

The Poisson's ratio in stretch of the hybrid pattern is then defined as,

$$\nu_{WL,h}^s = -\frac{dL'/L'}{dW'/W'} = -\frac{W'}{L'} \frac{dL'}{d\psi} \frac{d\psi}{dW'} \quad (5.93)$$

The derivatives are obtained as,

$$\frac{dL'}{d\psi} = n_e \frac{dL_e}{d\psi} + n_m \frac{dL_m}{d\psi} \quad (5.94)$$

$$\frac{dW'}{d\psi} = n \frac{dW}{d\psi} = nc \cos \frac{\psi}{2} \quad (5.95)$$

Using Eq. 5.89 and 5.90 and noting that $\phi_e = \phi_1 + \phi_2$, $\phi_m = \phi_1 - \phi_2$, we can derive the following analytical expression for in-plane Poisson's ratio of hybrid patterns:

$$\nu_{WL,h}^s = \frac{ab \sin^2 \frac{\psi}{2}}{L' \cos^3 \frac{\psi}{2}} \left[\frac{\cos \alpha}{\sin \phi_1} \left(\frac{n_e \sin \phi_e}{L_e} + \frac{n_m \sin \phi_m}{L_m} \right) + \frac{\cos \beta}{\sin \phi_2} \left(\frac{n_e \sin \phi_e}{L_e} - \frac{n_m \sin \phi_m}{L_m} \right) \right] \quad (5.96)$$

It is easy to show that when $\nu_{WL,h}^s = 0$, the ratio n_m/n_e depends only on the folded state of the system given by ψ and α, β . Therefore, it is possible to tune the switching of Poisson's ratio to occur at different folded states by appropriately choosing the ratio n_m/n_e .

5.6.3 Mode locking during in-plane deformation

The interplay between the contrasting Poisson's ratios of the Eggbox and Miura mode unit cells coupled with the global Poisson's ratio of the hybrid patterns leads to the *mode locking* behavior. Theoretically, a Morph pattern can be transformed into various hybrid patterns through smooth kinematics. In practice, this could be achieved by applying in-plane rigid origami deformations (stretching) to the hybrid system. The ability of a hybrid pattern to transform into a different hybrid pattern depends on whether the applied deformations allow the individual unit cells to move away from or towards the transition point. When the global stretching (either extension or contraction) of the system causes the unit cells to move away from the transition (i.e. both ψ_e and ψ_m decrease), the unit cells are locked to remain in the existing Eggbox and Miura modes without any further scope for mode morphing (see Fig. 5.14(a) and (b)). On the other hand, when the global stretching of the system causes the unit cells to move towards the transition (i.e. both ψ_e and ψ_m increase), it is possible for the Eggbox and the Miura modes to interchange (see Fig. 5.14 (c) and (d)). As shown in Fig. 5.14, it is possible to obtain either mode locking or mode morphing by appropriately applying extension or contraction on hybrid patterns that have positive or negative global Poisson's ratio.

The most obvious mode locking in practice is the tensile mode locking, as elaborated in Fig. 5.15. For certain types of hybrid modes, if we stretch the hybrid pattern along the **L** (axial) direction, the Miura mode cells, which normally would smoothly transition into Eggbox mode under stretching, would rather lock themselves in Miura mode and fold toward flat-folded state II. Tensile mode locking happens when a hybrid pattern displays a positive Poisson's ratio globally, such that it shrinks in the lateral direction under stretching.

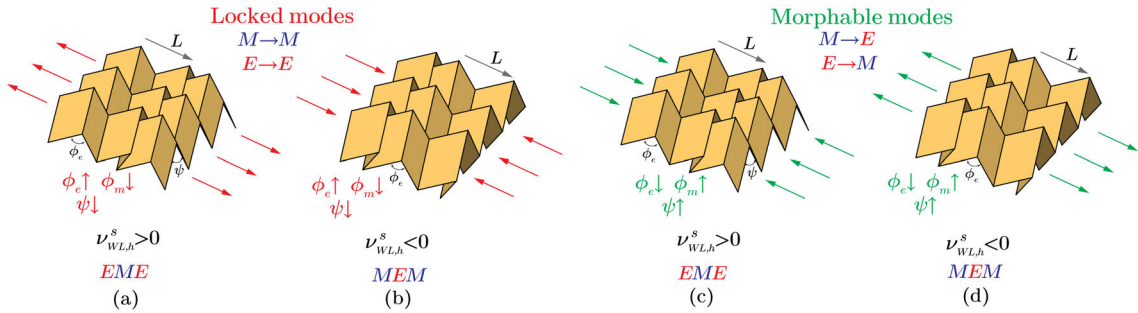


Figure 5.14: In-plane stretching of hybrid patterns. (a), (b) Mode locking phenomenon in which the Miura (M) and Eggbox (E) mode cells cannot change their mode as the deformation takes them away from transition. (c), (d) Deformations that take the Miura and Eggbox mode unit cells towards transition enabling morphability of hybrid patterns.

For a Miura mode unit cell, this means that it must contract in the axial direction (as well as the lateral direction), despite that the global pattern is expanding in the axial direction in which it is stretched, as illustrated in Fig. 5.15(b).

We remark that the mode locking of hybrid Morph pattern is topological. It locks the mountain/valley assignment of certain unit cells but still allows the pattern to fold smoothly as a rigid origami, which is different from motion locking as reported in the literature [142] that are geometrical because the rigid folding of an origami is stopped.

5.7 Concluding Remarks

The Morph pattern exhibits morphing characteristics by breaking mountain/valley assignment, which leads to smooth switching of Poisson's ratio across a very wide range of negative to positive values, and topological mode-locking as a consequence of kinematic bifurcation. Our analysis reveals that the Morph pattern exhibits Poisson's ratio with equal magnitude but opposite sign when subject to in-plane and out-of plane deformations. Moreover, we discuss hybrid patterns that can be created by coupling Morph unit cells in distinct modes, creating a tessellation with reprogrammable Poisson's ratio and topological mode-locking. The locking feature of the hybrid patterns can be useful in creating structures with multi-stability [43]. We envision that hybrid patterns can also have many applications

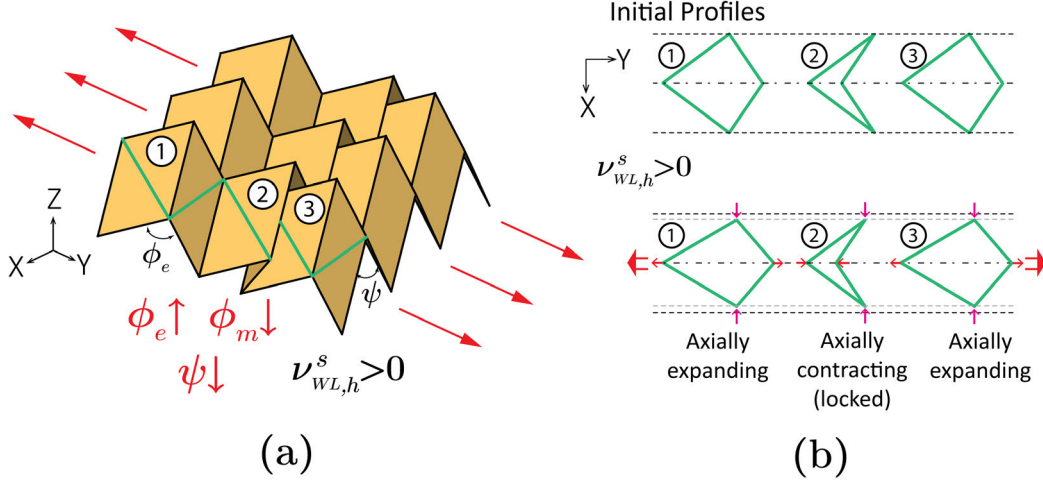


Figure 5.15: Mode locking due to extension in L direction when $\nu_{WL}^b > 0$, as depicted in Fig. 5.14(a). (a) The positive global Poisson's ratio implies contraction in the W direction, resulting in decrease of ψ_e and ψ_m . The oppositely signed unit cell Poisson's ratios of the two modes indicates that while ϕ_e increases, ϕ_m decreases, meaning the Miura mode cells are axially contracting, opposite to the global axial deformation. We say that the Miura mode cells with decreasing ϕ_m are locked because such a cell can no longer smoothly transition to its Eggbox mode in a rigid origami motion. (b) Contrasting global and local deformations that occur in hybrid patterns leading to mode locking behavior. The green lines represent the panel diagonals, whose projections provides a clean way of sketching the motions.

in topological mechanics due their ability to transform the symmetry of the system under in-plane deformations [139], [151], [161].

CHAPTER 6

PERIODIC ORIGAMI PATTERN WITH PROGRAMMABLE MULTI-STABILITY: BREAKING CONNECTEDNESS OF CONFIGURATION SPACE

Recently there has been a noticeable paradigm shift from avoiding instability to harnessing them [136], [137]. Applications to functional devices and mechanical metamaterials promotes research on multi-stable structures. In this Chapter, we propose an origami design, named the “Shrimp” pattern, that leads to multi-stable mechanical metamaterials. We show that the Shrimp pattern unit can be programmed to be either monostable or bistable, and the energy barrier between the bistable states can be tuned by geometric manipulations. The units possess regular shapes for easy assembly into multi-stable structures and metamaterials. Furthermore, the local variations of geometry can create complex but controllable energy landscape, leading to programmable multi-stability.

6.1 Introduction

Elastic structures with two or more possible equilibrium states can transition from one state to the other via a rapid process known as “snap-through.” Snap-through allows plants and animals to store elastic energy, and release it suddenly to generate rapid and powerful motions. Through a suite of structural modifications of their raptorial appendages, mantis shrimps generate forceful predatory strikes in a fraction of second, which is so fast that causes cavitation in the water [162], [163]. Venus flytraps snap their leaves together rapidly to capture insects, which is enabled by the doubly curved geometry of the leaves [164]. Ladybird beetles fold their wings in a non-rigid foldable origami pattern to stores elastic energy when stowed, which allows quick release of their wings when they start flying [11]. Similarly, the earwig wings have incompatible folding patterns, which remain open by a

bistable locking mechanism during flight, and self-folds rapidly without muscular actuation [12].

As suggested by the examples found in nature [11], [12], [164], origami patterns can organize geometry of thin sheets and membranes to produce functionality by harnessing their inherent elastic instabilities. There are many origami patterns that lead to structures with multi-stability. For instances, the square twist, the Kresling tube, and the hypar origami (as demonstrated in Chapter 3). However, we find two drawbacks of these patterns. First, many of them cannot be easily tessellated due to irregular geometry of unit cells, such as the Kresling tube. Second, most existing bistable or multi-stable pattern completely lose their rigid foldability, which means that any deformation away from the stable equilibrium states will exhibit bent and stretched panels [101] or hinges [12]. In contrast, the Shrimp pattern combines features of both rigid and non-rigid origami, allowing the pattern to be folded rigidly in a range of stable configurations.

In this Chapter, we propose a new origami pattern, named the Shrimp pattern, which is designed to be tessellatable, and combines the features of both rigid and non-rigid origami. We show that the bistability of a unit cell of this pattern can be programmed by a few geometric parameters. Tessellating the shrimp unit cells makes the multi-stable Shrimp pattern, which has application as multi-stable metamaterials [134], [165]. By programming the unit cell geometries, we can further achieve a controlled sequence of snap-through within the pattern.

6.2 Geometry of the standard “Shrimp” unit cell

The geometry of a standard Shrimp pattern unit cell is described in Fig. 6.1. The length parameters include panel width a , front panel length b , rare panel length c , and tail length d . The angular parameters include front panel angle α_F , rare panel angle α_R , and rib (triangle) panel angle α_B . For standard Shrimp pattern designs, edge length c satisfies the following

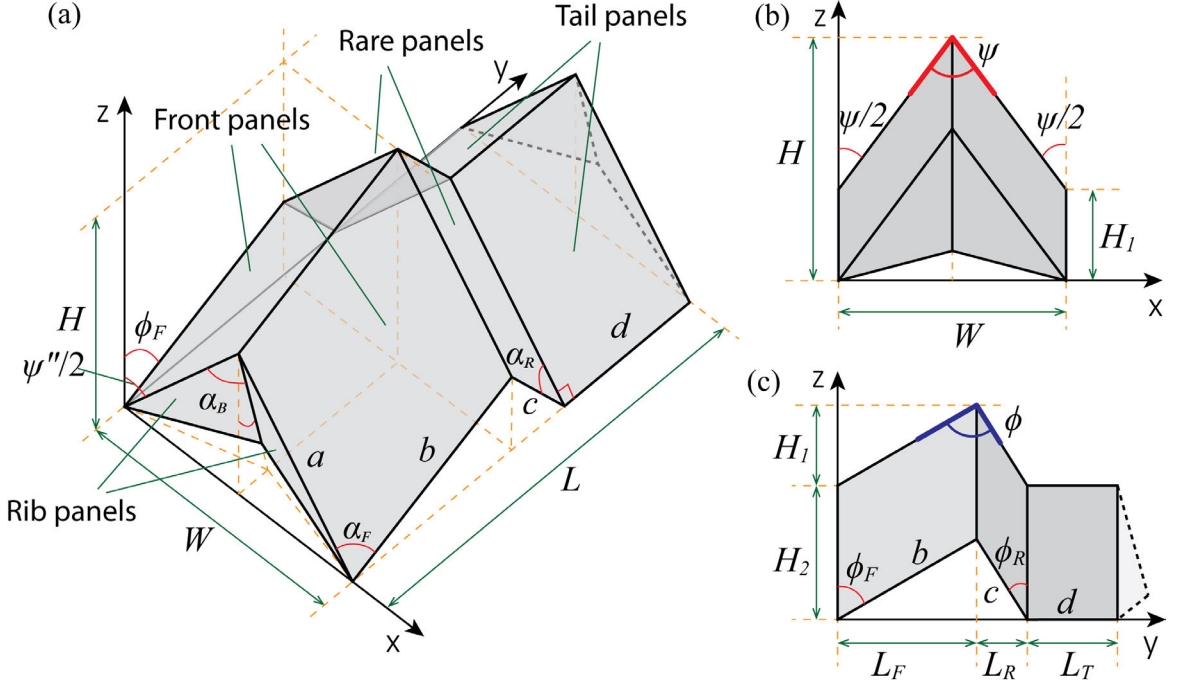


Figure 6.1: Geometry of a shrimp unit cell. (a) Isometric view. (b) and (c) side views.

condition:

$$c = \frac{a \cos \alpha_F}{\cos \alpha_R}, \quad (6.1)$$

The edges of length a lie in the xz -plane, as shown in Fig. 6.1. Although within each unit cell, the tail panels are not connected to the rib panels; in an assembly/tessellation of the Shrimp pattern, the rib panels are actually between the tail panels and front panels, and they should be attached to the last row of tail panels.

When $\psi \leq 2\alpha_B$, the Shrimp pattern allows rigid origami behavior with a single degree of freedom (DOF). The configuration is determined by any of the three edge inclination angles ($\psi/2$) ($= \psi_2$), ϕ_F , and ϕ_R , which are related as follows:

$$\cos(\psi/2) \cos \phi_F = \cos \alpha_F, \quad (6.2)$$

$$\cos(\psi/2) \cos \phi_R = \cos \alpha_R. \quad (6.3)$$

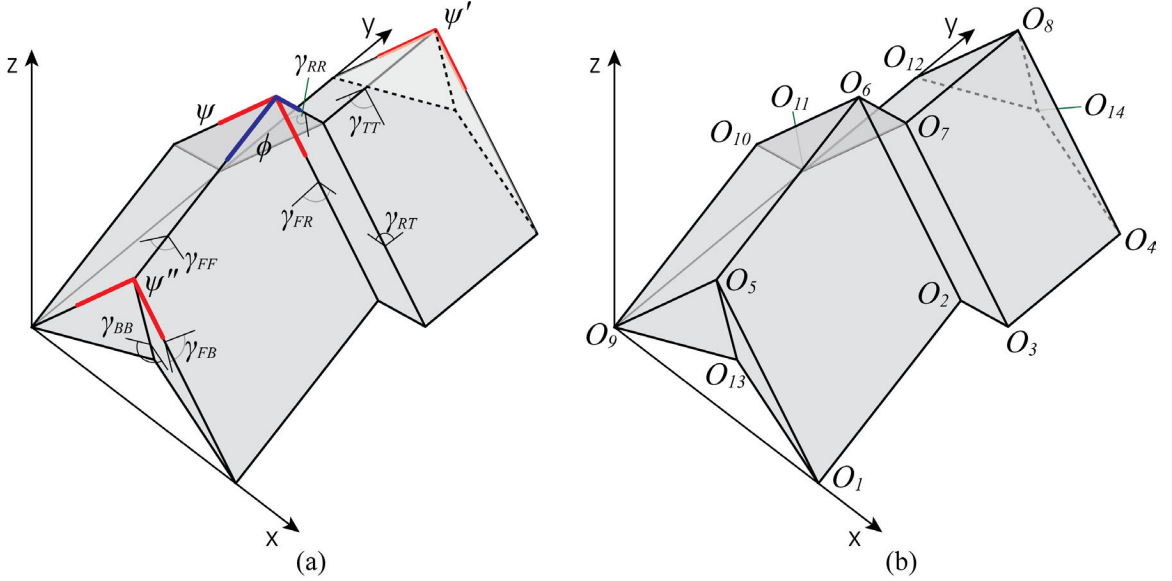


Figure 6.2: Labels of geometric quantities of a shrimp unit cell. (a) Dihedral folding angles. (b) Vertices.

We define the shaping angles of the Shrimp pattern by:

$$\phi = \phi_F + \phi_R, \quad (6.4)$$

$$\psi = \psi' = \psi''. \quad (6.5)$$

Accordingly, the heights (H, H_1, H_2), width (W), and lengths (L, L_1, L_2, L_3) of the shrimp unit cell are given by:

$$H_1 = b \cos \phi_F = c \cos \phi_R, \quad H_2 = a \cos(\psi/2), \quad H = H_1 + H_2, \quad (6.6)$$

$$W = 2a \sin(\psi/2), \quad (6.7)$$

$$L_F = b \sin \phi_F, \quad L_R = c \sin \phi_R, \quad L_T = d, \quad L = L_F + L_R + L_T. \quad (6.8)$$

To understand the folding of the Shrimp origami, it is also important to calculate the dihedral folding angles labeled in Fig. 6.2. We can derive that, when $\psi \leq 2\alpha_B$,

$$\gamma_{FR} = \sin^{-1} \left(\frac{\sin \phi_F}{\sin \alpha_F} \right) + \sin^{-1} \left(\frac{\sin \phi_R}{\sin \alpha_R} \right), \quad (6.9)$$

$$\gamma_{FF} = 2 \sin^{-1} \left(\frac{\sin(\psi/2)}{\sin \alpha_F} \right), \quad (6.10)$$

$$\gamma_{RR} = 2 \sin^{-1} \left(\frac{\sin(\psi/2)}{\sin \alpha_R} \right), \quad (6.11)$$

$$\gamma_{RT} = \frac{\pi}{2} + \sin^{-1} \left(\frac{\sin \phi_R}{\sin \alpha_R} \right), \quad (6.12)$$

$$\gamma_{TT} = \psi' = \psi = \psi'', \quad (6.13)$$

$$\gamma_{FB} = \pi - \sin^{-1} \left(\frac{\sin \phi_F}{\sin \alpha_F} \right) - \cos^{-1} \left(\frac{\tan(\psi/2)}{\tan \alpha_B} \right), \quad (6.14)$$

$$\gamma_{BB} = 2 \sin^{-1} \left(\frac{\sin(\psi/2)}{\sin \alpha_B} \right). \quad (6.15)$$

6.3 Creating topological bistability by breaking connectedness of configuration space

According to reference [125], when the different stable configurations of a multi-stable origami are not connected by any continuous rigid origami kinematic path, the origami is said to be topologically bistable, as its configuration space of rigid origami kinematics is disconnected. The vertex surrounded by the front and rare panels of the standard Shrimp pattern is the same as the Morph pattern investigated in Chapter 5. When there is no rib panel attached, the shaping angles ϕ and ψ ($= \psi' = \psi''$) are related by the following formula:

$$\cos \psi = \cos 2\alpha_F + \frac{2(\cos \alpha_R - \cos \alpha_F \cos \phi)^2}{\sin^2 \phi}, \quad (6.16)$$

which is plotted in Fig. 6.3, in terms of ψ' and ϕ .

However, owing to the existence of rib panels, ψ' and ψ'' cannot exceed $2\alpha_B$, and thus a certain range of folding (without the ribs) is blocked under rigid origami assumption, as indicated by the dashed lines in Fig. 6.3. The solid parts of the curves refer to the remaining rigidly foldable configurations of the Shrimp pattern, which is separated to two disconnected parts. The two limit configurations of the blocked range of rigid folding

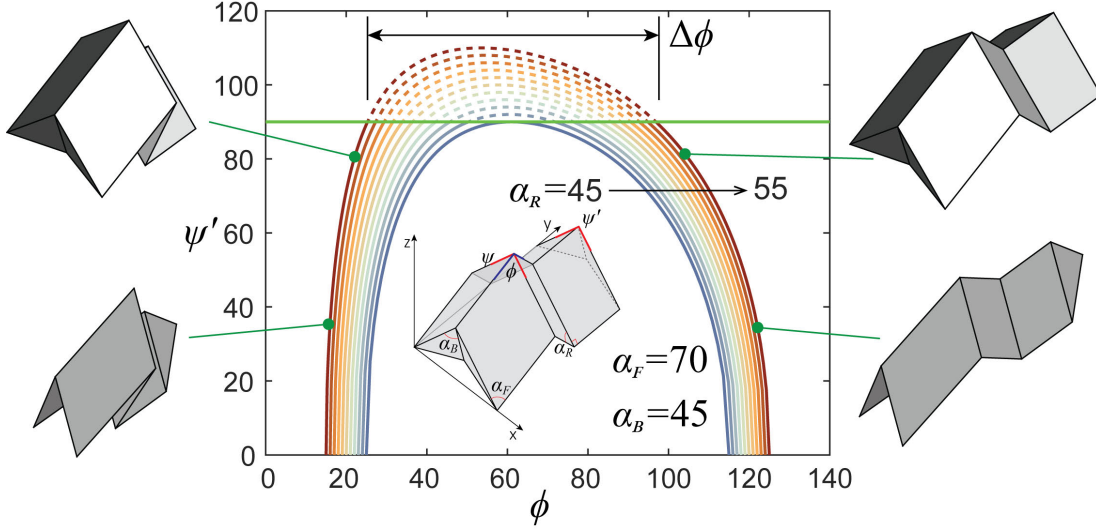


Figure 6.3: Configurations space of a Shrimp pattern in terms of ψ' and ϕ . The dashed portion of the curves cannot be reached kinematically under the assumption of rigid origami.

(dashed lines in Fig. 6.3) in terms of ϕ are given by:

$$\phi = \cos^{-1} \left(\frac{\cos \alpha_F}{\cos \alpha_B} \right) \pm \cos^{-1} \left(\frac{\cos \alpha_R}{\cos \alpha_B} \right). \quad (6.17)$$

We denote the difference between the two limit configurations as $\Delta\phi$,

$$\Delta\phi = 2 \cos^{-1} \left(\frac{\cos \alpha_R}{\cos \alpha_B} \right), \quad (6.18)$$

which becomes independent from α_F .

In reality, the compliance of materials offers extra DOF that allow the Shrimp pattern to transition between the two disconnected rigid origami configurational ranges through non-rigid deformation. The tail panels are added to allow the blocked range to be overcome by gentle panel bending; otherwise, the blocked range of rigid folding can only be overcome by stretching the materials, which is likely to generate rupture or other types of irreversible damages. Together, the addition of rib panels and tail panels leads to bistable snapping between the two disconnected parts of the rigid origami configurations of the Shrimp pattern. The conditions for the emergence of bistability is discussed later.

As illustrated in Fig. 6.4(a), the folding energy of the system increases as the pattern being folded away from the initial configuration, but the bending energy only appear within the blocked range of rigid folding, i.e. when $\psi > 2\alpha_B$. While the bending energy gradually vanishes after the range of non-rigid folding, the folding energy keeps increasing. Therefore, if the stored energy becomes smaller than the peak energy after the non-rigid deformation, the Shrimp pattern will experience bistability. We denote the initial configuration as Configuration 0, the peak energy state as Configuration 1, and the state after non-rigid folding as Configuration 2 (see Fig. 6.4(b)).

6.3.1 Estimating peak energy during the non-rigid folding range

Although the actual non-rigid deformation of the Shrimp pattern during the transitioning is a complex combination of bending, folding, and stretching, we may consider a simplified scenario to estimate the peak energy by assuming isometric deformations. We assume that only the front and tail panels will bend along one of their diagonals, as demonstrated in Fig. 6.4(a). Therefore, ψ can be different from ψ' and ψ'' , and can exceed $2\alpha_B$, as depicted in Fig. 6.4(b)-0.

Due to symmetry about the middle plane, we can consider that both front panels (or tail panels) experience the same amount of bending. We denote the bending angle of the front panels as δ_F , and the bending angle of the tail panels as δ_T . We define ρ as the rotation angle of edge O_1O_2 (see Fig. 6.4(b)-1), which can be approximated by:

$$\rho \approx \psi/2 - \alpha_B, \quad (6.19)$$

when the bending of panels are small. At vertex O_5 , using spherical trigonometry, we obtain:

$$\cos \delta_F = \frac{\cos \rho - \cos^2 \alpha_{Fc}}{1 - \cos^2 \alpha_{Fc}} \quad (6.20)$$

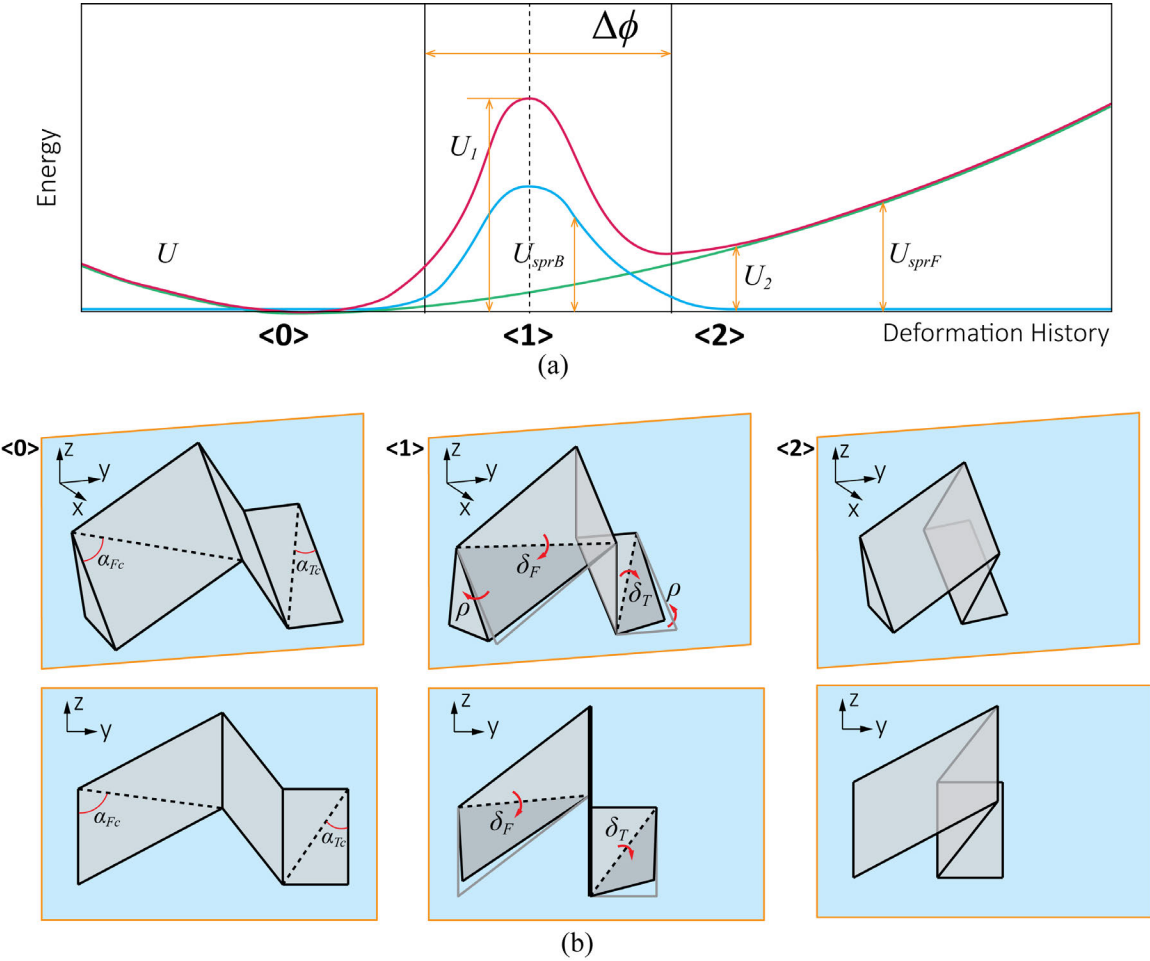


Figure 6.4: A hypothetical deformation process of a shrimp unit cell and the associated energy states of the system. (a) The change of system energy (U) for a deformed Shrimp pattern, as a summation of bending (U_{sprB}) and folding energy (U_{sprF}). Stretching deformation (and energy) are not considered by the isometry assumption. (b) The idealized configurations of a shrimp unit cell during its deformation. Configuration 0: The initial configuration. Configuration 1: The non-rigid deformed configuration during spanning, when the bending energy in the system reaches maximum. Configuration 2: The after-snapping configuration, we can see that the rare and tail panels are in mirror symmetric with their initial configuration about the panel spanned by O_2 , O_6 and O_{10} .

where,

$$\cos \alpha_{Fc} = \frac{a^2 - ab \cos \alpha_1}{a\sqrt{a^2 + b^2 - 2ab \cos \alpha_F}}. \quad (6.21)$$

For the tail panels, at vertex O_8 , we obtain:

$$\cos \delta_T = \frac{\cos \rho - \cos^2 \alpha_{Tc}}{1 - \cos^2 \alpha_{Tc}} \quad (6.22)$$

where,

$$\cos \alpha_{Tc} = \frac{a}{\sqrt{a^2 + d^2}}. \quad (6.23)$$

We can see that ρ is largest when $\psi = 2\alpha_R$, and consequently, δ_F and δ_T become maximal. Therefore, the total bending energy reaches peak when $\psi = 2\alpha_R$, when the two rare panels become coplanar. According to Eq. (6.20) and Eq. (6.22), the maximal bending angles are given by:

$$\delta_{F,max} = \cos^{-1} \left(\frac{\cos(\alpha_R - \alpha_B) - \cos^2 \alpha_{Fc}}{1 - \cos^2 \alpha_{Fc}} \right), \quad (6.24)$$

$$\delta_{T,max} = \cos^{-1} \left(\frac{\cos(\alpha_R - \alpha_B) - \cos^2 \alpha_{Tc}}{1 - \cos^2 \alpha_{Tc}} \right). \quad (6.25)$$

Hence, we obtain the peak bending energy as

$$U_{sprB,1} = k_0^B (\delta_{F,max}^2 + \delta_{T,max}^2). \quad (6.26)$$

Assuming the initial configuration of the Shrimp origami structure is at, the folding bending energy at $\psi = 2\alpha_R$ is calculated as,

$$\begin{aligned} U_{sprF,1} = & \frac{1}{2} k_0^F ((\gamma_{BB,1} - \gamma_{BB,0})^2 + 2(\gamma_{FB,1} - \gamma_{FB,0})^2 \\ & + (\gamma_{FF,1} - \gamma_{FF,0})^2 + 2(\gamma_{FR,1} - \gamma_{FR,0})^2 \\ & + (\gamma_{RR,1} - \gamma_{RR,0})^2 + 2(\gamma_{RT,1} - \gamma_{RT,0})^2 \\ & + (\gamma_{TT,1} - \gamma_{TT,0})^2), \end{aligned} \quad (6.27)$$

where the initial angles in Eq. (6.27) can be computed using Eq. (6.9) to Eq. (6.15) given ψ_0 and ϕ_0 . The deformed angles at Configuration 1 can be estimated by taking $\psi_1 = 2\alpha_R$ and $\phi_{R,1} = 0$ using the same set of equations. The total energy at peak is a combination of folding and bending energy:

$$U_1 = U_{sprB,1} + U_{sprF,1}. \quad (6.28)$$

Owing to the restricted kinematics, this estimated peak energy is greater than the actual peak.

6.3.2 Estimating stored energy after snapping

Configuration 2 is taken when the rare panels are at symmetric positions compared to the initial configuration (i.e. Configuration 0), that is when,

$$\psi_2 = \psi_0, \quad (6.29)$$

and,

$$\phi_2 = \begin{cases} \phi_{F,0} - \phi_{R,0}, & \text{if } \phi_0 = \phi_{F,0} + \phi_{R,0}, \\ \phi_{F,0} + \phi_{R,0}, & \text{if } \phi_0 = \phi_{F,0} - \phi_{R,0}, \end{cases} \quad (6.30)$$

where,

$$\begin{aligned} \phi_{F,0} &= \cos^{-1} \left(\frac{\cos \alpha_F}{\cos(\psi_0/2)} \right), \\ \phi_{R,0} &= \cos^{-1} \left(\frac{\cos \alpha_R}{\cos(\psi_0/2)} \right). \end{aligned} \quad (6.31)$$

At this configuration, only the angles of γ_{FR} , γ_{RR} , and γ_{RT} experience deformation, and they other folding hinges stay at the same angles as the initial configuration. The three dihedral angles can be derived based on Eq. (6.29) and (6.30), using Eq. (6.9) to Eq.

(6.15). Then we can compute the stored energy at Configuration 2 as:

$$U_2 = U_{sprF,2} = \frac{1}{2}k_0^F((2(\gamma_{FR,2} - \gamma_{FR,0})^2 + (\gamma_{RR,2} - \gamma_{RR,0})^2 + 2(\gamma_{RT,2} - \gamma_{RT,0})^2). \quad (6.32)$$

If exist, the bistable state with locally minimal energy happens before the assumed Configuration 2, thus Eq. (6.32) overestimates the minimal energy after the non-rigid folding. However, because Eq. (6.28) also overestimate the peak energy, when we use $\Delta U = U_1 - U_2$ to determine the existence of bistability, the error is reduced.

6.3.3 Determining emergence of bistability

As illustrated in Fig. 6.4, if $\Delta U = U_1 - U_2 > 0$, a local minimum of stored energy exists besides the initial configuration, and thus the Shrimp pattern exhibits bistability. This energy difference is affected by the geometry of the pattern, and material properties. Since we assume isometric deformations, according to Eq. (6.28) and Eq. (6.32), the material-associated parameter that influences the value of ΔU is k_0^B/k_0^F , the ratio between bending stiffness and folding stiffness.

Fig. 6.5(a) and (b) show the variation of ΔU with respect to the pairs of geometric parameters (α_F, α_R) , and (a, d) . We observe that α_R and a has positive influence on ΔU , while d has negative influence. We also find that α_F does not have significant influence on ΔU . The effect of k_0^B/k_0^F is plotted in Fig. 6.5(c) in pair with α_R . The emergence of the bistability is defined by the contour of $\Delta U = 0$, which is plotted in Fig. 6.5(d) as a function of α_R , d , and k_0^B/k_0^F . When k_0^B/k_0^F is larger, the Shrimp pattern exhibit bistability over a wider range of geometries.

6.4 Verifying bistable behavior by numerical simulations

To verify the analytical analysis about the bistable behavior of the Shrimp pattern unit cell, we conduct numerical simulations using the bar-and-hinge model. The implementation in

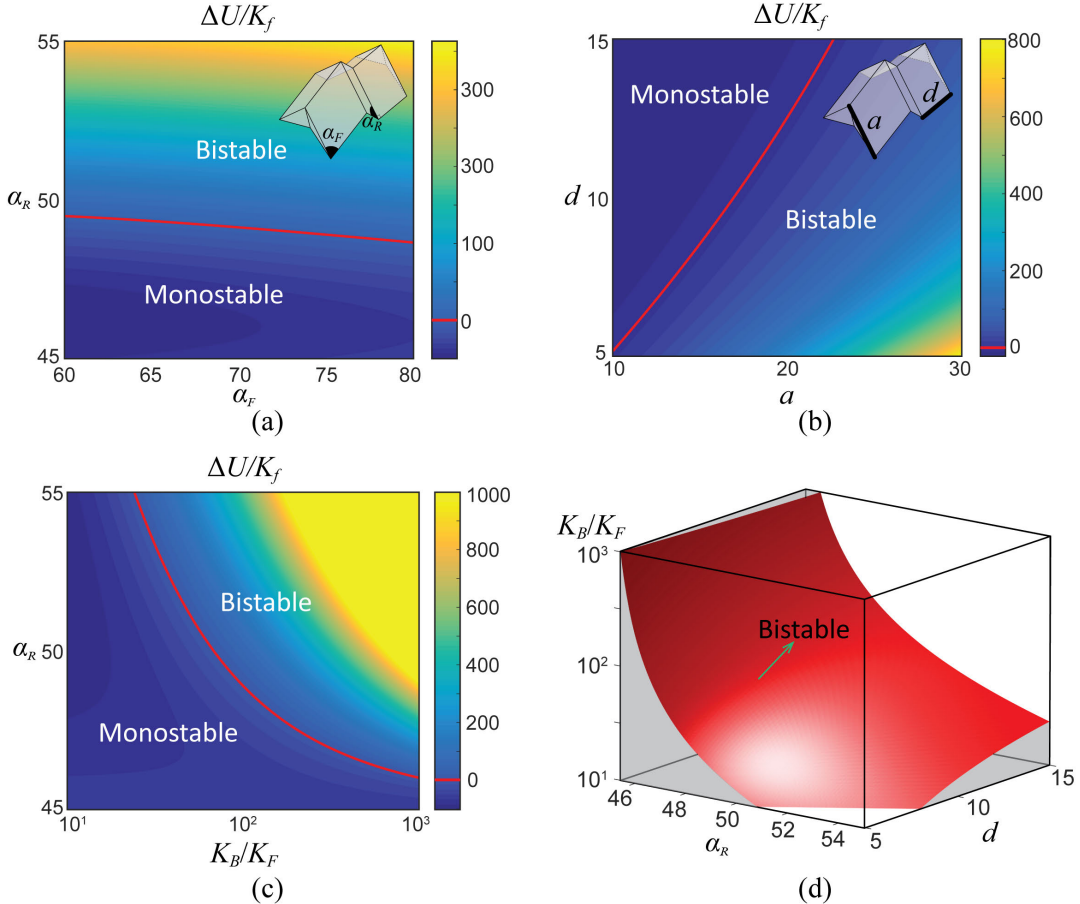


Figure 6.5: Programmable energy state of a shrimp unit cell. A positive energy difference ΔU indicates that the pattern is bistable. (a), (b), and (c) show how ΔU is affected by geometric parameters (i.e. α_F , α_R , a , d) and material properties (i.e. k_0^B/k_0^F). In (d), we plot the limit surface of the emergence of bistability in the configuration space spanned by α_R , d , k_0^B/k_0^F .

this work is based on the N5B8 discretization scheme [98]. The basic idea of the N5B8 discretization is explained in Chapter 2. We assume that the Young's modulus $E = 1\text{GPa}$, Poisson's ratio $\nu = 0.3$, and sheet thickness $t = 0.5\text{mm}$. The stiffness of folding hinges are assigned through a scalable formula [98], which is briefly explained in Section 2.2.7. We take the length scale factor L^* to be $30L_F$, relative to the length of each folding hinge, which yields an average ratio between bending and folding stiffness per length $k_0^B/k_0^F \approx 80$.

The results from numerical simulations of compressive folding are presented in Fig. 6.6. The boundary condition for the numerical analysis is shown in Fig. 6.6(a). In this study, we fix some geometric parameters as: $\alpha_F = 70^\circ$, $d = 10\text{mm}$, $a = 20\text{mm}$, and $b = 25\text{mm}$. When $\alpha_R > 49^\circ$, the bistable behavior starts to appear. The displacement u measures the movement of node O_8 in the direction of loading (i.e. $-y$). We normalize the displacement u by L_2 , such that (1) when $u/L_2 = 1$, the rare panels are approximately coplanar, similar to Configuration 1 in the analytical derivation; (2) when $u/L_2 = 2$, the rare panels snap inside the front panels, similar to Configuration 2 in the analytical derivation.

The negative forces in Fig. 6.6(b) during the bistable snapping display a long (negative) plateau without a strong peak, which behaves quite differently from most bistable structures, including the hyperbolic origami investigated in Chapter 3. The lack of strong negative peak force indicates that the snapping of the Shrimp pattern is a gentle process. We observe stiffening effect occurring immediately after the snapping, as indicated by the sharp increase of forces when $u/L_2 > 2$ in Fig. 6.6(b). As expected in the analytical analysis, if bistability appears, the stored energy of the Shrimp pattern experiences a peak near $u/L_2 = 1$, and a local minimum around $u/L_2 = 2$ (see Fig. 6.6(c)). As shown in Fig. 6.6(d), the analytical estimations of the energy difference ΔU agrees well with the numerically computed energy barriers. We record the angles of ψ' during the simulations. Compared with Fig. 6.3, we can clearly see that ψ' is kinematically constrained to be below $2\alpha_B$.

(= 90°).

The numerical simulations verify that the energy landscape of the Shrimp pattern is programmable, through geometric variations of the rare panel angle α_R . As α_R increases, both the peak force and magnitude of energy barrier (i.e. ΔU) increase accordingly. Such monotonic relationship allows for easy interpretation and manipulation of the mechanical properties of the Shrimp pattern.

6.5 Assembling “Shrimp” tessellations with programmable multi-stability

The programmable bistability of the Shrimp pattern unit cell allows us to create programmable multi-stability origami patterns by tessellating the shrimp unit cells. Fig. 6.7 shows an example of such designs. When three shrimp unit cells with different α_R 's are connected, under compression, based on the analysis in previous section, we can expect the unit with smallest α_R is going to snap first, and the unit with largest α_R will snap lastly. The numerical simulation shown in Fig. 6.7 verifies the expectation. The other geometric and material parameters are taken as the same as the numerical example in Section 6.4.

6.6 Fabricating the “Shrimp” pattern

The Shrimp pattern contains non-developable vertices, thus it is cannot be folded from a single piece of flat sheet, like the Miura-ori. We fabricate the Shrimp pattern by gluing thin sheets, or 3D printing.

We adopt a double layer technique to glue stripes of thin sheets, which is demonstrated in Fig. 6.8. The advantage of this strategy is that we obtain uniform thickness over the panels (double layers) and creases (single layer). The creases are treated by perforation or etching to reduced its folding stiffness. As we can observed from Fig. 6.5, to enable bistability, the Shrimp pattern need to have a large k_0^B/k_0^F ratio. By making the panels thicker, the double layer technique further increase the ratio of k_0^B/k_0^F .

Additive manufacturing technologies provide another venues of actualizing the Shrimp

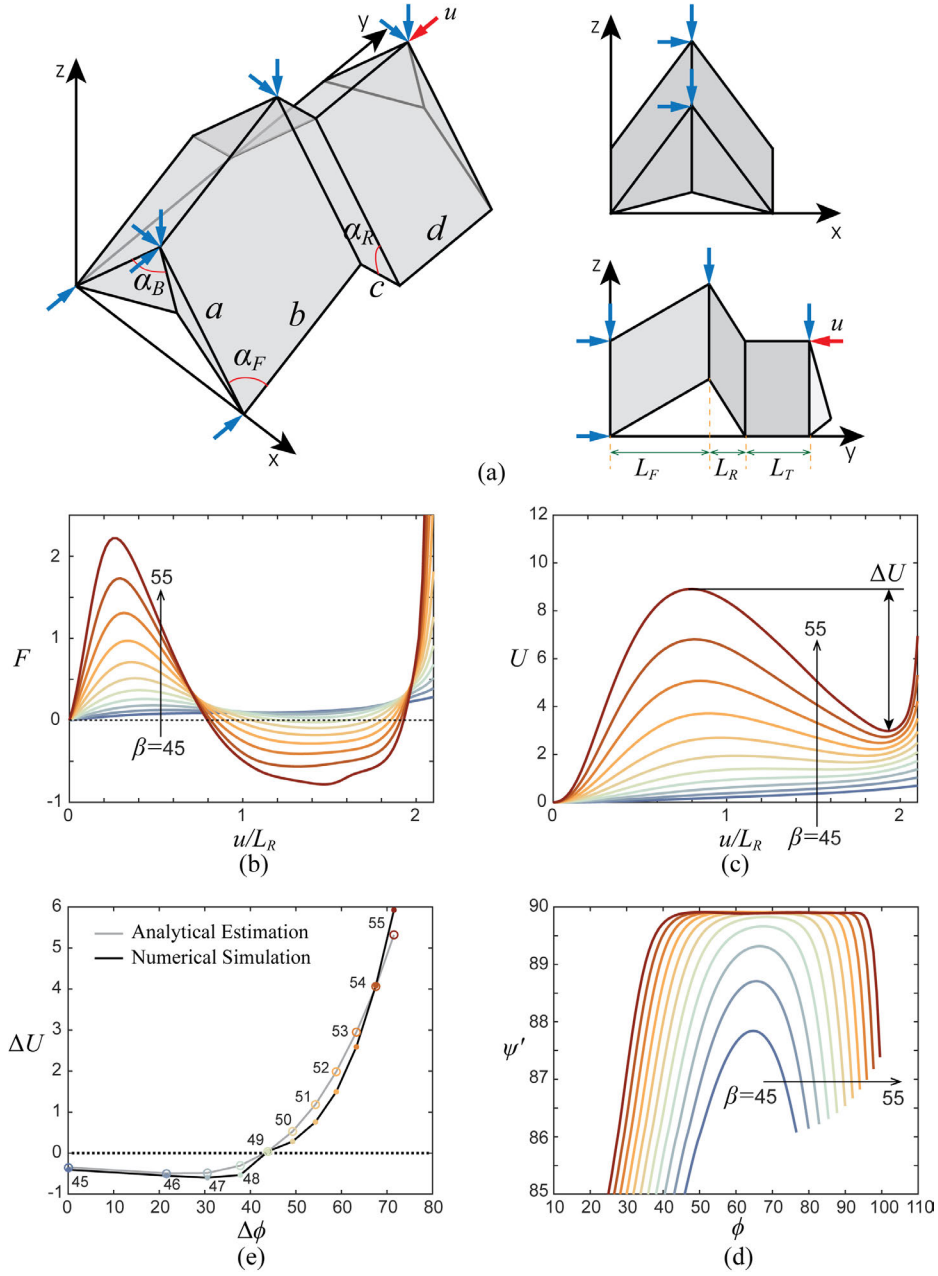


Figure 6.6: Numerical verification of the programmable energy landscape of shrimp unit cell. (a) Boundary conditions for the numerical simulation. Blue arrows are fixed DOF, and the red arrow refers to applied displacement u . (b) Force vs. (normalized) displacement curve. The displacement u is normalized by L_R of each design. We investigated the performance of a shrimp unit cell α_R varies from 45° to 55° . (c) The stored energy vs. (normalized) displacement. (e) Comparison between the analytical estimation of ΔU as formulated in Section 6.3 with the numerically obtained values. When the structure is monostable, ΔU is taken as the difference between the stored energy at $u/L_R = 1$ and $u/L_R = 2$, for the numerical models. (f) The opening of angle ψ' during deformation. We see that ψ' is always smaller than $2\alpha_B$ ($=90^\circ$).

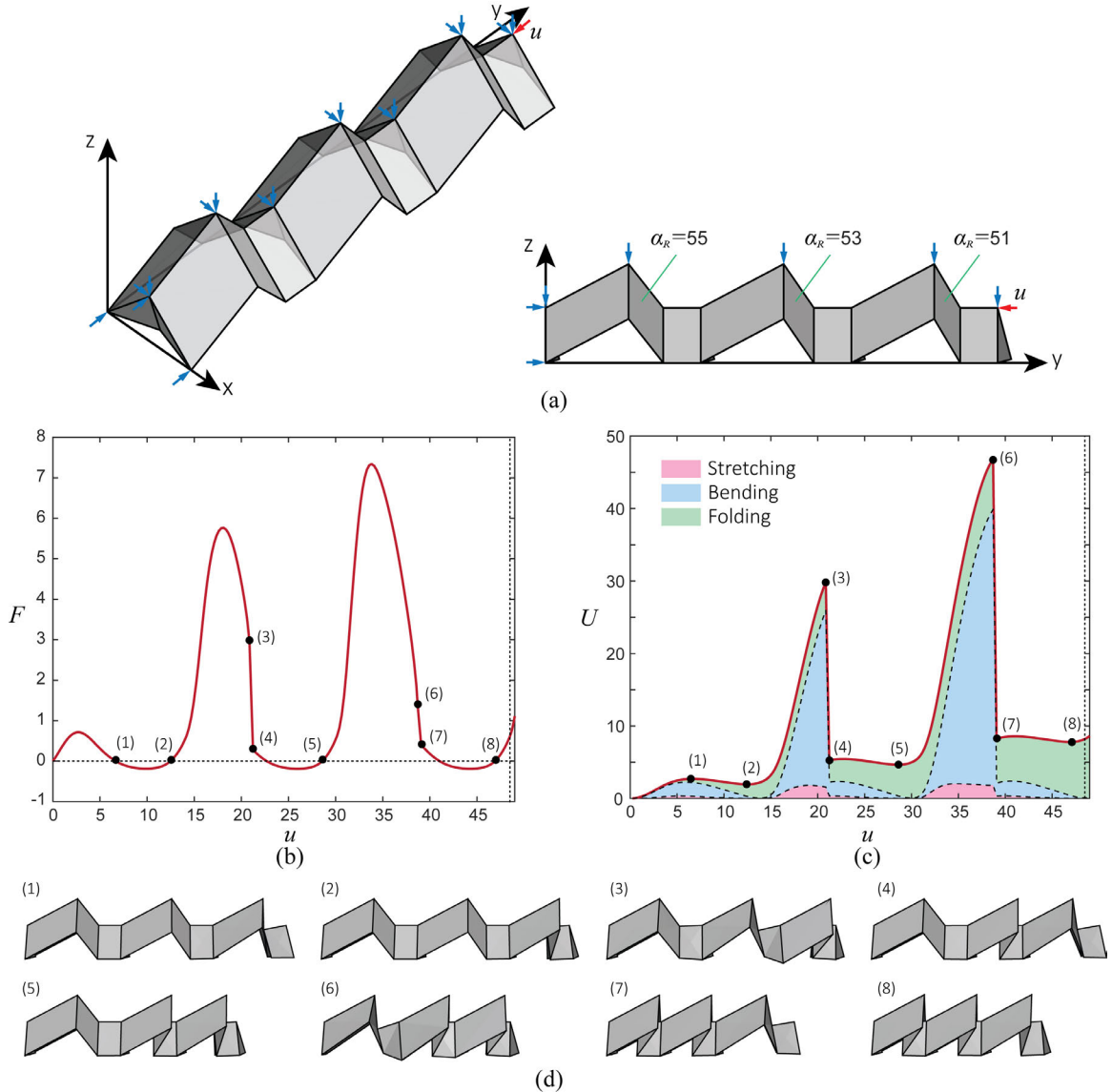


Figure 6.7: Sequential snapping of a 3×1 Shrimp pattern tessellation with programmed multi-stability. (a) Geometry and boundary conditions. (b) Force vs. displacement curve, with critical configurations labeled from (1) to (8). (c) Stored energy vs. displacement. Contributions from bending, folding, and stretching of panels are indicated. (d) Side views of the 8 critical configurations during the deformation history.

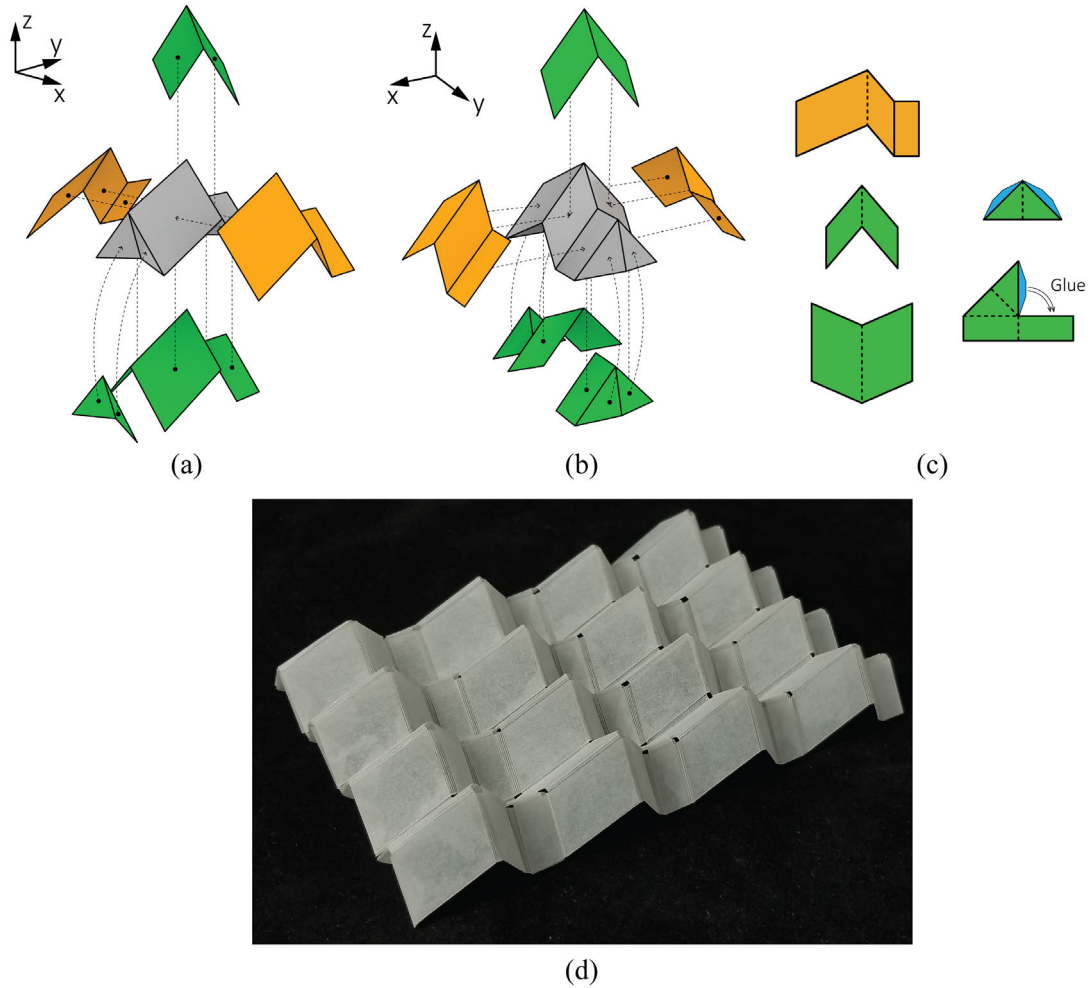


Figure 6.8: The double layer technique. We fabricate developable stripes and glue them in two directions to make the non-developable Shrimp pattern. We demonstrate the fabrication of a single unit cell in this figure. The correspondence of panels are shown in (a) and (b), from difference view angles. The designs of developable stripes are shown in (c). (d) A 4×4 patch of Shrimp pattern made using the double layer technique. The sheet material we used is the 63lb premium ICE paper (Durilla Durable Papers, CTI Paper USA, WI).

pattern design. A automatic algorithm is written in Rhino/Grasshopper to generate print-able solid given an origami design. The printable solid is thicker within panels and thinner along folding hinges, in order to differentiate their stiffness. The thin hinges and thick panels can also be printed with different materials. The procedure is outlines in Fig. 6.9.

6.7 Concluding Remarks

We propose a new Shrimp pattern which enables programmable and reconfigurable origami materials. The Shrimp pattern is created by modifying the geometry of a rigid foldable pattern to block a range of rigid folding kinematics, which can only be overcome by non-rigid origami deformation. The non-rigid deformation separates the rigid folding kinematics of a Shrimp pattern into two disconnected ranges. Thus the Shrimp pattern can behave like both rigid origami and non-rigid origami. We study the connection between the geometry of a shrimp unit cell and its bistable behavior. An analytical estimation function is derived to approximate the energy barrier between the two stable states of a shrimp unit cell. We conduct numerical simulations to verify the analytical predictions and find very good agreement. We demonstrate a Shrimp pattern with 3×3 unit cells for its programed sequence of snapping, using nonlinear numerical simulations. In addition, we discuss approaches to easily fabricate such developable patterns. For instance, we can glue developable stripes in a two-way, double layer manner, or 3D print the pattern with reduced thickness or stiffness near the folding hinges.

In the future, we plan to conduct experiments on the Shrimp pattern, to investigate the performance of the samples provided by different manufacturing techniques. We will also explore 3D stacking of the Shrimp pattern, towards applications as advanced cellular materials.

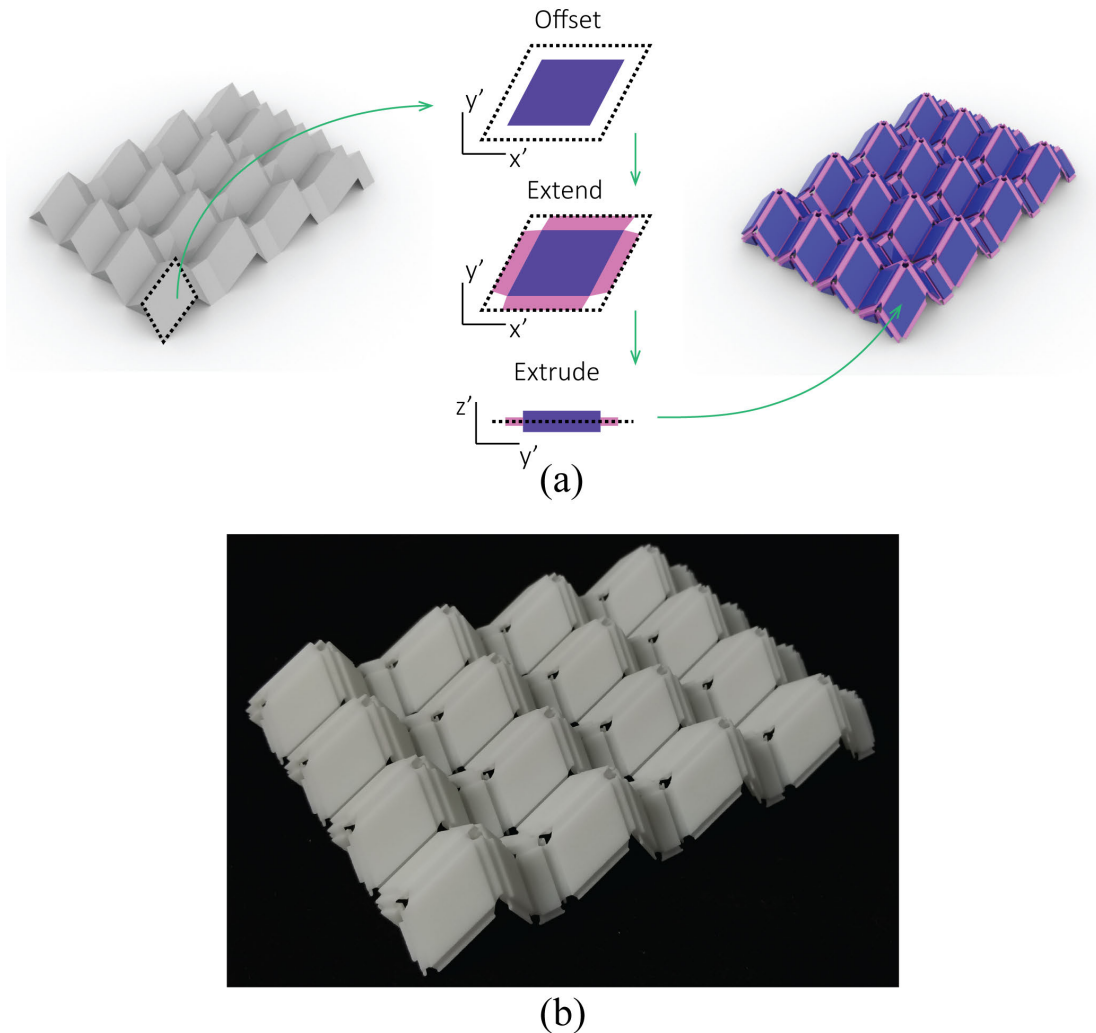


Figure 6.9: Shrimp pattern by 3D printing. (a) Procedure to prepare 3D printable solid from geometric data of a Shrimp origami surface. (b) A 3D printed Shrimp pattern using the Selective Laser Sintering (SLS) technology. The sample shown in (b) is printed by selective laser sintering (SLS) technology using a rubbery TPU material.

Part II

Tensegrity

CHAPTER 7

TENSEGRITY TOPOLOGY OPTIMIZATION BY FORCE MAXIMIZATION ON ARBITRARY GROUND STRUCTURES

This chapter presents an optimization approach for design of tensegrity structures based on graph theory. The formulation obtains tensegrities from ground structures, through force maximization using mixed integer linear programming. The method seeks a topology of the tensegrity that is within any given geometry, which provides an understanding of the tensegrity design from a geometric point of view. Although not explicitly enforced, the tensegrities obtained using this approach tend to be both stable and symmetric. Borrowing ideas from computer graphics, we allow “restriction zones” (i.e. passive regions in which no geometric entity should intersect) to be specified in the underlying ground structure. Such feature allows the design of tensegrity for actual engineering applications, such as robotics, in which the volume of the payload needs to be protected. To demonstrate the effectiveness of our proposed design method, we show that it is effective at extracting both well-known tensegrities and new tensegrities, some of which are prototyped with the aid of additive manufacturing.

7.1 Introduction

Tensegrity has shown significant potential for engineering applications [166]. The idea has been used to make structures that are deployable, actively tunable, and light weight [1], [2], [50], [58], [59], [101], [166]–[169]. Because design of new tensegrity for specific applications is challenging, most applications rely on existing tensegrity forms. Some analytical and numerical approaches have been proposed in the literature for from-finding of tensegrity.

The design of a tensegrity has two main aspects: the topology and the geometry. We

can classify the form-finding methods into two groups: the topology design method and the geometry design method. The distinction is based on the way to achieve self-equilibrium of the structure during design: by adjusting either the topology, or the geometry. In a typical geometry design method, the topology of the tensegrity is first defined, then the geometry evolves to achieve self-equilibrium [170]–[174]. Most numerical form-finding approaches fall into this group. On the contrary, in a topology design method, the geometry is specified a priori, while the topology evolves to ensure self-equilibrium [175]–[179]. The two groups are not exclusive from each other. A method can belong to both groups, for example, design by intuition. A detailed review of form-finding methods is presented in Section 7.2.

Here we propose a numerical approach for the design of tensegrity in the category of the “topology design method”. We perform a mixed integer linear programming (MILP) on ground structures to extract the tensegrity design. The ground structure method has been used in the field of (structural) topology optimization for a long time [180]–[182]. It provides a very dense set of potential members and joints where the desired structure can be extracted through the optimization process. In the topology optimization of tensegrity, the method selects members from the ground structure and finds the associated self-equilibrating prestress forces. All joints have fixed coordinates during the optimization, featuring a prescribed geometry of the tensegrity.

The originality and impact of this research is enabled by two main concepts: the development of a new tensegrity form-finding formulation, which yields effective design of tensegrities with fixed geometry; and the extension to use arbitrary shapes as the building blocks, with the possibility of concave geometric constraints such as holes and openings. The proposed formulation is simple, computationally efficient relative to similar formulations [175]–[179], and often converges to symmetric and stable structures. Borrowing the techniques that we have previously developed on the generation of complex three dimensional ground structures [182], we can impose different passive zones in the ground structure, which is useful for designing tensegrities aimed at actual engineering applica-

tions. For example, in the design of tensegrity for outer space explorers [1], some interior spaces need to be reserved for payloads. Combining these new features, the present formulation is able to reproduce many of the known forms of tensegrity, as verified in Section 7.4. With the confidence given by the verification study, we also show the discovery and design of new tensegrity structures, as presented in Section 7.4 and 7.5. Some of the designs are realized with actual models. We create a simple procedure aided by 3D printing technology to build tensegrities, which is described in Section 7.7.

7.2 Overview of form-finding methods

In this section, we cast the forming-finding problem of tensegrity in a generic form, and discuss how different methods fit into the framework. As a kind of prestressed discrete structure connected by joints, the configuration of tensegrity is totally defined by the following components:

- (1) Topology, which can be described using a graph G
- (2) Geometry, which is defined by the coordinates \mathbf{p} of the nodes
- (3) Self-equilibrium state, which contains the self-equilibrating prestress forces in the members (stored in a vector \mathbf{F})

The topology of such structures can be described using a graph G , which contains a set of vertices V and edges E , where edges reflect the pairing of vertices. The vertices of the graph can be interpreted as the indexing of the nodes of a tensegrity structure, and the edges represent the members. The geometry of a tensegrity is a map that assigns each vertex in the graph with a coordinate in the Euclidean space \mathbb{R}^d of dimension d . In this work, we restrict our scope to $d = 3$. The geometry can be represented by \mathbf{p} , a $3N_V \times 1$ vector that stores the (x, y, z) coordinates of each node sequentially. Furthermore, an associated self-equilibrium state is essential for a tensegrity structure by definition. The self-equilibrating

state is sustained by a set of forces attached to each member of the structure, such that the struts are in compression and cables are in tension.

The form-finding of tensegrity structures consists of finding a graph with associated geometry over the vertices and self-equilibrating forces over the edges. In general, a form-finding problem of tensegrity can be expressed as follows:

$$\text{Find: } G, \mathbf{p}, \mathbf{F} \quad (7.1a)$$

$$\text{such that: } \mathbf{B}(\mathbf{p}, G)\mathbf{F} = \mathbf{0} \quad (7.1b)$$

$$T(G) \leq n \quad (7.1c)$$

$$\mathbf{u}^T \mathbf{K} \mathbf{u} > 0, \quad \text{for any nontrivial displacement } \mathbf{u} \quad (7.1d)$$

The equilibrium matrix \mathbf{B} is determined by \mathbf{p} and G (see Section 7.3.5 for its derivation). The prestress forces \mathbf{F} should self-equilibrate the tensegrity, as stated in condition (7.1b). The self-equilibrating prestress forces are homogeneous solutions of the static equilibrium equations, and thus tensegrity structures are statically indeterminate structures. The term \mathbf{K} is the tangent stiffness matrix of the tensegrity which depends on the topology G , geometry \mathbf{p} , prestress forces \mathbf{F} , as well as member properties such as cross-sectional areas and material properties. Condition (7.1c) is a topological constraint which restricts the number of compressive members that can meet at each vertex. For Class-1 tensegrity, $n = 1$, that is, the compressive members are all disconnected. In order to ensure the tensegrity structure is free-standing, we also need to examine the stability. Condition (7.1d) is the stability requirement which states that the quadratic form of the tangent stiffness matrix with respect to any small nontrivial displacement of nodes is positive, which, in addition to the equilibrium constraint, implies that the total potential energy of the structure at its initial state is at a strict local minimum. The infinitesimal displacement of nodes, i.e. \mathbf{u} , is trivial if it represents a rigid-body motion or it is a zero vector. It is equivalent to say that \mathbf{K} is

positive definite after constraining the rigid-body motions. Assuming the elastic structure undergoes very small deformations, the tangent stiffness matrix is composed of a linear stiffness matrix \mathbf{K}_E and a geometrical stiffness matrix \mathbf{K}_G [53], [183], [184]. Because we assume that the strains in members are small, including prestrains (i.e. initial deformations) induced by the prestress, then it is sufficient to construct only the so-called “stress matrix” [185] as an approximation to the complete geometric stiffness matrix [166], [183], [184]. A brief derivation is presented in Section 7.3.5.

The above discussed stability condition is the minimum potential energy stability. However, the tangent stiffness matrix requires information about member properties, which can be cumbersome for preliminary studies [53]. There are two other criteria that are usually used in the study of stability of tensegrities, namely, prestress-stability and super-stability. Assume the rigid body motions are already properly restricted for a tensegrity. Prestress-stability requires that the quadratic form $\mathbf{u}_M^T \mathbf{K}_G \mathbf{u}_M$ be positive, for all $\mathbf{u}_M \in \{\mathbf{u} : \mathbf{B}^T \mathbf{u} = \mathbf{0}, \mathbf{u} \neq \mathbf{0}\}$. The transpose of the equilibrium matrix is the compatibility matrix [183]. A special case of prestress-stability is when the compatibility matrix has full row rank, which indicates there is no \mathbf{u}_M , and such a tensegrity is said to be infinitesimally rigid [52]. We clarify here that \mathbf{u}_M are not the first order mechanisms of the tensegrity, which are theoretically richer than \mathbf{u}_M as defined by Connelly and Whiteley [52], because \mathbf{u}_M preserves the lengths of all members while a first order mechanism of a tensegrity structure allows the cables to be shortened (i.e. slacked). When a tensegrity is said to be kinematically determinate, it actually means that the dual truss structure (if we replace all the members in a tensegrity with bars) that has the same geometry and topology is kinematically determinate. Notice that a kinematically determinate tensegrity is not equivalent to a kinematically determinate truss. An infinitesimally rigid truss is structurally stable, however, an infinitesimally rigid tensegrity may or may not be structurally stable without prestress because of slackness of cables. As proved by Connelly and Whiteley [52], an infinitesimally rigid tensegrity is only guaranteed to be stable with the

presence of prestress. In addition to the prestress-stability, if the geometrical stiffness matrix \mathbf{K}_G (or the stress matrix in current context) is positive semi-definite with maximal rank that equals to $3N_V - d(d + 1)$ [166], [185], then the structure is super-stable. In general, super-stability ensures minimum potential energy stability of the structure; however, a high level of prestress can make a super-stable tensegrity unstable owing to the significant initial deformations induced by prestress [184]. Therefore, we assume that the prestrains of members are small. Super-stability is usually preferred because pretress-stability is only a necessary condition for a stable structure [53]. In many form-finding approaches, condition (7.1b) and (7.1c) are the basic constraints, while condition (7.1d) may not be considered at first since it complicates the form-finding process. It is usually checked *a posteriori*, i.e. after the design is obtained.

The tensegrity design problem has been solved using intuition, analytical methods, and numerical methods. Analytical and intuitive methods of form-finding seek the topology and geometry simultaneously [186]. Only a small number of known solutions have been obtained analytically or based on intuition, and application of these solutions is limited due to the small number of known configurations. Numerical form-finding methods are usually done by first fixing either the topology or the geometry, and then finding the other to achieve self-equilibrium. Geometry design methods fix the topology and search for the geometry of a tensegrity as well as the corresponding self-equilibrium state. Examples of geometry design methods are adaptive force-density method [172], free-forming method [171], dynamic relaxation method [187], and Monte Carlo form-finding method [188]. Because one topology can have many geometries that are associated with a set of self-equilibrating forces, the obtained geometry always has some arbitrariness. The initial assignment of the topology is also tricky. Typically it is based on heuristic rules evolved from planar diagrams [170], [171]. Thus, if such methods are used to generate tensegrities with many members possessing a large space, a common characteristic of the final results are that the connectivities are local and the obtained geometries become hollow.

Topology design methods, which fix the geometry of the tensegrity and search for the topology and the underlying self-equilibrium state, have only emerged in recent years [175]–[179]. A ground structure is used to provide the candidate members for the self-equilibrating forces to attach to, and the topology of the tensegrity is determined as a consequence. A typical drawback of such method is that, due to the discrete nature of the topology, the problem is usually difficult to solve. However, the advantage is that one does not need to prescribe the topology, which is hard to guess at an initial design stage. Ehara and Kanno [175] proposed a two-step mixed integer linear programming (MILP) formulation, in which they first maximize the number of struts and then minimize the number of cables. Kanno [176]–[178] explored other one-step formulations with various objective functions and constraints, for example, minimization of total length of cables, minimization of compliance under some external loads, implicit symmetry constraint, kinematic indeterminacy constraint, contact constraint, etc. In this work, we propose a different objective function defined solely on the continuous variables in the MILP, which implicitly promotes stability and symmetry of the optimized design.

7.3 Topology optimization formulation

The proposed form-finding formulation is an optimization approach based on the ground structure method. The formulation does not enforce the stability of the tensegrity, but we will see that the method is prone to converge to a stable tensegrity. The obtained designs also inherit the symmetries possessed by the initial ground structures.

7.3.1 Formulation

Denote G_g as the graph that represents the topology of the ground structure. Its vertices V_g and edges E_g are the sets of all nodes and members respectively. The force vector \mathbf{F} contains the forces in members (i.e. E_g), which are the design variables. Any nonzero entry in the solution implies the existence of a corresponding member. A force attached to

member e with $F_e < 0$ is a compressive force. The proposed form-finding method takes the following mathematical form:

$$\max_{\mathbf{F}} \quad \mathbf{1}^T \mathbf{F} \quad (7.2a)$$

$$\text{s.t.} \quad \mathbf{B}\mathbf{F} = \mathbf{0} \quad (7.2b)$$

$$\sum_{e \sim v} \chi(F_e) \leq n, \forall v \in V_g \quad (7.2c)$$

$$-1 \leq F_e, \forall e \in E_g \quad (7.2d)$$

$$\text{with: } \chi(F_e) = \begin{cases} 1, & F_e < 0 \\ 0, & F_e \geq 0 \end{cases} \quad (7.2e)$$

The indicator function χ is a binary operator that indicates the presence of struts, as stated in Eq. (7.2e). The notation $e \sim v$ denotes that the edge e is incident on vertex v . In other words, member e is connected to vertex v . Thus, the second constraint in (7.2c) enforces the discontinuity of struts. The compressive forces are constrained with a maximal magnitude in (7.2d), as the null space of \mathbf{B} is unbounded. Physically, for a finite self-stressed discrete structure, the entries of a non-trivial \mathbf{F} cannot be all positive or all negative – thus, it is enough to impose only the constraint (7.2d) on the magnitude of compression forces to ensure that the feasible domain is bounded. Members in the ground structure that are not attached with any force are excluded from the optimized structure.

The trivial solution $\mathbf{F} = \mathbf{0}$ is always feasible and any nonzero feasible solution makes a tensegrity if neglecting the stability requirement. To find a desired solution to this under-determined system, an additional criterion is necessary. Here we choose to maximize the sum of forces in the structure, that is, the difference between total tension and compression. Intuitively, this objective will prompt structures that span the maximal space bounded by the ground structure such that we avoid trivial solutions. Based on observation, the objective function seems to favor a larger number of struts. A heuristic explanation is given as

follows. To maintain equilibrium, when the total compression in the structure increases, the total tension should increase accordingly, but usually at a faster rate (based on observation). Therefore, the difference between the sum of absolute tension and the sum of absolute compression, which is our objective function, tends to increase as the total compression increases. As the compressive force in each member is bounded, a larger number of compressive members are favored, possibly providing a higher sum of the compressive forces.

In addition to avoiding trivial solutions, the proposed objective leads to tensegrities with two other desirable properties. *First, the objective tends to generate tensegrity structures that are stiff and stable.* Note that as the difference between total tension and total compression is maximized, the ratio of total compression to total tension is minimized. This ratio can be regarded as a measure for the average angle between struts and cables, as illustrated in Fig. 7.1. When the ratio of total compression to total tension is smaller, the average angle between struts and cables is larger (i.e. closer to orthogonal). From a structural engineering point of view, each strut is provided with more efficient bracing by the cables that will help to stabilize the prestressed structures. An example from daily life is the bicycle wheel, in which the compressive forces are almost orthogonal to tensile forces.

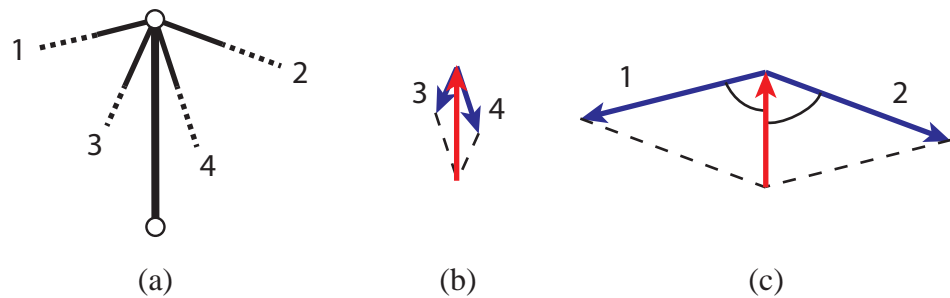


Figure 7.1: Preference of larger angle between struts and cables by the objective function. (a) A vertex in the ground structure connecting one member that has already been decided to be a strut (shown with a solid line) and four candidate cable members (shown with dashed lines). For a given compression load in the strut, if cables 3 and 4 are selected as in (b), the sum of tension and the average angle between struts and cables are small. If cables 1 and 2 are selected as in (c), the sum of tension and the average angle between struts and cables are large, which is preferred according to the objective function.

Furthermore, *the formulation encourages convergence to a structure that preserves some symmetries of the prescribed ground structure*. Suppose we have a symmetric ground structure G_g associated with a non-degeneratable symmetry group H that contains some transformations $h_i \in H$. Each transformation h_i of nodes and members of the ground structure is a symmetry operation under which the structure is unchanged [53], [189], [190].

Because this problem is a discrete programming problem which is complicated, we first look at a relaxed version of formulation (7.2) to check the symmetry preserving property of the optimal solution to this force maximization problem. Note that by increasing the integer n in constraint (7.2c), the topological constraint becomes inactive and we achieve a linear programming (LP) problem. We first show that when the topological constraint is inactive, the optimal solution of the resultant LP problem could preserve all symmetries of the initial ground structure. Let \mathbf{F} be a feasible solution of the LP problem that satisfies all the constraints. Since the objective function pushes more tension than compression, we can consider only \mathbf{F} 's with $\mathbf{1}^T \mathbf{F} \geq 0$. If $\mathbf{1}^T \mathbf{F} \leq 0$, we can simply multiply \mathbf{F} by a factor of -1 . Let G represent the topology of the structure indicated by \mathbf{F} . There exists a scalar $\xi \geq 1$, such that:

$$\min(\xi \mathbf{F}) = \min_i (\xi F_i) = -1. \quad (7.3)$$

Clearly, $\xi \mathbf{F}$ is a feasible solution, and it yields maximal objective on topology G along direction \mathbf{F} . Associated with G , suppose there is a non-degeneratable symmetry group K that is a subgroup of H , with symmetry operations $k_i \in K$, such that $k_i(G) = G$. If K is not equal to H , we can construct a new solution:

$$\mathbf{F}' = \mathbf{F}/(m+1) + \sum_{j=1}^m h_j(\mathbf{F})/(m+1), \text{ with } h_j \in H, h_j \notin K. \quad (7.4)$$

The number m counts the number of symmetry operations h_j as defined in Eq. (7.4). By applying a transformation h_j ($\notin K$) to G , we obtain a structure represented by $h_j(G)$, which is a different subset of G_g , as demonstrated in Fig. 7.2. Denote G' as the graph

representing the topology of new solution \mathbf{F}' , which is a union of the original graph G and its symmetric images (i.e. $h_j(G)$). Thus the new associated symmetry group (K') of G' expands to the same as H . Now, the new solution is clearly feasible, and $\min(\xi\mathbf{F}) \geq -1$, which means that the new solution might be able to be further maximized by a scalar $\xi > 1$ on G' . Therefore, we conclude that there is always a solution of full symmetry preserved from the input ground structure with larger or equal objective than any solution with less or no symmetry. The value of ξ depends on how much the compression field of the original solution overlaps with that of its symmetric images (under h_j 's). If there is no overlapping compression field, then $\xi = (m + 1)$. The level of overlapping is closely related to the symmetry number of the solution: a general observation is that the smaller symmetry number the less overlapping. Thus, a solution with less symmetry is likely to have objective value much smaller than the possible optimum (with full symmetry) because ξ can be larger. In other words, for a force maximization problem, a solution with more symmetry is likely to yield a larger objective than the ones with less or no symmetry.

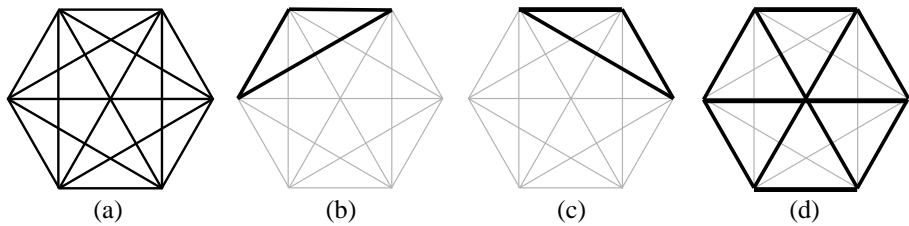


Figure 7.2: (a) A symmetric planar ground structure. (b) A subset of the ground structure (representation of G) indicated by black solid lines. (c) Another subset of the ground structure (representation of $h_j(G)$) obtained by applying a symmetry operation of the ground structure to the one shown in (b). The structures in (b) and (c) are physically equivalent, as the relative relationships between the nodes and members remain unchanged. (d) An embedded structure that has the same symmetry group as the initial ground structure.

The above discussion about the relaxed LP problem helps us to gain some insights into the original discrete problem. As the topological constraint becomes active, the feasible domain of the new problem reduces to some discrete rays within the feasible cone of the relaxed LP problem. Each of these rays represents a specific topology with a scalable

self-equilibrating prestress field that satisfies the discontinuity constraint of struts. In other words, the feasible domain of the discrete optimization problem is a subproblem of the relaxed continuous problem. As we discussed in previous paragraphs, symmetric designs yield larger objective functions in the relaxed continuous design space. Because adding a topological constraint does not change the underlying mechanics, performing force maximization on a subset (i.e. the discrete feasible domain) of the relaxed feasible domain should have the same feature: if we sweep the discrete feasible domain to the increasing direction of the objective function, we conjecture that a symmetric solution is still likely to yield a larger objective. However, as we foresee, it is almost impossible that the optimal solution to the discrete problem would inherit all symmetries of the input ground structure. Indeed, as we observe from the numerical examples, an optimized tensegrity structure may possess many symmetries if the input ground structure is highly symmetric, but the symmetry number is usually smaller than that of the ground structure. That is to say, it is possible to obtain asymmetric solutions from symmetric ground structures.

We note here that our formulation is not concerned about finding tensegrities with a kinematically indeterminate dual truss. If mechanical performance is the preferred metric over aesthetics, then kinematic indeterminacy is not a good choice of constraint in the design problem because it offers no benefits for stiffness and stability of the structure. This discussion also aligns with the last paragraph of Calladine's landmark paper [191]: “On the other hand, if the aim is to design economical but stiff engineering structures it is not clear that there is much point in making the outer network so sparse that the resulting frame has a number of infinitesimal modes whose stiffness is necessarily low.” Our method is able to produce tensegrity structures that are kinematically indeterminate as reported by the kinematic indeterminacy count in the manuscript. We show that kinematic indeterminacy can be obtained by fine tuning the geometry of the ground structure (see the example in Section 7.4.2).

7.3.2 Mixed integer linear programming (MILP) reformulation

In the aforementioned formulation (7.2), the force vector \mathbf{F} is unrestricted in sign. By splitting the force vector into two non-negative vectors and adding integer variables, the above formulation can be transformed equivalently to the following MILP problem:

$$\max_{\mathbf{t}, \mathbf{c}, \mathbf{s}} \quad \mathbf{1}^T(\mathbf{t} - \mathbf{c}) \quad (7.5a)$$

$$\text{s.t.} \quad \mathbf{B}(\mathbf{t} - \mathbf{c}) = \mathbf{0} \quad (7.5b)$$

$$\mathbf{G}\mathbf{s} \leq \mathbf{n} \quad (7.5c)$$

$$\mathbf{0} \leq \mathbf{t} \quad (7.5d)$$

$$\mathbf{0} \leq \mathbf{c} \leq \mathbf{s} \leq \mathbf{1} \quad (7.5e)$$

$$\mathbf{s} \in \mathbb{Z}^{N_{E_g}} \quad (7.5f)$$

In formulation (7.5), we replace the force vector \mathbf{F} with the difference of two non-negative vectors $(\mathbf{t} - \mathbf{c})$. This splitting leads immediately to the physical meaning that the vector \mathbf{t} corresponds to the tension forces and \mathbf{c} corresponds to the compression forces. Thus, we decouple the tension and compression field. The binary design variables \mathbf{s} indicate the presence of struts, serving to replace the non-differentiable function χ . The binary matrix \mathbf{G} is elaborated in Section 7.3.3.

While the objective function and most constraints are directly translated from formulation (7.2) to formulation (7.5), it is not obvious to see that constraints (7.5c) and (7.5e) ensure (7.2c). Based on $\mathbf{c} \leq \mathbf{s}$, we can see that $\mathbf{s} - \chi(\mathbf{F}) \geq \mathbf{0}$, because s_e can be 1 when the corresponding force (c_e) is 0 while $\chi(F_e)$ must be 0 when F_e is 0. Considering that all entries of \mathbf{G} are either 1 or 0, we find that,

$$\mathbf{G}(\mathbf{s} - \chi(\mathbf{F})) \geq \mathbf{0}, \quad (7.6)$$

thus,

$$\mathbf{G}\mathbf{s} \leq \mathbf{n} \implies \mathbf{G}\mathbf{s} - \mathbf{G}(\mathbf{s} - \chi(\mathbf{F})) \leq \mathbf{n} \implies \mathbf{G}(\chi(\mathbf{F})) \leq \mathbf{n} \implies \sum_{e \sim v} \chi(F_e) \leq n. \quad (7.7)$$

The proposed formulation has a natural and smooth relaxation to linear programming as we increase the allowed connectivity of struts, i.e. Class n . It is also observed that the proposed formulation is less computationally demanding than the other similar formulations [175]–[179] for problems of similar size, probably due to the simplicity of the formulation. Additionally, relative to existing formulations, we consider much fewer discrete variables (the minimal number required to define a tensegrity). The disadvantage of our treatment is that we do not have control over the physical contact of cables with other cables or struts. However, from a practical point of view, cables are usually very thin and flexible members such that even if they touch other members, the influence on the structure is very limited. It is also easy to handle the contact, for example, by making a small hole in the strut that can be passed through by an intersecting cable. More importantly, other formulations for topology design of tensegrity have not demonstrated their ability to capture a variety of known tensegrities. In contrast, the present formulation is effective in attaining many of the known configurations, as illustrated in Section 7.4.

7.3.3 Matrix notation for the topological constraints

The discontinuity of compressive members is a signature of tensegrity structures, although the generalized definition of tensegrity allows relaxation of the discontinuity. It is well known that this topological constraint can be expressed as a linear inequality on the integer variables related to presence of struts [175]–[179]. For the ease of numerical implementation, we explain the idea using matrix notations here. Define the incidence matrix \mathbf{G} based

on the ground structure such that:

$$G_{ij} = \begin{cases} 1, & \text{if member } j \text{ is connected to node } i \\ 0, & \text{otherwise} \end{cases} \quad (7.8)$$

Thus \mathbf{G} is an $N_{V_g} \times N_{E_g}$ binary matrix which contains the connectivity information, i.e., the topology, of a ground structure. The notation N_{V_g} and N_{E_g} refer to the number of nodes and members in the ground structure. Each column of \mathbf{G} contains exactly two nonzero entries whose row indices correspond to the end nodes of a member. We then define a binary vector of size $N_{E_g} \times 1$, whose k -th entry refers to the k -th member of the ground structure, with the value of 1 indicating the presence of a member. For any collection of members that are embedded in the ground structure, there exist a unique binary vector \mathbf{x} representing the collection. When we apply matrix vector multiplication as \mathbf{Gx} , the resultant vector is of size $N_{V_g} \times 1$, where each entry indicates the number of members connected to each node. Let us use the same vector \mathbf{s} as before for the collection of all compressive members. Then the discontinuity condition is written as a linear constraint:

$$\mathbf{Gs} \leq \mathbf{n} \quad (7.9)$$

where \mathbf{n} is a $N_{V_g} \times 1$ vector of positive integers confining the level of discontinuity of the struts. For Class-1 tensegrity, we have that $\mathbf{n} = \mathbf{1}$. This idea is often used in the field of graph theory for matching problems [192]. Indeed, this linear constraint reveals an interesting possibility when there are different connectivity constraints of struts at different nodes.

Considering practical construction of tensegrities, it is desirable to avoid physical contact of struts. One can address collisions between struts as a linear constraint about the integer design variables, similar to the discontinuity constraint. Although there are ways to get around the case when two struts collide mid-length (e.g. splitting one strut near the

collision point, or making struts curved), in practice these intersections should be avoided because they make the tensegrity difficult to manufacture. To control collisions in the design, an additional topological constraint can be added that prevents the physical intersection of struts [178]. Suppose that we have a criterion that judges whether there is a conflict between two struts. For each (potential) intersection of members (i, j) in the ground structure, a (binary) row vector is defined, with ones in the column positions for members i and j , respectively. Sweeping the entire ground structure, these row vectors are assembled into a binary matrix \mathbf{G}_p , whose number of rows is the number of (potential) conflicting pairs. Then the physical constraint is written in the following form:

$$\mathbf{G}_p \mathbf{s} \leq \mathbf{1} \quad (7.10)$$

The matrix \mathbf{G}_p works following the same logic as the topological constraint matrix \mathbf{G} . Each row of \mathbf{G}_p corresponds to a fictitious intersection point reporting an occurrence of conflict between two members. For the case that several members intersect at the same point, as we impose the constraint using Eq. (7.10), a violation happens whenever two of the intersected members are present in the structure. In this work, we set the collision criterion to be the intersection of centerlines of members. A different criterion can be found in reference [178]. The number of rows of \mathbf{G}_p depends on the specific geometry of the ground structure. The construction of matrix \mathbf{G}_p is conducted as an offline process a priori to the optimization. Using parallel computing and other techniques from computer graphics, the process can be finished in a reasonable amount of time.

It should be noted that this intersection test in our formulation does not involve the cables (tensile members), since they are not included in the vector \mathbf{s} . This follows from the assumption that the tensile members are thinner and typically flexible enough to handle intersections (collisions). Moreover, colliding cables can split at the intersection point creating a new node, with no effect on the principles and behavior of the tensegrity.

7.3.4 An illustrative example of the topological constraints

We use the following example to illustrate how the topological constraint and physical constraint work. Suppose we have a ground structure as shown in Fig. 7.3(a). Label the vertices from A to F and edges from 1 to 9. Based on the given topology, we can construct

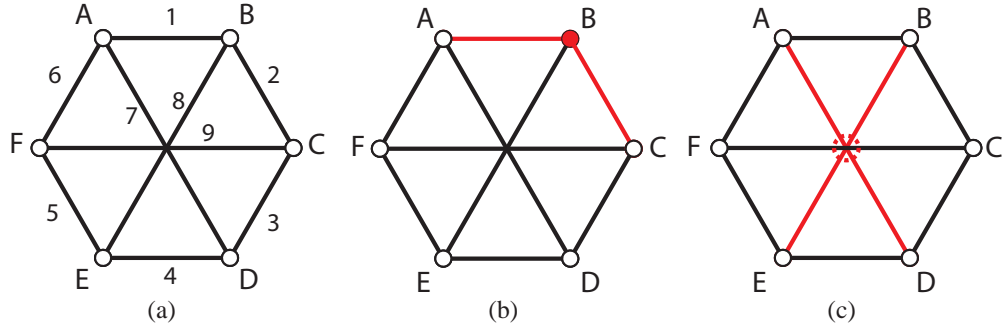


Figure 7.3: (a) A simple ground structure with 6 nodes and 9 members. (b) The collection of members 1 and 2 in the ground structure. The two members are connected at node B. (c) Members 7 and 8 are contacting each other in the middle, indicating a conflict in space.

the topological constraint matrix \mathbf{G} as:

$$\mathbf{G} = \begin{bmatrix} 1 & 0 & 0 & 0 & 0 & 1 & 1 & 0 & 0 \\ 1 & 1 & 0 & 0 & 0 & 0 & 0 & 1 & 0 \\ 0 & 1 & 1 & 0 & 0 & 0 & 0 & 0 & 1 \\ 0 & 0 & 1 & 1 & 0 & 0 & 1 & 0 & 0 \\ 0 & 0 & 0 & 1 & 1 & 0 & 0 & 1 & 0 \\ 0 & 0 & 0 & 0 & 1 & 1 & 0 & 0 & 1 \end{bmatrix}_{6 \times 9} \quad (7.11)$$

The rows of the matrix correspond to the connectivity information at nodes A to F. The columns contain the connectivity information of members 1 through 9. For example, the third row shows that member 2, 3, and 9 are connected to node C. Furthermore, since members 7, 8, and 9 intersect at one point, we have the physical constraint matrix \mathbf{G}_p

reads:

$$\mathbf{G}_p = \begin{bmatrix} 0 & 0 & 0 & 0 & 0 & 0 & 1 & 1 & 0 \\ 0 & 0 & 0 & 0 & 0 & 0 & 0 & 1 & 1 \\ 0 & 0 & 0 & 0 & 0 & 0 & 1 & 0 & 1 \end{bmatrix}_{3 \times 9} \quad (7.12)$$

As discussed before, the coincident intersection point is split into three fictitious intersection points.

Suppose we have a collection of members from the ground structure represented by the binary vector \mathbf{x} whose k -th entry reflects the presence of member k in the collection. Let $\mathbf{x}_1 = [1, 1, 0, 0, 0, 0, 0, 0, 0]^T$ meaning that members 1 and 2 are in the collection as shown in Fig. 7.3(b). The matrix vector multiplication $\mathbf{G}\mathbf{x}_1$ gives $[1, 2, 1, 0, 0, 0]^T$ which clearly shows that there are two members in the collection connected to node B. If the constraint is set for Class-1 tensegrity and the collection \mathbf{x}_1 represents the struts, \mathbf{x}_1 will violate the topological discontinuity constraint. To show how the physical constraint works, we set $\mathbf{x}_2 = [0, 0, 0, 0, 0, 0, 1, 1, 0]^T$, which contains members 7 and 8, as shown in Fig. 7.3(c). The linear operation $\mathbf{G}_p\mathbf{x}_2$ produces $[2, 1, 1]$ with first component larger than 1 indicating a violation. Thus the physical constraint successfully shows that members 7 and 8 cannot exist at the same time.

7.3.5 Structural Analysis of Tensegrity Structures

Tensegrity structures carry self-balanced prestress, which means that the initial undeformed configuration of a tensegrity structure consists of deformed states of its base materials. Thus, the stiffness matrix of a tensegrity structure shall be established following the Updated Lagrangian formulation [193], [194]. The deformation of a tensegrity structure should refer to the prestressed configuration, which is what we obtained from topology optimization. We briefly go through the derivation in this section. We use left-subscript to label the reference configuration of a quantity, and left-superscript to label the configuration when the quantity is evaluated (or occur).

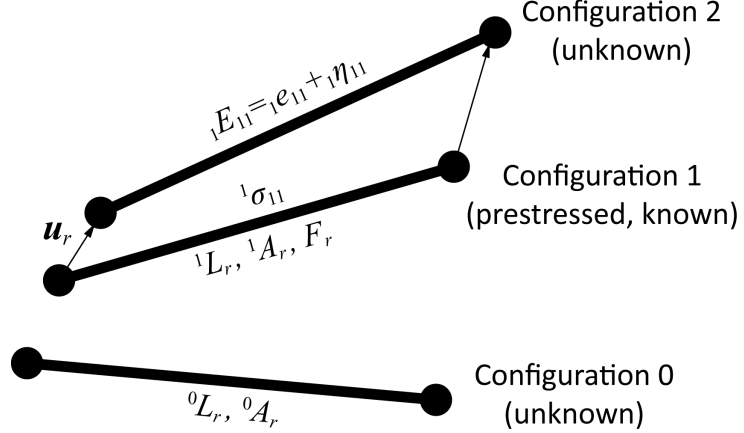


Figure 7.4: Illustration of the Updated Lagrangian formulation for derivation of stiffness matrix of tensegrity member (i.e. a prestressed rod) when only the prestressed state is known.

Using the principle of virtual work, the linearized equilibrium of a deformed one-dimensional elastic rod element is given by [194]:

$$\int_{^1V} (^1C)(^1e_{11})\delta(^1e_{11})d^1V + \int_{^1V} (^1\sigma_{11})\delta(^1\eta_{11})d^1V = \int_{^1S} ^2t\delta u d^1S - \int_{^1V} (^1\sigma_{11})\delta(^1e_{11})d^1V \quad (7.13)$$

where, 1V denotes the prestressed configuration, 1E is the tangent elastic modulus, ${}^1e_{ij}$ and ${}^1\eta_{ij}$ are the linear and nonlinear components of the incremental Green-Lagrange strain (denoted as ${}^1E_{11}$) defined on the prestressed configuration, and ${}^1\sigma_{11}$ is the Cauchy stress which is also defined on the prestressed configuration. The unknown displacement field is denoted as δu , and 2t is the deformation independent boundary traction vector (measured per unit boundary area at the prestressed state). Considering uniform strain and stress within an element, the incremental Green-Lagrange strain can be expressed as functions of nodal displacements of member r (denoted as \mathbf{u}_r) upon the prestressed configuration. The linear (${}^1e_{ij}$) and nonlinear (${}^1\eta_{ij}$) components of ${}^1E_{11}$ are given by:

$${}^1e_{11} = \frac{1}{^1L_r} \mathbf{B}_L^T \mathbf{u}_r, \quad {}^1\eta_{11} = \frac{1}{2(^1L_r^2)} \mathbf{u}_r^T \mathbf{B}_{NL} \mathbf{u}_r, \quad (7.14)$$

where,

$$\mathbf{u}_r = [\mathbf{u}_a^T, \mathbf{u}_b^T]^T, \quad \mathbf{u}_i = {}^2\mathbf{x}_i - {}^1\mathbf{x}_i \quad (i = a, b), \quad L_r = \|{}^1\mathbf{x}_b - {}^1\mathbf{x}_a\|, \quad (7.15)$$

$$\mathbf{B}_L = \frac{1}{L_r} \left[{}^1\mathbf{x}_a^T - {}^1\mathbf{x}_b^T, \quad {}^1\mathbf{x}_b^T - {}^1\mathbf{x}_a^T \right]^T, \quad \mathbf{B}_{NL} = \begin{bmatrix} +\mathbf{I}_3 & -\mathbf{I}_3 \\ -\mathbf{I}_3 & +\mathbf{I}_3 \end{bmatrix}. \quad (7.16)$$

Notice that \mathbf{B}_L is part of the global equilibrium matrix B . We remark that the nodal coordinates of the ground structure directly refer to the prestress configuration, that is, the \mathbf{x} in other sections of this chapter is the same as ${}^1\mathbf{x}$ in this derivation.

We remark that \mathbf{u}_r is measured taking reference to the prestressed configuration. Substituting Eq. (7.14) into Eq. (7.13), the equilibrium of the system can be discretized and rewritten in matrix form as:

$$\delta\mathbf{u}_r^T \mathbf{K}_{re} \mathbf{u}_r + \delta\mathbf{u}_r^T \mathbf{K}_{rg} \mathbf{u}_r = \delta\mathbf{u}_r^T {}^2\mathbf{f}_r - \delta\mathbf{u}_r^T {}^1\mathbf{f}_r \quad (7.17)$$

where \mathbf{K}_{re} is the elemental elastic stiffness matrix and \mathbf{K}_{rg} is the elemental geometric stiffness matrix. They are derived as:

$$\mathbf{K}_{re} = \frac{{}^1C_r}{{}^1L_r} {}^1A_r \mathbf{B}_L \mathbf{B}_L^T, \quad (7.18)$$

$$\mathbf{K}_{rg} = \frac{{}^1\sigma_{11}}{{}^1L_r} {}^1A_r \mathbf{B}_{NL}. \quad (7.19)$$

The external applied forces ${}^2\mathbf{f}_r$ to the prestressed element comes from the first part of the right hand side of Eq. (7.13), which is usually directly defined, and thus there is no need to carry out the integration. The internal prestress induced nodal forces are given by:

$${}^1\mathbf{f}_r = {}^1\sigma_{11}({}^1A_r) \mathbf{B}_L. \quad (7.20)$$

According to the design from our topology optimization formulation, we can decide the

values of (1L_r) and (${}^1\sigma_{11} {}^1A_r$), where the later term is the prestress force (i.e. $F_r = {}^1\sigma_{11} {}^1A_r$) of member r . If we assume linear elasticity, we may take a constant Young's modulus C_r such that ${}^1C_r = {}^0C_r = C_r$. For linear elastic materials, the original cross sectional area of a member (before prestress is applied) can be determined by solving the following equation:

$${}^1A_r = \left(1 - \frac{\nu F_r}{{}^0A_r C_r}\right)^2 ({}^0A_r) \quad (7.21)$$

where ν is the Poisson's ratio of the base material.

Assembling Eq. (7.17) over all elements in the structure and admitting the arbitrary nature of the virtual displacement ($\delta\mathbf{u}$), the incremental finite element equation of the entire structure is given by:

$$\mathbf{K}\mathbf{u} = (\mathbf{K}_e + \mathbf{K}_g)\mathbf{u} = {}^2\mathbf{f} - {}^1\mathbf{f}. \quad (7.22)$$

Notice that the self-equilibrium of a tensegrity structure requires that ${}^1\mathbf{f} = \mathbf{0}$. We note that in linear elastic analysis, the relaxation of cables under compression are not considered.

We briefly summarize the matrix implementation of the above derivations to get \mathbf{K}_e and \mathbf{K}_g . First let us define the modified incidence matrix \mathbf{G}^* . In graph theory, the incidence matrix is binary (like the matrix \mathbf{G} in Eq. (7.5c)), but here, the modified matrix is composed of 0's, 1's, and -1's. Suppose member i links nodes a and b . Then \mathbf{G}^* is defined as:

$$G_{ij}^* = \begin{cases} 1, & \text{if member } i \text{ is connected to node } j, \text{ and } j = a \\ -1, & \text{if member } i \text{ is connected to node } j, \text{ and } j = b \\ 0, & \text{otherwise} \end{cases} \quad (7.23)$$

The size of the modified incidence matrix \mathbf{G}^* is $N_E \times N_V$. Then the augmented incidence matrix that connects the degrees of freedom to the members is defined as:

$$\mathbf{G}_{aug}^* = \mathbf{G}^* \otimes \mathbf{1}_{1 \times 3} \quad (7.24)$$

where \otimes means the Kronecker product, so that \mathbf{G}_{aug}^* has size $N_E \times 3N_V$. The vector $\mathbf{1}$ is a vector of ones. The total degrees of freedom in the structure is $3N_V$ because we are considering three dimensional space. We assemble all nodal coordinates of the prestressed configuration into a vector ${}^1\mathbf{x}$ by blocks of 3 components. We denote ${}^1\mathbf{L}$ the vector that collects all member lengths in the prestressed configuration. The global equilibrium matrix \mathbf{B} (as in Eq. (7.1b)) is given as:

$$\mathbf{B} = \text{diag}({}^1\mathbf{x}) \mathbf{G}_{aug}^{+T} \text{diag}({}^1\mathbf{L})^{-1} \quad (7.25)$$

where the operation “ $\text{diag}(\cdot)$ ” maps a vector to a diagonal matrix. Define a diagonal matrix \mathbf{D} of size $N_E \times N_E$, such that,

$$D_{rr} = \frac{{}^1C_r {}^1A_r}{{}^1L_r} \quad (7.26)$$

Then the linear stiffness matrix \mathbf{K}_E of a tensegrity is given as:

$$\mathbf{K}_e = \mathbf{B} \mathbf{D} \mathbf{B}^T \quad (7.27)$$

which is a symmetric matrix with $3N_V$ rows and $3N_V$ columns. We define a vector \mathbf{q} such that:

$$q_r = \frac{F_r}{{}^1L_r} \quad (7.28)$$

The ratio q_r is known as the force density. The so-called force density matrix [53] (or reduced stress matrix [166], [185]) is then formed by:

$$\mathbf{Q} = \mathbf{G}^{+T} \text{diag}(\mathbf{q}) \mathbf{G}^* \quad (7.29)$$

which is of size $N_V \times N_V$. Then the geometrical stiffness matrix is constructed by:

$$\mathbf{K}_g = \mathbf{Q} \otimes \mathbf{I}_{3 \times 3} \quad (7.30)$$

where \mathbf{I} is the identity matrix. Finally the tangent stiffness matrix of a tensegrity is the summation of the linear stiffness matrix and the geometrical stiffness matrix:

$$\mathbf{K} = \mathbf{K}_e + \mathbf{K}_g \quad (7.31)$$

7.3.6 Ground structure method

A typical ground structure [180], [181] is a set of nodes and members within a fixed geometry, as illustrated by Fig. 7.5. In structural topology optimization, the ground structure method is particularly suitable for design of discrete structures [195]. *The importance of the geometry and layout of ground structures has not yet been discussed for topology design of tensegrity.* As the main input to the optimization, the properties of the ground structures can have a big influence on the solution. For example, defining passive regions in the ground structure where no member can cross provides some control over the final tensegrity design. We adopt the techniques on ground structure generation developed for typical topology optimization, and explore how they can be used to tune the final design of tensegrities.

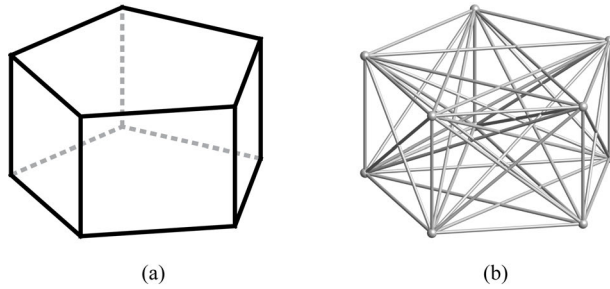


Figure 7.5: The ground structure generated within pentagon prism. (a) Geometry of the pentagon prism. (b) The ground structure connecting every pair of nodes, which are located on the vertices of the prism.

The ground structure can be generated inside arbitrary domains with various geometries. For convex domains, it is relatively easy to generate a geometrically conforming ground structure inside the domain. However, the challenge arises for ground structures filling concave geometries, in which members with both ends within the valid domain can

have a part that is outside. We adopt the restriction zone idea from Zegard and Paulino [182], which is inspired by the collision detection algorithm used in computational geometry, to resolve this issue. Members with any portion within the restriction zone are removed, resulting in a ground structure that conforms to the specified concave geometry.

We can control the length of members by further adjusting the ground structure, which may be useful, for example, if we want to avoid members that can easily buckle. If the constraint applies to both struts and cables, we simply remove the members from the ground structure that exceed the length limit. If the length constraint is only applicable to the struts, we impose a zero upper bound on the corresponding design variables in the vector \mathbf{c} and \mathbf{s} . Notice that this strategy is only effective for unstructured ground structures without collinear members, which are typically used for topology design of tensegrity. When Class-1 tensegrity is used, the “length constraint” is also effective for structured ground structures because no pair of collinear struts are allowed to connect to each other.

7.4 Numerical examples: verification and extension

In this section, we demonstrate that the proposed formulation is effective in reproducing known tensegrity structures by feeding specific geometries of the ground structure. Additionally, by varying the geometric parameters of the known tensegrities, we discover new forms of tensegrity. Hence, we provide a new perspective on the classification of tensegrity by its geometry rather than its topology.

For each example, numerical data is provided in tables. The numbers of nodes and members in the ground structure are denoted N_{V_g} and N_{E_g} . The terms N_V and N_E are the numbers of nodes and members in the final topology, respectively. The stability status of the obtained designs are also provided based on the criteria discussed in Section 7.2. The degree of kinematic indeterminacy (KI) of the dual truss of a tensegrity is also included in the tables. We observe that for symmetric ground structures, the optimized solutions usually have one or more mechanisms associated with their dual truss. When a length limit

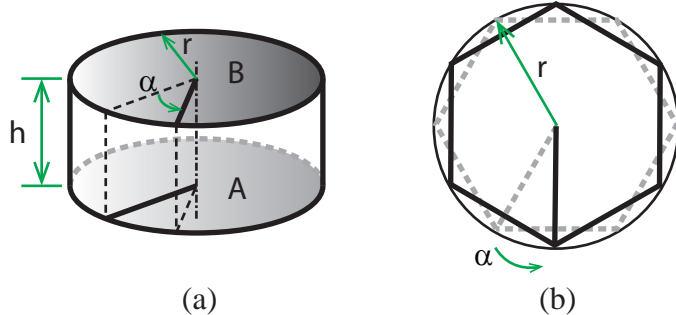


Figure 7.6: The geometry and generation of a twisted prism. (a) The base polygon laid on the top circle B is obtained by rotating the same polygon on the bottom circle A with an angle α . (b) The top view of the twisting of a hexagonal base.

for struts is applied, the number of reduced integer variables is given as N_I . The running time of MILP is reported as T_{opt} for reference.

We explore the classes of prismatic tensegrity, symmetric star-shaped tensegrity, tower tensegrity, and spherical tensegrity in this section. The physical constraint is applied to restrict the intersection of the centerlines of struts, using the method proposed in Section 7.3.3.

7.4.1 On Reproducing Known Tensegrities: A Verification Study

One of the most well-known types of tensegrity is the prismatic tensegrity. This type of tensegrity has various configurations, but all of them obeys the dihedral symmetry. Zhang and Ohsaki systematically studied the configuration and stability of the prismatic tensegrity [173], [190]. The nodes of a prismatic tensegrity are located on the vertices of a twisted prism with each base face a regular N -gon. The N vertices of the N -gon are incident on a circle. The twisting angle between the two parallel base faces is denoted as α , as shown in Fig. 7.6.

We first generate the ground structure based on the twisted prism with full connectivity between nodes. The prism has a height of 1.0 (i.e., $h = 1$), and the radius of the outline circle of the base polygon is also 1 (i.e., $r = 1$). The results are shown in Fig. 7.7 for different geometries of the twisted prism. All of the results are super-stable, which has

Table 7.1: Computational results for designs shown in Fig. 7.7

Design	N_{V_g}	N_{E_g}	N_V	N_E	Obj.	KI	Stability	T_{opt}
(a)	6	15	6	12	1.31	1	Super-Stable	<0.01s
(b)	8	28	8	16	2.21	3	Super-Stable	<0.01s
(c)	10	45	10	20	4.67	5	Super-Stable	0.02s
(d)	12	66	12	24	6.66	7	Super-Stable	0.02s
(e)	16	120	16	32	13.44	11	Super-Stable	0.02s
(f)	32	496	32	64	63.54	33	Super-Stable	0.58s

Table 7.2: Computational results for designs shown in Fig. 7.8

Design	N_{V_g}	N_{E_g}	N_V	N_E	Obj.	KI	Stability	T_{opt}
(a)	8	28	8	12	3.33	7	Super-Stable	<0.01s
(b)	10	45	10	16	3.78	9	Super-Stable	<0.01s
(c)	12	66	12	20	5.96	11	Super-Stable	0.01s

been proved analytically by Zhang and Ohsaki [173], [190].

There is another family of tensegrity that has similar configurations to the prismatic tensegrities, namely the symmetric star-shaped tensegrity [53], which also satisfies the dihedral symmetry. The difference is that a star-shaped tensegrity structure has two additional nodes lying on the centroids of the base faces. Therefore, in a prismatic tensegrity structure, there is essentially only one type of node, but in a star-shaped tensegrity, there are two types of nodes. To reproduce the known star-shaped tensegrities, we generate the ground structure using the nodes on the vertices of the twisted prism and the two additional nodes at the centroids of the top and bottom faces.

7.4.2 Tower tensegrity

The general composition of the geometry of tower tensegrity is shown in Fig. 7.9. We restrict our study to two-layer towers, in which two twisted prisms are aligned vertically with an overlapping height h_d . The angles α_1 and α_2 measure the twisting of the twisted prisms, and β is the relative rotation between the two prisms. Following this rule, by altering α_1 , α_2 , β , h_d , as well as the base polygon of the twisted prisms, we can find different embedded tensegrity structures.

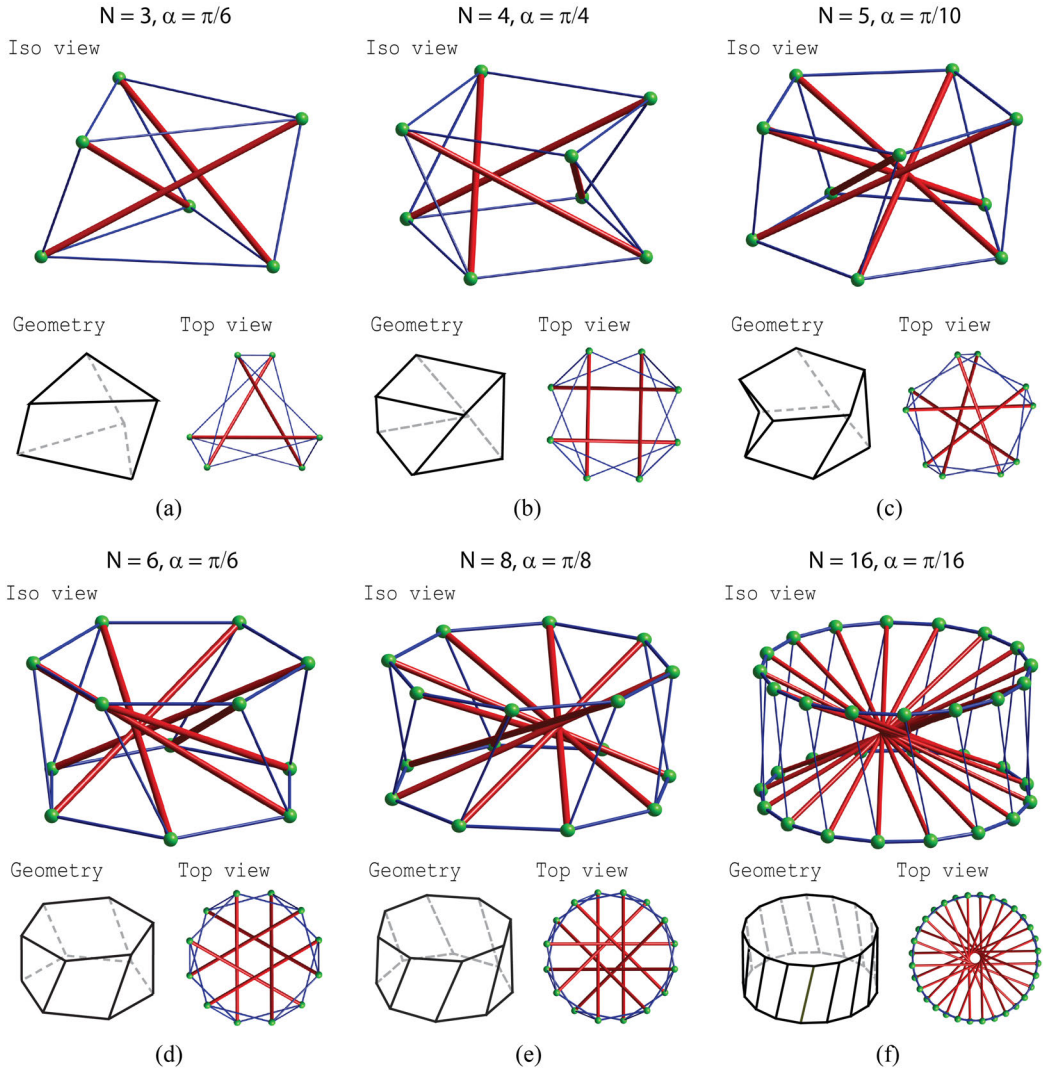


Figure 7.7: Examples of prismatic tensegrities that are reproduced using the proposed method. Different base polygons are used to generate the twisted prism geometries: (a)-(f). For N -gon based twisted prism, $\alpha = \pi/N$ if N is even, and $\alpha = \pi/2N$ if N is odd. Quantitative date is provided in Table 7.1.

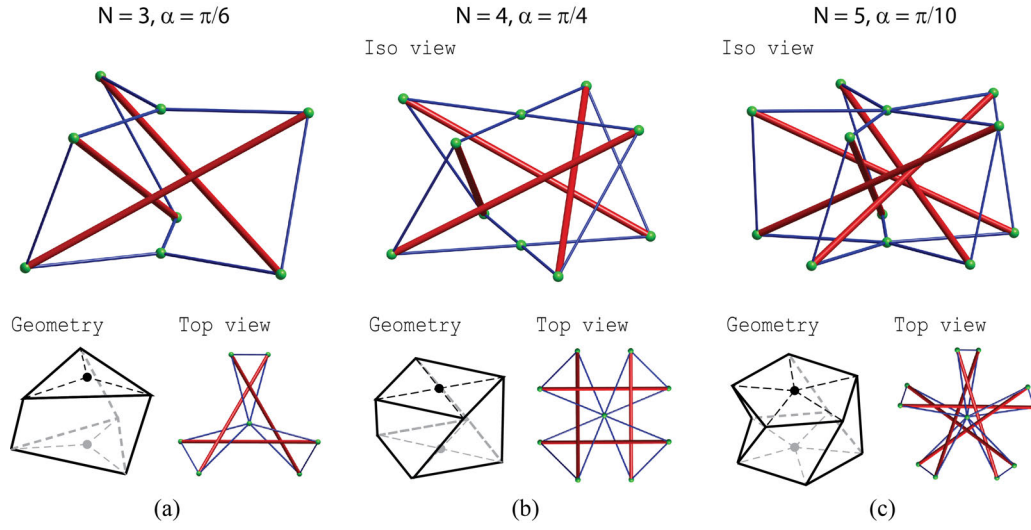


Figure 7.8: Examples of star-shaped tensegrities that are reproduced using the proposed method. Different base polygons are used to generate the twisted prism geometries: (a)-(c). Compared to the prismatic tensegrities, the initial ground structures have two more nodes that are located at the centroids of the two base polygons.

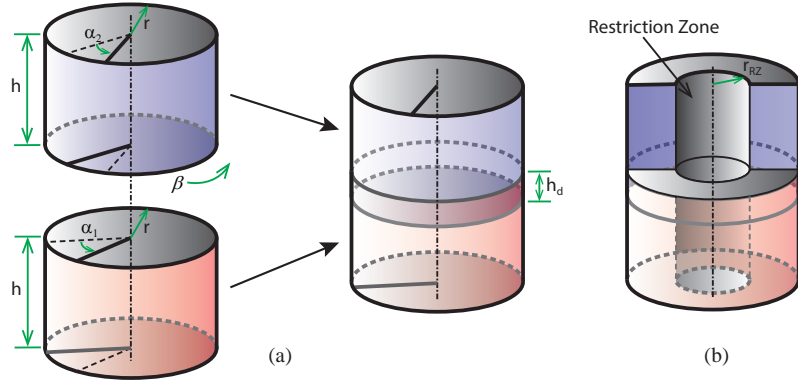


Figure 7.9: (a) The geometry and generation of the tower tensegrity. (b) Illustration of the cylindrical restriction zone adopted in this example. Any member in the initial ground structure that passes through this region is removed.

One famous example in this category is the “Saddle-Vertical-Diagonal” (SVD) tensegrity [58]. The geometry of the two-stage tower tensegrity can be obtained by laying one twisted triangular prism on top of another, as illustrated in Fig. 7.10(a). To recover the specific configuration of the SVD tower tensegrity, the geometric parameters listed in Fig. 7a are selected to satisfy the formula given by Tibert [2]. The resulting tensegrity is plotted in Fig. 7.10(b). The optimization selects 6 struts and 24 cables out of 66 candidate members in the ground structure within 0.06 seconds. The obtained tensegrity is known to have a dual truss with 1 degree of kinematic indeterminacy.

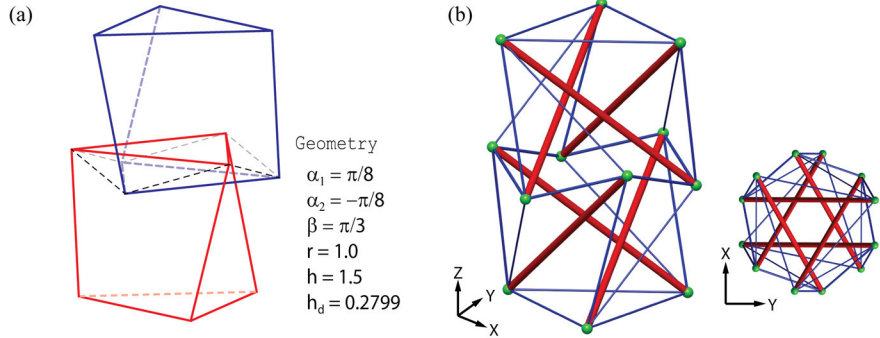


Figure 7.10: The SVD tower tensegrity. (a) Geometric decomposition of the SVD tower, where the 12 vertices are the nodes used to generate the ground structure. (b) The design obtained using the proposed formulation, which recovers the known form of the SVD tower tensegrity.

A free choice of the parameters leads to new tensegrities. For example, the designs shown in Fig. 7.11 are obtained based on hexagonal prisms with $\alpha_1 = \alpha_2 = \pi/8$ and $\beta = \pi/8$. We further show that by adding a hole in the ground structure and adding length constraints, we can tune the design to different configurations, as shown in Fig. 7.11(c) and (d). If we adjust the overlapping depth h_d to be 0.283, the resulting tensegrity design becomes kinematically indeterminate – its dual truss has 7 infinitesimal mechanisms (see Fig. 7.11(e)). This example shows that the geometry of the ground structure is a crucial aspect in the topology optimization of tensegrity. By fine tuning the geometry of a ground structure, we can generate a family of tensegrities with different features. Information for all four designs is provided in Table 7.3.

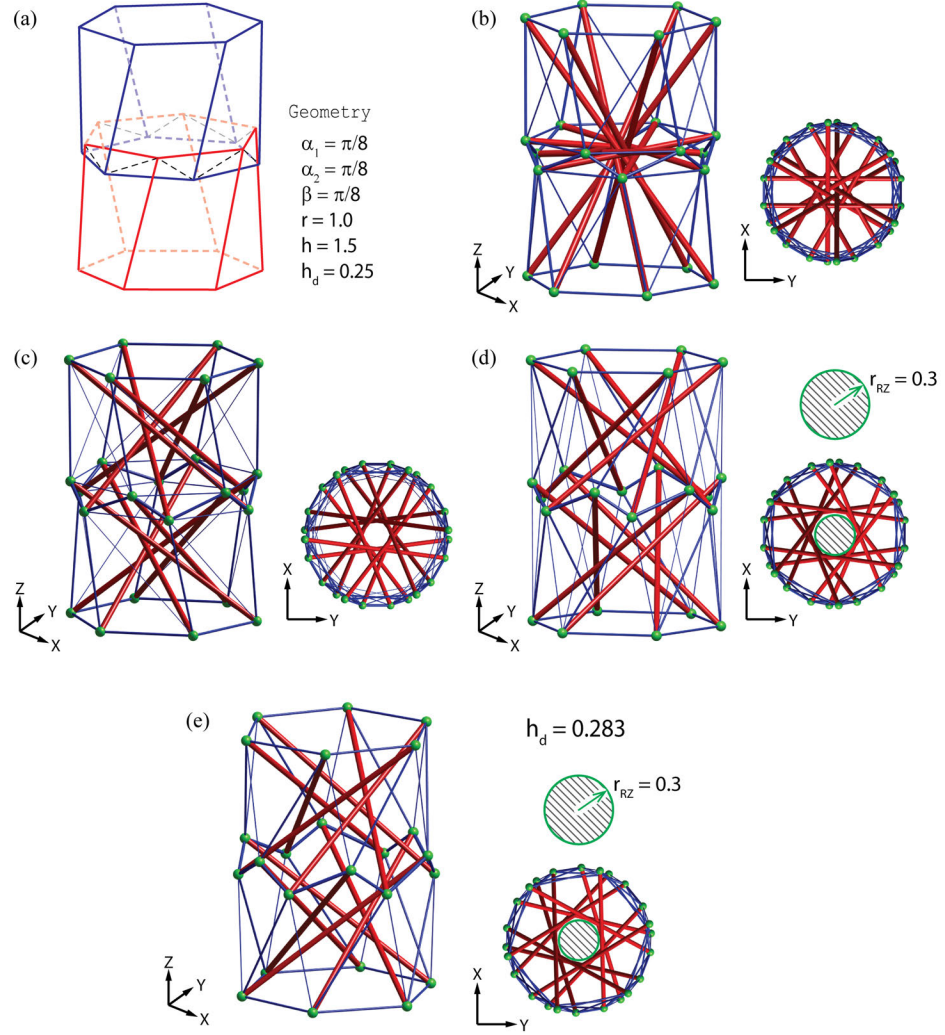


Figure 7.11: Extended examples of tower tensegrity. (a) The basic geometry. (b) The design obtained directly from the ground structure generated with full connectivity in (a). (c) The tensegrity obtained by limiting the length of struts to 2.5, which is in consistent units with the dimension of the geometry. (d) In addition to length limit, a cylindrical restriction zone is applied with $r_{RZ} = 0.3$. (e) Based on (d), by adjusting the overlapping height h_d , a kinematically indeterminate tensegrity design emerges naturally as a result.

7.4.3 Spherical tensegrity

Spherical tensegrity makes a large family among the known tensegrities. In this section, we will design tensegrities with nodes on a sphere. We will first recover some of the designs that are already known. Then we propose some new designs obtained by the proposed method. We will adopt the restriction zone method to generate ground structures with a central hollow ball region. This can be useful for tensegrity robots or protectors design in which a central void may need to contain some functional devices [1]. The geometry of the restriction zone for this example is illustrated in Fig. 7.12. The nodes are on the outer sphere and an inner ball with radius r_{RZ} is defined as the restriction zone.

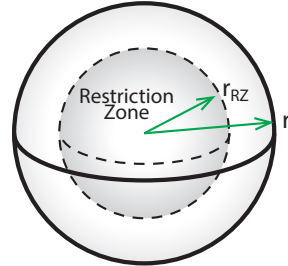


Figure 7.12: Illustration of the ball-shaped restriction zone adopted in this example.

The known spherical tensegrity structures often outline regular polyhedrons or truncated regular polyhedrons. We present three such structures that are reproduced by the proposed formulation, as shown in Fig. 7.13(a)-(c). The outline polyhedrons are icosahedron, dodecahedron, cuboctahedron. The first one (Fig. 7.13(a)) is obtained based on a ground structure generated based on the vertices of an icosahedron, with a restriction ball of radius $r_{RZ} = 0.2$. The second tensegrity (Fig. 7.13(b)) has cables on the surface of a do-

Table 7.3: Computational results for designs shown in Fig. 7.11

Design	N_{V_g}	N_{E_g}	N_V	N_E	N_I	Obj.	KI	Stability	T_{opt}
(b)	24	276	24	72	276	22.23	0	Super-Stable	0.43s
(c)	24	276	24	72	240	22.03	0	Super-Stable	0.16s
(d)	24	228	24	72	198	19.47	0	Super-Stable	0.20s
(e)	24	228	24	60	198	19.61	7	Prestress-Stable	0.09s

decahedron. The restriction zone for the ground structure has a radius $r_{RZ} = 0.5$. The last one shown in Fig. 7.13(c) is a Class-2 tensegrity, in which at most two struts can connect at each node. There are four triangles of struts in this tensegrity, and each of the closed chain of struts are named “strut circuits” by Motro [50]. The initial ground structure for this one has no restriction zone. Quantitative data is provided in Table 7.4.

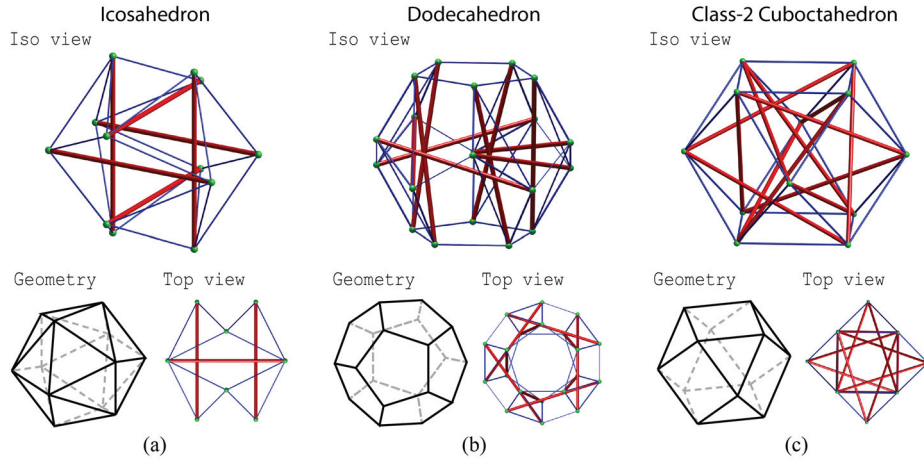


Figure 7.13: Some known spherical tensegrities that are reproduced. The ground structure of design (a) has a restriction zone with $r_{RZ} = 0.1$, design (b) has a restriction zone with $r_{RZ} = 0.5$, and No restriction zone is used in design (c).

Table 7.4: Computational results for designs shown in Fig. 7.13

Design	N_{V_g}	N_{E_g}	N_V	N_E	Obj.	KI	Stability	T_{opt}
(a)	12	60	12	30	3.80	1	Super-Stable	0.01s
(b)	20	150	20	50	30.18	5	Super-Stable	0.50s
(c)	12	66	12	36	32.78	1	Super-Stable	<0.01s

By taking different point sets on a sphere, we discover new tensegrities. Fig. 7.14 to 7.17 list some of the new designs of tensegrity that have been discovered by the proposed formulation. For some of them, restriction zones are used. The first one shown in Fig. 7.14(a) outlines a small rhombicuboctahedron. The one in Fig. 7.14(b) comes from the truncated icosahedron, which is usually known as the “Bucky ball”. There is an existing design of tensegrity [170] that looks similar to the geometry of a truncated icosahedron, but their nodes are not exactly at the vertices of the polyhedron, and the topologies are also

different from the one we obtained. The tensegrity shown in Fig. 7.15(a) is obtained as the best candidate optimal solution when the optimization hits the time limit. The realization of this design is shown in Fig. 7.15(b). We also construct a model, which is shown in Fig. 7.16(b), based on the design shown in Fig. 7.16(a). The structure shown in Fig. 7.17(b) is a Class-2 tensegrity embedded in the geometry of an icosahedron, in which the struts make a single loop of circuit. Quantitative data is provided in Table 7.5.

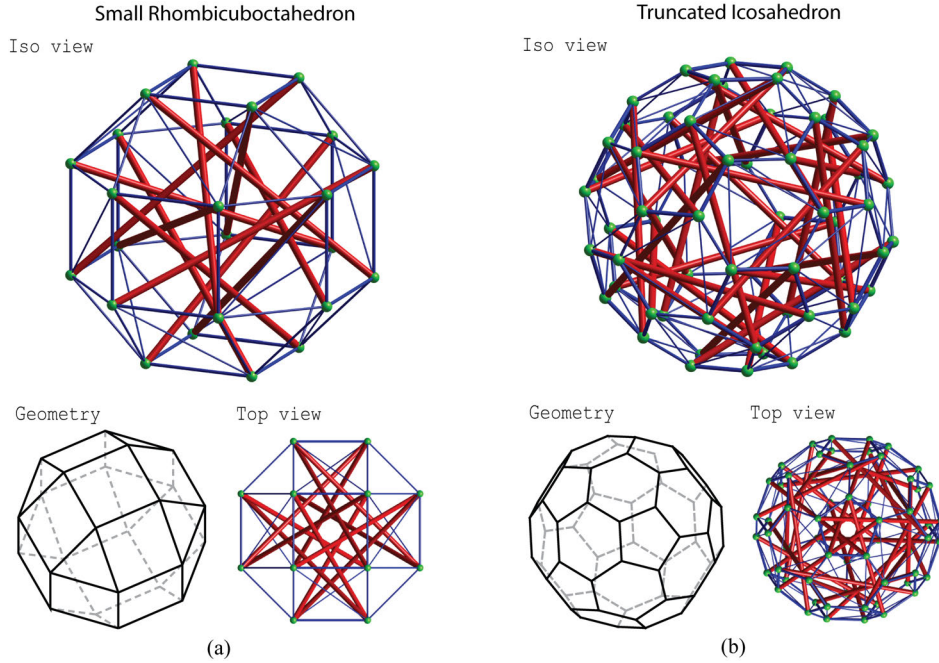


Figure 7.14: New examples of spherical tensegrities obtained using the proposed method. The radii of the restriction zones as defined in Fig. 7.12 are: (a) $r_{RZ} = 0.20$, (b) $r_{RZ} = 0.65$.

Table 7.5: Computational results for designs in Section 7.4.3

Design	N_{V_g}	N_{E_g}	N_V	N_E	Obj.	KI	Stability	T_{opt}
Fig. 7.14(a)	24	264	24	72	18.24	1	Super-Stable	0.53s
Fig. 7.14(b)	60	990	60	180	74.26	3	Super-Stable	640s
Fig. 7.15	60	870	60	180	55.27	0	Prestress-Stable	43200s
Fig. 7.16	16	120	16	50	8.99	0	Super-Stable	0.03s
Fig. 7.17(a)	120	4108	120	414	202.08	0	Super-Stable	706s
Fig. 7.17(b)	12	66	12	42	7.55	0	Super-Stable	<0.01s

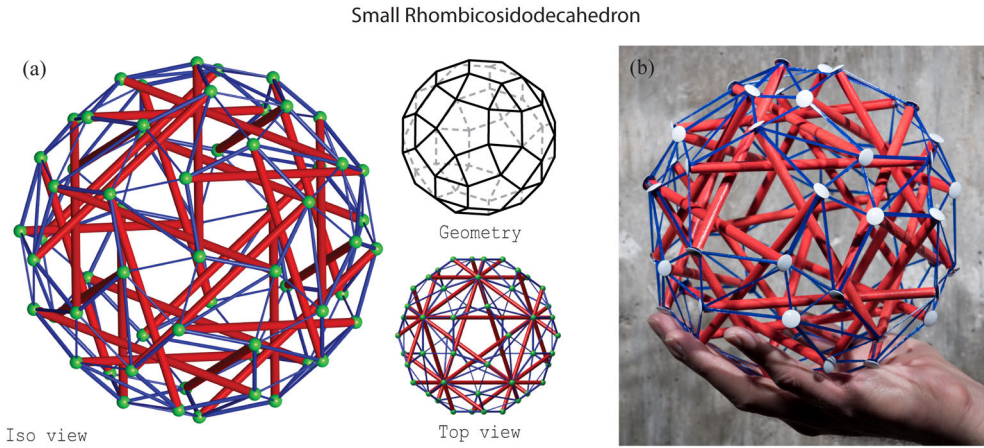


Figure 7.15: A tensegrity that outlines a small rhombicosidodecahedron. (a) Digital rendering of the obtained design, using restriction zone with radius $r_{RZ} = 0.70$. (b) A physical model made of wood struts and 3D printed cables. The cables are printed with a rubber-like material known as Ninja Flex.

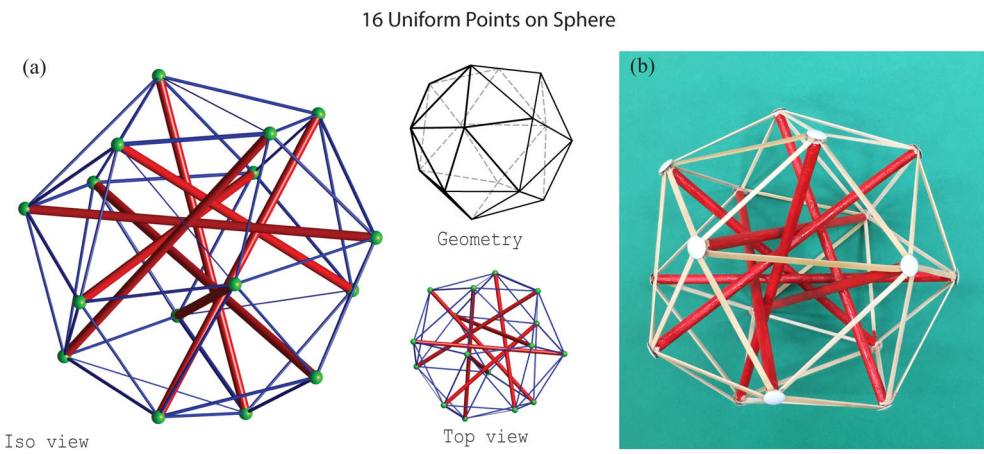


Figure 7.16: A spherical tensegrity optimized from a ground structure generated based on 16 uniformly distributed points on the unit sphere and no restriction zone. (a) Digital rendering of the obtained design. (b) The physical model made of wood struts and rubber band cables.

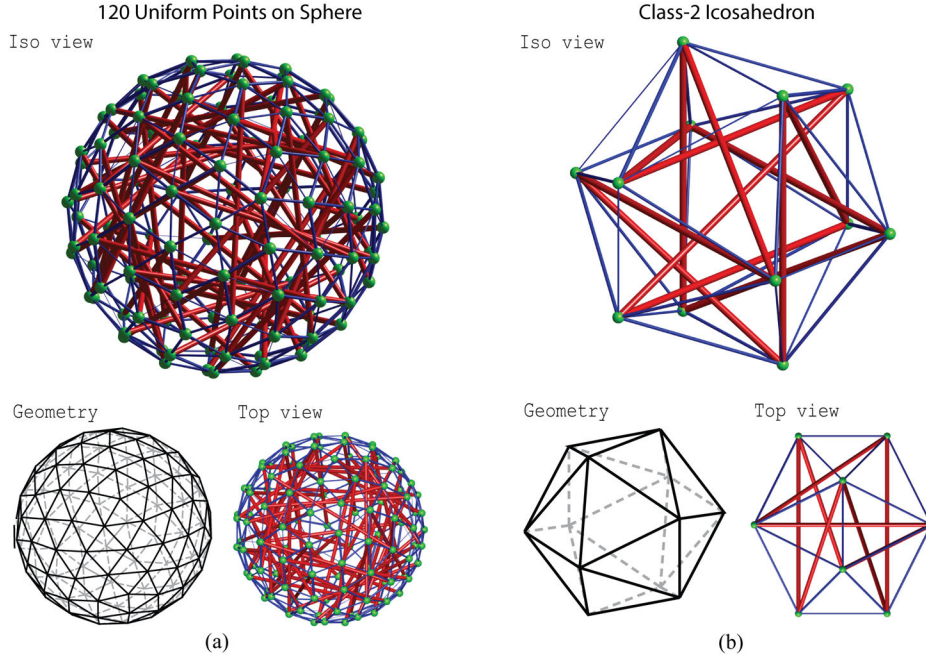


Figure 7.17: Other new designs of spherical tensegrities obtained using the proposed method. (a) A dense tensegrity that has 120 nodes uniformly placed on a sphere and restriction zone with radius $r_{RZ} = 0.65$. (b) A Class-2 tensegrity that has a continuous loop of struts.

7.5 Free-form design

In this section, we seek tensegrities that conform to arbitrary non-regular geometries, which is desirable for designing tensegrities for real applications.

7.5.1 Double-layer tensegrity dome

Tensegrities are sometimes used for roof structures [167], [168]. In this section we will show a cylindrical dome design obtained by solving the proposed optimization formulation. The design domain is shown in Fig. 7.18(a). The ground structure is generated on 54 grid points placed on the surface of the design domain. The members are all confined in the design domain by applying a restriction zone in the interior of the inner cylinder.

The optimization takes 97.61 seconds to converge. We impose Class-1 discontinuity constraint (i.e. $n = 1$), and prohibit the collision of the centerlines of struts. There is no length limit on the members. A posterior structural analysis shows that obtained tensegrity

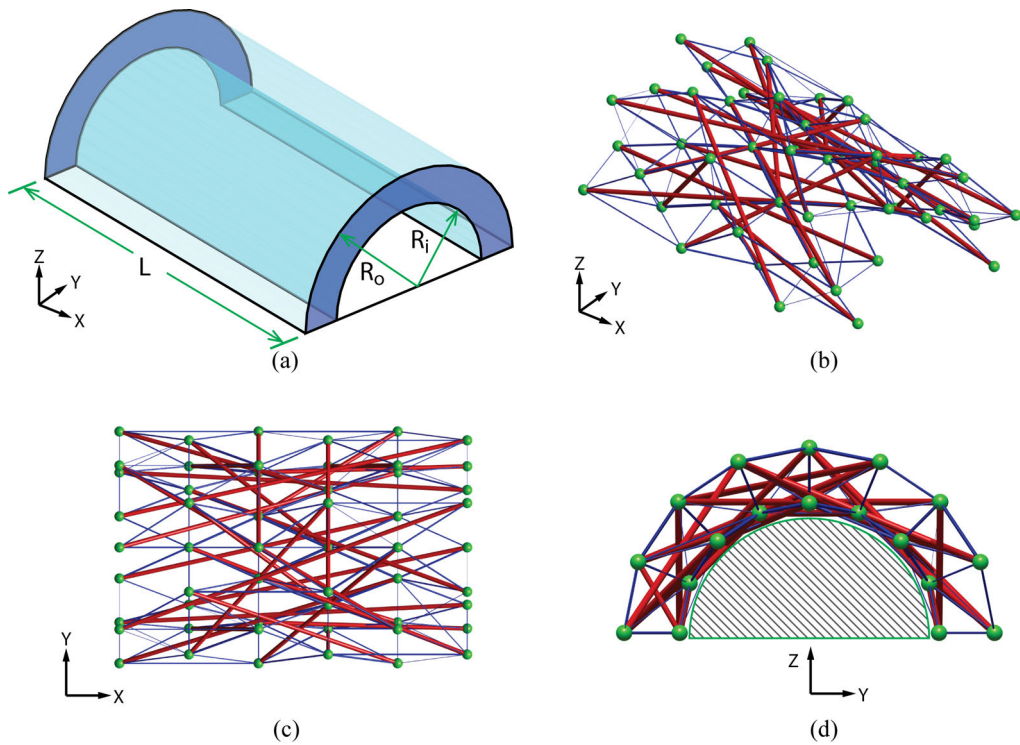


Figure 7.18: Design of a Class-1 cylindrical double-layer tensegrity dome. (a) The design domain: $L = 3$, $R_o = 1$, $R_i = 0.7$. The initial ground structure has 54 nodes and 882 members. (b)-(d) Different views of the obtained tensegrity. The design contains 54 nodes, 27 struts, and 153 cables. The dual truss of the tensegrity has 2 first-order mechanisms ($KI=2$). The tensegrity structure is super-stable.

is super-stable, and its dual truss is not infinitesimally rigid.

7.5.2 Taubin's heart

Here we design a tensegrity structure with Taubin's heart shape [196]. The shape of the surface is defined by a level set:

$$(x^2 + \frac{9}{4}y^2 + z^2 - 1) - x^2z^3 - \frac{9}{80}y^2z^3 = 0 \quad (7.32)$$

where x, y, z are the Cartesian coordinates in \mathbb{R}^3 . The size is scaled uniformly such that the heart surface has the dimensions shown in Fig. 7.19. Then a triangular mesh is generated on the surface that contains 107 nodes and 210 faces. The ground structure is generated based on the nodes of the mesh without restriction zones. We forbid the intersection of centerlines of struts, and constrain the lengths of the struts to be smaller than 1.2, in consistent units with the size of the heart surface.

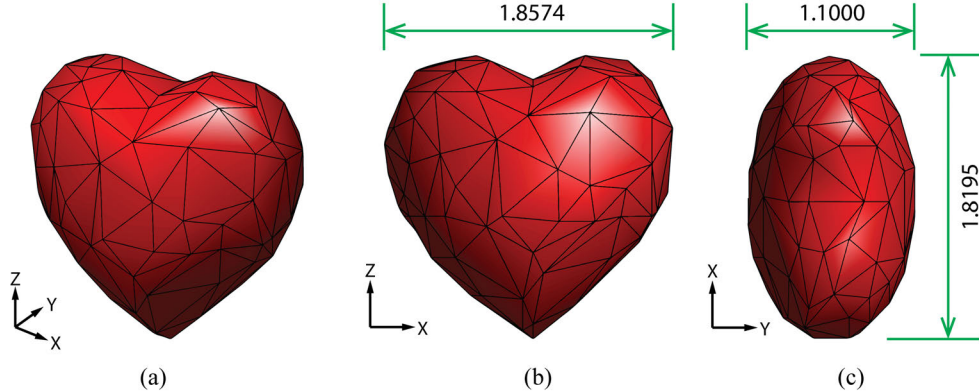


Figure 7.19: Different views (a)-(c) of Taubin's heart. The mesh nodes are used to generated the ground structure.

The obtained tensegrity is shown in Fig. 7.20, which takes 9032 seconds to converge. The tensegrity has 53 struts and 312 cables, optimized from 5671 candidates, among which $N_I = 3282$ members are potential struts. One of the nodes in the initial ground structure is ignored as no member is connected to it. The tensegrity has an infinitesimally rigid dual truss, ensuring prestress stability. Its geometrical stiffness matrix is also positive semi-

definite, indicating it is super-stable.

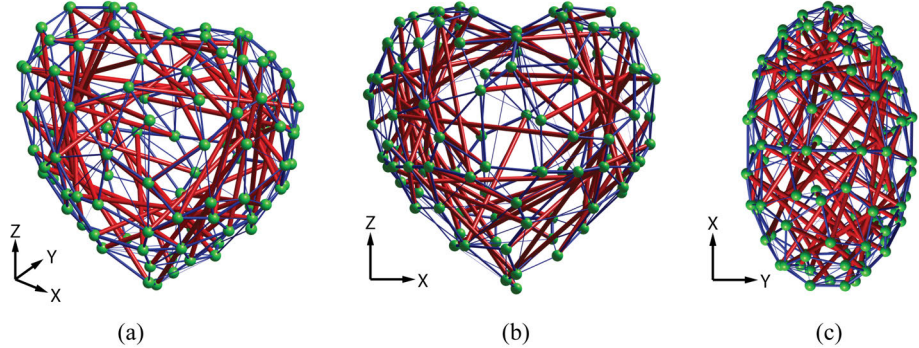


Figure 7.20: Different views (a)-(c) of the tensegrity which outlines the Taubin's heart. The tensegrity contains 53 struts and 312 cables. The lengths of the struts are limited to 1.2, with consistent units to the dimensions of heart surface. Structural analysis shows that the structure is super-stable.

7.6 Discussion on numerical aspects: implementation and efficiency

The numerical implementation of the formulation is memory efficient. All of the constraint matrices can be constructed and stored in a compressed format as sparse matrices. Furthermore, the topological constraint and physical constraint matrices are binary. The bottleneck for the efficiency of the approach is the integer restrictions of design variables s .

The basic algorithm for MILP is the branch-and-bound method. Advanced implementations usually adopt strategies such as presolve and cutting-planes to reduce the problem size, and heuristics and parallelism to speed up the branching search. The fundamental idea is to relax and branch the MILP problem to many LP relaxations by allowing the discrete integer variables to become continuous. In each branch and bound search, the subproblem is solved as an LP problem. If there is an optimal solution of the LP relaxation found during the branching process that satisfies the integer restrictions, then we have found a feasible candidate optimal solution to the original MILP.¹

¹The examples in this work are solved by the optimization software Gurobi 6.5 [197] executed by a MATLAB code. The code is operating on a desktop with an 8-core 3.0GHz Intel Xeon CPU. It is also possible to use other solvers such as the MATLAB built-in function “intlinprog” to solve the problem.

Note that, the problem posed by our proposed formulation does not guarantee existence of a solution. The existence of a non-trivial optimal solution depends on the number of bars in the ground structure and the geometry of the ground structure. However, usually we can find a solution for a dense ground structure.

Additionally, as we observe from the examples, the computational cost of the MILP varies significantly from problem to problem and does not only depend on the problem size. This is because for some problems, an optimal integer solution might appear at an early stage of the branching process. Therefore, the time that the optimization needs to converge is highly problem dependent. A larger size problem might be solved within less time than a smaller size problem (for example, the designs shown in Fig. 7.15 and 7.17(a)). In addition, the authors want to stress that it is not always necessary to find a strictly converged solution. If the solving time is limited, it is fine to accept a feasible suboptimal solution, like the case of Fig. 7.15. However, we observe that the implementation of the proposed formulation is generally more efficient than other MILP formulations in the literature [175]–[178], based on computational time comparisons for problems with ground structures of similar complexity.

7.7 Fabrication of the tensegrity models aided by additive manufacturing

In this section we will briefly describe the fabrication process for the physical model shown in Fig. 7.15(b).

For such a complex design, it is extremely difficult to attain the required prestress by connecting the cables one-by-one to the struts. Ideally, we want to make the cable net as a whole piece of network. However, the cable net outlines a polyhedron, and it is very difficult to print such three dimensional frame-like structures with the soft material that we are using. Therefore, we decompose the three dimensional cable net into 12 planar pieces, each containing a pentagon, as shown in Fig. 7.21(a). Actually, the 12 pieces are made from only three different patterns (7 of one, 4 of the second, and 1 of the third) as shown

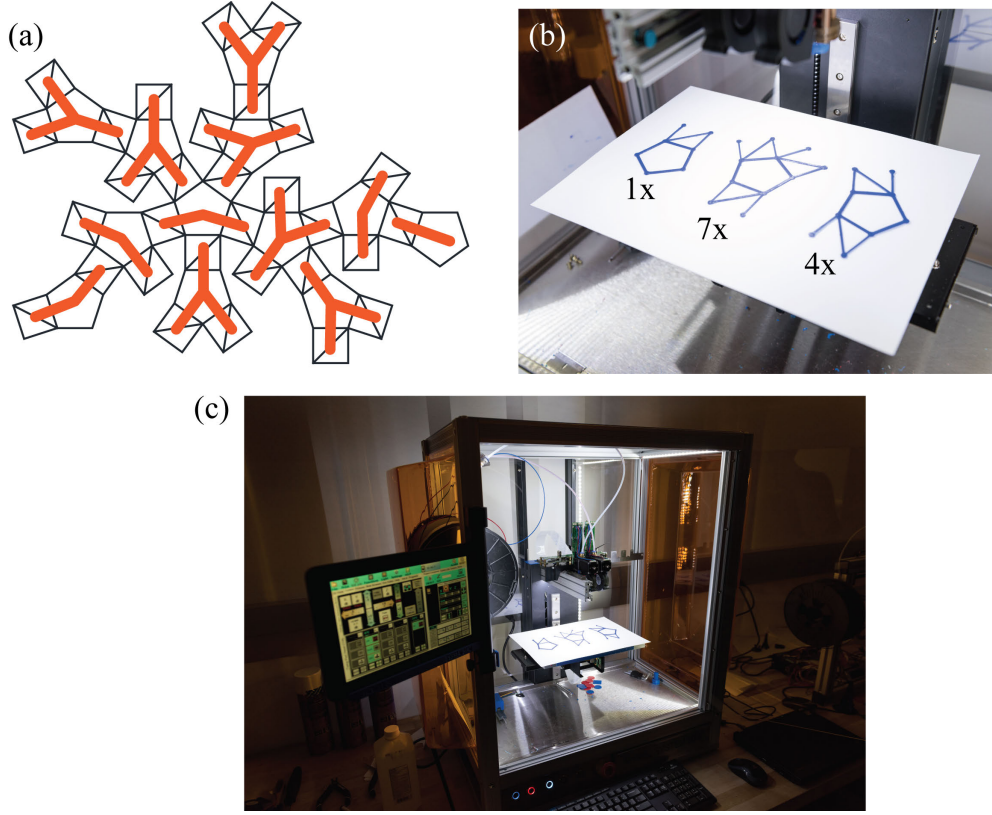


Figure 7.21: (a) The thin black lines shows the flatten cable net. The thick orange lines mark the 12 pieces that are printed separately. (b) The printed pattern pieces. The number on the side of each pattern indicates the number of this pattern embedded in the whole cable net. (c) HYREL 3D printer producing the elastic cable nets. Image courtesy: Rob Felt.

in Fig. 7.21(b). By printing 12 flat pieces, there is no need to print a supporting scaffold, which makes the printing process significantly easier than for the full, 3D cable net. The cable net pieces were fabricated using the Fused Filament Fabrication (FFF) technology on a HYREL 3D Printer². The material of the filament is called Ninjaflex³, which is a rubber-like soft material that can sustain large elastic deformations. The cross sectional areas of the cables are determined proportionally to the magnitudes of designated prestress forces. Furthermore, there are at most two pieces of cable net connected to one node, which lead to an easy and clean assembly process of the tensegrity structure using the printed cable components and the wood rods (0.25 inch diameter). The fabrication precision is also easy

²System 30M, HYREL 3D Inc, Norcross, GA, USA

³NINJATEK, Manheim, PA, USA

to control using the 3D printer as compared to making all the components by hand.

With the help of additive manufacturing, making complex tensegrity models (desk-top size), which is usually a difficult task, becomes a relatively easy procedure as described in this section. Thus, researchers and designers can quickly prototype their tensegrity designs. Moreover, such an approach can have a positive impact in engineering education. For instance, 3D printing the tensegrity models designed using our topological optimization approach is a means to bring the computational design to reality, which motivates students to design their own tensegrities and add a new dimension to their learning, so that the learning spans from the formulation to the computational modeling to the fabrication.

7.8 Concluding Remarks

We have proposed a topology optimization formulation for the design of tensegrity structures based on the ground structure method and a MILP approach. The formulation is simple, elegant and easy to implement. During optimization, a tensegrity is extracted from the many potential members in a ground structure by maximizing the summation of self-equilibrating forces. The obtained tensegrity design satisfies the self-equilibrium condition and the discontinuity condition of compressive members.

The effectiveness of the formulation is verified by numerical examples. The reproduction of existing well-known tensegrities is important because it shows that as long as the specific geometry is provided, the proposed formulation, although simple, automatically converges to desired solutions. The topology design of tensegrity is an open problem without a naturally defined objective, thus, the choice of the objective function can make a big difference. In this context, the force maximization formulation appears with some nice features. Although not enforced explicitly, the formulation usually leads to tensegrity structures that are stable and symmetric, which are commonly desirable features. We also explore the possibility to obtain tensegrities with desired geometrical and topological features by controlling the design space offered by the ground structure. This feature could be

very useful when designing for engineering applications, in which the tensegrity structures must adapt their shapes in order to carry payloads or avoid nearby objects. The numerical implementation of our formulation is efficient in comparison to other mixed integer formulations, and enables designs of relatively complex tensegrities, as shown in some of the examples. These benefits make it suitable for preliminary designs of engineering tensegrity structures (e.g. tensegrity protectors carrying a payload).

We remark that the formulation presented here is a basic one that can incorporate other constraints for different purposes. For instance, examples of constraints previously reported can be found in references [175]–[179], which are also applicable, with some modifications, to our basic formulation. In future development as we plan to adopt some strategies such as a multi-step optimization [198], to allow flexibility on the position of nodes so that we can combine the advantages of both topology and geometry design methods for tensegrity.

CHAPTER 8

PROGRAMMABLE DEPLOYMENT OF TENSEGRITY STRUCTURES BY STIMULUS-RESPONSIVE POLYMERS

Tensegrity structures with detached-struts are naturally suitable for deployable applications, both in terrestrial and outer-space structures, as well as morphing devices. Composed of discontinuous struts and continuous cables, such systems are only structurally stable when prestress is induced; otherwise, they lose the original geometrical configuration (while keeping the topology) and thus can be tightly packed. We exploit this feature by using stimulus responsive polymers to introduce a paradigm for creating actively deployable 3D structures with complex shapes. The shape-change of 3D printed smart materials adds an active dimension to the configurational space of some structural components. Then we achieve dramatic global volume expansion by amplifying component-wise deformations to global configurational change via the inherent deployability of tensegrity. Through modular design, we can generate active tensegrities that are relatively stiff yet resilient with various complexities. Such unique properties enable structural systems that can achieve gigantic shape change, making them ideal as a platform technology for super light-weight structures, shape-changing soft robots, morphing antenna and RF devices, and biomedical devices.

8.1 Introduction

Deployable structures have important applications, such as space structures [2], [199], [200], robotics [1], [56], morphing antenna and RF devices [201], and biomedical devices [46]. Integrated only by prestress, tensegrity structures [8], [10] are inherently deployable. They do not require mechanisms to lock the deployed shape, as many other deployable systems do, because the prestress also provide structural stability [50], [51], [53], [54], [191].

As the struts are connected by flexible cables, complex articulated joints that are typical in truss-made or origami-inspired deployable structures are also circumvented. These features apply to both terrestrial and outer-space structures [2], [58], [202]–[204], scaling from nanometers [205] to meters [199]. Beyond deployability, tensegrity displays aesthetic formation 8, high-precision controllability and easy tunability [50], [51], [206]. In nature, tensegrity structures are found in living systems and play an important role to the fundamental structure and function of cells [13], [14].

Recently, advanced additive manufacturing technologies using active materials, such as shape memory polymers (SMP) [207]–[210], hydrogels [211] or composites [212], [213], have provided the capability to print shape-evolving products, and thus adds time as the fourth dimension to the shape forming process, or 4D printing. Among active materials, SMPs exhibit excellent recoverability, easy tailoring of properties. More recently, 3D printing SMPs become available, making them a good fit for fabricating active structural systems with complicated geometries.

In this research, we use 3D printed thermally responsive SMPs to create actively deployable tensegrities. Thanks to the aforementioned unique properties of tensegrity, our paradigm for creating self-deployable structures distinguishes itself from related attempts for reconfigurable structures [207]–[213] in many aspects, such as superior volume expansion, design simplicity, resilience after deployment, and modularity. Figure 1A shows schematically the overall concept and the details of the design. The struts, which are made of SMP and are straight in their permanent shape, can be programmed into compact shapes. They are then connected by elastic cables (Fig. 8.1(a)-i). Once the assembly is heated, the struts recover their original straight shapes. However, because of constraints imposed by the cables, prestress are generated in both cables and struts, and the loosely connected struts and cables can stand up and form a fully functional 3D tensegrity structure (Fig. 8.1(a)-ii).

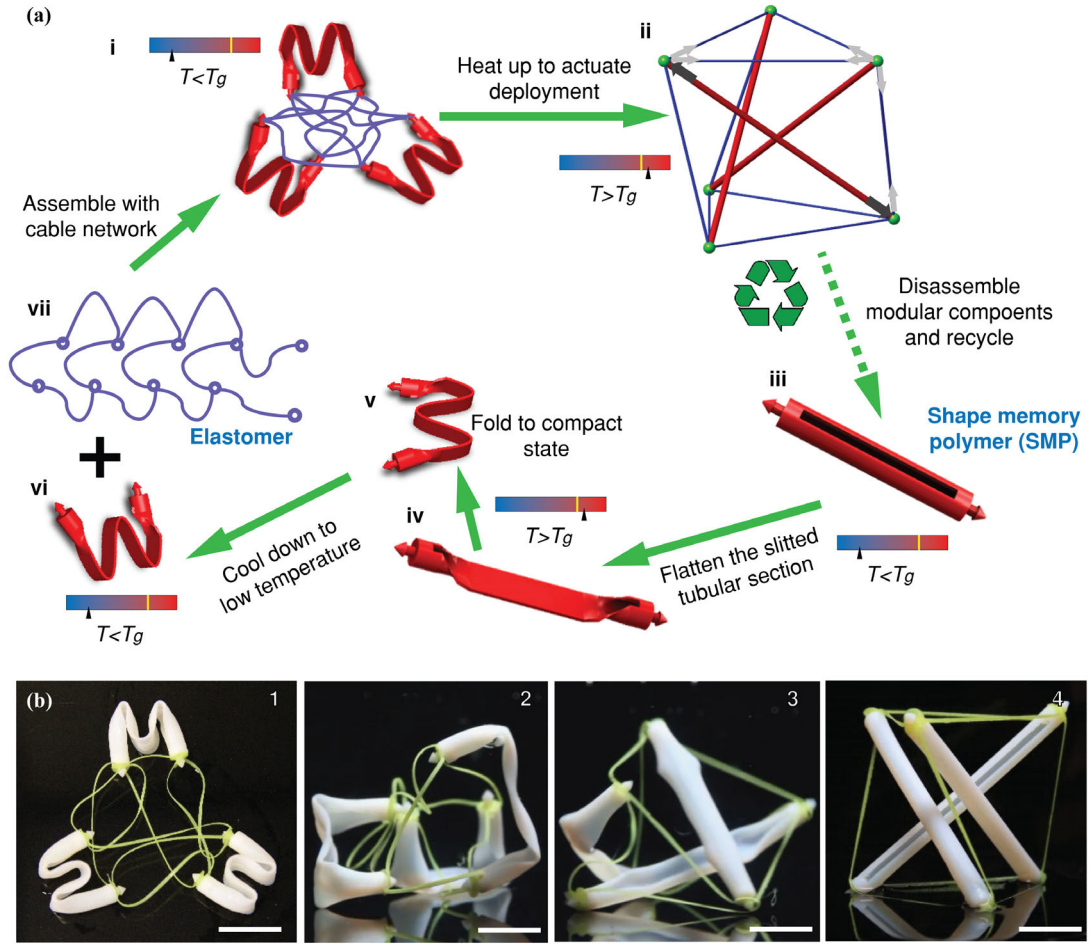


Figure 8.1: Procedure for creating an active tensegrity. Deployment of an active tensegrity is based on the shape recovery property of shape memory polymers (SMP). (a) Schematic of the overall concept and design. (i) The struts, which are programmed to compact shapes, are connected by a network of elastomer cables. (ii) Upon heating, the recovery of the struts to their straight shapes leads to actuation of the structure to a 3D resilient tensegrity structure. To achieve this concept, (iii) the struts are designed to have a tubular shape with a longitudinal slit which are 3D-printed using SMPs; (iv-v) the SMP struts are folded into compact shapes at a temperature that is above the glass transition temperature (T_g) of the SMP; (vi) decreasing the temperature below T_g fixes the struts in the compact shapes, which are then assembled with the elastomer cables (vii), according to the topology of the design to form a loose assembly (i); heating the assembly to a temperature above T_g leads the struts to their original shapes, and thus the constraints from the cables induce prestress. As a consequence, a stable tensegrity structure is obtained. (b) The experimental result shows the deployment process. The scale bars represent 15mm.

8.2 Deployment of a simple 3-strut tensegrity

To realize the aforementioned concept, we design the struts and cables and use 3D printing to implement our design – Fig. 8.1(a) shows design details. The struts have a tubular shape with slit central portions so that they can be easily packed by bending (Fig. 8.1(a)-iii). The two ends of the struts are designed with arrowheads to help mounting the cable network. Struts are printed by an acrylate-based photopolymer, named Verowhite, which is one of the model materials in our multi-material 3D printer (Objet 260 Connex), and is a SMP with the glass transition temperature (T_g) around 60°C [209], [212]. The printed struts are then heated to a temperature (65°C) above its T_g for programming. We first flatten the central portion (Fig. 8.1(a)-iv) then bend it into a W-shape to enable favorable compaction (Fig. 8.1(a)-v). Finally, we lower the temperature to 10°C and the struts are fixed in the W-shape (Fig. 8.1(a)-vi). For the cables, because they form a continuous network [51], [53], we design it (Fig. 8.1(a)-vii) according to the structural topology and print it using an FFF (Fused Filament Fabrication) printer with FilaFlex, which is a stretchable elastomeric filament material. The nodes in the cable network are designed with small holes so that they match the arrowheads of the struts. Finally, we attach the cable network with programmed struts (Fig. 8.1(a)-i). Up to this step, the tensegrity structure gains its topology but not its geometry; it is unconstrained in configuration and thus could be tightly packed into almost any shape. We then increase the temperature to deploy the structure. Fig. 8.1(b) shows the deployment when the assemblage is inserted into a tank of hot water at $\sim 65^\circ\text{C}$. As the struts recover their original straight shapes, cables are stretched and prestress are developed within the system. This renders “life” to our tensegrity, i.e. it stands up, to reach its designated geometry, resulting in a giant configurational change, although *it had never been built to this shape before*.

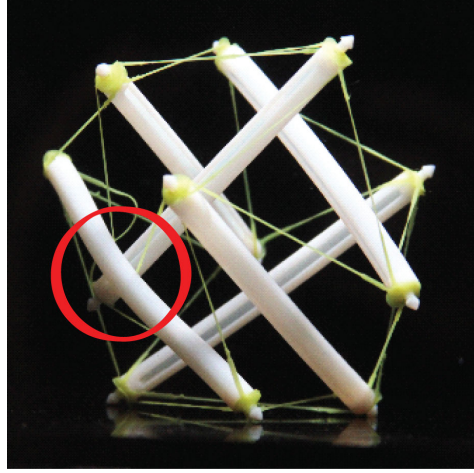


Figure 8.2: Failed deployment of a 6-strut spherical tensegrity, due to physical contact between struts, as highlighted by the red circle. As discussed in the main text, when the cables are loose, the folded struts are almost free to move in space. In this example, a strut blocks the recovery of another strut.

8.3 Deployment of a 6-strut tensegrity with reduced degree-of-freedom

In our design, the cables are loose before deployment and the folded struts are free to move in space. Such excessive degree-of-freedom (DOF) may lead to incorrect positioning of struts and may create the risk of cable entanglement, or trap the structure at an undesirable configuration, as shown in Fig. 8.2. To overcome such drawback, we reduce the DOF of the pre-deployed structure. One approach is to take advantage of the decoupled hierarchies and reduce the number of folded struts, i.e., leaving some struts straight. In this way, the tensegrity deployment becomes more deterministic, while the structure can still be stored in a compact state that occupies much less space than its deployed configuration. This design concept is illustrated by the 6-strut spherical tensegrity shown in Fig. 8.3(a), where three of the struts are deprogrammed and are made partially solid to have an eccentric center of gravity, which stabilize the structure against gravity as it stands up. Such a design leads to successful deployment.

Our active tensegrity can be used to form 3D structures with surfaces that can serve as a platform to host functional devices. As a demonstration, we attached elastomer membranes

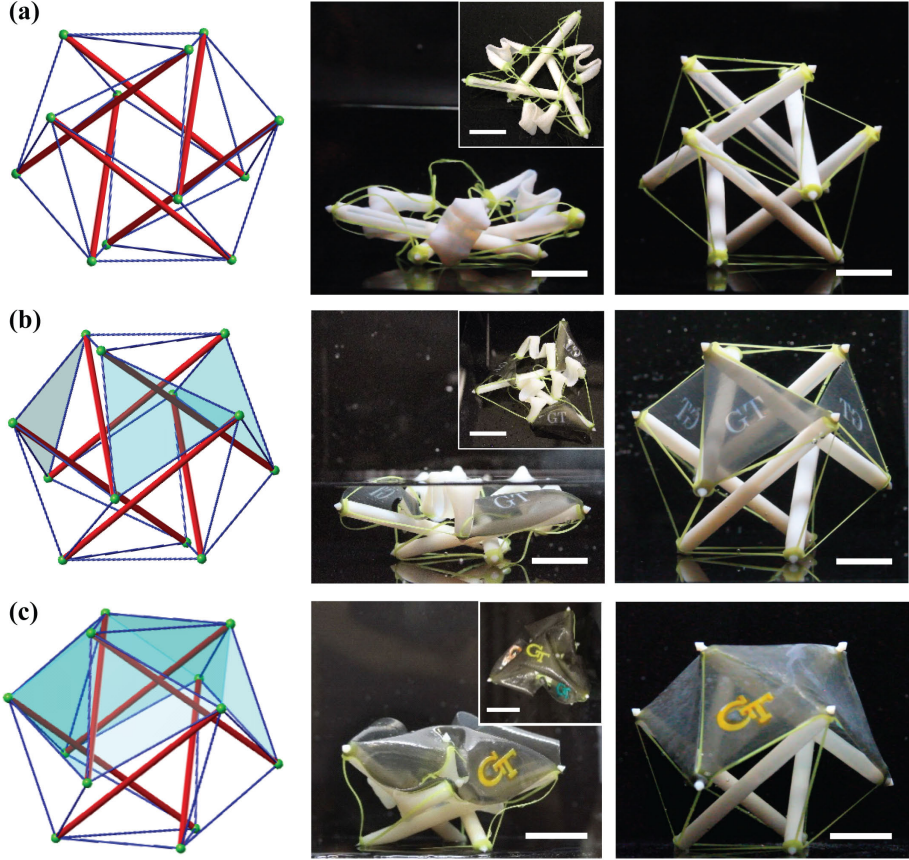


Figure 8.3: Deployment of 6-strut spherical tensegrity. (a) Deployment of a spherical tensegrity using the partial folding strategy to improve reliability of deployment. (b) Positioning of three discrete pieces of surfaces into space. (c) Deployment of a continuous surface supported by the active tensegrity to form a tent. The resultant structural system mimics the fundamental structure of vertebrates, with the membrane as skin, elastic cables as muscles, and relatively rigid struts as the skeleton (biomimetics). The scale bars represent 15mm.

on the previous 6-strut tensegrity (Fig. 8.3(b) and (c)). On both discrete and continuous surfaces, we printed the “GT” (Georgia Tech) logo; it is not hard to imagine that one can print electronic circuits, to take advantage of the gigantic shape-change and to enable functionalities of the structure. The configuration of the deployed surfaces depends on the base tensegrity. With some state-of-art form-finding approaches for tensegrity [170]–[172], [187], [188], we can generate space covering surfaces of almost any geometry. In addition, the attached surfaces increase the reliability of the deployment, as they provide additional constraints and reduce arbitrariness during the deployment.

8.4 Deployment of tower tensegrities with programmed sequence

The development of digital materials in 3D printing allows us to print parts using polymers with different T_g 's, thus offering different shape memory characteristics that permit sequential shape changes [208], [214]. We take advantage of digital SMPs and program the deployment sequence to further pursue complex tensegrities in a controlled manner. Here, we choose three SMPs: DM-1 with T_g around 37°C; DM-2 with T_g around 57°C; and the SMP used in the above (Verowhite, termed as BM here) with T_g around 60°C. We first create one 2-layer prismatic tower tensegrity (Fig. 8.4(a)), and one “3-Layer Tensegrity” 1,30 (Fig. 8.4(b)), by using DM-1 and BM, to demonstrate the capability of the programmed deployment. The struts with different materials are programmed in the same manner as shown in Fig. 8.1. They are then assembled with the elastomer cable networks. Fig. 8.4(a)-1 and (b)-1 show the pre-deployed shapes of the structures. As there are no prestress, they lay on the ground. To activate the deployment of the structures, we first increase the temperature to 40°C, submerging the structure in a hot water bath. As shown in Fig. 8.4(a)-2 and (b)-2, the struts made by DM-1 recovered first, forming partially deployed tensegrity structures, with the right and middle parts not activated in Fig. 8.4(a)-2 and (b)-2, respectively. Finally, we increase the temperature to 65°C to deploy the struts made with the BM, as shown in Fig. 8.4(a)-3 and (b)-3.

To further demonstrate control over the deployment sequence, we prepare a three-layer structure with DM-1, DM-2, and BM (Fig. 8.5). To deploy the structure, we increase the temperature in three steps: first to 40°C, then to 57°C and finally to 65°C. The 2nd and 4th frames in Fig. 8.5 show the sequential deployment. Because the glass transition temperatures of DM-2 and BM are close, the distinction between the actuations of the middle layer and the right layer are not very clear; better distinction can be achieved if more digital materials were available with more distinguishable T_g 's.

The obtained tensegrity structures allow elastic deformation to a significant amount of

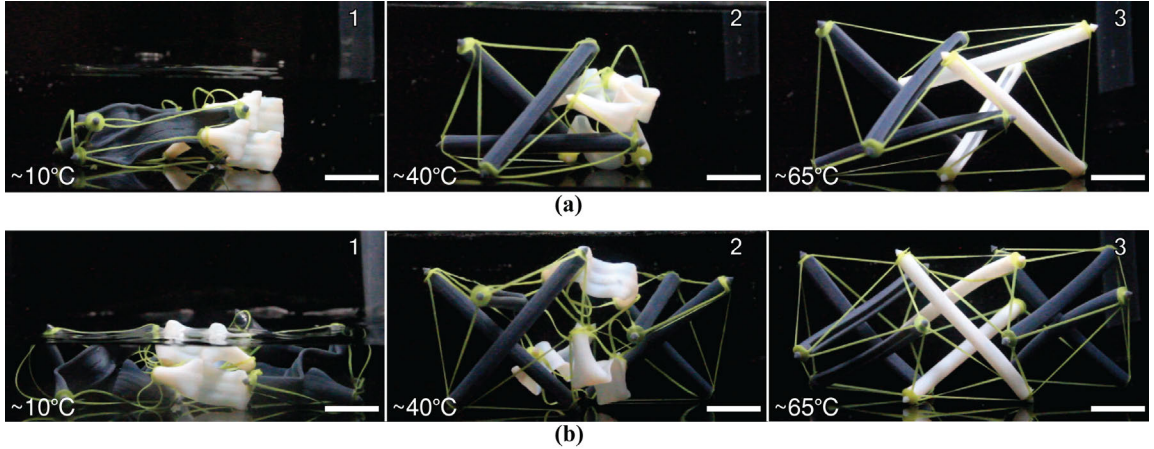


Figure 8.4: Programmed deployment of layered tensegrity structures, using 2 different SMPs for the struts: DM-1 (the dark gray material) and BM (the white material). (a) Programmed deployment sequence of the “2-Layer Tensegrity”. (b) Programmed deployment sequence of the “3-Layer Tensegrity”. The two end layers have struts made with SMP of a lower T_g than the middle layer. The scale bars represent 15mm.

magnitude without fracture or yielding. Fig. 8.6 shows compression tests of the three tower tensegrity structures in Fig. 8.4 and 8.5. Since the stiffness of the cables is much lower than the struts, the global deformation of the tensegrity is mainly carried by local deformation of the elastomer cables. The plateau in the loading curve and the small dip in the unloading curve in Fig. 8.6(b) and (c) are caused by the inherent instability of this tensegrity design. That is, the ideal structure has multiple local minima of stored energy at different configurations. For example, when one layer of the tower is fully flattened, the structure is at an alternative stable state (other than the fully deployed configuration). Due to the contact of struts, the alternative stable configurations cannot be reached. However, it still leads to a reduction in stiffness of the structure (instability). The “3-Layer Tensegrity” in Fig. 8.6(c) displays this effect more clearly than the one in Fig. 8.6(b) because the two-material structure has larger number of DM-1 struts, which are less stiff than DM-2 and BM struts in room temperature ($\sim 25^\circ\text{C}$). Thus, when contact between struts happens, the DM-1 struts bend, leading the structure closer to the ideal alternative stable configuration, even though this state still cannot be fully reached.

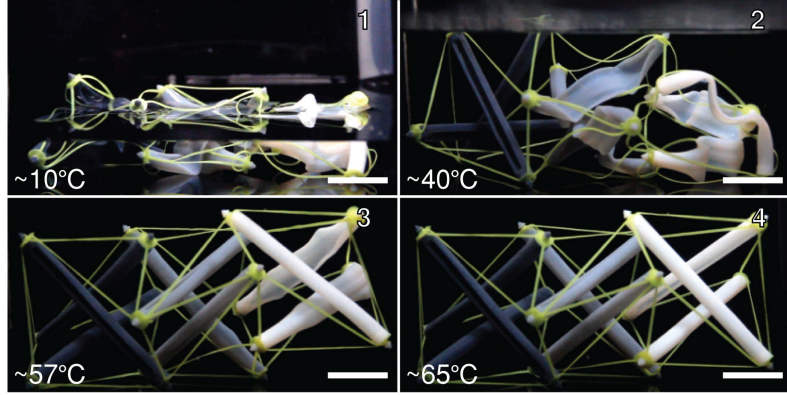


Figure 8.5: Programmed deployment sequence of the “3-Layer Tensegrity” using 3 different SMPs for the struts: DM-1, DM-2, and BM. The three SMPs have increasing T_g ’s from left to right as shown in the images. The darker the color, the lower the T_g . The scale bars represent 15mm.

8.5 Design philosophy

The mismatch between the initial lengths of the struts and cables is critical for determining the prestress, which in turn dictates if the deployment can be successful and the stiffness of the tensegrity is enough. In general, neither too small nor too large prestress can deploy the structure. This is because too small prestress would not provide enough stiffness to support the total weight, but too large prestress would prevent the strut from full recovery. Therefore, it is important to design proper initial lengths. Toward this end, we conduct theoretical analysis of the prestress generated during and after the strut recovery to gain insight. We also conduct finite element (FE) simulations to confirm our theoretical analysis.

8.5.1 Stiffness of tensegrity designs

According to Section 7.3.5, the stiffness matrix of a tensegrity is a function of its prestress forces \mathbf{F} . Suppose that the desired prestress level is $\mathbf{F} = \gamma \bar{\mathbf{F}}$, where $\bar{\mathbf{F}}$ is the normalized prestress induced force vector with maximum compression in struts equal to 1. Assuming small deformation and small prestress [184], the higher the prestress, the stiffer the tensegrity. We find the relationship between the initial tangent modulus of a tensegrity under

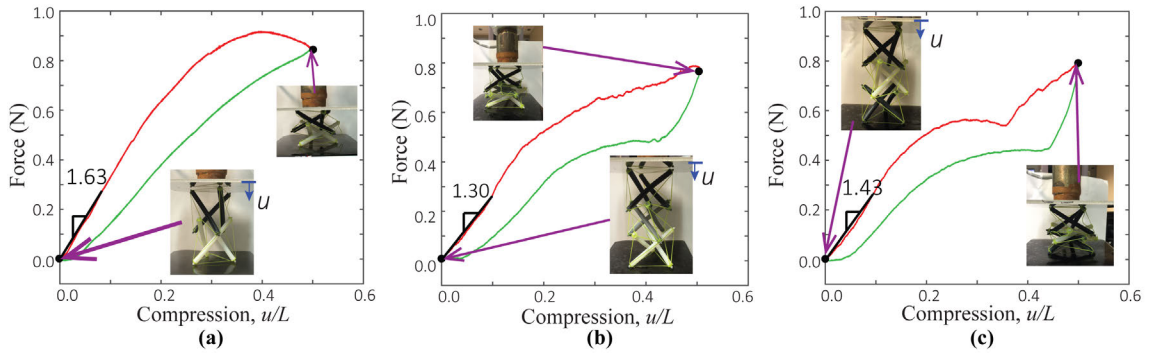


Figure 8.6: Compression test of the deployed tensegrities. (a) Compression test of the deployed “2-Layer Tensegrity” using 2 different SMPs for struts (BM and DM-1). The red line indicates the loading process while the green line indicates the unloading process. According to Fig. 8.7, we estimate the maximal compression in the deployed tensegrity to be 0.12N by the initial slope of the curve. (b) Compression test of the deployed “3-Layer Tensegrity” made with 3 different SMPs (BM, DM-1, and DM-2). The test reveals a maximum compression in the struts around 0.12N. (c) Compression test of the deployed “3-Layer Tensegrity” made with 2 different SMPs (BM and DM-1). Maximal compression in the struts is estimated to be around 0.14N.

global uniaxial compression and the prestress level γ . The initial tangent modulus is the ratio of the applied force over the compression magnitude (in terms of displacement). Fig. 8.7 plots the curve of initial tangent modulus versus prestress level for three tensegrity designs, including the one demonstrated in Fig. 8.1, using real material properties and actual geometry that is used to make active tensegrity structures. The tangent modulus shown here is calculated using the non-dimensional displacements, which is the downward compression displacements normalized by the heights of the tensegrity designs, and thus, the unit of the tangent modulus is in Newton (N). The two 3-layer tensegrities (with different materials) yield almost identical curves, so only one is plotted for clarity. This curve does not start from (0,0) because the “3-Layer Tensegrity” is kinematically determinate, thus its stiffness matrix is not singular when there is no prestress. According to the experimental compression tests of the active tensegrities, we can approximate the initial tangent modulus of a tensegrity. Therefore, based on the curves shown in Fig. 8.7(b), we can inversely approximate the magnitude of induced prestress in the deployed tensegrities, by matching the initial stiffness with theoretical predictions.

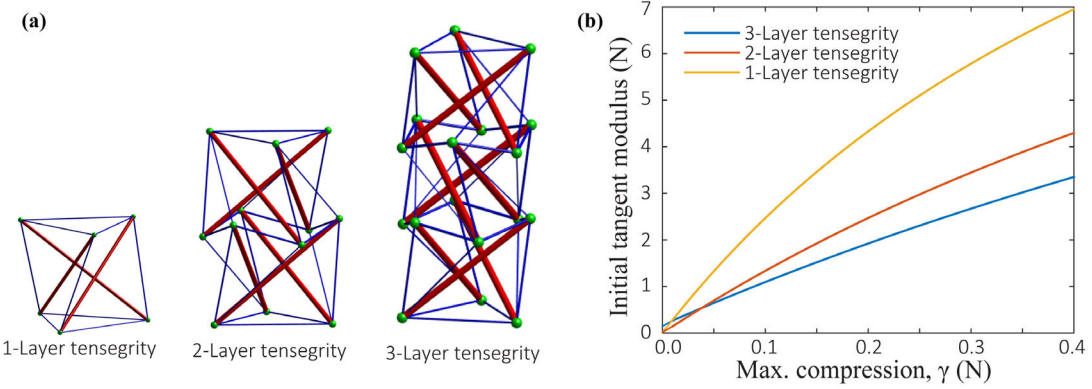


Figure 8.7: The change of tensegrity compression stiffness with respect to prestress level. (a) Illustration of three tensegrity designs. (b) Initial tangent modulus vs. maximum pre-stress compression forces in struts (i.e. γ).

8.5.2 Design of struts

The achievable prestress level of an active tensegrity is not arbitrary, as it is determined by two critical factors. The first factor is that the compression on struts should not prevent their full recovery. In the final stage of deployment, some SMP struts in the active tensegrity will be subject to compression before full recovery, with their tubular cross-section still open. The second critical factor is that, after deployment, the struts should not buckle under the prestress compression. If the struts buckle, then the tensegrity will lose some prestress and cannot completely reach the designated shape. In the following, we will derive analytical estimations of these two critical strut loads. We first compute the critical force during the recovery, when the tubular cross section of a strut is open, as shown in Fig. 8.8. We make the following assumptions: (1) a tube can be analyzed using shell theory because the thickness is relatively small; (2) the mid-surface is subject to isometric deformation; (3) the static behavior of the SMP can be regarded as elastic when the temperature is fixed and the strain is relatively small. The meaning of the symbols used in the derivation is illustrated in Fig. 8.8. Therefore, supposing that the changes in the curvatures along the two principle directions are $(1/r, 1/R)$, we can write the total strain energy at the bending region as

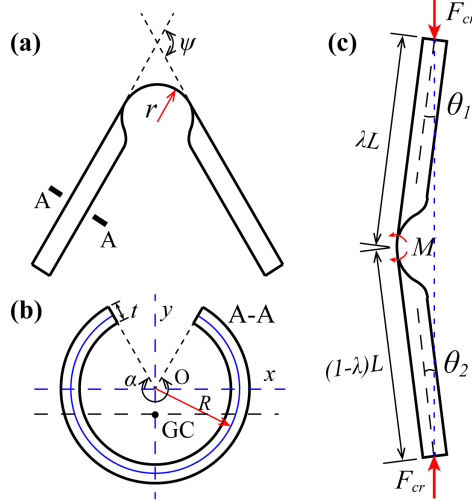


Figure 8.8: Design of struts. (a) Schematic of a folded strut with opened cross section. (b) Cross section (A-A) of the struts. (c) Sketch of the critical scenario in the recovery of struts (during the deployment of an active tensegrity), based on observations from the experiments.

[215]:

$$U_B = \frac{D\alpha R\psi}{2} \left(\frac{1}{r} + \frac{r}{R^2} - \frac{2\nu}{R} \right). \quad (8.1)$$

The symbol D denotes the flexural rigidity, which is defined as:

$$D = \frac{C_0^s t^3}{12(1-\nu)}, \quad (8.2)$$

where, C_0^s is the Young's modulus and ν is the Poisson's ratio of the strut material (i.e. Verowhite). The value of r is determined when bending energy U_B is minimized [215].

Therefore, we obtain that $r = R$. The corresponding bending moment is calculated as:

$$M = \frac{\partial U_B}{\partial \psi} = D\alpha(1-\nu). \quad (8.3)$$

At the final stage of the strut's recovery, a single kink about a quarter from the end of a strut is usually observed. Thus, we can draw the shape schematically as shown in Fig. 8.8. The regions that are not opened are much stiffer than the bending region. Therefore, we

may assume those regions are rigid. Notice that,

$$\lambda L \sin \theta_1 = (1 - \lambda)L \sin \theta_2. \quad (8.4)$$

If the two applied forces are aligned along the same line, then equilibrium is obtained as:

$$M = F_{cr}(\lambda L \theta_1 + R \cos \theta_1). \quad (8.5)$$

Thus the critical force is given by:

$$F_{cr} = \frac{M}{\lambda L \sin \theta_1 + R \cos \theta_1} \geq \frac{C_0^s t^3 \alpha}{12(\lambda L \theta_1 + R)}, \quad (0 < \theta_1 < \pi/2). \quad (8.6)$$

In our case, the typical value of λ is around 0.25. The angle θ_1 can be computed from the deformed length of the strut ($\lambda L + \cos \theta_1 + (1 - \lambda)L \cos \theta_2$). The equality in Eq. (8.6) holds when θ_1 is small. The later expression provides a conservative estimation to the critical force. The derivation requires a portion with fully opened cross section along the strut (which forms a “kink”), thus it is not accurate when the strut is almost straight (i.e. θ_1 becomes very small), because in reality the opened cross section starts to enclose before the strut recovers to straight, so the deformation mode no longer has a “kink”.

The critical load before the buckling of the struts after deployment is given by the Euler buckling formula [216]:

$$F_{EB} = \frac{\pi C_0^s I_{min}}{L_{eff}^2}. \quad (8.7)$$

The effective length L_{eff} depends on the boundary conditions of the strut. In the compression tests, the fixture of the sample constrains the free rotation at the two ends, resulting in an effective length around $0.75L$. However, in the tensegrity, the two ends are assumed to be pinned, and thus $L_{eff} = L$. The minimum static moment of inertia I_{min} is determined to be the static moment of inertia of the X-X axis at the geometric centroid GC, which is

denoted as I_{GC-XX} ,

$$I_{GC-XX} = R^3 t \left[\frac{\alpha}{2} + (\alpha - \pi) \frac{\sin^2(\alpha/2)}{(\alpha/2)^2} + \frac{\sin \alpha}{2} \right]. \quad (8.8)$$

We note that, in the experiment, the struts are not loaded at the geometric center (GC) of the cross section. Instead, the compressive forces are loaded at point O (at the center of the mid-surface circle). As a consequence, the actual critical buckling force will be lower than the estimation, since the buckling mode involves a combination of bending and twisting.

8.5.3 Design of cables

As explained before, the prestress in the tensegrity is induced by prescribed length differences between cables and struts. We assume that after successful deployment, the struts become straight and their deformation under compression is negligible (recall that the struts are much stiffer than the cables). Therefore, we control the level of prestress magnitude by manipulating the initial length of cables. We did this for two reasons. First, we do not want the initial length of cables to be too long so that the deployed tensegrity cannot gain enough prestress to become stable and stiff. Second, the initial lengths of cables should not be so short that the struts cannot recover during deployment or stay straight after deployment, due to the excessive prestress magnitude.

We assume member i is a cable. Given the normalized force vector $\bar{\mathbf{F}}$, we can determine the initial length of a cable as:

$${}^0L_i = \frac{{}^1L_i - 2\delta}{F_i / ({}^0A_i C_0^c) + 1} + 2\delta. \quad (8.9)$$

In this equation, 0L_i denotes the initial length of cable member i ; 1L_i is the design length of the cables (in the prestressed configuration) obtained from the tensegrity design; F_i is the desired tension in the cable; A_i is the cross-sectional area of the cable; C_0^c is the Young's modulus of this cable; and δ is the ineffective length at each end of a cable which changes

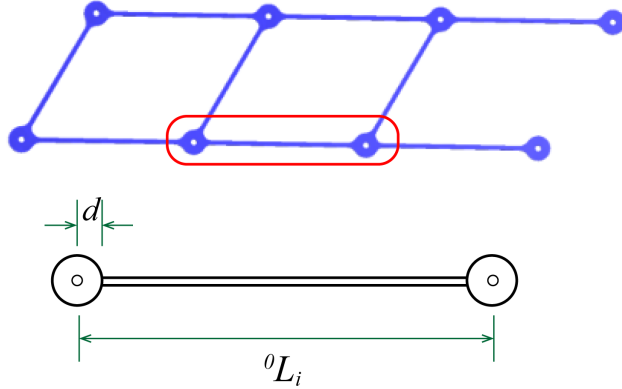


Figure 8.9: Schematic of the cable network design for the “1-Layer Tensegrity” as shown in Fig. 8.7(a).

very little. Considering the contact angles of cables and struts, δ is generally 1.4 to 3 times the distance d shown in Fig. 8.9. Typically, the prestress forces are small, and we can assume linear behavior for the cables. Hence the initial elastic modulus C_0^c is used.

Such calculation provides an approximate guide for determining the initial lengths of cables based on the value of γ , which needs to be greater than 0, but less than the minimum critical load of the strut. In reality, the control of the prestress level and final geometry are not precise due to many practical factors, for example: the twisting of cables, the plasticity of the cable material, the printing accuracy, and the entanglement of the cables near the joints. In some cases, adjustment based on the outcomes of the experiments is needed, especially for tensegrity designs with complex geometries.

8.5.4 Finite element analysis

A multi-branch model is used to describe the viscoelastic properties of the printed SMP materials. In this model, one elastic equilibrium branch and several thermo-viscoelastic non-equilibrium branches are arranged in parallel. The non-equilibrium branch is described by the Maxwell element, represented by a viscous damper and an elastic spring connected

in series. The total stress of the material can be expressed as:

$$\sigma_{total} = \sigma_{Eq} + \sum_{m=1}^n \sigma_{non}^m = C_{Eq}\varepsilon + \sum_{m=1}^n C_{non}^m \int_0^t \frac{\partial \varepsilon}{\partial s} \exp \left[- \int_s^t \frac{dt'}{\tau_m(T)} \right] ds, \quad (8.10)$$

where C_{Eq} is the Young's modulus of the equilibrium branch, C_{non}^m and τ_m are the Young's modulus and temperature dependent relaxation time of the m -th non-equilibrium branch, respectively. The strain ε is defined as the true strain. To consider the temperature effects, the time temperature superposition principle (TTSP) is used. The relaxation time τ_m at temperature T can be calculated using the relaxation time τ_m^R at the reference temperature, given by:

$$\tau_m(T) = a^{shift}(T)\tau_m^R, \quad (8.11)$$

where $a^{shift}(T)$ is the time temperature superposition shifting factor. According to O'Connell and McKenna [217], the shifting factors can be calculated by combining the Williams-Landel-Ferry (WLF) equation [218] and the Arrhenius-type equation [219]. If the temperature is higher than the reference temperature, the shifting factor can be expressed using the WLF equation:

$$\log [a^{shift}(T)] = - \frac{c_1(T - T_{ref})}{c_2 + (T - T_{ref})}, \quad (T \geq T_{ref}). \quad (8.12)$$

The parameters c_1 , c_2 and T_{ref} are material parameters to be characterized by experiments. We denote c_A , U_C , and k^{Boltz} as the material constant, configurational energy, and Boltzmanns constant, respectively. When the temperature is lower than the reference temperature T_{ref} , the shifting factor is expressed by the Arrhenius-type equation:

$$\ln [a^{shift}(T)] = - \frac{c_A U_C}{k^{Boltz}} \left(\frac{1}{T} - \frac{1}{T_{ref}} \right), \quad (T < T_{ref}). \quad (8.13)$$

The parameters including C_{Eq} , C_{non}^m , τ_m^R , c_1 , c_2 and $(c_A U_C / k^{Boltz})$ are determined from the DMA tests. The storage modulus at high temperature (90°C for BM, 65°C for DM-1, 85°C

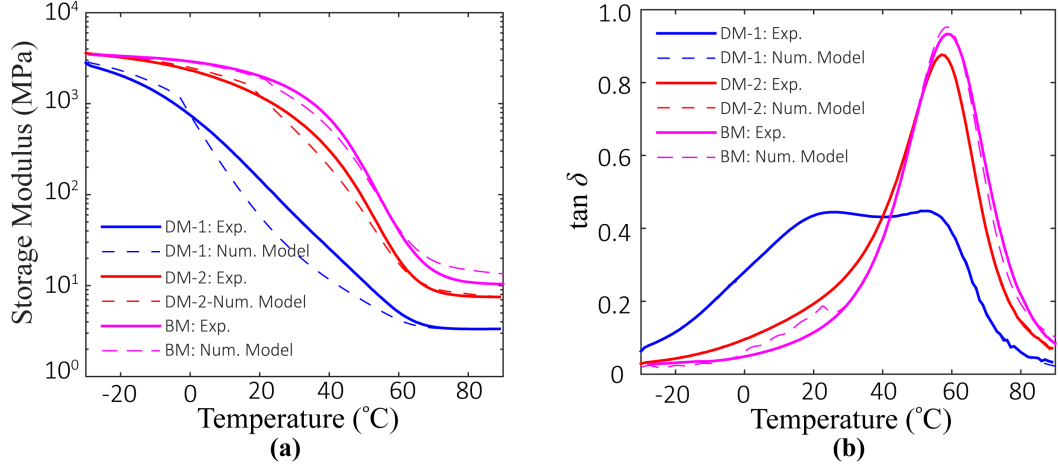


Figure 8.10: Comparison of the DMA curves between experimental data and numerical models for three SMP materials used in this research.

for DM-2) is the equilibrium modulus C_{Eq} for each of the materials. For the multi-branch model, the temperature dependent storage modulus $C_s(T)$, loss modulus $C_\ell(T)$, and loss tangent $\tan \delta(T)$ can be respectively computed by:

$$C_s(T) = C_{Eq} + \sum_{m=1}^n \frac{C_{non}^m \omega^2 [\tau_m(T)]^2}{1 + \omega^2 [\tau_m(T)]^2}, \quad (8.14)$$

$$C_\ell(T) = \sum_{m=1}^n \frac{C_{non}^m \omega \tau_m(T)}{1 + \omega^2 [\tau_m(T)]}, \quad (8.15)$$

$$\tan \delta(T) = \frac{C_\ell(T)}{C_s(T)}. \quad (8.16)$$

The symbol ω denotes the test frequency. By employing a nonlinear regression software [220], [221], the parameters C_{Eq} , C_{non}^m , τ_m^R , c_1 , c_2 and $(c_A U_C / k^{Boltz})$ are determined by fitting the loss tangent and storage modulus from experimental DMA tests. The material parameters used in this work are provided in Table 1. To show the capability of this model, the comparison of the DMA curves between the experiment and the simulation are shown in Fig. 8.10. We can see that the multi-branch model explains the thermo-mechanical behavior of the printed strut materials in the temperature range used for programming and actuation processes.

The recovery process and mechanical properties of struts are modeled using the FE analysis software ABAQUS (Simulia, Providence, RI, USA). The hybrid C3D8RHT element is used. We implement the multi-branch model based on Prony's series, which is defined as:

$$G(t) = G_{Eq} + \sum_n^{m=1} G_m \varepsilon^{-t/\tau_m}, \quad (8.17)$$

where G is the total shear modulus, G_{Eq} and G_m are the shear modulus of the equilibrium branch and m -th non-equilibrium branches. Applying the incompressible condition, the shear modulus G is calculated as $G_m = C_m/3$, where C_m is the elastic modulus from the multi-branch model. To apply the temperature effects, the shift factors are calculated using the WLF equation and Arrhenius-type equation [218], [219]. The UTRS subroutine is used to implement the WLF equation and Arrhenius-type equation.

Considering the symmetry of the strut and boundary conditions, only 1/4 of a strut is used for simulation of free recovery. The slit of the strut is first opened into a nearly flat configuration in the middle part of the strut at 65°C, which is above the Tg of the BM (Verowhite). The pressure used to open the slit is applied on the inner surface of the slit near the opening. After the slit is opened, we fix the middle section of the strut (one end in the 1/4 model) and add a pressure load on the end of the strut and in the transverse direction of the strut to bend it into a “U”-shape. To further deform the strut into the “W”-shape, we fix the 1/4 section of the strut and apply pressure at the end in the opposite direction of the previous step. After the deformation process is finished, we cool the temperature to 25°C, at which the material is in a glassy state. Then all the external loading and constraints are removed, and the deformed shape of the strut is “frozen” due to viscoelasticity. To simulate the recovery process, the temperature is increased to 65°C.

The strut under compression is also modeled to determine the after-recovery critical force (F_{EB}). In this simulation, the whole strut is modeled to consider asymmetric deformation modes. We impose an ambient temperature of 65°C. One end of the strut is pinned in directions x, y, z within the central zone (radius of 1mm), creating a partially fixed end.

At the other end, the center zone is pinned in x , y directions (partially fixed), and a displacement load of rate 0.25mm/s is applied in the $-z$ direction. This boundary condition is similar to the case of the strut compression experiment, but more restrictive than the actual boundary condition as embedded in the tensegrity structures. A similar procedure can be applied to predict the mechanical performance of struts made with various SMPs.

8.5.5 Theoretical, finite element, and experimental results

Fig. 8.11(a) and (b) show the comparison between the experiment and the FE simulation of the shape change of a strut during a free recovery. Fig. 8.11(c) shows the opening angles (defined in the inset) measured during the recovery. Overall, the FE simulation results match the experiments reasonably well. The difference mainly comes from the uncertainty from experimental measurement, which is a challenge due to the dynamic nature of the free recovery. To estimate the maximum prestress beyond which the deployed struts will buckle, we conducted a compression test to measure the critical force (Fig. 8.11(d)). In addition, by using the effective length ratio of 0.75, the estimated buckling load derived using the Euler buckling criteria (i.e. Eq. 8.7) is close to those in the experiment and the FE simulation. The FE simulation shows relatively large deviation after the peak force is reached because instability occurs in the post-buckling regime. Nonetheless, the peak force is the most important design parameter. Fig. 8.11(e) compares the theoretical estimation and the experimental result of the critical force in the strut during the recovery when the cross-section is open (i.e. Eq. 8.6). The critical force for a strut during its recovery is typically smaller than the Euler buckling load after its recovery, which is commonly observed in the buckling and recovery test. The reason is that the energy level of deformation state before the buckling is high, so the system quickly buckles into the post-buckling state, which is a more energetically favorable state. Nevertheless, during recovery, the system is driven by its internal energy following a low energy path, which gives a lower force. This difference in the buckling force and the recovery force is beneficial; this is because the low

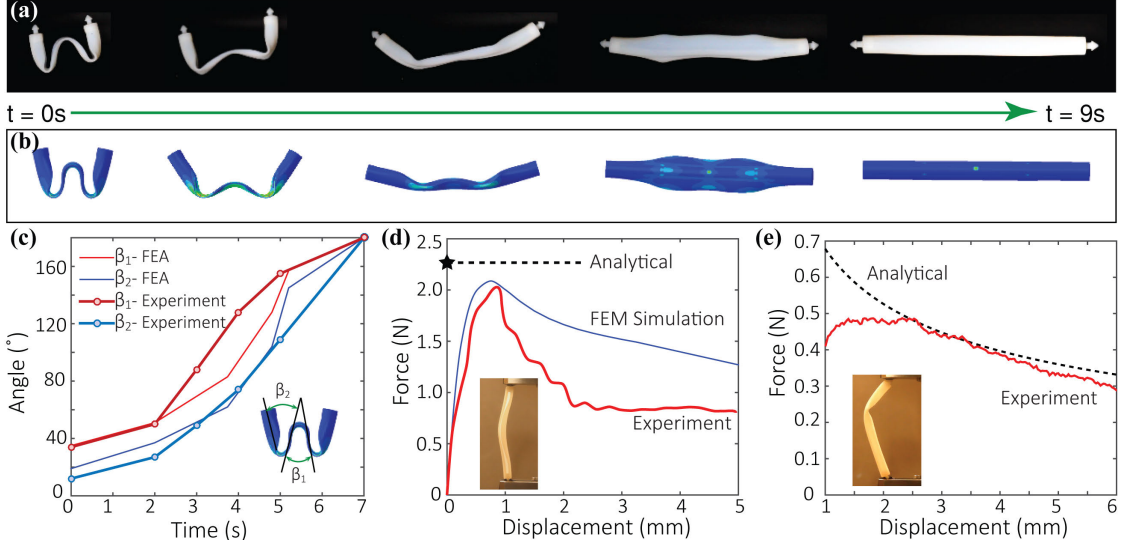


Figure 8.11: Properties of the slitted tubular struts via 4D printing. (a) The snapshot images of the free recovery sequence of a strut at 65°C. (b) the predictions from the corresponding FE simulation. (c) The opening angles of the strut during the free recovery and the comparison with FE simulations. The inset shows the definitions of the two opening angles. (d) the critical load of a single strut during uniaxial compression from the experiment and the FE simulation. The inset shows the experimental setup. Considering the boundary condition in the experimental setup, a 0.75 effective length ratio gives the upper bound on the critical buckling load of a single strut. In practical designs, because the joints in our tensegrity are almost free in rotation, 1.0 effective length shall be used. (e) Critical load of a single strut during its recovery. In the experiment, a small initial displacement (1mm) is imposed to prevent the opened cross section from closing.

recovery force makes the recovery relatively easy and the high buckling force can prevent the deployed tensegrity structure from buckling.

Hence, for our design of struts, the critical force shown in Fig. 8.11(e) determines whether a strut can successfully deploy when embedded in the tensegrity system. Based on the theoretical and FE analyses, for instance, the “1-Layer Tensegrity” design is determined to have the initial length of the struts to be 70mm, horizontal cables to be 49mm, and the titled cables to be 45mm. This design yields a maximum compression force in the struts to be 0.15N, about half of the minimum critical force (i.e. the recovery force) of the strut. A compression test is applied on the final structure. By matching the initial stiffness with theoretical predictions (as shown in Fig. 8.7), we can inversely determine the magnitude of induced prestress. We achieve approximately a maximal compression in the struts around

0.20N, larger than the designed value, but still less than the critical forces.

8.6 Methods and materials

8.6.1 Sample fabrication

The slotted tubular struts were fabricated using an Objet 3D printer (Objet 260 Connex, StrataSys Inc, Eden Prairie, MN, USA) in digital material mode using the PolyJet technology. The printer can combine two base materials, using pre-determined ratios to make the so-called digital materials. The digital materials differ in mechanical and thermal properties. The curable liquid photopolymer was jetted onto the build tray and then cured by UV polymerization. The three digital materials used in this research are Verowhite plus, DM9895 (DM-1) and DM8530 (DM-2) in Stratasys material library (see Fig. 8.12(a) and (b)). The cables were fabricated using the Fused Filament Fabrication (FFF) technology on a HYREL 3D Printer (System 30M, Hyrel 3D Inc, Norcross, GA, USA). A rubbery material named FilaFlex (Recreus, Elda, Spain) was used, which is a thermoplastic elastomer base polyurethane (see Fig. 8.12(c)). The extruder was especially equipped with a dual drive system to fulfill the task of printing flexible filaments. The filament was melted at $\sim 232^{\circ}\text{C}$ and deposited through a nozzle of $500\ \mu\text{m}$ diameter onto the tray. The cable nets were printed by two passes of reversed orientation. The extrusion paths were optimized to ensure the quality of the printing.

8.6.2 Deployment control

A water temperature control system was built, which includes a glass water tank, a DC water pump, a water heater, an electrical thermometer, and plastic tubes. The tank held some cold water ($\sim 10^{\circ}\text{C}$) at the beginning of each experiment. The level of the cold water submerged the pre-deployed tensegrity assemblies. To activate the deployment, hot water ($\sim 95^{\circ}\text{C}$) was pumped from the water heater into the tank to increase the temperature of the cold water, which is monitored by an electrical thermometer. In the programmed deploy-

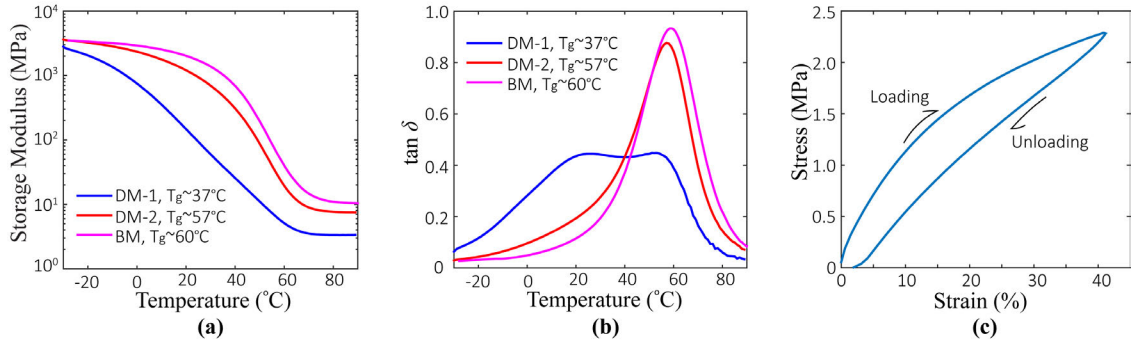


Figure 8.12: Material properties measured by experiments. (a) Storage modulus (C_s) vs. temperature curves of the three SMPs. (b) Loss tangent ($\tan \delta$) vs. temperature curves of the three SMPs. (c) The stress-strain curve of FilaFlex material at $\sim 25^\circ\text{C}$.

ment test, we stopped injecting hot water once the water reached the desired temperature. After the whole tensegrity deployed, we were able to drain the water from the tank.

8.6.3 Compression tests of the deployed tensegrity

We performed the compression tests of the deployed tensegrity structures using an electromechanical universal material test machine (MTS Criterion Series 40, Eden Prairie, MN, USA)) at room temperature ($\sim 25^\circ\text{C}$). The deployed tensegrity was placed on a flat stage and then compressed by another flat plate mounted to the load cell. The stage and plate were lubricated to reduce friction. The compression loading rate is 0.2 mm/s. The forces and displacements were recorded at a 10 Hz sampling rate. A load cycle was performed. The unloading starts when the global deformation reached half the height of the tensegrity.

8.7 Concluding Remarks

The tensegrity in our design paradigm consists of two hierarchies: the first hierarchy is the compaction and recovery of individual struts; the second hierarchy is the final geometry of the tensegrity, i.e. the global structure. Therefore, the final configurational change is composed of both material-induced shape change and topology-induced shape change. The second hierarchy amplifies the first hierarchy to achieve gigantic volume expansions.

Table 1.

Material parameters for the multi branch model.

	Verowhite (BM)		DM9895 (DM-1)		DM8530 (DM-2)	
Branch	C _{non} (MPa)	τ _i	C _{non} (MPa)	τ _i	C _{non} (MPa)	τ _i
C ₁	148.7076	2.00e-08	300	0.0001	170	1e-07
C ₂	119.7517	4.27e-07	275	0.000657	188	9.93e-07
C ₃	131.9798	5.47e-06	296	0.003872	212	0.00001
C ₄	147.1372	5.89e-05	305	0.02	239	9.08e-05
C ₅	282.3444	0.000547	350	0.1	268	0.00074
C ₆	320.9668	0.004524	378	0.576863	293	0.005374
C ₇	354.2126	0.032439	292	3.401616	308	0.035368
C ₈	427.2871	0.2	215	20	291	0.2
C ₉	178.2132	1	147	96.82391	285	0.954957
C ₁₀	143.8276	3.250259	95.213467	362.9461	138	3.182197
C ₁₁	151.2221	9.451896	63.12765	1000	162	7.497457
C ₁₂	162.8788	30.23741	62.0921	2671.527	178	25.11365
C ₁₃	162.4149	100	52.099306	7912.87	153	87.11596
C ₁₄	151.456	315.2367	42.374719	23498.79	133	283.7953
C ₁₅	141.8913	927.9366	35.205449	71461.38	122	905.6253
C ₁₆	111.7587	8849.219	27.897552	228551.6	112	3025.975
C ₁₇	140.7818	2849.202	20.760769	726401	98.09554	10000
C ₁₈	81.89721	25294.7	15.532429	2277776	83.26095	32677.22
C ₁₉	52.68197	72900	11.281878	7091525	65.70456	96510.16
C ₂₀	12.47854	653520.3	8.305791	21997171	59.12021	267333.4
C ₂₁	28.03173	213000	5.959708	68236585	51.92218	773277.7
C ₂₂	1.712558	5370000	4.351312	2.08e+08	44.76933	2339554
C ₂₃	4.830405	2000000	3.329757	6.41e+08	34.59949	7613180
C ₂₄	1.197657	85400000	2.644468	2.07e+09	21.72712	26070126
C ₂₅	1.383214	20000000	2.196711	7.07e+09	9.995279	1e+08
C ₂₆	0.000183	3.61e+08	1.578065	2.4e+10	2.916758	5.22e+08
C ₂₇	2.537188	2e+09	0.1070122	1e+11	0.957138	5.77e+09
C _{eq} (MPa)	10.4		3.30		7.5	
T _g (°C)	60		37		57	
T _{ref} (°C)	22		-3		17	
c ₁	17.44		17.44		17.44	
c ₂	66.35		42.1		50.5	
c _A U _C /k ^{Boltz}	-23000		-23000		-24000	

Furthermore, these two hierarchies are decoupled, i.e. the final tensegrity does not depend on how we design and compact the strut (the first hierarchy). Therefore, other designs of the struts, such as different cross-section shape or programmed shape can be used. In this research, our design of each strut is inspired by the storable tubular extendable member (STEM) [222] usually used on satellites. Such a design provides a relatively high critical force after recovery. The slit design enables favorable deployments. However, this is not the only design alternative and thus one can design the strut based on other considerations [148], [208], [211]. As shown above, we avoid specialized design and dedicated fabrication for every new active structure, but can apply components of the same design to create different structures by varying combinations, in a way similar to the LEGO toy, which opens a new venue that allows for quick fabrication of 3D active structures through modular designs. We can even recycle the struts to save material and reduce waste.

In retrospect, we create a method for realizing active tensegrity by combining 4D printing with actuation to deploy 3D structures that respond to environmental stimuli. Our paradigm of active tensegrity is unique and novel as it integrates the complementary features of tensegrity structures and smart materials, merging the frontiers of material science and structural mechanics. The intriguing properties of tensegrity allows the active deployment to have two decoupled hierarchies: programming the SMP struts into compact shapes, and the topology of the actual tensegrity. Such a decoupling strategy leads to gigantic shape change, allows for modular design, and provides rich programmability and tunability. The struts are allowed to have other shapes and be programmed into a compact shape so that they can be assembled with the elastomer cables according to the topology of the tensegrity. The active tensegrity structures can be programmed to deploy in a sequential fashion by differentiating the glass transition temperatures of the SMPs used for the struts. Further enrichment includes, for example, using shape memory composites [210] to achieve finer control of shape change, or using materials such as hydrogels [211], [213] to design the structure to respond to different types of environmental stimuli. In addition, surfaces,

which could be used as a platform for integrating functionality, can be attached to the nodes in the tensegrity to enable active devices with dramatic property changes. Therefore, our paradigm of active tensegrity offers a platform for generic devices/applications that can benefit from the gigantic shape changes reported in the present research.

With unique properties of tensegrity and remote controllable actuation by temperature, we can foresee the active deployable tensegrity has great potential in variety applications. For example, in the space engineering, tensegrity structures have been successfully exploited as deployable antenna and reflectors in satellites. Tibert et al. [2], [202] have used tensegrity to design contractible reflector for the small satellite that can be packaged within an envelope. Another potential application of the deployable tensegrity is used as tensegrity robot for locomotion and duct systems [203], [223]. In addition, Carpentieri et al. [204] recently provides a method to use the minimal mass deployable tensegrity for solar energy harvesting on water canals. These traditional applications of tensegrity usually need mechanical drivers to deploy. Now, empowered by SMP, the active tensegrity structure is self-deployable, with the capability to adapt automatically to environmental changes. The active tensegrity may also be applied for biomedical purpose, such as stents [46], [224], [225], which are flexible tubular devices for minimum invasive surgery. A stent is capable of being folded into small dimensions and then deployed to open up a blocked lumen. The active tensegrity could be suitable for self-deployable stent which deploys under human body temperature once inserted. There are various tensegrity designs that approximate tubular shapes [53]. In addition, deployed active tensegrity structures have great resilience to undergo large elastic deformations, which is a desired feature for biomedical devices so that the stent can also adapt to the deformation of human tissues.

CHAPTER 9

AUTOMATED GENERATION OF TENSEGRITY TESSELLATIONS FOR METAMATERIALS WITH TUNABLE STIFFNESS AND BANDGAPS

Tensegrity structures resemble biological tissues: a structural system that holds an internal balance of prestress. Owing to the presence of prestress, biological tissues can dramatically change their properties, making tensegrity a promising platform for tunable and functional metamaterials. However, tensegrity metamaterials require harmony between form and force in an infinitely-periodic scale, which makes the design of such systems challenging. In order to explore the full potential of tensegrity metamaterials, a systematic design approach is required. In this work, we propose an automated design framework that provides access to unlimited tensegrity metamaterial designs. The framework generates tensegrity metamaterials by tessellating blocks with designated geometries that are aware of the system periodicity. We show that tensegrity metamaterials offer tunable effective elastic moduli, Poisson’s ratio, and phononic bandgaps by properly changing their prestress levels, which provides a new dimension of programmability beyond geometry.

9.1 Introduction

Biological tissues (such as muscles) are capable of actively changing their material properties [226]–[228]. Through the contraction of myofibrils, muscle cells generate prestress that leads to tunable stiffness and shape. This mechanism offers a route to create smart tunable materials. The structural system of tensegrities is known to mechanically resemble biological tissues [13], [14], [205], which has been shown to produce large changes in stiffness and shape [169]. Therefore, we expect that if a material is composed of tensegrity micro-structures; it can reproduce (or mimic) the behavior of biological tissues.

Tensegrities are structural systems with a continuous network of tensile members (i.e.

cables), and disjointed compressive members (i.e. struts), whose integrity is maintained by self-balanced prestress in the cables and struts [50], [51], [53], [184], [191]. In engineering, a more general classification of tensegrity is proposed by Skelton & de Oliveira [51] where a Class- n tensegrity structure has at most n struts connected at each node. Under this expanded concept, the classical design of tensegrity, such as the sculptures by Kenneth Snelson [8], belongs to the Class-1 category. Engineering applications of tensegrities include deployable [169], [200], [202], actively tunable [1], [56], [203], and lightweight structures [168]. These advantages, if successfully transferred to the micro-scale, could lead to metamaterials with unprecedented mechanical properties and functionalities [50].

A straightforward way to make a metamaterial based on a tensegrity micro-structure is to tessellate a tensegrity unit cell in space to create a bulk assemblage (i.e. the metamaterial). Metamaterials based on lattice micro-structures have been used to create super lightweight materials. The mechanical properties and density of the metamaterials, as well as a wide range of other properties (e.g., acoustic, thermal, and biological properties), can be altered by adjusting the cellular architecture. This micro-lattice approach has led to lightweight materials that exhibit strength–stiffness ratios previously unachievable at low densities [229]–[232].

Recently, a few pieces of pioneering work have shown that tensegrity metamaterials exhibit some unusual properties [233]–[240]. Fraternali *et al.* [233] study solitary waves in a one-dimensional tensegrity chain composed of three-strut tensegrity prisms, indicating that such system might be used for impact mitigation. This one-dimensional system presents tunable frequency bandgaps by having two three-strut tensegrity prism designs with different height and stiffness [234]. Rimoli and Pal [235] investigate the mechanical properties of a tensegrity metamaterial design with truncated octahedron elementary cells. They also observe that cable prestrains can significantly affect the acoustic wave speeds in this tensegrity metamaterial [239]. However, these proposals of tensegrity metamaterials are based on *ad hoc* designs; i.e. they are based on known stand-alone tensegrity designs that are not

fully aware of the system periodicity once tessellated to become a metamaterial. This type of approach results in tensegrities of Class-2 or higher after the periodic tessellation. This deprives our control on the topological features of the tensegrity metamaterial, specifically the Class. Thus, the full potential of tensegrity metamaterials cannot be explored. Moreover, the previously proposed approaches cannot lead to a Class-1 tensegrity tessellation. In practice, we are particularly interested at Class-1 tensegrity tessellations: they are easier to manufacture since they are composed of straight “struts” and “cables”; no special hinge is necessary since two struts never intersect; the structure is less likely to develop undesirable bending forces in the struts; large deformations in the system (shortening of the struts) due to prestress or service loads are easier to account for; etc. Thus, there is a need for a systematic approach to design tensegrity metamaterials with a desired unit cell geometry and Class category – this is our focus.

Multiple approaches exist for the design of stand-alone tensegrities [170]–[179]. However, it is challenging to incorporate periodicity in these approaches, especially concerning the topology of the design. To overcome these challenges, we propose a design framework based on topology optimization that can automatically create tensegrity-based metamaterials with periodic unit cells, as illustrated by Figure 9.1. The framework utilizes topology optimization to find tensegrity tessellation blocks with prescribed tiling geometries (periodicity). The resulting units can be tessellated, either densely or porously, to create metamaterials. Using this automated process, we can create a library of tensegrity metamaterial designs (see Table 9.1). The following key terms are used in this manuscript: *tessellation block*, the building block of a tessellation unit cell; *design domain*, the geometric space within which the tensegrity (tessellation block) is designed; *unit cell*, the periodic micro-structure of the tensegrity metamaterial. To demonstrate the applications of the proposed approach, we use one example from the obtained tensegrity tessellation blocks to create both, densely and porously tessellated Class-1 tensegrity metamaterials. We investigate their mechanical properties through homogenization, and acoustic proper-

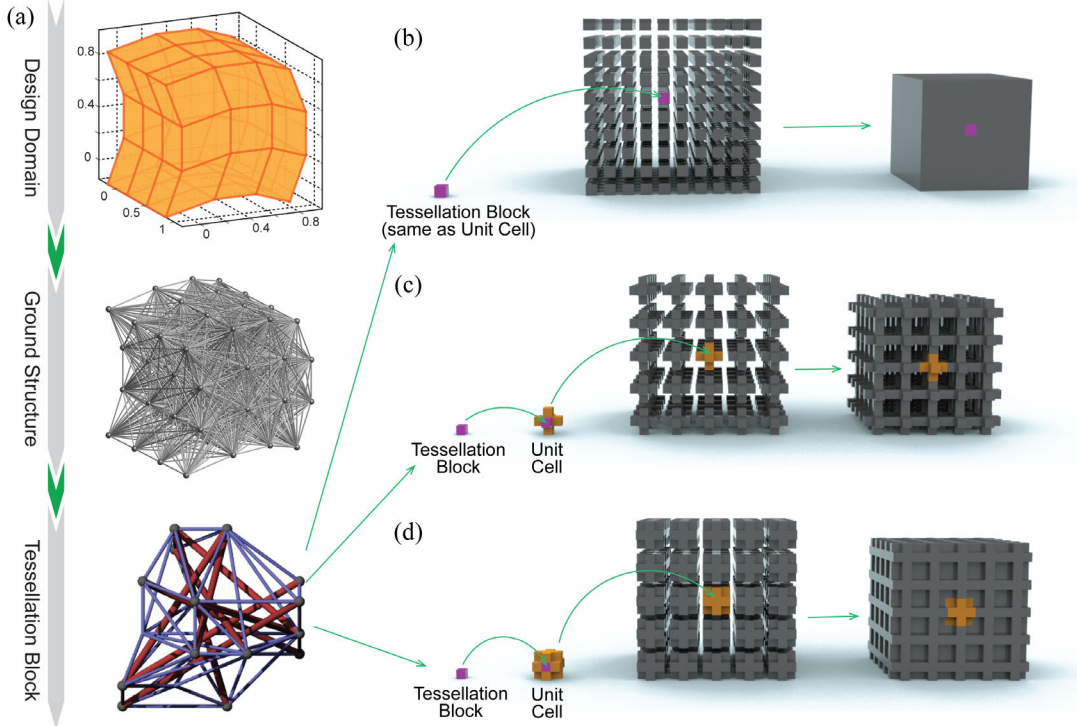


Figure 9.1: Schematic of the design framework to create tensegrity metamaterials. (a) From a (periodic) geometric design to a tensegrity tessellation block. (b)-(d) From tessellation block to tensegrity metamaterials. (b) The tessellation block is directly the unit cell for the bulk assembly, which is named as *dense tessellation*. (c) The tessellation block is first used to sub-assemble a porous unit cell which is re-tessellated into a bulk assembly, called the *porous tessellation*. This particular sub-assembled unit cell leads to truss-like assemblies. (d) The same tessellation block can be sub-assembled into different unit cells, leading to various *porous tessellations*. This particular *porous tessellation* is a honeycomb-like assembly.

ties through Bloch wave analyses. We show that the effective elastic moduli, Poisson's ratio, and phononic bandgaps of the tensegrity metamaterials can be effectively tuned by changing prestress level, our design parameter of interest.

9.2 Topology design formulation

We adopt the optimization formulation presented in Chapter 7 for design of stand-alone tensegrity as the basis of the design of tensegrity metamaterials, which is reviewed as follows. Let us denote t as the tension forces in all candidate members, and c the compression forces. The real force in a member is therefore $(t - c)$. By decoupling tension and com-

pression, we obtain two vectors of non-negative design variables, each of size $N_{E_g} \times 1$, where N_{E_g} is the number of candidate members provided by the ground structure. The binary design variables \mathbf{s} indicate the presence of struts: $s_k = 1$ indicated that the k -th candidate member is a strut (as opposed to a cable). Eventually, the optimization formulation is written as a mixed integer linear programming (MILP) problem:

$$\max_{\mathbf{t}, \mathbf{c}, \mathbf{s}} \quad \mathbf{1}^T(\mathbf{t} - \mathbf{c}) \quad (9.1a)$$

$$\text{s.t.} \quad \mathbf{B}(\mathbf{t} - \mathbf{c}) = \mathbf{0} \quad (9.1b)$$

$$\mathbf{G}\mathbf{s} \leqslant n\mathbf{1} \quad (9.1c)$$

$$\mathbf{G}_p\mathbf{s} \leqslant \mathbf{1} \quad (9.1d)$$

$$\mathbf{1}^T\mathbf{s} \leqslant N_{S,max} \quad (9.1e)$$

$$\mathbf{0} \leqslant \mathbf{t} \quad (9.1f)$$

$$\mathbf{0} \leqslant \mathbf{c} \leqslant \mathbf{s} \leqslant \mathbf{1} \quad (9.1g)$$

$$\mathbf{s} \in \mathbb{Z}^{N_{E_g}} \quad (9.1h)$$

The constraints restrict the solution space to feasible tensegrity designs. Eq. (9.1b) requires self-balance of prestress forces, where \mathbf{B} is the equilibrium matrix [53]. Eq. (9.1c) imposes discontinuity of struts. The incidence matrix \mathbf{G} is a $N_{V_g} \times N_{E_g}$ binary matrix which contains the connectivity information, i.e., the topology, of a ground structure, where N_{V_g} refers to the number of nodes in the ground structure. Each column of \mathbf{G} contains exactly two entries of value 1, with the row indices indicating the start/end nodes of a member. The product $\mathbf{G}\mathbf{s}$ results in an $N_{V_g} \times 1$ vector whose entries indicate the numbers of struts connected to each node, which need to be smaller than the Class number n . Eq. (9.1d) prevents collisions between struts, which considers the manufacturability of the design. The \mathbf{G}_p matrix is defined such that if the result of $\mathbf{G}_p\mathbf{s}$ has an entry greater than 1; there are two struts colliding each other in space. Each row of \mathbf{G}_p corresponds to a fictitious intersection

point reporting an occurrence of collision between two members. Eq. (9.1e) limits the number of struts (denoted as N_S) in a tensegrity design by $N_{S,max}$. Eqs. (9.1f) to (9.1h) define bounds for the design variables, among which Eq. (9.1g) also ensures that the strut indicator is 1 when an element takes the form of a strut.

As demonstrated in Chapter 7, this formulation is able to effectively reproduce many of the renowned stand-alone tensegrities, and create new stable tensegrities [61]. However, directly applying Formulation (9.1) for designing tessellation blocks for tensegrity metamaterials will not produce desired results. The reason being that tensegrity metamaterials are periodic tessellations of the unit cells: the periodicity of tessellation block must be considered in the formulation. The periodicity leads to shared nodes on the common boundaries of each tessellation block, which makes our strut discontinuity constraint defined in Eq. (9.1c) ineffective, as sketched in Fig. 9.2(a). Therefore, the periodic boundary conditions (PBCs) must be included in the strut discontinuity constraint (9.1c), as shown in Fig. 9.2(b). For the self-balance constraint in Eq. (9.1b) the PBCs are not enforced: a self-balanced tessellation block (naturally) results in a self-balanced periodic assembly. Hence, there is no force flowing between adjacent tessellation block in a tensegrity for metamaterial design. This leads to an unintended advantageous property: a finite assembly of tessellation blocks does not require additional support over its boundary to maintain the equilibrium of the (metamaterial) system.

To incorporate the PBCs, we need to identify the common nodes on the tessellation block's boundaries. There are several independent groups of nodes: each group contains the indices of nodes that are images of each other under translational symmetry (i.e. periodicity). For example, two nodes belong to the same group if their coordinates satisfy:

$$\mathbf{x}_j = \mathbf{x}_i + (n_1\mathbf{a}_1 + n_2\mathbf{a}_2 + n_3\mathbf{a}_3), \quad n_1, n_2, n_3 \in \{-1, 0, 1\}. \quad (9.2)$$

where \mathbf{x}_i and \mathbf{x}_j denote the coordinates of nodes i and j , respectively; while \mathbf{a}_1 , \mathbf{a}_2 , and \mathbf{a}_3 are the three primitive vectors of the tessellation. Node groups may be of different size

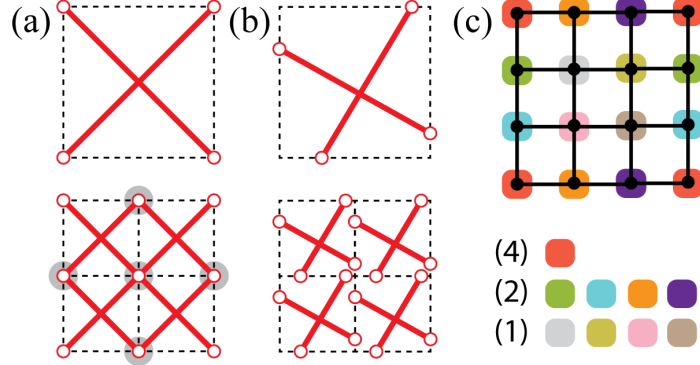


Figure 9.2: Effect of periodic boundary condition on the topology of struts. (a) Tessellating Class-1 tessellation block creates nodes connecting multiple struts, which is not desired. The red bars indicate struts. If the struts are placed as shown in (b), the tessellation preserves the tessellation block’s Class category – there is no pair of struts connected at one node. (Note: intersections within the length of struts is ignored in this demonstration) (c) Identification of independent groups of nodes for a 4×4 ground structure. Different groups are identified by different colours. The numbers in parenthesis provide the numbers of nodes in different groups. The 4 corner nodes belong to the same group.

under translational symmetry – we refer to Fig. 9.2(c) for a 2D example. As an example, in a cubic design domain, the 8 corner nodes belong to the same group. It should be noted that an internal node belongs to an independent group by itself. Nodes can classified into independent groups automatically, as illustrated by the algorithm described in Section 9.5.1. After generating the node groups, an identification matrix \mathbf{Q} can be constructed as:

$$Q_{ij} = \begin{cases} 0, & \text{if node } j \text{ does not belong to group } i \\ 1, & \text{if node } j \text{ belongs to group } i. \end{cases} \quad (9.3)$$

The number of rows of \mathbf{Q} equals to the number of independent groups, and the number of columns equals to the total number of nodes in the ground structure. For tensegrity meta-material designs, the strut discontinuity of a tessellation block (tensegrity Class) is counted for each independent group, as opposed to individual nodes. Using the identification matrix \mathbf{Q} , we can rewrite Eq. (9.1c) for tensegrity metamaterial design as:

$$\mathbf{Q}\mathbf{G}\mathbf{s} \leq n\mathbf{1}. \quad (9.4)$$

which is an elegant constraint to achieve the intended metamaterial design. We note that, in general, the obtained tensegrity tessellation block designs do not display any apparent symmetry. In particular, reflection symmetry is not allowed if the design needs to be globally Class-1, as implied by the schematics in Fig. 9.2.

9.3 Geometry of tessellation units

To perform the topology optimization, we need to build a ground structure, which is generated by a set of nodes that conforms to prescribed geometries. Our experience shows that *balloon-like* domains are likely to result in better tensegrity designs. In that regard, we develop a set of algorithms and tools with the purpose of making the design domains simple to define and manipulate (i.e. the nodes of the ground structure). The goal of these algorithms is not to span the infinitely rich space of potential unit geometries; but provide enough design freedom and easy-usage to allow for a large variety of designs to be conceived. The described algorithm for generating the unit geometry is summarized by the simplified flowchart in Fig. 9.3(a).

After a unit geometry is defined, a second set of transformations and variations can be applied. These transformations and variations are based on: (a) inner holes, and (b) morphing of the geometry. These are also parametrized, and thus the space of design domains for tensegrities (while not infinite) is reasonably large.

The simplest manner to define a polyhedron is by using only the vertices and making the polyhedron the convex hull of these [241], [242]. If the polyhedron is tessellated, a set of primitive vectors that replicate the unit and span the entire space must also be defined. Thus, the required user input to define a design domain consists of two pieces of information: (a) spatial nodes (vertices) defining the boundary of the design domain; (b) a set of primitive vectors which span the three-dimensional space.

As demonstrated in Fig. 9.2, extra nodes within the connecting facets are also needed in addition to the basic (convex hull) vertices. This is necessary to allow freedom of the strut

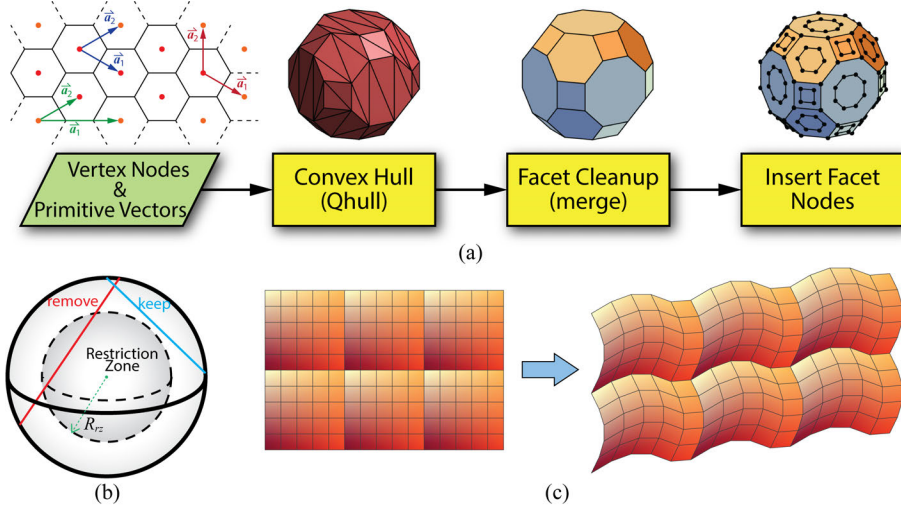


Figure 9.3: Creation of the design domain (i.e. geometry of the tessellation block). (a) Domain unit-cell generation based on convex hulls. The black dots are the nodes used to generate the ground structure for topology optimization. (b) Restriction zone creates holes in the design domain (i.e. the ground structure) by removing all members across the prescribed zone(s). (c) Morphing example: original (un-morphed) tessellation block and morphed tessellation block (in 2×3 assemblies).

layout. These additional facet nodes can be added in a parametric manner, for instance, by shrinking the facet boundary and including these (shrunk) vertices in the domain. However, it should be noted that other options are available and can be easily implemented.

The tensegrity topology optimization formulation can handle concavities and even holes (or voids) in the domain. While the nature of the convex-hull approach does not result in tessellation blocks with concavities, the addition of inner holes (or concavities) as a subsequent step is possible (optional), and is fully compatible with the tessellation block generation algorithm. This feature leads to a better tuning of the resulting micro geometry of the tessellated metamaterial. The inner hole and concavities use the concept of *restriction zones* [182], [243], as illustrated in Fig. 9.3(b). Typically, a spherical restriction zone with radius R_{rz} centered at the centroid of the unit geometry is used.

Additional variations for a given unit geometry and primitive vectors can be achieved by morphing: the geometry of a tessellation block (and its primitive vectors) can be “de-formed” (in a virtual sense) while keeping their space-spanning property. Fig. 9.3(c) il-

lustrates a two-dimensional example of a square design domain being morphed into a new design domain, while keeping its space-spanning property.

9.4 Variations of tessellation strategy

We explore different strategies to tessellate the obtained tessellation blocks. The tensegrity tessellation block obtained by topology optimization (see Section 9.2) from the unit geometry (as defined in Section 9.3) can be directly tessellated in space in accordance to the primitive vectors to make the metamaterial bulk assembly. Moreover, it should be noted that these primitive vectors are often not unique: any set of vectors that span the entire space and correctly tessellate the tessellation block (no overlaps) are valid, as long as the nodes in some of the facets are common among neighboring units. We also note that it is not required for the tessellation to be *space filling*, i.e. to completely fill the three-dimensional space: voids may be left in the tessellation. Therefore, we can explore porous strategies to tile the tessellation block in order to achieve different bulk assemblies. Furthermore, owing to the self equilibrium of the tessellation block (refer to Section 9.2), units can be removed from the bulk assembly without compromising the stability of the system: i.e. holes can be intentionally left in the tessellation.

A porous tessellation can be constructed as follows: the tessellation block is tessellated a few times in a porous manner (i.e. leaving certain positions empty); this porous unit cell is then re-tessellated to make metamaterial bulk assemblies, as demonstrated in Fig. 9.1(b)-(c). The porous unit cell is encoded by a three-dimensional array \mathbf{N}_s of size $N_{s1} \times N_{s2} \times N_{s3}$ with true/false values. The tessellation block is then tessellated along each of the 3 primitive vectors, but a structure is only created/appended to the unit cell when a true is found. This is repeated for all three primitive vectors (all three dimensions of \mathbf{N}_s). Thus, the same tensegrity tessellation block can result in various metamaterials; either by itself or in a sub-assembled unit cell. The sub-assembly approach is general: a single true value in \mathbf{N}_s (matrix of size $1 \times 1 \times 1$) refers to the original case when no porous unit cell is used

to create a densely tessellated metamaterial.

9.5 Tunable elastostatic properties

Assuming the unit cell dimension is sufficiently small compared to the macroscale dimension of the metamaterial, we can obtain the effective properties of the tensegrity metamaterial through homogenization [244]. We use computational homogenization to obtain the effective properties of a tensegrity metamaterial based on the unit cell. Periodic boundary conditions (PBCs) are applied to a tensegrity unit cell [245], such that:

$$\mathbf{u}_m - \mathbf{u}_s = (\mathbf{F} - \mathbf{I})(^1\mathbf{x}_m - ^1\mathbf{x}_s), \quad \mathbf{f}_m + \mathbf{f}_s = \mathbf{0}, \quad (9.5)$$

which represent periodic deformations and anti-periodic tractions on the boundaries of the unit cell. The subscripts m and s refer to master and slave nodes on opposite boundaries. The nodal displacements of a master-slave pair are \mathbf{u}_m and \mathbf{u}_s . The nodal positions in the prestressed state are $^1\mathbf{x}_m$ and $^1\mathbf{x}_s$, which equals to the primitive vector of the lattice in the corresponding direction of the two nodes. In linear analysis, these two boundary conditions can be directly condensed into the stiffness matrix and force vectors. Following the procedure proposed by Vigliotti & Pasini [245], we derive the full homogenized linear elasticity tensor \mathbf{D} of the tensegrity metamaterial. We use the reduced format (Voigt notation) of the elasticity tensor, and thus, \mathbf{D} is a 6×6 symmetric matrix. The computational implementation is elaborated upon in Section 9.5.2.

To demonstrate how the elastic properties of a tensegrity metamaterial can be tuned, we use the tessellation block design based on a cuboctahedron geometry as an example: 13 struts and 96 cables. The cuboctahedron tessellation block is used to create two metamaterial designs: one using a dense tessellation (Fig. 9.4(a) and (c)); and a second one with a porous tessellation (Fig. 9.4(b) and (d)). We denote the Young's modulus of strut material as C_S , and cable material as C_C . For this example, we consider a cuboctahedron unit

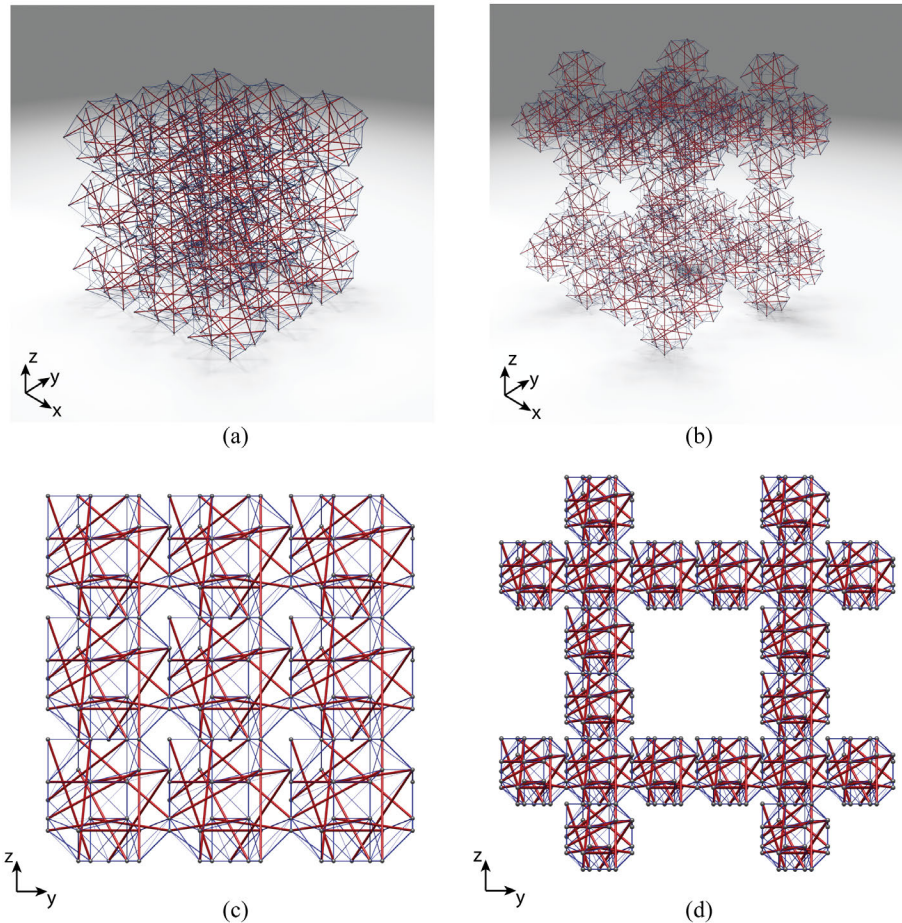


Figure 9.4: Examples of tensegrity metamaterial designs. (a) 3D view of the dense tessellation. (b) 3D view of a porous tessellation. (c) Side view of the dense tessellation. (d) Side view of a porous tessellation.

cell bounded in a $10\text{mm} \times 10\text{mm} \times 10\text{mm}$ box. We assume that all members have a circular cross-section, and the maximum radius of struts is $r = 0.5\text{mm}$ in the prestressed state. The areas of other struts and cables are determined proportionally based on the prestress forces. We find that all struts in the cuboctahedron tessellation block have the same pre-stress forces; they all have the same area which is ${}^1A_S = 0.25\pi\text{mm}^2$. while the cables are sized to ensure uniform magnitude of stress (${}^1\sigma_{11}$) in all of them. The proportional property of the cross-section of the members allows for simultaneous prestressing of the entire metamaterial via external stimuli such as temperature or magnetic field – an advantage towards its potential manufacturability. Otherwise, each member has to be individually tuned such

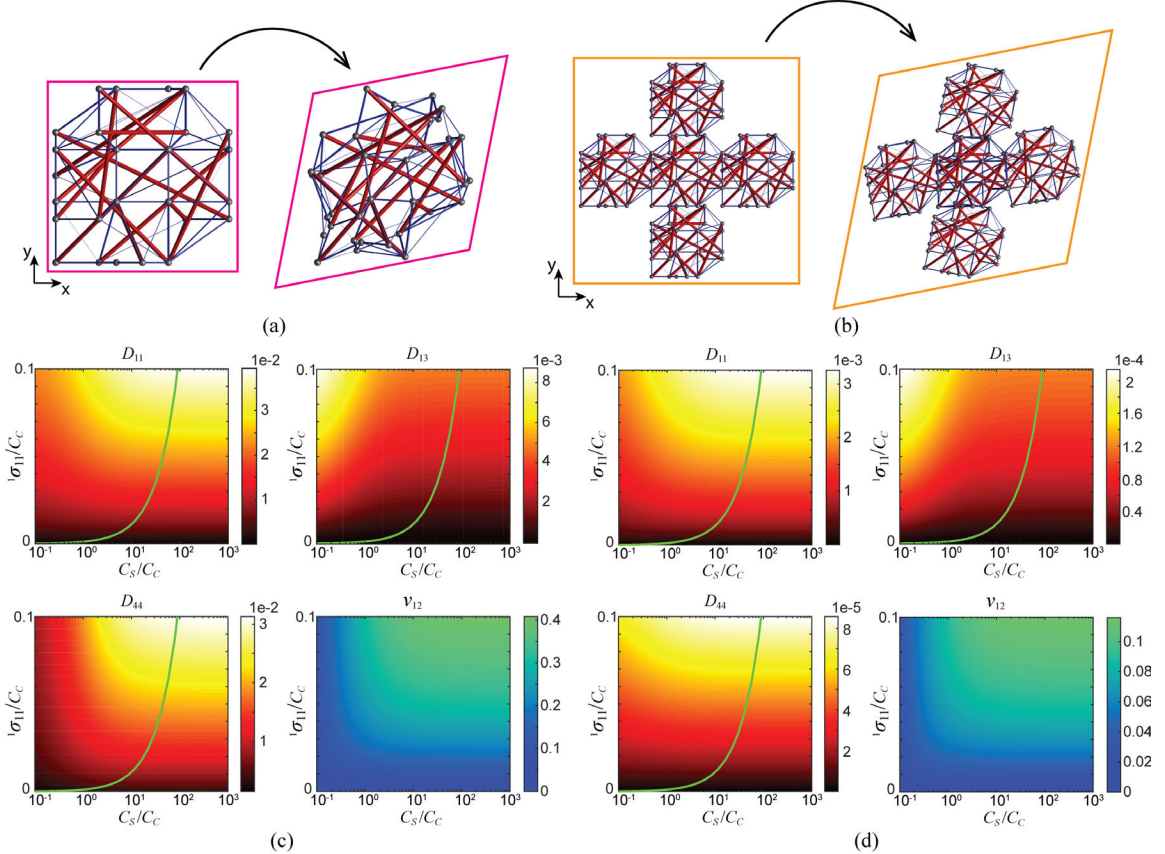


Figure 9.5: Tunability of homogenized elastic properties. (a)-(b) Shear mode of the unit cells of the two metamaterials in undeformed and simply sheared configurations: (a) Densely tessellated metamaterial, (b) Porously tessellated metamaterial. (c)-(d) Tunable elastic properties (including elastic modulus D_{11} , D_{13} , D_{44} ; and Poisson's ratio ν_{12}): (c) Densely tessellated metamaterial, (d) Porously tessellated metamaterial. The green lines indicate the limit of prestress that may cause buckling of struts. To the right of the green line, buckling is unlikely to happen.

that its force maintains the self-equilibrium of the metamaterial. However, this work does not consider geometric changes of the tensegrity metamaterials due to varying external stimuli, i.e. we assume that the prestressed configurations of the tensegrity metamaterial under different prestress level are within infinitesimal (linear) deformations, and thus can be ignored.

Let us take $C_S = 2600\text{MPa}$ and $C_C = 12\text{MPa}$, which are the typical properties of polymers used in 3D printing. We assume that the prestress in the metamaterial is ${}^1\sigma_{11} = (0.05C_C) = 0.60\text{MPa}$. We can obtain the homogenized elasticity tensor of the densely

tessellated metamaterial (see Fig. 9.4(a)) as:

$$\mathbf{D}_{dense} = \begin{bmatrix} 23.76 & 4.90 & 2.69 & 0.10 & 1.06 & -1.79 \\ & 17.03 & 2.65 & 2.07 & -0.60 & 1.71 \\ & & 23.48 & 1.41 & -3.26 & -2.95 \\ & & symm. & 20.48 & 1.07 & 2.64 \\ & & & & 13.93 & 4.82 \\ & & & & & 14.38 \end{bmatrix} \times 10^{-3} \text{ MPa.} \quad (9.6)$$

Moreover, the homogenized elasticity tensor of the porously tessellated metamaterial (see Fig. 9.4(b)) is given by:

$$\mathbf{D}_{porous} = \begin{bmatrix} 20.73 & 1.38 & 0.76 & -0.07 & -0.05 & -0.06 \\ & 15.68 & 0.69 & 0.10 & -0.01 & -0.08 \\ & & 22.33 & -0.05 & 0.02 & -0.03 \\ & & symm. & 0.48 & 0.04 & 0.01 \\ & & & & 0.46 & 0.03 \\ & & & & & 0.45 \end{bmatrix} \times 10^{-4} \text{ MPa.} \quad (9.7)$$

We observe that both metamaterials exhibit anisotropy. The porously tessellated tensegrity metamaterial is much softer than the densely tessellated metamaterial, especially in shear. The unit cell deformations under a simple shear of the two metamaterials are illustrated in Fig. 9.5(a) and (b).

Fig. 9.5(c) and (d) shows how some of the elastic moduli change in response to various material properties and prestress level (normalized by C_C). The densely tessellated metamaterial has a much larger Poisson's ratio (in the xy -plane) than the porously tessellated one, when the prestress level is high. The tunability due to variations in the prestress is more effective when compression members are much stiffer than tension members: changes of diagonal moduli of the elasticity tensor are more sensitive to changes in the prestress level

when $C_S/C_C > 10^2$. In addition, when $C_S/C_C > 10^2$, buckling of compression members (i.e. struts) is unlikely to happen. Considering Euler buckling [216], the stress of the longest compression member (with circular cross section) should satisfy:

$${}^1\sigma_{11} \leq \frac{\pi C_S({}^0A_{Smin})}{4{}^0L_{Smax}^2} \leq \frac{\pi C_S({}^1A_{Smin})}{4{}^1L_{Smax}^2}, \quad (9.8)$$

where ${}^0A_{Smin}$ (and ${}^1A_{Smin}$) is the minimal area of struts, and ${}^0L_{Smax}$ (and ${}^1L_{Smax}$) is the maximal length of struts, evaluated at Configuration 0 (and Configuration 1). The states of configurations are demonstrated in Fig. 7.4. The middle term in Eq. (9.8) is the actual critical stress before buckling, which shall be evaluated in the undeformed configuration (i.e. Configuration 0). However, in this research we are specifying the lengths and areas of members at the prestressed configuration (i.e. Configuration 1), thus the last term is used to provide an approximate upper bound for the compressive stress in struts, assuming that the strut material has a positive Poisson's ratio. Since 1A_S and ${}^1L_{max}$ are given for the design, this lower bound is a function of C_S , which is plotted as the green lines in Fig. 9.5(c) and (d), normalized by C_C .

9.5.1 Computation of identification matrix \mathbf{M}

First, we need to find pairs of boundary nodes that are images of each other under translational symmetry. We assume that the primitive vectors are \mathbf{a}_1 , \mathbf{a}_2 , and \mathbf{a}_3 . We can translate the unit cell nodal coordinates by different combinations of primitive vectors. If a node after the translation has the same coordinate as another node before the translation; these two nodes are identified as a pair. Supposing that there are m pairs of identified nodes, we can store their nodal incidence in a $m \times 2$ array.

Second, we use a union-find algorithm [246] with path compression and weighting to obtain the independent groups of nodes, as well as the identification matrix \mathbf{Q} . The MATLAB code that implements this algorithm is given below. The input array `SameNodePairs`

contains the indices of the identified pairs, and where N_V is refer as N_V in the main body of the manuscript. The output array Q is the identification matrix Q , and the array Pairs is a $N_V \times 2$ matrix with the pairs of identified nodes.

```

1 function [Q,Pairs] = CondenseTopMat(SameNodePairs,Nv)
2 % union-find algorithm with path compression and weighting
3 id = 1:Nv;
4 sz = ones(1,Nv);
5
6 FirstNd = SameNodePairs(:,1);
7 SecondNd = SameNodePairs(:,2);
8
9 for i = 1:length(FirstNd)
10 %make every node in path point to its grandparent (path compression)
11 FNdi = FirstNd(i);
12 while FNdi ~= id(FNdi)
13 id(FNdi) = id(id(FNdi));
14 FNdi = id(FNdi);
15 end
16 SNdi = SecondNd(i);
17 while SNdi ~= id(SNdi)
18 id(SNdi) = id(id(SNdi));
19 SNdi = id(SNdi);
20 end
21
22 %merge smaller tree into larger tree (weighted quick union)
23 if FNdi ~= SNdi
24 if sz(FNdi) < sz(SNdi)
25 id(FNdi) = SNdi;
26 sz(SNdi) = sz(SNdi) + sz(FNdi);
27 else

```

```

28 id(SNdi) = FNdi;
29 sz(FNdi) = sz(FNdi) + sz(SNdi);
30 end
31 end
32 end
33
34 % Compress to root
35 for i = Nv
36 while id(i)≠id(id(i))
37 id(i) = id(id(i));
38 end
39 end
40 Pairs = [id;(1:Nv)]';
41
42 idnew = id; iduni = unique(id);
43 for i = 1:numel(unique(id))
44 idnew(id==iduni(i)) = i;
45 end
46 Q = sparse(1:Nv,idnew,ones(Nv,1),Nv,numel(unique(idnew)));

```

9.5.2 Computation of homogenized elasticity tensor

We write a MATLAB function to implement the homogenization procedure as explained in [245]. The input arguments are: array of nodal coordinates (`NODE`), array of member connectivities (`BARS`), array of three primitive vectors (`Amat`), array of prestress forces (`P`), array of member areas (`A`), array of Young's modulus of all members C_y , the identification matrix (`Q`) and identified pairs of nodes (`Pairs`). The output array `Dhom` is the homogenized elasticity tensor D . The function also gives the six deformation modes (stored in `Modes`) of the unit cell under six elementary displacement-type boundary conditions, corresponding to three uniaxial extensions and three pure shear loadings. Denoting S as the

elastic compliance, we have $\mathbf{S} = \mathbf{D}^{-1}$. The Poisson's ratio ν_{12} is derived as [111]:

$$\nu_{12} = -\frac{\varepsilon_{22}}{\varepsilon_{11}} = -\frac{S_{12}}{S_{11}}. \quad (9.9)$$

```

1 function [Dhom, Modes] = GetHomProp(NODE,BARS,Amat,P,A,E,Q,Pairs)
2 %% Get unit cell full stiffness matrix Kuc
3 Nn = size(NODE,1);
4 Nb = size(BARS,1);
5 % Length vector and equilibrium matrix
6 D = ...
7 [NODE(BARS(:,2),1)-NODE(BARS(:,1),1),...
8 NODE(BARS(:,2),2)-NODE(BARS(:,1),2),...
9 NODE(BARS(:,2),3)-NODE(BARS(:,1),3)];
10 L = sqrt(D(:,1).^2+D(:,2).^2+D(:,3).^2);
11 D = [D(:,1)./L D(:,2)./L D(:,3)./L];
12 B = sparse(repmat((1:Nb)',1,6),[3*BARS(:,1)-2 3*BARS(:,1)-1 ...
13 3*BARS(:,1),...
14 3*BARS(:,2)-2 3*BARS(:,2)-1 3*BARS(:,2)], [D -D],Nb,3*Nn);
15 % Linear elastic stiffness matrix
16 Ke = B'*sparse(1:Nb,1:Nb,(Cy.*A./L))*B;
17 % Geometric Stiffness Matrix
18 G = ...
19 sparse([1:Nb,1:Nb],reshape(BARS,[],1),[ones(Nb,1);-ones(Nb,1)],Nb,Nn);
20 Kg = kron((G'*sparse(1:Nb,1:Nb,P./L)*G),speye(3));
21 % Assembly unit cell stiffness matrix
22 Kuc = Ke+Kg;
23 % Eliminate numerical rounding errors
24 Kuc = 0.5*(Kuc+Kuc');
25

```

```

24 %% Get unit cell periodic topology
25 B0 = kron(Q,eye(3));
26 Bep = ...
27 [Amat(1,1), 0, 0, Amat(2,1)/2, 0, ...
28 Amat(3,1)/2;
29 0, Amat(2,1), 0, Amat(1,1)/2, Amat(3,1)/2, 0;
30 0, 0, Amat(3,1), 0, Amat(2,1)/2, Amat(1,1)/2;
31 Amat(1,2), 0, 0, Amat(2,2)/2, 0, ...
32 Amat(3,2)/2;
33 0, Amat(2,2), 0, Amat(1,2)/2, Amat(3,2)/2, 0;
34 0, 0, Amat(3,2), 0, Amat(2,2)/2, Amat(1,2)/2;
35 Amat(1,3), 0, 0, Amat(2,3)/2, 0, ...
36 Amat(3,3)/2;
37 0, Amat(2,3), 0, Amat(1,3)/2, Amat(3,3)/2, 0;
38 0, 0, Amat(3,3), 0, Amat(2,3)/2, Amat(1,3)/2];
39 BaTopInt = Amat \ (NODE(Pairs(:,2),:) - NODE(Pairs(:,1),:))';
40 BaTopInt(abs(BaTopInt)<1e-3) = 0;
41 BaTop = sign(BaTopInt)';
42 Ba = kron(BaTop,eye(3));
43 Nrn = size(B0,2);
44 D0 = -pinv(full(B0'*Kuc*B0))*(B0'*Kuc*Ba); % Pseudo inverse
45 Da = B0*D0+Ba;
46 Kda = Da'*Kuc*Da;
47 Dhom = Bep'*Kda*Bep/det(Amat);
48 Modes = Da*Bep;

```

9.6 Tunable elastodynamic bandgaps

Besides tunable *static* properties, the prestressed tensegrity metamaterials also provide tunable *dynamic* properties. Hence, tensegrity metamaterials can be used for applications such as impact absorption, vibration isolation, or acoustic cloaking [247]–[249]. In this chapter, we focus on the phononic bandgaps of the tensegrity metamaterial, which are the frequency

ranges prohibiting elastic wave propagation. The freedom provided by our design framework allows us to tailor the unit cells for better likelihood of bandgaps. For instance, the porous unit cell is comprised of voids in the tessellation that renders the system heterogeneous which could lead to bandgaps [248], [250].

Using the same tessellation blocks as in previous section, we are interested in finding all the free vibration modes of wave propagation in the infinite tensegrity metamaterials, by means of Bloch wave analysis. The free vibration modes of a structure are the eigenvectors of the generalized eigenvalue problem:

$$\mathbf{K}\mathbf{u} = \omega^2\mathbf{M}\mathbf{u}, \quad (9.10)$$

where, \mathbf{K} and \mathbf{M} represent the stiffness and mass matrices of the infinite global system defined in the real space, and ω are the natural frequencies of harmonic wave propagation through the metamaterial. For periodic metamaterials consisting very large assembly of unit cells, direct evaluation of their eigenmodes is computationally intractable. To overcome this challenge, the dynamics of periodic structural systems is typically studied using the Bloch wave analysis [250], [251] framework, which reduces the generalized eigenvalue problem to that on a single unit cell, by virtue of Bloch's theorem and spatial Discrete Fourier Transform.

We calculate the eigenvalues of a reduced eigenvalue problem on the unit cell for each of the wavevectors defined in the *Irreducible Brillouin Zone* (IBZ) of the periodic system [250]:

$$\tilde{\mathbf{K}}_m \tilde{\mathbf{u}}_m = \omega^2 \tilde{\mathbf{M}} \tilde{\mathbf{u}}_m, \quad \text{with,} \quad \tilde{\mathbf{K}}_m = \sum_{n=-1}^1 e^{-ik_m \cdot x_n} \mathbf{K}_{0n}, \quad (9.11)$$

where, $\tilde{\mathbf{K}}_m$ is the reduced stiffness matrix defined in the reciprocal space, which depends on the wavevector k_m as shown above. The summation above goes over a reference unit cell as well as its immediate neighboring cells (with lattice position vectors x_n) of the tensegrity

metamaterial. The matrix \mathbf{K}_{0n} is a matrix extracted from \mathbf{K} with rows corresponding to the degrees-of-freedom (DOFs) of the reference unit cell, and columns corresponding to the DOFs of the n -indexed unit cell. The matrix $\tilde{\mathbf{M}}$ is the diagonal mass matrix obtained using a lumped mass technique over the members in the unit cell.

Using Eq. 9.11, we can obtain the dispersion diagrams of the tensegrity metamaterials at any given level of prestress. For the sake of simplicity and clear presentation, here we focus on the wave propagation in 1D and 2D tessellations. However, the analysis framework is equally applicable to 3D tessellations.

We locate the bandgaps (if present) across the wavevectors in the IBZ at all the frequencies and for varying levels of prestress. Similar to the elastostatic properties, the frequency bandgaps also exhibit tunability in response to changing prestress, as demonstrated in Figs. 9.6 and 9.7. We observe that the one-dimensional dense tessellation has wider bandgaps at lower frequencies (e.g. between 0 to 2.5 kHz), compared to the two-dimensional dense tessellation. Similarly, the porous tessellations that possess voids result in wider bandgaps at lower frequencies, compared to the dense tessellations. In both cases, this is explained by the reduction of mobility restraint from neighboring unit cells leading to wider bandgaps at lower frequencies. The examples show that by varying the level of prestress, tensegrity metamaterials can provide versatile and tunable properties for acoustic applications.

9.7 Concluding Remarks

We present a design framework that allows for automated creation of tensegrity metamaterials. The proposed methodology begins by specifying a geometry of the tessellation block that tiles space according to primitive vectors. Then a tessellation block is designed within this geometry by topology optimization which considers the periodicity of the final system. This resulting tessellation block can be tessellated in various ways in space to create metamaterials. Together with the unit geometry, additional and optional procedures

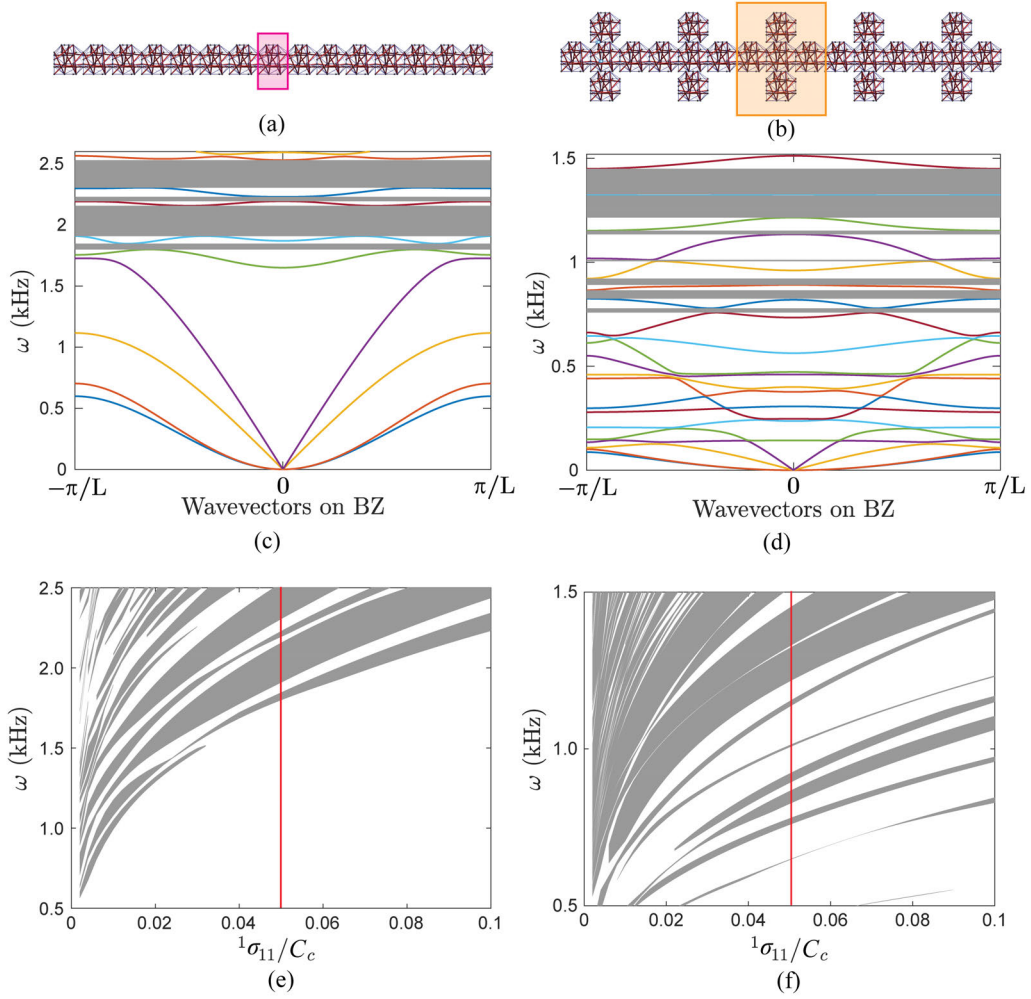


Figure 9.6: Schematics of the quasi one-dimensional tensegrity chains with (a) Dense and (b) Porous tensegrity unit cells (shown in shaded rectangles) and their corresponding variation of bandgaps with prestress shown in (e) and (f). (c), (d) Band structure diagrams at a prestress of $(0.05C_C)$ represented by red lines in (e) and (f), respectively. The gray shaded regions illustrate the elastic bandgaps.

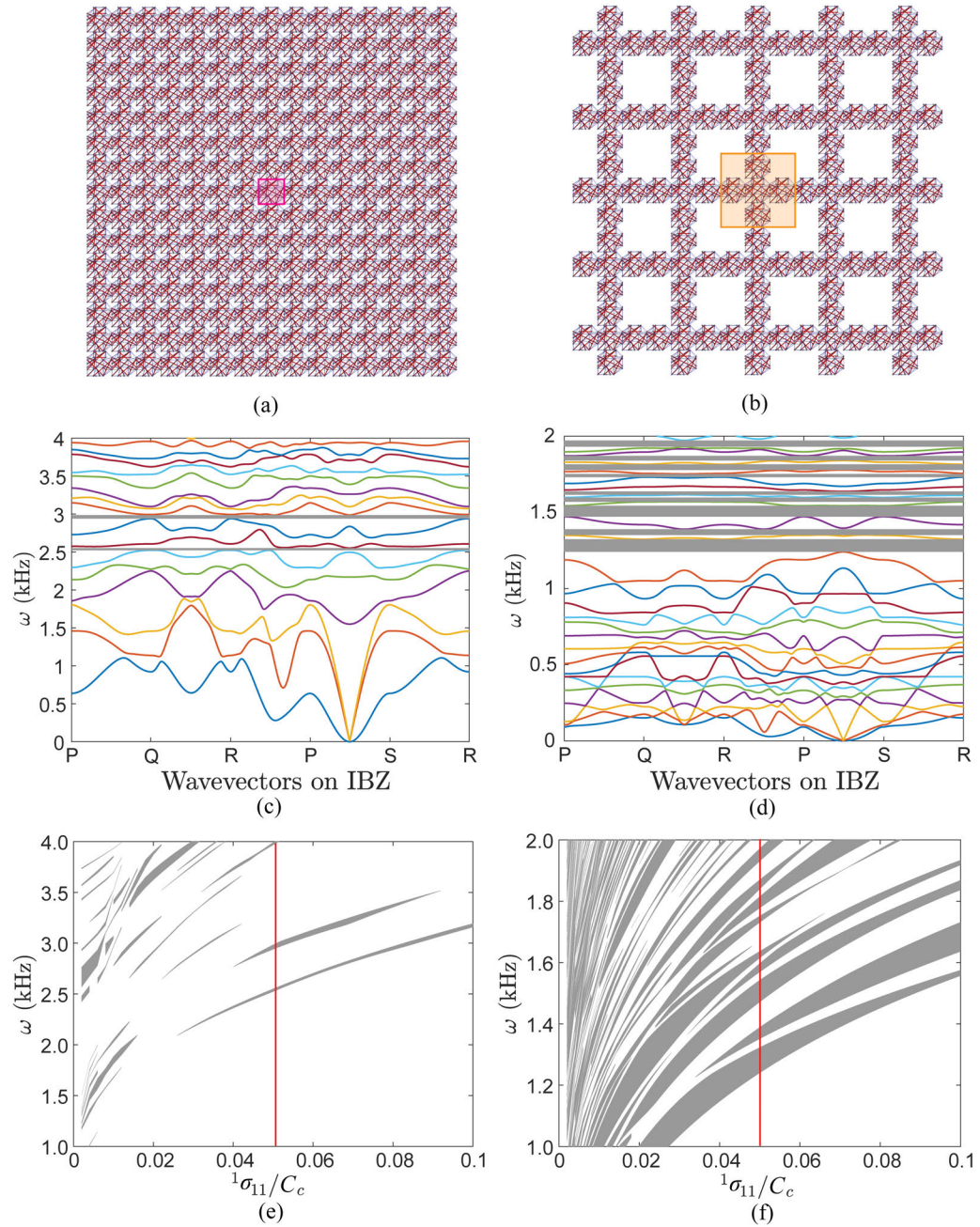


Figure 9.7: Schematics of the quasi two-dimensional tensegrity tessellations with (a) Dense and (b) Porous tensegrity unit cells (shown in shaded rectangles) and their corresponding variation of bandgaps with prestress shown in (e) and (f). (c), (d) Band structure diagrams at a prestress of $(0.05E_C)$ represented by red lines in (e) and (f), respectively. The gray shaded regions illustrate the elastic bandgaps.

such as concavities, morphing, and various strategies for tessellation, provide a rich design space for tensegrity metamaterials. While the resulting tensegrity properties cannot be easily predicted, parametric analysis on a few of these techniques offer sufficient control for the purpose of the present work. We present a library of various designs of the tessellation block in Table 9.1. Examples in the present work demonstrate how the elastic and acoustic properties of the tensegrity metamaterials designed using our approach can be tuned by changing the prestress level of the system.

The current framework may be enhanced in the future by taking account the mechanical properties of resultant metamaterial into the optimization formulation, and allowing the nodes to morph around in order to obtain simpler designs. However, such an objective or constraint is likely to lead to nonlinear integer programming problems. Therefore, how to efficiently solve those problems still poses a challenge. Moreover, the manufacturing of tensegrity metamaterials with properly induced prestress needs to be investigated. Additive manufacture technologies with the capability of printing multiple materials appear as the most promising at the time of this writing [252]. For example, we can print the cables and struts using two materials with different thermal expansion coefficients, and then by changing ambient temperature, the thermal deformation induced incompatibility can generate prestress in the system.

Library of tensegrity tessellation units

In the table, we provide ten different tensegrity units that can create space-spanning tessellation. The “Specification” column provides some detailed information about each design. The symbol R_{rz} is the radius of the restriction zone centered at the centroid of each unit geometry as shown in the first column. The number of struts in the tensegrity unit is given by N_S . The resultant global Class category of tensegrity metamaterial tessellated from each tensegrity unit is also provided.

Table 9.1: Tensegrity tessellations

Unit Cell	Vertices	Primitive Vectors (columns)	Assembly Sample	Specifications	Tensegrity Unit
Cube	$\mathbf{v}_{1 \rightarrow 8} = [\pm 1, \pm 1, \pm 1]$	$\mathbf{A}_1 = \begin{bmatrix} 2, & 0, & 0 \\ 0, & 2, & 0 \\ 0, & 0, & 2 \end{bmatrix}$		$R_{rz} = 0.1$ $N_S = 24$ Class-4	
Truncated Octahedron	$\mathbf{v}_{1 \rightarrow 24} = \text{perm } [0, \pm 1, \pm 2]$	$\mathbf{A}_1 = \begin{bmatrix} 2, & 2, & 2 \\ -2, & 2, & 2 \\ 2, & -2, & 2 \end{bmatrix}$ $\mathbf{A}_2 = 4 \cdot \begin{bmatrix} 1, & 0, & 0 \\ 0, & 1, & 0 \\ 0, & 0, & 1 \end{bmatrix}$		$R_{rz} = 0.75$ $N_S = 24$ Class-1	
Rhombic Dodecahedron	$\mathbf{v}_{1 \rightarrow 8} = [\pm 1, \pm 1, \pm 1]$ $\mathbf{v}_{9 \rightarrow 10} = [\pm 1, 0, 0]$ $\mathbf{v}_{11 \rightarrow 12} = [0, \pm 1, 0]$ $\mathbf{v}_{13 \rightarrow 14} = [0, 0, \pm 1]$	$\mathbf{A}_1 = \begin{bmatrix} 2, & 2, & 0 \\ 2, & -2, & 0 \\ 2, & 0, & 2 \end{bmatrix}$		$R_{rz} = 0.5$ $N_S = 24$ Class-1	

Table 9.1: (continued)

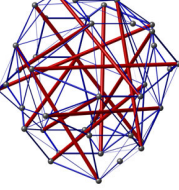
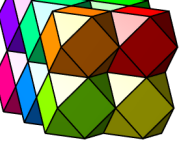
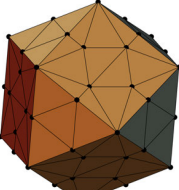
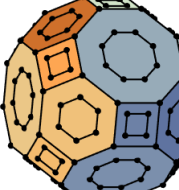
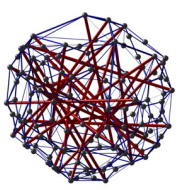
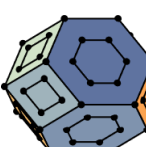
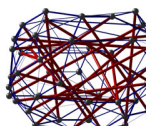
Unit Cell	Vertices	Primitive Vectors (columns)	Assembly Sample	Specifications	Tensegrity Unit
Cuboctahedron	 $\mathbf{v}_{1 \rightarrow 4} = [\pm 1, \pm 1, 0]$ $\mathbf{v}_{5 \rightarrow 8} = [\pm 1, 0, \pm 1]$ $\mathbf{v}_{9 \rightarrow 12} = [0, \pm 1, \pm 1]$ $\mathbf{A}_1 = \begin{bmatrix} 2 & 0 & 0 \\ 0 & 2 & 0 \\ 0 & 0 & 2 \end{bmatrix}$		 $R_{rz} = 0.75$ $N_S = 13$ Class-1		
Truncated Cuboctahedron	 $\phi_1 = 1 + \sqrt{2}$ $\phi_2 = 1 + 2\sqrt{2}$ $\phi_3 = 2 + 2\sqrt{2}$ $\phi_4 = 2 + 3\sqrt{2}$ $\mathbf{v}_{1 \rightarrow 48} = \text{perm}[\pm 1, \pm \phi_1, \pm \phi_1, \pm \phi_2]$ $\mathbf{A}_1 = 2\phi_2 \cdot \begin{bmatrix} 1, 0, 0 \\ 0, 1, 0 \\ 0, 0, 1 \end{bmatrix}$ $\mathbf{A}_2 = \phi_3 \cdot \begin{bmatrix} 1, 1, 1 \\ -1, 1, 1 \\ 1, -1, 1 \end{bmatrix}$ $\mathbf{A}_3 = \phi_4 \cdot \begin{bmatrix} 1, 1, 0 \\ -1, 1, 0 \\ 1, 0, 1 \end{bmatrix}$	 $R_{rz} = 1.5$ $N_S = 24$ Class-1	 $R_{rz} = 1.5$ $N_S = 24$ Class-1	 $R_{rz} = 1.5$ $N_S = 24$ Class-1	

Table 9.1: (continued)

Unit Cell	Vertices	Primitive Vectors (columns)	Assembly Sample	Specifications	Tensegrity Unit
	$\phi = 1/\sqrt{3}$ $\mathbf{v}_{1 \rightarrow 8} = [\pm 1, \quad \pm 1, \quad \pm\phi]$ $\mathbf{v}_{9 \rightarrow 12} = [\pm 1, \quad 0, \quad \pm 2\phi]$ $\mathbf{v}_{13 \rightarrow 16} = [0, \quad \pm 1, \quad \pm 2\phi]$ $\mathbf{v}_{17 \rightarrow 18} = [0, \quad 0, \quad \pm\sqrt{3}]$ Elongated Dodecahedron	$\mathbf{A}_1 = \begin{bmatrix} 2, & 0, & 0 \\ 0, & 2, & 0 \\ 1, & 1, & 4\phi \end{bmatrix}$		$R_{xz} = 0.5$ $N_S = 24$ Class-1	
	$\mathbf{v}_{1 \rightarrow 8} = [\pm 1, \quad \pm 1, \quad \pm 1]$	$\mathbf{A}_1 = \begin{bmatrix} 2, & 0, & 0 \\ 0, & 2, & 0 \\ 0, & 0, & 2 \end{bmatrix}$		$N_S = 24$ Class-1	Morphed Cube

Part III

Closure

CHAPTER 10

CONCLUSIONS & FUTURE WORK

Multi-functional structural systems are ubiquitous in nature, with potential applications across scales: from deployable outer space structures, to transformable multi-role robots, and to microstructures of metamaterials. To achieve the desired functionality, the system has to be able to change its behavior on demand, which usually involves programmable physical states, such as geometry, and stress distribution. Compared to other reconfigurable and programmable structural systems, such as membranes and truss frames, the present understanding of origami and tensegrity is incipient and thus there is room for further investigation and great creativity – this is the focus of this thesis.

Both origami and tensegrity are deeply rooted in art, and are found to abound in nature under various forms, implying their exclusive performance as multi-functional platforms. Thus, we study the mechanics and physics of origami and tensegrity while emphasizing their subtle artistic connection. We explore their potential applications to reconfigurable structures and programmable metamaterials by means of examples of informative and illuminative designs. For instance, we demonstrate that by harnessing rigid and non-rigid folding of origami, we can generate a globally smooth hyperbolic paraboloid surfaces by folding a flat sheet; we can design metamaterials with arbitrary Poisson's ratio; and we can obtain programmable multi-stable structures and metamaterials. We also show that the mechanical properties of origami assemblages can be very sensitive to geometric imperfections. Moreover, by taking advantage of the prestress within tensegrity systems, we can deploy a stable structural platform of desired geometry from an unstable and compact assembly; we can create metamaterials whose elastostatic and elastodynamic properties are responsively tunable to changing prestress level, which provides a new dimension of programmability beyond geometry. The aforementioned findings open new avenues enabling

their exploration beyond the realm of this thesis, while laying the path to unanticipated interdisciplinary discoveries.

10.1 Summary of Contributions

The contributions of the present work are summarized as follows (Chapter-wise):

Part I: Origami

- By combining the compatibility equations with material models inspired by conventional nonlinear continuum elasticity, we formulate an efficient computational approach to analyze the structure behavior of origami structures involving large displacement and deformation. We implemented our formulation in the open-source software MERLIN, which can be obtained from [62], aiming at speeding origami design cycles and educating students in origami science and engineering.
- By homogenizing local folds to establish a differential map of the global geometry, we prove mathematically that the theoretical limit of the beautiful shape folded from concentrically pleated squares, known as the hypar origami, is indeed a hyperbolic paraboloid, as its name suggests. Our experimental and numerical analyses verify the theory and further extend the study to origami made with real materials, and lead to the discovery of a mechanically preferred pattern for dominant bending ridges within the panels.
- By breaking the perfect symmetry and/or periodicity of the origami patterns, geometric imperfections can significantly alter the mechanical behavior of origami metamaterials. Our combined experimental and numerical analyses show that, unlike conventional cellular materials, geometric imperfections increase the materials compressive stiffness and strength. Moreover, we discover an intriguing result, namely that the residual of an origami design constraint, given by the famous Kawasaki theorem,

strongly correlates with the stiffness and strength of imperfect origami metamaterials.

- By breaking the strict symmetries of the geometry of the standard Miura-ori and Eggbox, and allowing creases to switch between mountains and valleys, we create a “Morph” pattern, which morphs between the Miura-ori and Eggbox pattern, and thus combines features of its parent patterns. The Morph pattern possesses unique properties such as topological morphing of creases, tunable switching of Poisson’s ratio (spanning continuously from positive, to zero, to negative), and mode-locking.
- By blocking a range of rigid folding kinematics of rigid origami, we arrive at a rational origami design that combines the features of both rigid and non-rigid origami, named the “Shrimp” pattern. We show that the bistability of a unit cell of this pattern can be programmed by a few geometric parameters. The “Shrimp” unit cells can be easily tessellated to make multi-stable patterns, leading to applications involving multi-stable mechanical metamaterials. By programming the unit cell geometries, we can achieve controlled sequence of snap-throughs within the metamaterial.

Part II: Tensegrity

- By maximizing prestress forces within arbitrarily shaped ground structures (i.e. a dense set of potential members), our proposed formulation for tensegrity design can generate relatively complex tensegrities with prescribed geometry, including concave domains. This could be very useful when designing for engineering applications, where the tensegrity structures need to reverse space for payload or nearby objects. The effectiveness of the proposed formulation is verified by reproducing known tensegrity forms. However, more importantly, it also allows the creation of new tensegrity forms.
- By fabricating the compression members of a tensegrity from shape memory polymers, we were able to use 3D printers to create objects capable of transforming dra-

matically under thermal stimuli – no tethers or motors involved. Enabled by the intrinsic properties of tensegrity and remote controllable actuation by temperature, we can foresee the great potential of active tensegrity in a broad variety of applications. These objects can be either scaled up and made more complex, as for space structures; or scaled-down, to the size of something that could fit in the human body, e.g. for drug delivery.

- By imposing periodicity into the design formulae of tensegrity, we create an automatic design framework that allows for access to an unlimited number of tensegrity metamaterial designs. The framework generates tensegrity metamaterials by tessellating unit cells with designated geometries that are aware of system periodicity. Tensegrity metamaterials demonstrate great potential to become advanced materials by offering tunable static and dynamic properties by changing prestress levels, which could possibly be realized by applying external physical stimuli.

10.2 Future Work

The work described in this thesis opens a wide range of possible future research avenues.

- **Scaling up and down of the proposed designs of new origami and tensegrity.** This thesis proposed several new designs of origami and tensegrity. As we only demonstrate their properties through numerical simulations or meso-scale experiments, it is important to explore how to scale up and down the designs and ideas towards real terrestrial and/or outer-space applications. For example, can the active deployment of tensegrity structure be used to create emergency shelters? Can the tensegrity tessellations be manufactured as materials with suitable properties tuned when desired?
- **Continuous and discrete differential geometry of origami sheets.** Origami tessellated sheets have the ability to change their global Gaussian curvature, with purely isometric deformations at local level (i.e. no stretching). It is interesting how by

simply changing the arrangement of creases, the folded sheets display distinct global shapes. As we show in Chapter 3, we can analytically describe the global geometry of the hyperbolic origami throughout its folding process, by connecting global continuous and local discrete differential geometry. *Is there a general analytical framework that connects the local and global geometries of origami?* Can we use such a framework to explain philosophically the intriguing phenomenon found with the Miura-ori, standard Eggbox, and the Morph pattern, as proposed in Chapter 5, that the effective Poisson's ratio was oppositely signed for stretching and bending (i.e. $\nu^b = -\nu^s$)? We are curious to understand deeper such elegant result both at the pattern-level and conceptual-level, i.e. generalizability.

- **Structural analysis considering material deterioration.** The structural analysis formulation presented in Chapter 2 is based on the theory of elasticity. Therefore, it does not consider plastic and/or fatigue induced change of material properties, which is noticeable in real applications. It would be worthwhile to extend and enrich the current nonlinear formulation to more general mechanics models, by considering plasticity, fracture, and fatigue in a simple manner that suits the reduced order model.

REFERENCES

- [1] K. Caluwaerts, J. Despraz, A. İşçen, A. P. Sabelhaus, J. Bruce, B. Schrauwen, and V. SunSpiral, “Design and control of compliant tensegrity robots through simulation and hardware validation,” *Journal of The Royal Society Interface*, vol. 11, no. 98, pp. 1–13, 2014.
- [2] A. G. Tibert, “Deployable Tensegrity Structures for Space Applications,” PhD thesis, Royal Institute of Technology, 2002, p. 220.
- [3] D. Rus and T. T. Michael, “Design, fabrication and control of origami robots,” *Nature Review Materials*, vol. 3, pp. 101–112, 2018.
- [4] S. Miyashita, S. Guitron, S. Li, and D. Rus, “Robotic metamorphosis by origami exoskeletons,” *Science Robotics*, vol. 2, no. 10, eaao4369, 2017.
- [5] E. T. Filipov, T. Tachi, and G. H. Paulino, “Origami tubes assembled into stiff, yet reconfigurable structures and metamaterials,” *Proceedings of the National Academy of Sciences*, p. 201 509 465, 2015.
- [6] M. Schenk and S. D. Guest, “Geometry of Miura-folded metamaterials,” *Proceedings of the National Academy of Sciences*, vol. 110, no. 9, pp. 3276–3281, 2013.
- [7] J. T. B. Overvelde, J. C. Weaver, C. Hoberman, and K. Bertoldi, “Rational design of reconfigurable prismatic architected materials,” *Nature*, vol. 541, pp. 347–352, 2017.
- [8] E. Heartney and K. Snelson, *Kenneth Snelson: Forces Made Visible*. Hudson Hills, 2009, p. 193.
- [9] R. J. Lang and A. Bateman, “Every Spider Web has a Simple Flat Twist Tessellation,” in *Origami 5: Fifth International Meeting of Origami Science Mathematics and Education*, P. Wang-Iverson, R. J. Lang, and M. Yim, Eds., CRC Press, 2011, pp. 455–473.
- [10] K. Snelson, “The art of tensegrity,” *International Journal of Space Structures*, vol. 27, no. 2-3, pp. 71–80, 2012.
- [11] K. Saito, S. Nomura, S. Yamamoto, R. Niiyama, and Y. Okabe, “Investigation of hindwing folding in ladybird beetles by artificial elytron transplantation and microcomputed tomography,” *Proceedings of the National Academy of Sciences*, vol. 114, no. 22, pp. 5624–5628, 2017.

- [12] J. A. Faber, A. F. Arrieta, and A. R. Studart, “Bioinspired spring origami,” *Science*, vol. 359, pp. 1386–1391, 2018.
- [13] D. E. Ingber, “The architecture of life,” *Scientific American*, vol. 278, no. 1, pp. 48–57, 1998.
- [14] G. Scarr, *Biotensegrity: The structural basis of life*. Hardspring Publishing, 2014.
- [15] M. P. Do Carmo, *Differential Geometry of Curves and Surfaces*. Prentice-Hall, 1976.
- [16] T. Tachi, “Origamizing polyhedral surfaces,” *IEEE Transactions on Visualization and Computer Graphics*, vol. 16, no. 2, pp. 298–311, 2010.
- [17] H. Nassar, A. Lebée, and L. Monasse, “Curvature, metric and parametrization of origami tessellations: Theory and application to the eggbox pattern,” *Proceedings of the Royal Society A*, vol. 473, no. 2197, p. 20 160 705, 2017.
- [18] J. T. Overvelde, T. A. de Jong, Y. Shevchenko, S. A. Becerra, G. M. Whitesides, J. C. Weaver, C. Hoberman, and K. Bertoldi, “A three-dimensional actuated origami-inspired transformable metamaterial with multiple degrees of freedom,” *Nature Communication*, vol. 7, p. 10 929, 2016.
- [19] M Eidini and G. H. Paulino, “Unraveling metamaterial properties in zigzag-base folded sheets,” *Science Advances*, vol. 1, no. 8, e1500224–e1500224, 2015.
- [20] K. Saito, A. Tsukahara, and Y. Okabe, “Designing of self-deploying origami structures using geometrically misaligned crease patterns,” *Proceedings of the Royal Society A*, vol. 472, p. 20 150 235, 2016.
- [21] A. Rafsanjani and K. Bertoldi, “Buckling-induced kirigami,” *Physical Review Letters*, vol. 118, no. 8, p. 084 301, 2017.
- [22] Y. Zhang, Z. Yan, K. Nan, D. Xiao, Y. Liu, H. Luan, H. Fu, X. Wang, Q. Yang, J. Wang, W. Ren, H. Si, F. Liu, L. Yang, H. Li, J. Wang, X. Guo, H. Luo, L. Wang, Y. Huang, and J. A. Rogers, “A mechanically driven form of Kirigami as a route to 3D mesostructures in micro/nanomembranes,” *Proceedings of the National Academy of Sciences*, vol. 112, no. 38, p. 201 515 602, 2015.
- [23] Y. Chen, R. Peng, and Z. You, “Origami of thick panels,” *Science*, vol. 349, no. 6246, pp. 396–400, 2015.
- [24] T. Tachi, “Rigid-foldable thick origami,” in *Origami 5*, CRC Press, 2011, pp. 175–187.

- [25] A. Yellowhorse, R. J. Lang, K. Tolman, and L. L. Howell, “Creating linkage permutations to prevent self-intersection and enable deployable networks of thick-origami,” *Scientific Reports*, vol. 8, p. 12 936, 2018.
- [26] J. S. Ku and E. D. Demaine, “Folding flat crease patterns with thick materials,” *Journal of Mechanisms and Robotics*, vol. 8, no. 3, p. 031 003, 2016.
- [27] S. Kamiya, *Works of Satoshi Kamiya*. Gallery Origami House, 2005.
- [28] M. A. Dias, L. H. Dudte, L. Mahadevan, and C. D. Santangelo, “Geometric mechanics of curved crease origami,” *Physical Review Letters*, vol. 109, p. 114 301, 11 2012.
- [29] E. T. Filipov, G. H. Paulino, and T. Tachi, “Origami tubes with reconfigurable polygonal cross-sections,” *Proceedings of the Royal Society A*, vol. 472, p. 20 150 607, 2016.
- [30] H. Yasuda and J. Yang, “Reentrant origami-based metamaterials with negative poisson’s ratio and bistability,” *Physical Review Letters*, vol. 114, p. 185 502, 18 2015.
- [31] H. Yasuda, Z. Chen, and J. Yang, “Multitransformable leaf-out origami with bistable behavior,” *Journal of Mechanisms and Robotics*, vol. 8, p. 031 013, 3 2016.
- [32] H. Yasuda, T. Tachi, M. Lee, and J. Yang, “Origami-based tunable truss structures for no--volatile mechanical memory operation,” *Nature Communicationsvolume*, vol. 8, p. 962, 2017.
- [33] S. Li, H. Fang, and K. W. Wang, “Recoverable and programmable collapse from folding pressurized origami cellular solids,” *Physical Review Letters*, vol. 117, p. 114 301, 11 2016.
- [34] X. Zhou, S. Zang, and Z. You, “Origami mechanical metamaterials based on the Miura-derivative fold patterns,” *Proceedings of the Royal Society A*, vol. 472, no. 2191, p. 20 160 361, 2016.
- [35] Z. Y. Wei, Z. V. Guo, L. Dudte, H. Y. Liang, and L. Mahadevan, “Geometric mechanics of periodic pleated origami,” *Physical Review Letters*, vol. 110, no. 21, pp. 1–5, 2013.
- [36] E. Boatti, N. Vasios, and K. Bertoldi, “Origami metamaterials for tunable thermal expansion,” *Advanced Materials*, vol. 29, no. 26, p. 1 700 360, 2017.
- [37] J. L. Silverberg, A. A. Evans, L. McLeod, R. C. Hayward, T. Hull, C. D. Santangelo, and I. Cohen, “Using origami design principles to fold reprogrammable mechanical metamaterials,” *Science*, vol. 345, no. 6197, pp. 647–650, 2014.

- [38] J. L. Silverberg, J. H. Na, A. A. Evans, B. Liu, T. Hull, C. D. Santangelo, R. J. Lang, R. C. Hayward, and I. Cohen, “Origami structures with a critical transition to bistability arising from hidden degrees of freedom,” *Nature Materials*, vol. 14, pp. 389–393, 2015.
- [39] Z. Zhai, Y. Wang, and H. Jiang, “Origami-inspired, on-demand deployable and collapsible mechanical metamaterials with tunable stiffness,” *Proceedings of the National Academy of Sciences*, p. 1720171115, 2018.
- [40] P.-O. Mouthuy, M. Coulombier, T. Pardoen, J.-P. Raskin, and A. M Jonas, “Over-curvature describes the buckling and folding of rings from curved origami to foldable tents,” *Nature Communications*, vol. 3, p. 1290, 2012.
- [41] J. Rogers, Y. Huang, O. G. Schmidt, and D. H. Gracias, “Origami MEMS and NEMS,” *MRS Bulletin*, vol. 41, no. 2, 123129, 2016.
- [42] L. H. Dudte, E. Vouga, T. Tachi, and L. Mahadevan, “Programming curvature using origami tessellations,” *Nature Materials*, vol. 15, no. 5, p. 583, 2016.
- [43] S. Waitukaitis, R. Menaut, B. G. Chen, and M. van Hecke, “Origami multistability: From single vertices to metasheets,” *Physical Review Letters*, vol. 114, no. 5, p. 055503, 2015.
- [44] K. Miura, “Method of Packaging and Deployment of Large Membranes in Space,” Institute of Space and Astronautical Science, Tech. Rep., 1985, p. 9.
- [45] R. J. Lang, S. Magleby, and L. L. Howell, “Single-degree-of-freedom rigidly foldable cut origami flashers,” *Journal of Mechanisms and Robotics*, vol. 8, p. 031005, 3 2015.
- [46] K. Kurabayashi, K. Tsuchiya, Z. You, D. Tomus, M. Umemoto, T. Ito, and M. Sasaki, “Self-deployable origami stent grafts as a biomedical application of Ni-rich TiNi shape memory alloy foil,” *Materials Science and Engineering A*, vol. 419, no. 1-2, pp. 131–137, 2006.
- [47] J. Ma and Z. You, “Energy Absorption of Thin-Walled Square Tubes With a Pre-folded Origami Pattern Part I : Geometry and Numerical Simulation,” *Journal of Applied Mechanics*, vol. 81, no. January 2014, pp. 1–11, 2013.
- [48] R. J. Lang, *White-tailed deer, opus 550*, Folded for the ”Origami Inside Out” exhibition at Franklin Park Conservatory. URL: <http://www.langorigami.com/artwork/white-tailed-deer-opus-550-0>. Accessed August 20, 2016, 2016.
- [49] R. B. Fuller, *Tensile-integrity structures*, United States Patent 3063521, 1962.

- [50] R. Motro, *Tensegrity: Structural Systems for the Future*. Elsevier, 2006, p. 280.
- [51] R. E. Skelton and M. de Oliveira, *Tensegrity Systems*. Springer US, 2009.
- [52] R. Connelly and W. Whiteley, “Second-Order Rigidity and Prestress Stability for Tensegrity Frameworks,” *SIAM Journal on Discrete Mathematics*, vol. 9, no. 3, pp. 453–491, 1996.
- [53] J. Y. Zhang and M. Ohsaki, *Tensegrity Structures - Form, Stability, and Symmetry*. Springer Japan, 2015, p. 300.
- [54] A. Hanaor, “Debunking “Tensegrity” - A personal perspective,” *International Journal of Space Structures*, vol. 27, no. 2&3, pp. 179–183, 2012.
- [55] D. Williamson and R. E. Skelton, “General Class of Tensegrity Structures: Topology and Prestress Equilibrium Analysis,” *Journal of Guidance, Control, and Dynamics*, vol. 26, no. 5, pp. 685–694, 2003.
- [56] K. W. Moore, T. H. Kemp, N. E. Houle, and H. Bart-Smith, “Analytical predictions, optimization, and design of a tensegrity-based artificial pectoral fin,” *International Journal of Solids and Structures*, vol. 48, no. 22-23, pp. 3142–3159, 2011.
- [57] Manhattan, *Skwish*.
- [58] C. Sultan, “Modeling, design, and control of tensegrity structures with applications,” PhD thesis, Purdue University, 1999, p. 196.
- [59] L.-G.-A. Rhode-Barbarigos, “An Active Deployable Tensegrity Structure,” PhD thesis, École Polytechnique Fédérale de Lausanne, 2012, p. 172.
- [60] K. Liu and G. H. Paulino, “MERLIN : A MATLAB implementation to capture highly nonlinear behavior of non-rigid origami,” in *Proceedings of the IASS Annual Symposium*, K Kawaguchi, M. Ohsaki, and T Takeuchi, Eds., Tokyo, Japan, 2016.
- [61] K. Liu and G. H. Paulino, “Highly efficient nonlinear structural analysis of origami assemblages using the MERLIN2 software,” in *Origami 7*, Tarquin, 2018.
- [62] K. Liu, Matlab code of MERLIN and MERLIN2 is available at <http://paulino.ce.gatech.edu/software.html>.
- [63] S.-M. Belcastro and T. C. Hull, “Modelling the folding of paper into three dimensions using affine transformations,” *Linear Algebra and its Applications*, vol. 348, pp. 273–282, 2002.

- [64] T. Tachi, “Simulation of rigid origami,” in *Origami 4*, R. J. Lang, Ed., A K Peters/CRC Press, 2006, pp. 175–187.
- [65] W. Wu and Z. You, “Modelling rigid origami with quaternions and dual quaternions,” *Proceedings of the Royal Society A*, vol. 466, pp. 2155–2174, 2010.
- [66] J. M. Gattas, W. Wu, and Z. You, “Miura-base rigid origami: parameterizations of first-level derivative and piecewise geometries,” *Journal of Mechanical Design*, vol. 135, p. 111 011, 2013.
- [67] J. N. Reddy, *Theory and Analysis of Elastic Plates and Shells*, Second. CRC Press, 2006, p. 568.
- [68] J. M. Gattas and Z. You, “Quasi-static impact of indented foldcores,” *International Journal of Impact Engineering*, vol. 73, pp. 15–29, 2014.
- [69] J. M. Gattas and Z. You, “The behaviour of curved-crease foldcores under low-velocity impact loads,” *International Journal of Solids and Structures*, vol. 53, pp. 80–91, 2015.
- [70] C. Lv, D. Krishnaraju, G. Konjevod, H. Yu, and H. Jiang, “Origami based mechanical metamaterials,” *Scientific Reports*, vol. 4, no. 5979, pp. 1–6, 2014.
- [71] R. Hauptmann and K. Schweizerhof, “A systematic development of ‘solid-shell’ element formulations for linear and non-linear analyses employing only displacement degrees of freedom,” *International Journal for Numerical Methods in Engineering*, vol. 42, pp. 49–69, 1998.
- [72] E. Ramm and W. A. Wall, “Shell structures - A sensitive interrelation between physics and numerics,” *International Journal for Numerical Methods in Engineering*, vol. 60, no. 1, pp. 381–427, 2004.
- [73] P.-S. Lee, H.-C. Noh, and K.-J. Bathe, “Insight into 3-node triangular shell finite elements: the effects of element isotropy and mesh patterns,” *Computers and Structures*, vol. 85, pp. 404–418, 2007.
- [74] N. S. N. Ota, L. Wilson, A. Gay Neto, S. Pellegrino, and P. M. Pimenta, “Nonlinear dynamic analysis of creased shells,” *Finite Elements in Analysis and Design*, vol. 121, pp. 64–74, 2016.
- [75] R. D. Resch and H. Christiansen, “The design and analysis of kinematic folded plate systems,” in *IASS Symposium on Folded Plates and Prismatic Structures*, Vienna, 1970, pp. 1–38.

- [76] P. Kumar and S. Pellegrino, “Computation of kinematic paths and bifurcation points,” *International Journal of Solids and Structures*, vol. 37, no. 46-47, pp. 7003–7027, 2000.
- [77] A. A. Evans, J. L. Silverberg, and C. D. Santangelo, “Lattice mechanics of origami tessellations,” *Physical Review E*, vol. 92, p. 013 205, 2015.
- [78] T. Tachi, “Interactive Form-Finding of Elastic Origami,” in *Proceedings of the International Association for Shell and Spatial Structures (IASS) Symposium 2013*, 2013, pp. 7–10.
- [79] V. Brunck, F. Lechenault, A. Reid, and M. Adda-Bedia, “Elastic theory of origami-based metamaterials,” *Physical Review E*, vol. 93, no. 3, pp. 1–14, 2016.
- [80] M. Schenk, “Folded Shell Structures,” Clare College, University of Cambridge, 2011, p. 149.
- [81] M. Schenk and S. D. Guest, “Origami folding: A structural engineering approach,” in *Origami 5*, P. Wang-Iverson, R. J. Lang, and M. Yim, Eds., CRC Press, 2011, pp. 293–305.
- [82] T. A. Witten, “Stress focusing in elastic sheets,” *Reviews of Modern Physics*, vol. 79, no. 2, pp. 643–675, 2007.
- [83] R Bridson, S Marino, and R Fedkiw, “Simulation of clothing with folds and wrinkles,” in *Proceedings of the Eurographics/SIGGRAPH Symposium on Computer Animation*, D Breen and M Lin, Eds., vol. 21, 2003, pp. 28–36.
- [84] S. D. Guest and S Pellegrino, “The folding of triangulated cylinders, Part III: experiments,” *ASME Journal of Applied Mechanics*, vol. 63, pp. 77–83, 1996.
- [85] K. Fuchi, P. R. Buskohl, G. Bazzan, M. F. Durstock, G. W. Reich, R. A. Vaia, and J. J. Joo, “Origami actuator design and networking through crease topology optimization,” *Journal of Mechanical Design*, vol. 137, no. 9, p. 091 401, 2015.
- [86] K. Fuchi and A. R. Diaz, “Origami design by topology optimization,” *Journal of Mechanical Design*, vol. 135, no. 11, p. 111 003, 2013.
- [87] R. H. Gallagher, “Techniques for the derivation of element stiffness matrices,” *AIAA Journal*, vol. 1, no. 6, pp. 1431–1432, 1963.
- [88] R. H. Gallagher, *A Correlation Study of Methods of Matrix Structural Analysis*. Pergamon, 1964.

- [89] W. McGuire, R. H. Gallagher, and R. D. Ziemian, *Matrix Structural Analysis*, Second. Wiley, 2000, p. 482.
- [90] R. H. Gallagher, *Finite Element Analysis: Fundamentals*, First. Prentice Hall, 1975, p. 420.
- [91] J. Bonet and R. D. Wood, *Nonlinear Continuum Mechanics for Finite Element Analysis*, 2nd ed. Cambridge University Press, 2008, p. 248.
- [92] R. W. Ogden, *Non-Linear Elastic Deformations*. New York: Dover Publications, 1997.
- [93] P. Wriggers, *Nonlinear Finite Element Methods*. Springer, 2008, p. 559.
- [94] R. C. van Schaik, H. J. C. Berendsen, A. E. Torda, and W. F. van Gunsteren, “A structure refinement method based on molecular dynamics in four spatial dimensions,” *Journal of Molecular Biology*, vol. 234, no. 3, pp. 751–762, 1993.
- [95] H. Bekker, “Molecular dynamics simulation methods revised,” PhD thesis, University of Groningen, 1996, pp. 1–160.
- [96] M. Heath, *Scientific Computing: An Introductory Survey*, ser. Second Edition. McGraw-Hill, 1997, ISBN: 9780071153362.
- [97] A. S. Ramos Jr and G. H. Paulino, “Convex topology optimization for hyperelastic trusses based on the ground-structure approach,” *Structural and Multidisciplinary Optimization*, vol. 51, no. 2, pp. 287–304, 2015.
- [98] E. T. Filipov, K. Liu, T. Tachi, M. Schenk, and G. H. Paulino, “Bar and hinge models for scalable analysis of origami,” *International Journal of Solids and Structures*, vol. 124, pp. 26–45, 2017.
- [99] A. Lobkovsky, “Boundary layer analysis of the ridge singularity in a thin plate,” *Physical Review E*, vol. 53, no. 4, pp. 3750–3759, 1996.
- [100] M. Bern and D. Eppstein, “Mesh generation and optimal triangulation,” in *Computing in Euclidean Geometry*, D. Z. Du and H. F. K., Eds., 2nd, World Scientific, 1995, pp. 47–123.
- [101] K. Liu and G. H. Paulino, “Nonlinear mechanics of non-rigid origami: An efficient computational approach,” *Proceedings of the Royal Society A*, vol. 473, p. 20170348, 2017.
- [102] M. A. Crisfield, *Non-Linear Finite Element Analysis of Solids and Structures, Volume 1: Essentials*. Wiley, 1996.

- [103] S. E. Leon, G. H. Paulino, A. Pereira, I. F. M. Menezes, and E. N. Lages, “A unified library of nonlinear solution schemes,” *Applied Mechanics Reviews*, vol. 64, p. 040 803, 2011.
- [104] S. E. Leon, E. N. Lages, C. N. de Araújo, and G. H. Paulino, “On the effect of constraint parameters on the generalized displacement control method,” *Mechanics Research Communications*, vol. 56, pp. 123–129, 2014.
- [105] Y. B. Yang and M. S. Shieh, “Solution method for nonlinear problems with multiple critical points,” *AIAA Journal*, vol. 28, pp. 2110–2116, 1990.
- [106] B. Kresling, “Natural twist buckling in shells: From the Hawkmoth’s Bellows to the deployable kresling-pattern and cylindrical Miura-ori,” in *Proceedings of the 6th International Conference on Computation of Shell and Spatial Structures*, J. F. Abel and J. R. Cooke, Eds., Ithaca, 2008, pp. 1–4.
- [107] E. A. Paulino, *Personal communication*, 2015.
- [108] S. Liu, G. Lu, Y. Chen, and Y. W. Leong, “Deformation of the Miura-ori patterned sheet,” *International Journal of Mechanical Sciences*, vol. 99, pp. 130–142, 2015.
- [109] C. W. Smith, R. J. Wootton, and K. E. Evans, “Interpretation of experimental data for Poisson’s ratio of highly nonlinear materials,” *Experimental Mechanics*, vol. 39, pp. 356–362, 1999.
- [110] M. F. Beatty and D. O. Stalnaker, “The Poisson function of finite elasticity,” *ASME Journal of Applied Mechanics*, vol. 53, pp. 807–813, 1986.
- [111] T. C. T. Ting and T. Chen, “Poisson’s ratio for anisotropic elastic materials can have no bounds,” *The Quarterly Journal of Mechanics and Applied Mathematics*, vol. 58, no. 1, pp. 73–82, 2005.
- [112] J. Cai, X. Deng, Y. Zhou, J. Feng, and Y. Tu, “Bistable behavior of the cylindrical origami structure with Kresling pattern,” *Journal of Mechanical Design*, vol. 137, no. 6, p. 061 406, 2015.
- [113] S. D. Guest and S Pellegrino, “The folding of triangulated cylinders, Part I: geometric considerations,” *ASME Journal of Applied Mechanics*, vol. 61, pp. 773–777, 1994.
- [114] S. D. Guest and S Pellegrino, “The folding of triangulated cylinders, Part II: the folding process,” *ASME Journal of Applied Mechanics*, vol. 61, pp. 778–783, 1994.
- [115] T. Tachi, “Freeform variations of origami,” *Journal for Geometry and Graphics*, vol. 14, no. 2, pp. 203–215, 2010.

- [116] T. Tachi, “Generalization of rigid foldable quadrilateral mesh origami,” in *Proceedings of the International Association for Shell and Spatial Structures (IASS) Symposium 2009*, A. Domingo and C. Lazaro, Eds., Valencia, Spain, 2009.
- [117] H. Liang and L. Mahadevan, “Growth, geometry, and mechanics of a blooming lily,” *Proceedings of the National Academy of Sciences*, vol. 108, no. 14, pp. 5516–5521, 2011.
- [118] E. Sharon, B. Roman, M. Marder, G. Shin, and H. Swinney, “Buckling cascades in free sheets,” *Nature*, vol. 419, pp. 579–579, 2002.
- [119] T. Savin, N. A. Kurpios, A. E. Shyer, P. Florescu, H. Liang, L. Mahadevan, and C. J. Tabin, “On the growth and form of the gut,” *Nature*, vol. 476, pp. 57–62, 2011.
- [120] T. Tallinen, J. Y. Chung, F. Rousseau, N. Girard, J. Lefèvre, and L. Mahadevan, “On the growth and form of cortical convolutions,” *Nature Physics*, vol. 12, pp. 588–593, 2016.
- [121] Y. Klein, E. Efrati, and E. Sharon, “Shaping of elastic sheets by prescription of non-euclidean metrics,” *Science*, vol. 315, pp. 1116–1120, 2007.
- [122] W. H. Koo, S. M. Jeong, F. Araoka, K. Ishikawa, S. Nishimura, T. Toyooka, and H Takezoe, “Light extraction from organic light-emitting diodes enhanced by spontaneously formed buckles,” *Nature Photonics*, vol. 4, pp. 222–226, 2010.
- [123] M. A. Dias and B. Audoly, “A non-linear rod model for folded elastic strips,” *Journal of the Mechanics and Physics of Solids*, vol. 62, pp. 57–80, 2014.
- [124] H. M. Wingler, *Bauhaus: Weimar, Dessau, Berlin, Chicago*. MIT Press, 1969.
- [125] B. Liu, J. L. Silverberg, A. A. Evans, C. D. Santangelo, R. J. Lang, T. C. Hull, and I. Cohen, “Topological kinematics of origami metamaterials,” *Nature Physics*, vol. 14, pp. 811–815, 8 2018.
- [126] E. D. Demaine, M. L. Demaine, V. Hart, G. N. Price, and T. Tachi, “(non)existence of pleated folds: How paper folds between creases,” *Graphs and Combinatorics*, vol. 27, no. 3, pp. 377–397, 2011.
- [127] E. T. Filipov and M. Redoutey, “Mechanical characteristics of the bistable origami hypar,” *Extreme Mechanics Letters*, vol. 25, pp. 16–26, 2018.
- [128] K. A. Seffen, “Compliant shell mechanisms,” *Philosophical Transactions of the Royal Society of London A: Mathematical, Physical and Engineering Sciences*, vol. 370, no. 1965, pp. 2010–2026, 2012.

- [129] J. J. Craig, *Introduction to Robotics: Mechanics and Control*, 3rd. Pearson, 2004.
- [130] C. R. Calladine, *Theory of Shell Structures*. Cambridge University Press, 1983.
- [131] M. Stern, M. B. Pinson, and A. Murugan, “The complexity of folding self-folding origami,” *Physical Review X*, vol. 7, p. 041 070, 4 2017.
- [132] B. G.-g. Chen and C. D. Santangelo, “Branches of triangulated origami near the unfolded state,” *Physical Review X*, vol. 8, p. 011 034, 1 2018.
- [133] H. R. Schiffman, *Sensation and Perception: An Integrated Approach*, 5th. Wiley, 2001.
- [134] K. Che, C. Yuan, J. Wu, H. Qi, and J. Meaud, “3D-printed multistable mechanical metamaterials with a deterministic deformation sequence,” *Journal of Applied Mechanics*, vol. 84, p. 011 004, 2017.
- [135] R. N. Wilson, *Reflecting Telescope Optics I: Basic Design Theory and Its Historical Development*, 2nd ed. Springer Verlag, 1996.
- [136] P. M. Reis, “A perspective on the revival of structural (in)stability with novel opportunities for function: From buckliphobia to buckliphilia,” *ASME Journal of Applied Mechanics*, vol. 82, p. 111 001, 11 2015.
- [137] D. M. Kochmann and K. Bertoldi, “Exploiting microstructural instabilities in solids and structures: From metamaterials to structural transitions,” *ASME Applied Mechanics Reviews*, vol. 69, p. 050 801, 5 2017.
- [138] L. R. Meza, A. J. Zelhofer, N. Clarke, A. J. Mateos, D. M. Kochmann, and J. R. Greer, “Resilient 3D hierarchical architected metamaterials,” *Proceedings of the National Academy of Sciences*, vol. 112, no. 37, pp. 11 502–11 507, 2015.
- [139] D. Z. Rocklin, B. G. Chen, M. Falk, V. Vitelli, and T. C. Lubensky, “Mechanical Weyl modes in topological Maxwell lattices,” *Physical Review Letters*, vol. 116, p. 135 503, 13 2016.
- [140] K. H. Matlack, A. Bauhofer, S. Krödel, A. Palermo, and C. Daraio, “Composite 3D-printed metastructures for low-frequency and broadband vibration absorption,” *Proceedings of the National Academy of Sciences*, vol. 113, no. 30, pp. 8386–8390, 2016.
- [141] K. Bertoldi, V. Vitelli, J. Christensen, and M. van Hecke, “Flexible mechanical metamaterials,” *Nature Reviews Materials*, vol. 2, p. 17 066, 2017.

- [142] H. Fang, S. Li, and K. W. Wang, “Self-locking degree-4 vertex origami structures,” *Proceedings of the Royal Society A*, vol. 472, p. 20160682, 2016.
- [143] Z. Wang, L. Jing, K. Yao, Y. Yang, B. Zheng, C. M. Soukoulis, H. Chen, and Y. Liu, “Origami-based reconfigurable metamaterials for tunable chirality,” *Advanced Materials*, vol. 29, no. 27, p. 1700412, 2017.
- [144] J. L. Grenestedt, “Influence of wavy imperfections in cell walls on elastic stiffness of cellular solids,” *Journal of the Mechanics and Physics of Solids*, vol. 46, no. 1, pp. 29–50, 1998.
- [145] D. D. Symons and N. A. Fleck, “The imperfection sensitivity of isotropic two-dimensional elastic lattices,” *Journal of Applied Mechanics*, vol. 75, p. 051011, 5 2008.
- [146] E. Baranger, P.-A. Guidault, and C. Cluzel, “Numerical modeling of the geometrical defects of an origami-like sandwich core,” *Composite Structures*, vol. 93, no. 10, pp. 2504–2510, 2011.
- [147] L. Liu, P. Kamm, F. Garca-Moreno, J. Banhart, and D. Pasini, “Elastic and failure response of imperfect three-dimensional metallic lattices: The role of geometric defects induced by selective laser melting,” *Journal of the Mechanics and Physics of Solids*, vol. 107, pp. 160–184, 2017.
- [148] J. Ma, D. Hou, Y. Chen, and Z. You, “Quasi-static axial crushing of thin-walled tubes with a kite-shape rigid origami pattern: Numerical simulation,” *Thin-Walled Structures*, vol. 100, pp. 38–47, 2016.
- [149] E. D. Demaine and J. O’Rourke, *Geometric Folding Algorithms: Linkages, Origami, Polyhedra*. Cambridge University Press, 2007.
- [150] W. K. Schief, A. I. Bobenko, and T. Hoffmann, “On the Integrability of Infinitesimal and Finite Deformations of Polyhedral Surfaces,” in *Discrete Differential Geometry*, A. Bobenko, P. Schröder, J. Sullivan, and G. Ziegler, Eds., vol. 38, Birkhäuser Verlag Basel/Switzerland, 2008, pp. 67–93.
- [151] B. G. G. Chen, B. Liu, A. A. Evans, J. Paulose, I. Cohen, V. Vitelli, and C. D. Santangelo, “Topological Mechanics of Origami and Kirigami,” *Physical Review Letters*, vol. 116, no. 13, pp. 1–5, 2016.
- [152] R. J. Lang, *Twists, Tilings, and Tessellations*. CRC Press, 2018.
- [153] E. D. Demaine, M. L. Demaine, D. A. Huffman, T. C. Hull, D. Koschitz, and T. Tachi, “Zero-area reciprocal diagram of origami,” in *Proceedings of the IASS Symposium 2016*, 2016.

- [154] L. J. Gibson and M. F. Ashby, *Cellular Solids: Structure and Properties*, 2nd ed. Cambridge University Press, 1997.
- [155] H. Xu and P. Gardoni, “Spatial covariance function for non-stationary random fields based on improved latent dimension approach,” *Spatial Statistics*, vol. 23, pp. 160–181, 2018.
- [156] C. E. Rasmussen and C. K. I. Williams, *Gaussian Processes for Machine Learning*. MIT Press, 2006, p. 248.
- [157] A. Ajdari, H. Nayeb-Hashemi, and A. Vaziri, “Dynamic crushing and energy absorption of regular, irregular and functionally graded cellular structures,” *International Journal of Solids and Structures*, vol. 48, no. 3, pp. 506–516, 2011.
- [158] D. T. Ho, S. Park, S. Kwon, K. Park, and S. Y. Kim, “Negative Poissons ratios in metal nanoplates,” *Nature Communication*, vol. 5, p. 3255, 2014.
- [159] A. Rafsanjani and D. Pasini, “Bistable auxetic mechanical metamaterials inspired by ancient geometric motifs,” *Extreme Mechanics Letters*, vol. 9, pp. 291–296, 2016.
- [160] J. Liu and Y. Zhang, “Soft network materials with isotropic negative Poisson’s ratios over large strains,” *Soft Matter*, vol. 14, no. 5, pp. 693–703, 2018.
- [161] D. Z. Rocklin, S. Zhou, K. Sun, and X. Mao, “Transformable topological mechanical metamaterials,” *Nature Communications*, vol. 8, p. 14 201, 2017.
- [162] S. N. Patek, B. N. Nowroozi, J. E. Baio, R. L. Caldwell, and A. P. Summers, “Linkage mechanics and power amplification of the mantis shrimps strike,” *The Journal of Experimental Biology*, vol. 210, pp. 3677–3688, 2007.
- [163] S. N. Patek, “The most powerful movements in biology,” *American Scientist*, vol. 103, pp. 330–337, 2015.
- [164] Y. Forterre, J. M. Skotheim, J. Dumais, and L. Mahadevan, “How the Venus flytrap snaps,” *Nature*, vol. 433, pp. 421–425, 2005.
- [165] B. Haghpanah, L. Salari-Sharif, P. Pourrajab, J. Hopkins, and L. Valdevit, “Multistable shape-reconfigurable architected materials,” *Advanced Materials*, vol. 28, pp. 7915–7920, 2016.
- [166] M. Schenk, S. D. Guest, and J. L. Herder, “Zero stiffness tensegrity structures,” *International Journal of Solids and Structures*, vol. 44, no. 20, pp. 6569–6583, 2007.

- [167] B. A. Hanaor and M.-k. Liao, “Double-layer Tensegrity Grids: Static Load Response I: Analytical Study,” *Journal of Structural Engineering*, vol. 117, no. 6, pp. 1660–1674, 1991.
- [168] S. Pellegrino, “A class of tensegrity domes,” *International Journal of Space and Structures*, vol. 7, pp. 127–142, 1992.
- [169] K. Liu, J. Wu, G. H. Paulino, and H. J. Qi, “Programmable deployment of tensegrity structures by stimulus-responsive polymers,” *Scientific Reports*, vol. 7, p. 3511, 2017.
- [170] Y. Li, X.-Q. Feng, Y.-P. Cao, and H. Gao, “Constructing tensegrity structures from one-bar elementary cells,” *Proceedings of the Royal Society A*, vol. 466, no. 2113, pp. 45–61, 2010.
- [171] T. Tachi, “Interactive Freeform Design of Tensegrity,” in *Advances in Architectural Geometry 2012*, L. Hesselgren, S. Sharma, J. Wallner, N. Baldassini, P. Bompas, and J. Raynaud, Eds., Springer Vienna, 2013, pp. 259–268.
- [172] J. Y. Zhang and M. Ohsaki, “Adaptive force density method for form-finding problem of tensegrity structures,” *International Journal of Solids and Structures*, vol. 43, no. 18-19, pp. 5658–5673, 2006.
- [173] M. Ohsaki and J. Zhang, “Nonlinear programming approach to form-finding and folding analysis of tensegrity structures using fictitious material properties,” *International Journal of Solids and Structures*, vol. 69-70, pp. 1–10, 2015.
- [174] S. Lee and J. Lee, “Advanced automatic grouping for form-finding of tensegrity structures,” *Structural and Multidisciplinary Optimization*, vol. 55, no. 3, pp. 959–968, 2016.
- [175] S. Ehara and Y. Kanno, “Topology design of tensegrity structures via mixed integer programming,” *International Journal of Solids and Structures*, vol. 47, no. 5, pp. 571–579, 2010.
- [176] Y. Kanno, “Topology optimization of tensegrity structures under self-weight loads,” *Journal of the Operations Research Society of Japan*, vol. 55, no. 2, pp. 125–145, 2012.
- [177] Y. Kanno, “Topology optimization of tensegrity structures under compliance constraint: A mixed integer linear programming approach,” *Optimization and Engineering*, vol. 14, no. 1, pp. 61–96, 2013.
- [178] Y. Kanno, “Exploring new tensegrity structures via mixed integer programming,” *Structural and Multidisciplinary Optimization*, vol. 48, no. 1, pp. 95–114, 2013.

- [179] X. Xu, Y. Wang, Y. Luo, and A. M. Asce, “General approach for topology-finding of tensegrity structures,” *Journal of Structural Engineering*, vol. 142, no. 10, p. 04016061, 2016.
- [180] W. S. Dorn, R. E. Gomory, and H. J. Greenberg, “Automatic Design of Optimal Structures,” *Journal de Mécanique*, vol. 3, no. 1, pp. 25–52, 1964.
- [181] O. D. S. Smith, “Generation of ground structures for 2D and 3D design domains,” *Engineering with Computers*, vol. 15, no. 4, pp. 462–500, 1998.
- [182] T. Zegard and G. H. Paulino, “GRAND3 - Ground structure based topology optimization for arbitrary 3D domains using MATLAB,” *Structural and Multidisciplinary Optimization*, vol. online, pp. 1–24, 2015.
- [183] S. Guest, “The stiffness of prestressed frameworks: A unifying approach,” *International Journal of Solids and Structures*, vol. 43, no. 3-4, pp. 842–854, 2006.
- [184] S. D. Guest, “The stiffness of tensegrity structures,” *IMA Journal of Applied Mathematics*, vol. 76, pp. 57–66, 2011.
- [185] R. Connelly, “Tensegrity structures: Why are they stable?” In *Rigidity Theory and Applications*, M. F. Thorpe and P. M. Duxbury, Eds., Kluwer Academic, 1999, pp. 47–54.
- [186] R. Connelly, “Globally Rigid Symmetric Tensegrities,” *Structural Topology*, vol. 21, pp. 59–78, 1995.
- [187] L. Zhang, B. Maurin, and R. Motro, “Form-Finding of Nonregular Tensegrity Systems,” *Journal of Structural Engineering*, vol. 132, no. 9, pp. 1435–1440, 2006.
- [188] Y. Li, X.-Q. Feng, Y.-P. Cao, and H. Gao, “A Monte Carlo form-finding method for large scale regular and irregular tensegrity structures,” *International Journal of Solids and Structures*, vol. 47, no. 14-15, pp. 1888–1898, 2010.
- [189] S. D. Guest, “Tensegrities and rotating rings of tetrahedra: a symmetry viewpoint of structural mechanics,” *Philosophical Transactions of the Royal Society of London A*, vol. 358, no. 1765, pp. 229–243, 2000.
- [190] J. Y. Zhang, S. D. Guest, and M. Ohsaki, “Symmetric prismatic tensegrity structures: Part I. Configuration and stability,” *International Journal of Solids and Structures*, vol. 46, no. 1, pp. 1–14, 2009.
- [191] C. R. Calladine, “Buckminster Fuller’s “Tensegrity” structures and Clerk Maxwell’s rules for the construction of stiff frames,” *International Journal of Solids and Structures*, vol. 14, pp. 161–172, 1978.

- [192] C. Godsil and G. F. Royle, *Algebraic Graph Theory*. New York: Springer-Verlag, 2001, p. 443.
- [193] K. Bathe, E. Ramm, and E. L. Wilson, “Finite element formulations for large deformation dynamic analysis,” *International Journal for Numerical Methods in Engineering*, vol. 9, no. 2, pp. 353–386, 1975.
- [194] K.-J. Bathe, *Finite element procedures*, Second. Klaus-Jürgen Bathe, 2014.
- [195] M. Bendsøe and O. Sigmund, *Topology Optimization: Theory, Methods and Applications*. Springer, 2003.
- [196] G. Taubin, “An accurate algorithm for rasterizing algebraic curves and surfaces,” *IEEE Computer Graphics and Applications*, vol. 14, pp. 14–23, 1994.
- [197] Gurobi Optimization, *Gurobi Optimizer reference manual*, 6.0. Houston TX: Gurobi Optimization Inc., 2014, p. 572.
- [198] J. J. Felix and G. N. Vanderplaats, “Configuration optimization of trusses subject to strength, displacement and frequency constraints,” *Journal of Mechanisms, Transmissions, and Automation in Design*, vol. 109, no. 2, pp. 233–241, 1987.
- [199] A. G. Tibert and S. Pellegrino, “Deployable tensegrity masts,” in *Proceedings of the 44th AIAA/ASME/ASCE/AHS/ASC Structures, Structural Dynamics, and Materials Conference*, 2003.
- [200] S. Pellegrino, *Deployable structures*. Springer-Verlag Wien, 2001.
- [201] X. Liu, S. Yao, B. S. Cook, M. M. Tentzeris, and S. V. Georgakopoulos, “An origami reconfigurable axial-mode bifilar helical antenna,” *IEEE Transactions on Antennas and Propagation*, vol. 63, pp. 5897–5903, 2015.
- [202] A. G. Tibert and S. Pellegrino, “Deployable tensegrity reflectors for small satellites,” *Journal of Spacecraft and Rockets*, vol. 39, pp. 701–709, 2002.
- [203] K. Kim, A. K. Agogino, D. Moon, L. Taneja, A. Toghyan, B. Dehghani, V. SunSpiral, and A. M. Agogino, “Rapid prototyping design and control of tensegrity soft robot for locomotion,” in *2014 IEEE International Conference on Robotics and Biomimetics (ROBIO 2014)*, 2014.
- [204] G. Carpentieri, R. E. Skelton, and F. Fraternali, “A minimal mass deployable structure for solar energy harvesting on water canals,” *Structural and Multidisciplinary Optimization*, vol. 55, pp. 449–458, 2016.

- [205] T. Liedl, B. Höglberg, J. Tytell, D. E. Ingber, and W. M. Shih, “Self-assembly of three-dimensional prestressed tensegrity structures from DNA,” *Nature Nanotechnology*, vol. 5, pp. 520–524, 2010.
- [206] R. E. Skelton, W. W. Helton, W. Chan, J.-P. Pinaud, and R. Adhikari, “An Introduction to Tensegrity Structures,” in *Proceedings of the 40th IEEE Conference on Decision and Control*, Orlando, Florida: IEEE, 2001, pp. 4254–4259.
- [207] Q. Ge, H. J. Qi, and M. L. Dunn, “Active materials by four-dimension printing,” *Applied Physics Letters*, vol. 103, p. 131901, 2013.
- [208] Y. Mao, K. Yu, M. S. Isakov, J. Wu, M. L. Dunn, and H. J. Qi, “Sequential self-folding structures by 3D printed digital shape memory polymers,” *Scientific Reports*, vol. 5, p. 13616, 2015.
- [209] D. Raviv, W. Zhao, C. McKnelly, A. Papadopoulou, A. Kadambi, B. Shi, S. Hirsch, D. Dikovsky, M. Zyracki, C. Olgun, R. Raskar, and S. Tibbits, “Active printed materials for complex self-evolving deformations,” *Scientific Reports*, vol. 4, p. 7422, 2014.
- [210] J. Wu, C. Yuan, Z. Ding, M. Isakov, Y. Mao, T. Wang, M. L. Dunn, and H. J. Qi, “Multi-shape active composites by 3D printing of digital shape memory polymers,” *Scientific Reports*, vol. 6, p. 24224, 2016.
- [211] S. A. Gladman, E. A. Matsumoto, R. G. Nuzzo, L. Mahadevan, and J. A. Lewis, “Biomimetic 4D printing,” *Nature Materials*, vol. 15, pp. 413–418, 2016.
- [212] Q. Ge, K. D. Conner, H. J. Qi, and M. L. Dunn, “Active origami by 4D printing,” *Smart Materials and Structures*, vol. 23, p. 094007, 2014.
- [213] Y. Mao, Z. Ding, C. Yuan, S. Ai, M. Isakov, J. Wu, T. Wang, M. L. Dunn, and H. J. Qi, “3D printed reversible shape changing components with stimuli responsive materials,” *Scientific Reports*, vol. 6, p. 24761, 2016.
- [214] T. Xie, “Recent advances in polymer shape memory,” *Polymer*, vol. 52, pp. 4985–5000, 2011.
- [215] C. R. Calladine, “The theory of thin shell structures 1888-1988,” in *Proceedings of the Institution of Mechanical Engineers, Part A: Power and Process Engineering 1983-1988*, 1988.
- [216] S. P. Timoshenko and J. M. Gere, *Theory of elastic stability*, Second. Dover Publications, 2009.

- [217] P. A. OConnell and G. B. McKenna, “Arrhenius-type temperature dependence of the segmental relaxation below T_g,” *The Journal of Chemical Physics*, vol. 110, p. 11 054, 1999.
- [218] M. L. Williams, R. F. Landel, and J. D. Ferry, “The temperature dependence of relaxation mechanisms in amorphous polymers and other glass-forming liquids,” *Journal of the American Chemical Society*, vol. 77, pp. 3701–3707, 1955.
- [219] E. A. Di Marzio and A. J. M. Yang, “Configurational entropy approach to the kinetics of glasses,” *Journal of Research of NIST*, vol. 102, pp. 135–157, 1997.
- [220] J. Diani, P. Gilormini, and I. Frédy C. & Rousseau, “Predicting thermal shape memory of crosslinked polymer networks from linear viscoelasticity,” *International Journal of Solids and Structures*, vol. 49, pp. 793–799, 2012.
- [221] P. H. Sherrod, *Nonlinear Regression Analysis Program*, NLREG Version 5.0, 2000.
- [222] F. P. J. Rimrott, “Storable tubular extendible member,” *Machine Design*, vol. 37, pp. 156–165, 1965.
- [223] J. Friesen, A. Pogue, T. Bewley, M. de Oliveira, R. Skelton, and V. Sunspiral, “DuCTT: A tensegrity robot for exploring duct systems,” in *2014 IEEE International Conference on Robotics and Automation (ICRA)*, 2014.
- [224] T. Htay and M. W. Liu, “Drug-eluting stent: A review and update,” *Vascular Health and Risk Management*, vol. 1, no. 4, pp. 263–276, 2005.
- [225] L. Huo, T. Liu, X. Sun, Y. Cai, A. J. Heeger, and Y. Sun, “Singlejunction organic solar cells based on a novel widebandgap polymer with efficiency of 9.7%,” *Advanced Materials*, vol. 27, pp. 2938–2944, 2015.
- [226] Y. Tamura, I. Hatta, T. Matsuda, H. Sugi, and T. Tsuchiya, “Changes in muscle stiffness during contraction recorded using ultrasonic waves,” *Nature*, vol. 299, pp. 631–633, 1982.
- [227] G. J. C. Ettema and P. A. Huijing, “Skeletal muscle stiffness in static and dynamic contractions,” *Journal of Biomechanics*, vol. 27, no. 11, pp. 1361–1368, 1994.
- [228] I. V. Ogneva, D. V. Lebedev, and B. S. Shenkman, “Transversal stiffness and Young’s Modulus of single fibers from rat Soleus muscle probed by Atomic Force Microscopy,” *Biophysical Journal*, vol. 98, no. 3, pp. 418–424, 2010.
- [229] X. Y. Zheng, H. Lee, T. H. Weisgraber, M. Shusteff, J. DeOtte, E. B. Duoss, J. D. Kuntz, M. M. Biener, Q. Ge, J. A. Jackson, S. O. Kucheyev, N. X. Fang, and C. M.

- Spadaccini, “Ultralight, ultrastiff mechanical metamaterials,” *Science*, vol. 344, no. 6190, pp. 1373–1377, 2014.
- [230] L. R. Meza, S. Das, and J. R. Greer, “Strong, lightweight, and recoverable three-dimensional ceramic nanolattices,” *Science*, vol. 345, no. 6202, pp. 1322–1326, 2014.
- [231] J. Christensen, M. Kadic, O. Kraft, and M. Wegener, “Vibrant times for mechanical metamaterials,” *MRS Communications*, vol. 5, no. 3, pp. 453–462, 2015.
- [232] T. A. Schaedler and W. B. Carter, “Architected cellular materials,” *Annual Review of Materials Research*, vol. 46, no. 1, pp. 187–210, 2016.
- [233] F. Fraternali, L. Senatore, and C. Daraio, “Solitary waves on tensegrity lattices,” *Journal of the Mechanics and Physics of Solids*, vol. 60, no. 6, pp. 1137–1144, 2012.
- [234] F. Fraternali, G. Carpentieri, A. Amendola, R. E. Skelton, and V. F. Nesterenko, “Multiscale tunability of solitary wave dynamics in tensegrity metamaterials,” *Applied Physics Letters*, vol. 105, p. 201903, 2014.
- [235] J. J. Rimoli and R. K. Pal, “Mechanical response of 3-dimensional tensegrity lattices,” *Composites Part B: Engineering*, vol. 115, pp. 30–42, 2016.
- [236] F. Fabbrocino and G. Carpentieri, “Three-dimensional modeling of the wave dynamics of tensegrity lattices,” *Composite Structures*, vol. 173, pp. 9–16, 2017.
- [237] A. Al Sabouni-Zawadzka and W. Gilewski, “Smart metamaterial based on the simplex tensegrity pattern,” *Materials*, vol. 11, no. 5, p. 673, 2018.
- [238] Q. Zhang, Y. Dobah, F. Scarpa, F. Fraternali, and R. E. Skelton, “Tensegrity cell mechanical metamaterial with metal rubber,” *Applied Physics Letters*, vol. 113, p. 031906, 2018.
- [239] R. K. Pal, M. Ruzzene, and J. J. Rimoli, “Tunable wave propagation by varying prestrain in tensegrity-based periodic media,” *Extreme Mechanics Letters*, vol. 22, pp. 149–156, 2018.
- [240] A. Amendola, A. Krushynska, C. Daraio, N. M. Pugno, and F. Fraternali, “Tuning frequency band gaps of tensegrity mass-spring chains with local and global prestress,” *International Journal of Solids and Structures* (2018), 2018.
- [241] F. P. Preparata and M. I. Shamos, *Computational Geometry: An Introduction*. Springer, 1993.

- [242] M. de Berg, O. Cheong, M. van Kreveld, and M. Overmars, *Computational Geometry: Algorithms and Applications*. Springer, 2008.
- [243] T. Zegard and G. H. Paulino, “GRAND - Ground structure based topology optimization for arbitrary 2D domains using MATLAB,” *Structural and Multidisciplinary Optimization*, vol. 50, no. 5, pp. 861–882, 2014.
- [244] B. Hassani and E. Hinton, *Homogenization and Structural Topology Optimization: Theory, Practice and Software*. Springer-Verlag London, 1999.
- [245] A. Vigliotti and D. Pasini, “Stiffness and strength of tridimensional periodic lattices,” *Computer Methods in Applied Mechanics and Engineering*, vol. 229–232, pp. 27–43, 2012.
- [246] R. Sedgewick and K. Wayne, *Algorithms*, Fourth. Addison-Wesley Professional, 2011.
- [247] M. Maldovan, “Sound and heat revolutions in phononics,” *Nature*, vol. 503, no. 7475, pp. 209–217, 2013.
- [248] M. I. Hussein, M. J. Leamy, and M. Ruzzene, “Dynamics of phononic materials and structures: Historical origins, recent progress, and future outlook,” *Applied Mechanics Reviews*, vol. 66, no. 4, p. 040 802, 2014.
- [249] P. Wang, F. Casadei, S. Shan, J. C. Weaver, and K. Bertoldi, “Harnessing buckling to design tunable locally resonant acoustic metamaterials,” *Physical Review Letters*, vol. 113, no. 1, p. 014 301, 2014.
- [250] P. P. Pratapa, P. Suryanarayana, and G. H. Paulino, “Bloch wave framework for structures with nonlocal interactions: Application to the design of origami acoustic metamaterials,” *Journal of the Mechanics and Physics of Solids*, vol. 118, pp. 115–132, 2018.
- [251] A. S. Phani, J. Woodhouse, and N. A. Fleck, “Wave propagation in two-dimensional periodic lattices,” *The Journal of the Acoustical Society of America*, vol. 119, no. 4, pp. 1995–2005, 2006.
- [252] Q. Wang, J. A. Jackson, Q. Ge, J. B. Hopkins, C. M. Spadaccini, and N. X. Fang, “Lightweight mechanical metamaterials with tunable negative thermal expansion,” *Physical Review Letters*, vol. 117, p. 175 901, 2016.